
Search for electroweakinos using the ATLAS detector



LUDWIG-MAXIMILIANS-UNIVERSITY MUNICH
FACULTY OF PHYSICS

DISSERTATION

Eric Schanet
March 2021

Suche nach Elektroweakinos mit dem ATLAS Detektor



LUDWIG-MAXIMILIANS-UNIVERSITÄT MÜNCHEN
FAKULTÄT FÜR PHYSIK

DISSERTATION

Eric Schanet
March 2021

Supervisor: PD Dr. Jeanette Lorenz

There is a particularly common and—at least until recently—widely believed seafarers' tale which may be heard everywhere from the most noisome seafront dives to the elegant drawing rooms of the ship-owning aristocracy. This is ‘supersymmetry’. It is a seductive story. It offers many things to the excitable traveller, and one of the things it offers is Dark Matter.

Let us hope that new experiments … will soon reveal new physics beyond the Standard Model. Perhaps it will look something like the possibilities discussed, but let us hope that it will take us beyond the beyonds imagined by theorists.

Abstract

My abstract

Zusammenfassung

Meine Zusammenfassung

Contents

I	Fundamental concepts	5
1	Theory	7
1.1	The Standard Model of Particle Physics	7
1.1.1	Particle content of the SM	8
1.1.2	The SM as a gauge theory	9
1.1.3	Renormalisation and divergencies	19
1.2	Supersymmetry	19
1.2.1	Shortcomings of the Standard Model	20
1.2.2	Supersymmetric Algebra	24
1.2.3	Supermultiplets	25
1.2.4	Supersymmetric Lagrangian	25
1.2.5	The Minimal Supersymmetric Standard Model	27
1.2.6	The phenomenological MSSM	32
1.2.7	Simplified models	33
1.3	Search for electroweakinos	34
1.3.1	Production of electroweakinos at the Large Hadron Collider	35
1.3.2	Models used within this work	35
2	Experiment	37
2.1	The Large Hadron Collider	37
2.1.1	Pile-up	39
2.1.2	Luminosity and data-taking	40
2.2	ATLAS Experiment	42
2.2.1	Coordinate system	43
2.2.2	Magnet system	44

2.2.3	Inner detector	45
2.2.4	Calorimeters	46
2.2.5	Muon spectrometer	49
2.2.6	Forward detectors	50
2.2.7	Trigger and data acquisition system	50
2.2.8	Monte Carlo simulation	51
3	Statistical data analysis	57
3.1	The likelihood function	57
3.2	Parameter estimation	59
3.3	Statistical tests	59
3.4	CL_s approach	62
3.5	Sensitivity estimation	63
II	The 1-lepton analysis	65
4	Analysis overview	67
4.1	Search for electroweakinos in the 1-lepton final state	67
4.2	Standard Model backgrounds	68
4.3	Monte Carlo samples	69
4.3.1	Signal samples	69
4.3.2	Background samples	70
4.4	Object definitions	70
4.4.1	Tracks and vertices	71
4.4.2	Electrons and Photons	72
4.4.3	Muons	73
4.4.4	Jets	74
4.4.5	Flavour tagging	75
4.4.6	Missing transverse momentum	75
4.5	Overlap removal	76
4.6	Analysis variables	77
4.7	Trigger strategy	81
4.8	Event cleaning	82

5 Signal region optimisation	83
5.1 Optimisation methods	83
5.1.1 Multidimensional cut scan	83
5.1.2 N-1 plots	85
5.1.3 Fit scans	85
5.2 Optimisation procedure	85
5.2.1 Benchmark signal points	85
5.2.2 Towards the final signal regions	87
5.3 Signal region definitions	89
6 Background estimation	95
6.1 General strategy	95
6.1.1 Transfer factor approach	95
6.1.2 Analysis blinding	96
6.1.3 Data versus Monte Carlo plots	97
6.2 Control regions	97
6.3 Validation regions	99
7 Systematic uncertainties	103
7.1 Experimental uncertainties	103
7.1.1 Pile-up reweighting and luminosity	103
7.1.2 Triggers	104
7.1.3 Leptons	104
7.1.4 Jets	104
7.1.5 Flavour tagging	105
7.1.6 Missing transverse energy	105
7.2 Theoretical uncertainties	105
7.2.1 Background	106
7.2.2 Signal	108
7.3 Impact on signal regions	108
8 Results	111
8.1 Background-only fit results	111
8.1.1 Results in the control regions	111

8.1.2	Results in the validation regions	113
8.1.3	Results in the signal regions	115
8.2	Interpretation	119
8.2.1	Model-independent upper limits	119
8.2.2	Model-dependent exclusion limits	119
8.3	Discussion	120
III	Reinterpretation	121
9	Simplified likelihoods	123
10	Reinterpretation in the pMSSM	125
10.1	Sampling	125
IV	Summary and Outlook	127
11	Summary	129
V	Appendix	131
	Appendix A	133
A.1	N-1 plots for cut-scan results	133
	Appendix B	143
B.1	Background estimation	143
	Bibliography	149

Notes

Natural units and Minkowski metric	3
Couplings and masses are measured from experiment	8
Write somewhere SU2xU1 to U1 breakdown	18
Mass dimension needs to be < 4	19
DM relic density	20
Mention link to gravity	25
Reference, why?	36
is this true?	51
simulation tools allow to plugin any Lagrangian and get events at detector level	52
Explain this further	58
refer to observables	67
truth jets	74
Need presel plots for these	85
is this conf up-to-date?	86
prefit plots of VR?	99
Plots from HF numbers?	108
quote exact numbers	113
citation	120

Introduction

Here is my introduction

Natural
units and
Minkowski
metric

Part I

Fundamental concepts

Chapter 1

Theory

This chapter starts with an outline of the basic principles and concepts of the Standard Model of Particle Physics, the theoretical framework describing nature on the level of elementary particles. This is followed by an introduction to Supersymmetry, a promising class of theories aiming to solve some of the shortcomings of the Standard Model of Particle Physics (SM). By no means intended to be a full description, this chapter aims to highlight the important relations and consequences of the SM and Supersymmetry. A much more detailed introduction can be found in the references that the mathematical description in this chapter is based upon, namely Refs. [1, 2] for the SM and Refs. [3, 4] for Supersymmetry.

1.1 The Standard Model of Particle Physics

By the end of the 1920s, quantum mechanics and general relativity had been relatively well established and the consensus among physicists was that matter is composed of nuclear atoms consisting of electrons and protons. During the 1930s, a multitude of new experimental discoveries and theoretical puzzles excited physicists in three main currents of research: nuclear physics, cosmic rays and relativistic quantum mechanics [5]. Open questions at this time included e.g. the continuous spectrum of the β -decay, the nature of cosmic rays, or the negative energy states in Dirac's relativistic electron theory. As a result of these currents ultimately flowing together, the following decades saw elementary particle physics emerge as a new field of research.

Since these early times of particle physics, extraordinary progress has been made in describing nature at the subatomic scale. Today, a century later, the resulting theoretical framework, the SM, is the most fundamental, experimentally validated theory of nature known to mankind. It provides an extremely precise description of the interactions of elementary particles and—using the Large Electron Positron (LEP) collider—has been tested to an unprecedented level of accuracy up to the electroweak (EWK) scale. Given the remarkable success of the SM, it is not surprising that its history is paved with numerous awards for both experimental and theoretical work. In 1964, the Nobel prize was awarded to Feynman, Schwinger and Tomonaga for their fundamental work in quantum electrodynamics (QED), a quantum field theory allowing the precise calculation of fundamental processes like e.g. the anomalous magnetic moment of the electron that is known to a relative experimental uncertainty of 2.3×10^{-10} [6]. In 1979,

Table 1.1: Names, electric charges and masses (rounded to three significant digits if known to that precision) of all observed fermions in the SM [7]. The symbols used in the following are indicated in parentheses after the particle names.

	generation	particle	electric charge [e]	mass
leptons	1	electron (e)	-1	511 keV
		electron neutrino (ν_e)	0	< 1.1 eV
	2	muon (μ)	-1	106 MeV
		muon neutrino (ν_μ)	0	< 0.19 MeV
	3	tau (τ)	-1	1.78 GeV
		tau neutrino (ν_τ)	0	< 18.2 MeV
quarks	1	up (u)	$\frac{2}{3}$	2.16 MeV
		down (d)	$-\frac{1}{3}$	4.67 MeV
	2	charm (c)	$\frac{2}{3}$	1.27 GeV
		strange (s)	$-\frac{1}{3}$	93 MeV
	3	top (t)	$\frac{2}{3}$	173 GeV
		bottom (b)	$-\frac{1}{3}$	4.18 GeV

Glashow, Weinberg and Salam were awarded the Nobel prize for their work towards electroweak unification. The most prominent recent progress undoubtedly is the discovery of the Higgs boson, not only resulting in the Nobel prize being awarded to Englert and Higgs, but also completing the SM, roughly 50 years after the existence of the Higgs boson had been theorised.

Couplings and masses are measured from experiment

1.1.1 Particle content of the SM

Apart from the experimentally non-vanishing neutrino masses, the SM successfully describes ordinary matter as well as their interactions, namely the electromagnetic, weak and strong interactions, leaving gravity as the only fundamental force not described within the SM. The particles in the SM are classified into two main categories, depending on their spin. Particles with half-integer spin follow Fermi-Dirac statistics and are called *fermions*. As they are subject to the Pauli exclusion principle, they make up ordinary matter. Particles with integer spin are called *bosons*, follow Bose-Einstein statistics and mediate the fundamental interactions between fermions.

Fermions are further divided into leptons and quarks, that each come in three generations with increasing masses[†]. The three electrically charged leptons are each associated to a corresponding neutral neutrino (more on this association in chapter section 1.1.2). While the SM assumes massless neutrinos, the observation of neutrino oscillations [8] implies the existence of at least two massive neutrinos. By extending the SM to allow non-vanishing neutrino masses, neutrino oscillations can be introduced through lepton generation mixing, described by the Pontecorvo–Maki–Nakagawa–Sakata (PMNS) matrix [9]. Apart from an electric charge, the six quarks also carry a colour charge, of which three types exist: *red*, *green* and *blue* as well as their respective anti-colours. The mixing in the quark sector through the weak interaction can be described by the Cabibbo–Kobayashi–Maskawa (CKM) matrix [10, 11]. Finally, each fermion comes with its

[†] Neutrinos might not exist in a normal mass hierarchy but could also have an inverted mass hierarchy.

Table 1.2: Names, electric charges and masses (rounded to three significant digits if known to that precision) of all observed bosons in the SM [7]. The symbols used in the following are indicated in parentheses after the particle names.

particle	spin	electric charge [e]	mass
photon (γ)	1	0	0
gluon (g)	1	0	0
W^\pm	1	± 1	80.4 GeV
Z^0	1	0	91.2 GeV
Higgs boson (h)	0	0	125 GeV

own anti-particle with same mass and spin, but inverted charge-like quantum numbers[†]. All fermions in the SM are listed in table 1.1.

The fundamental forces described by the SM are propagated by bosons with spin-1. The photon γ couples to electrically charged particles and mediates the electromagnetic interaction. As the photon is massless, the electromagnetic force has infinite range. The strong force is mediated by gluons carrying one unit of colour and one unit of anti-colour. Due to colour-confinement, colour charged particles like quarks and gluons cannot exist as free particles and instead will always form colour-neutral bound states. Although nine gluon states would theoretically be possible, only eight of them are realised in nature—the colour-singlet state $\frac{1}{\sqrt{3}}(|r\bar{r}\rangle + |g\bar{g}\rangle + |\bar{b}\bar{b}\rangle)$ would result in long-range strong interactions, which have not been observed. Finally, the weak force is mediated by a total of three bosons, two charged W^\pm bosons and a neutral Z boson. The mediators of the weak force are massive, resulting in a finitely ranged interaction. They gain their masses through the Higgs mechanism (discussed in chapter section 1.1.2). All bosons known to the SM are listed in table 1.2.

1.1.2 The SM as a gauge theory

Formally, the SM is a collection of a special type of quantum field theories (QFTs), called gauge theories. QFT is the application of quantum mechanics to dynamical systems of fields—just as quantum mechanics is the quantisation of dynamical systems of particles—providing a uniform description of quantum mechanical particles and classical fields, while including special relativity.

In classical mechanics, the fundamental quantity is the action S , which is the time integral of the Lagrangian L , a functional characterising the state of a system of particles in terms of generalised coordinates q_1, \dots, q_n . In field theory, the Lagrangian can be written as spatial integral of a Lagrangian density $\mathcal{L}(\phi_i, \partial_\mu \phi_i)$, which is a function of fields ϕ_i and their spacetime derivatives $\partial_\mu \phi_i$. In the following, the Lagrangian density \mathcal{L} will simply be referred to as the *Lagrangian*. The action can then be written as

$$S = \int L dt = \int \mathcal{L}(\phi_i, \partial_\mu \phi_i) d^4x. \quad (1.1)$$

[†] The exact nature of anti-neutrinos is still an open question and ties into whether or not the neutrino mass matrix contains non-vanishing Majorana mass terms.

Using the principle of least action $\delta S = 0$, the equation of motions for each field are given by the Euler-Lagrange-equation,

$$\partial_\mu \left(\frac{\partial \mathcal{L}}{\partial (\partial_\mu \phi_i)} \right) - \frac{\partial \mathcal{L}}{\partial \phi_i} = 0. \quad (1.2)$$

As opposed to the Hamiltonian formalism, the Lagrange formulation of field theory is especially well suited for the relativistic dynamics in particle physics, as it exhibits explicit Lorentz-invariance [2]. This is a direct consequence of the principle of least action, since boosted extrema in the action will still be extrema for Lorentz-invariant Lagrangians.

Symmetries are of central importance in the SM. As Emmy Noether has famously shown in 1918 for classical mechanics, every continuous symmetry of the action has a corresponding conservation law [12]. In the context of classical field theory, each generator of a continuous internal or spacetime symmetry transformation leads to a conserved current, and thus to a conserved charge. In QFTs, quantum versions of Noether's theorem, called Ward–Takahashi identities [13, 14] for Abelian theories and Slavnov–Taylor identities [15–17] for non-Abelian theories relate the conservation of quantum currents and charge-like quantum numbers to continuous symmetries of the Lagrangian.

From a theoretical point of view, the SM can be described by a non-Abelian Yang-Mills type [18] gauge theory based on the symmetry group

$$SU(3)_C \otimes SU(2)_L \otimes U(1)_Y,$$

where $U(n)$ ($SU(n)$) describes (special) unitary groups, i.e. the Lie groups of $n \times n$ unitary matrices (with determinant 1, if special). $SU(3)_C$ generates quantum chromodynamics (QCD), describing the interaction of particles with colour charge C through exchange of gluons, and $SU(2)_L \otimes U(1)_Y$ generates the electroweak interaction. Here, the subscript Y represents the weak hypercharge, while the L indicates that $SU(2)_L$ only couples to left-handed particles (right-handed antiparticles).

Feynman diagrams

Transitioning from classical field theory to quantum field theory is typically done through either canonical quantisation or the usage of path integral formalism. As only the the simplest field theories can be solved analytically, i.e. those containing only free fields and no interactions, perturbation theory is used for calculating scattering cross sections and decay rates for any QFT containing interactions. Any transition matrix can then be written as a series expansion in the coupling constant, with each term represented by Feynman diagrams.

Using appropriate Feynman rules dictating the possible vertices (representing interactions between fields) and propagators (representing the propagation of fields), an infinite number of Feynman diagrams can be written down. Given the incoming and outgoing particles, all possible combinations of propagators and vertices that can be placed in between (i.e. all possible Feynman diagrams) represent the full perturbation series. Only the lowest order in the series is considered at leading order (LO), the next-lowest at next-to-leading order (NLO), and so on.

Gauge principle

The gauge principle is fundamental to the SM and dictates that the existence of gauge fields is directly related to symmetries under local gauge transformations. QED, being the simplest gauge theory, can be taken to illustrate this important principle. The free Dirac Lagrangian for a single, non-interacting fermion with mass m is given by

$$\mathcal{L}_{\text{Dirac}} = \bar{\psi} (i\gamma^\mu \partial_\mu - m) \psi, \quad (1.3)$$

where ψ is a four-component complex spinor field, $\bar{\psi} = \psi^\dagger \gamma^0$, and γ^μ with $\mu = 0, 1, 2, 3$ are the Dirac matrices with the usual anticommutation relations generating a matrix representation of the Dirac algebra

$$\{\gamma^\mu, \gamma^\nu\} \equiv \gamma^\mu \gamma^\nu + \gamma^\nu \gamma^\mu = 2\eta^{\mu\nu} \mathbb{1}_4. \quad (1.4)$$

It is worth noting that the free Dirac Lagrangian is invariant under a global $U(1)$ transformation

$$\psi \rightarrow e^{i\theta} \psi, \quad (1.5)$$

where the phase θ is spacetime independent and real-valued. In order to produce the physics of electromagnetism, the free Dirac Lagrangian however has to be invariant under *local* $U(1)$ phase transformations, which is not the case, as the transformed Lagrangian picks up an additional term from the spacetime derivative of the phase, $\partial_\mu \theta(x)$.

For the Dirac Lagrangian to become invariant under a local gauge transformation, a new vector field $A_\mu(x)$ has to be introduced and the partial derivative has to be replaced with the covariant derivative

$$\partial_\mu \rightarrow D_\mu \equiv \partial_\mu + ieA_\mu, \quad (1.6)$$

where e can be identified with the elementary charge and represents the coupling of the fermion field to the gauge field A_μ . The prescription of achieving local gauge invariance by replacing ∂_μ with D_μ is called *minimal coupling* and leads to a Lagrangian that is invariant under the transformations

$$\psi \rightarrow e^{i\theta(x)} \psi, \quad A_\mu \rightarrow A_\mu - \frac{1}{e} \partial_\mu \theta(x). \quad (1.7)$$

The modified Lagrangian now includes a term for interactions between the gauge field and the fermion field,

$$\begin{aligned} \mathcal{L} &= \mathcal{L}_{\text{Dirac}} + \mathcal{L}_{\text{int}} \\ &= \bar{\psi} (i\gamma^\mu \partial_\mu - m) \psi - (e\bar{\psi} \gamma^\mu \psi) A_\mu, \end{aligned} \quad (1.8)$$

and is indeed invariant under a local phase transformation. Yet, it cannot be complete as it is still missing a term describing the kinematics of the free gauge field A_μ . For a vector field, the kinetic term is described by the Proca Lagrangian

$$\mathcal{L}_{\text{Proca}} = -\frac{1}{4} F_{\mu\nu} F^{\mu\nu} + \frac{1}{2} m_A^2 A^\nu A_\nu, \quad (1.9)$$

where $F^{\mu\nu} \equiv (\partial^\mu A^\nu - \partial^\nu A^\mu)$ is the field strength tensor that is invariant under the transformation in eq. (1.7). Since $A^\nu A_\nu$ is not invariant under the same transformation, the only way to

keep the full Lagrangian invariant under a local phase transformation is by requiring $m_A = 0$, i.e. the introduced gauge field A_μ has to be massless, giving the Maxwell Lagrangian (ultimately generating the Maxwell equations),

$$\mathcal{L}_{\text{Maxwell}} = -\frac{1}{4}F_{\mu\nu}F^{\mu\nu}. \quad (1.10)$$

This finally yields the full Lagrangian

$$\begin{aligned} \mathcal{L}_{\text{QED}} &= \mathcal{L}_{\text{Dirac}} + \mathcal{L}_{\text{Maxwell}} + \mathcal{L}_{\text{int}} \\ &= \bar{\psi}(i\gamma^\mu\partial_\mu)\psi - m\bar{\psi}\psi - \frac{1}{4}F^{\mu\nu}F_{\mu\nu} - (e\bar{\psi}\gamma^\mu\psi)A_\mu, \end{aligned} \quad (1.11)$$

which can be identified to be the full Lagrangian of QED. The introduced gauge field A_μ is therefore nothing else than the electromagnetic potential with its associated massless particle, the photon. Thus, by applying the gauge principle on the free Dirac Lagrangian, i.e. forcing a global phase invariance to hold locally, a new massless gauge field has to be introduced, including interaction terms with the existing fields in the Lagrangian. In the case of the free Dirac Lagrangian, local gauge invariance produces all of QED.

As Yang and Mills have shown in 1954 [18], requiring a global phase invariance to hold locally is perfectly possible in the case of any continuous symmetry group. Considering a general non-Abelian symmetry group G , represented by a set of $n \times n$ unitary matrices $U(\alpha^1, \dots, \alpha^N)$, parametrised by N real parameters $\alpha^1, \dots, \alpha^N$, then a gauge-invariant Lagrangian can be constructed with a similar prescription [1] as previously in the case of $U(1)$.

A total of n fermion fields with mass m are needed, arranged in an n -dimensional multiplet $\Psi = (\psi_1, \dots, \psi_n)^T$. The free Lagrangian,

$$\mathcal{L}_{\text{free}} = \bar{\Psi}(i\gamma^\mu\partial_\mu - m)\Psi, \quad (1.12)$$

is invariant under a global phase transformation of the form

$$\Psi(x) \rightarrow U(\alpha^1, \dots, \alpha^N)\Psi(x). \quad (1.13)$$

Each element in the set of transformations U can be written in terms of the group generators T^a as

$$U(\alpha^1, \dots, \alpha^N) = e^{i\alpha^a T^a}, \quad (1.14)$$

where the group indices $a = 1, \dots, N$ are to be summed over. The group generators T^a satisfy the commutation relations

$$[T^a, T^b] = if^{abc}T^c, \quad (1.15)$$

where f^{abc} are the so-called structure constants quantifying the lack of commutativity between the generators. By convention, the basis for the generators T^a is typically chosen such that f^{abc} is completely anti-symmetric [1]. In order to make the Lagrangian invariant under local phase transformations, i.e. under transformations with a set of spacetime-dependent real parameters $\alpha^a(x)$, a vector field \mathbf{W}_μ together with a coupling constant g have to be introduced through the covariant derivative

$$\partial_\mu \rightarrow D_\mu = \partial_\mu - ig\mathbf{W}_\mu. \quad (1.16)$$

As D_μ acts on the n -dimensional multiplet Ψ , the introduced gauge field \mathbf{W}_μ has to be an $n \times n$ matrix and can thus be expanded in terms of the generators

$$\mathbf{W}_\mu(x) = T^a W_\mu^a(x), \quad (1.17)$$

thereby explicitly illustrating, that a total of N gauge fields W_μ^a are introduced through the covariant derivative. Similar to QED above, the covariant derivative also introduces an interaction term of the form

$$\mathcal{L}_{\text{int}} = g \bar{\Psi} \gamma^\mu \mathbf{W}_\mu \Psi, \quad (1.18)$$

into the Lagrangian in eq. (1.12), coupling the gauge fields W_μ^a to the fermion multiplet. For infinitesimal $\alpha^a(x)$, the gauge fields gauge transform according to

$$W_\mu^a \rightarrow W_\mu^a + \frac{1}{g} \partial_\mu \alpha^a + f^{abc} W_\mu^b \alpha^c, \quad (1.19)$$

where the term with α^a looks familiar from the $U(1)$ example and corresponds to the Abelian case, while the term with f^{abc} introduces the non-Abelian structure into the theory [1]. The same non-Abelian structure is again clearly visible when introducing a kinetic term for the gauge fields into the Lagrangian

$$\mathcal{L}_W = -\frac{1}{4} F_{\mu\nu}^a F^{\mu\nu,a}, \quad (1.20)$$

with the field-strength tensor now $F_{\mu\nu}^a = \partial_\mu W_\nu^a - \partial_\nu W_\mu^a + g f^{abc} W_\mu^b W_\nu^c$. As was already the case for QED, the above Lagrangian contains Abelian terms quadratic in W , describing the propagation of the free gauge fields. This time, the Lagrangian however also contains non-Abelian terms cubic and quartic in W , leading to self-interaction of the gauge fields.

Quantum chromodynamics

QCD, the gauge theory describing the strong interaction between quarks and gluons in the SM, is an example for a non-Abelian Yang-Mills theory. QCD is based on the gauge group $SU(3)_C$, with the subscript C indicating that the quantum number associated with the symmetry group is the *colour*. Each quark is described by a triplet of fermion fields $q = (q_r, q_g, q_b)^T$, where the subscripts refer to the three different colours. The symmetry group $SU(3)$ has a total of $n^2 - 1 = 8$ generators, usually expressed in terms of the Gell-Mann matrices λ^a [2]. The covariant derivative introducing the gauge fields G_μ^a acting on the quark triplets is then

$$D_\mu = \partial_\mu - i g_s \frac{\lambda^a}{2} G_\mu^a, \quad (1.21)$$

with g_s the coupling constant of the strong interaction, typically written as $\alpha_s = g_s^2/(4\pi)$ in analogy to the fine-structure constant in QED. Gauge invariance thus introduces a total of $N = 8$ gauge fields that can be identified with the eight gluons, leading to the full Lagrangian of QCD

$$\mathcal{L}_{\text{QCD}} = \sum_q \bar{q} (i \gamma^\mu \partial_\mu - m_q) q - \sum_q -g_s \bar{q} \gamma^\mu \frac{\lambda^a}{2} q G_\mu^a - \frac{1}{4} G_{\mu\nu}^a G^{\mu\nu,a}, \quad (1.22)$$

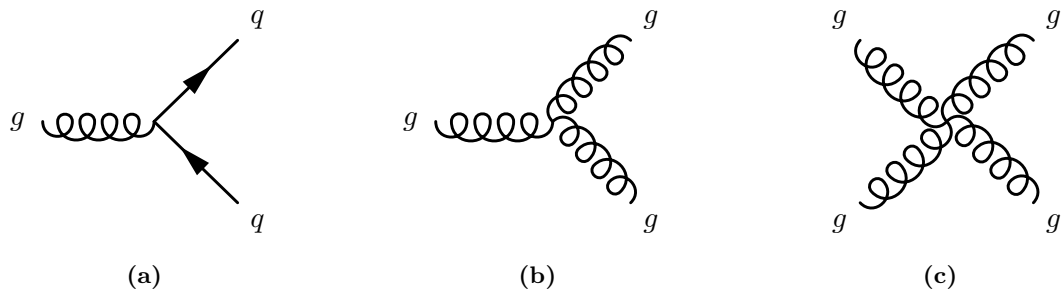


Figure 1.1: Possible vertices in QCD.

where $q = u, d, s, c, b, t$ and $G_{\mu\nu}^a$ are the gluon field strengths given by

$$G_{\mu\nu}^a = \partial_\mu G_\nu^a - \partial_\nu G_\mu^a + g_s f^{abc} G_\mu^b G_\nu^c. \quad (1.23)$$

As expected from the previous section, \mathcal{L}_{QCD} contains terms that are cubic and quartic in the gluon fields, resulting in gluon self-interaction in the theory. All possible QCD interaction vertices involving gluons and quarks are shown in fig. 1.1. The gluon self-interaction leads to a number of phenomena unknown to Abelian theories, rendering the kinematics of QCD highly non-trivial.

In QCD, an effect similar to the electric charge screening in QED happens through quark-antiquark pairs, resulting in a screening of the colour charge. However, the existence of gluon loops in the gluon propagator due to gluon self-interaction creates an opposing *antiscreening* effect of colour charges. At short distances or large momentum scales, colour-charged particles essentially become free particles, a phenomenon called *asymptotic freedom*. In this regime, where α_s is sufficiently small, QCD processes can be calculated using perturbation theory. At large distances or small moment scales however, α_s becomes large and gluons interact very strongly with colour-charged particles, meaning that no free gluons or quarks can exist. This phenomenon is called *confinement* and implies that free quarks and gluons will be subject to *hadronisation*, i.e. form colourless bound states by combining with other quarks or gluons (that can be created from the vacuum). In a particle detector, hadronisation manifests itself as collimated showers of particles, called *jets*. At momentum scales where the strong coupling α_s becomes large ($\alpha_s \approx \mathcal{O}(1)$), QCD processes can no longer be calculated using perturbation theory and instead lattice QCD [19, 20] is used.

Electroweak interaction

During the 1960s, Glashow, Weinberg and Salam [21–23] developed a unified theory of the electromagnetic and weak interactions, based on the $SU(2)_L \otimes U(1)_Y$ symmetry group. Known already experimentally from the Wu experiment [24] in 1956, weak interaction violates parity, i.e. the symmetry transformations have to act differently on the left-handed and right-handed fermion fields. The left- and right-handed components of a fermion field can be projected out using

$$\psi_L = \frac{1 - \gamma^5}{2} \psi, \quad \psi_R = \frac{1 + \gamma^5}{2} \psi, \quad (1.24)$$

with $\gamma^5 = i\gamma^0\gamma^1\gamma^2\gamma^3$. As the weak interaction only acts on left-handed fermions, they can be ordered as $SU(2)$ doublets

$$\begin{pmatrix} \nu_e \\ e \end{pmatrix}_L, \quad \begin{pmatrix} u \\ d \end{pmatrix}_L, \quad \begin{pmatrix} \nu_\mu \\ \mu \end{pmatrix}_L, \quad \begin{pmatrix} c \\ s \end{pmatrix}_L, \quad \begin{pmatrix} \nu_\tau \\ \tau \end{pmatrix}_L, \quad \begin{pmatrix} t \\ b \end{pmatrix}_L. \quad (1.25)$$

The quantum number associated with $SU(2)$ symmetry transformations is called weak isospin I with third component I_3 . Fermion doublets have $I = 1/2$, with the upper component having $I_3 = 1/2$ and the lower component $I_3 = -1/2$. Right-handed fermion fields have $I = 0$, i.e. are singlet states in weak isospin space

$$e_R, u_R, d_R, \quad \mu_R, c_R, s_R, \quad \tau_R, t_R, b_R, \quad (1.26)$$

and thus do not couple to the weak interaction. In the electroweak theory, neutrinos are assumed to be strictly massless, therefore no right-handed neutrino singlets exist.

The fermion doublets can be written in a free Lagrangian similar to eqs. (1.3) and (1.12),

$$\mathcal{L} = \bar{\psi}_L i\gamma^\mu \partial_\mu \psi_L, \quad (1.27)$$

with one crucial difference—the omission of the fermion masses. As $\bar{\psi}\psi = \bar{\psi}_L\psi_R + \bar{\psi}_R\psi_L$, mass terms would mix left- and right-handed terms and break gauge invariance. Section 1.1.2 will illustrate how fermion masses will instead be generated in the electroweak theory. For left-handed fermion fields, local $SU(2)_L$ transformations can be written as

$$\psi_L \rightarrow \exp\left(ig_2\alpha^a \frac{\sigma^a}{2}\right) \psi_L, \quad (1.28)$$

where g_2 is the coupling constant, α^a (with $a = 1, 2, 3$) are real parameters and the Pauli matrices σ^a are the generators of $SU(2)_L$. By introducing the covariant derivative $D_\mu = \partial_\mu + ig_2 \frac{\sigma^a}{2} W_\mu^a$ and including the usual kinetic term for the gauge fields, the Lagrangian becomes invariant under $SU(2)_L$ transformations and reads

$$\mathcal{L} = \bar{\psi}_L i\gamma^\mu D_\mu \psi_L - \frac{1}{4} W_{\mu\nu}^a W^{\mu\nu,a}, \quad (1.29)$$

with the gauge field strength tensors $W_{\mu\nu}^a = \partial_\mu W_\nu^a - \partial_\nu W_\mu^a + g_2 \epsilon^{abc} W_\mu^b W_\nu^c$ where ϵ^{abc} are the structure constants. As previously in the case of QCD, the non-Abelian structure of the symmetry group causes self-interactions of the gauge fields.

In order to include electromagnetic interactions, the weak isospin group is extended with the $U(1)_Y$, corresponding to the multiplication of a phase factor $e^{i\alpha \frac{Y}{2}}$ to each of the preceding doublets and singlets. Here, Y is the weak hypercharge as given by the Gell-Mann–Nishijima relation [25–27],

$$Q = I_3 + \frac{Y}{2}, \quad (1.30)$$

with Q the electric charge. The electromagnetic group $U(1)_{\text{em}}$ is then a subgroup of the combined electroweak gauge group [2].

By modifying the covariant derivative to include a $U(1)_Y$ gauge field and ensuring that $U(1)_Y$ acts the same on left-handed and right-handed fermions, it becomes $D_\mu = \partial_\mu + ig_2 \frac{\sigma^a}{2} W_\mu^a + ig_1 \frac{Y}{2} B_\mu$ for left-handed fermions and $D_\mu = \partial_\mu + ig_1 \frac{Y}{2} B_\mu$ for right-handed fermions. The full electroweak Lagrangian then is

$$\begin{aligned}\mathcal{L}_{\text{electroweak}} &= \sum_j^6 \bar{\psi}_L^j i\gamma^\mu \left(\partial_\mu - ig_2 \frac{\sigma^a}{2} W_\mu^a + ig_1 \frac{Y}{2} B_\mu \right) \psi_L^j \\ &\quad + \sum_j^9 \bar{\psi}_R^j i\gamma^\mu \left(\partial_\mu + ig_1 \frac{Y}{2} B_\mu \right) \psi_R^j,\end{aligned}\tag{1.31}$$

where $B_{\mu\nu} = \partial_\mu B_\nu - \partial_\nu B_\mu$, as usual.

Spontaneous symmetry breaking

In the electroweak theory a total of three vector fields W_μ^a and one vector field B_μ are associated with the gauge groups $SU(2)_L$ and $U(1)_Y$, respectively. As has been shown explicitly through the example of QED in section 1.1.2, the gauge fields need to be massless for the resulting Lagrangian to be gauge invariant under the respective symmetry group. In addition, the electroweak symmetry group does not allow for fermion masses. Both gauge bosons of the weak interaction and the fermion are however manifestly massive, hence the electroweak symmetry has to be broken in the SM.

This spontaneous symmetry breaking is achieved through the Brout–Englert–Higgs mechanism [28–30]. In the SM, an isospin doublet of complex scalar fields, called Higgs doublet, is introduced

$$\Phi(x) = \begin{pmatrix} \phi^+(x) \\ \phi^0(x) \end{pmatrix}.\tag{1.32}$$

The Higgs doublet has hypercharge $Y = 1$, hence according to eq. (1.30), ϕ^+ has electric charge $+1$ while ϕ^0 is electrically neutral. With the covariant derivative introduced in section 1.1.2, the Higgs doublet gets an associated part in the SM Lagrangian,

$$\mathcal{L}_h = (D_\mu \Phi)^\dagger (D^\mu \Phi) - V(\Phi),\tag{1.33}$$

where $V(\Phi)$ is a gauge invariant potential

$$V(\Phi) = -\mu^2 \Phi^\dagger \Phi + \frac{\lambda}{4} (\Phi^\dagger \Phi)^2.\tag{1.34}$$

For positive and real parameters μ^2 and λ , this potential has the form of a *Mexican hat* and an infinite number of minima for field configurations with $\Phi^\dagger \Phi = 2\mu^2/\lambda$. In the vacuum, i.e. in the ground state of the theory with minimal potential energy of the field, one of these minima is chosen such that the Higgs receives a vacuum expectation value (VEV)

$$\langle \Phi \rangle = \frac{1}{\sqrt{2}} \begin{pmatrix} 0 \\ v \end{pmatrix} \quad \text{with} \quad v = \frac{2\mu}{\sqrt{\lambda}} \approx 246 \text{ GeV}.\tag{1.35}$$

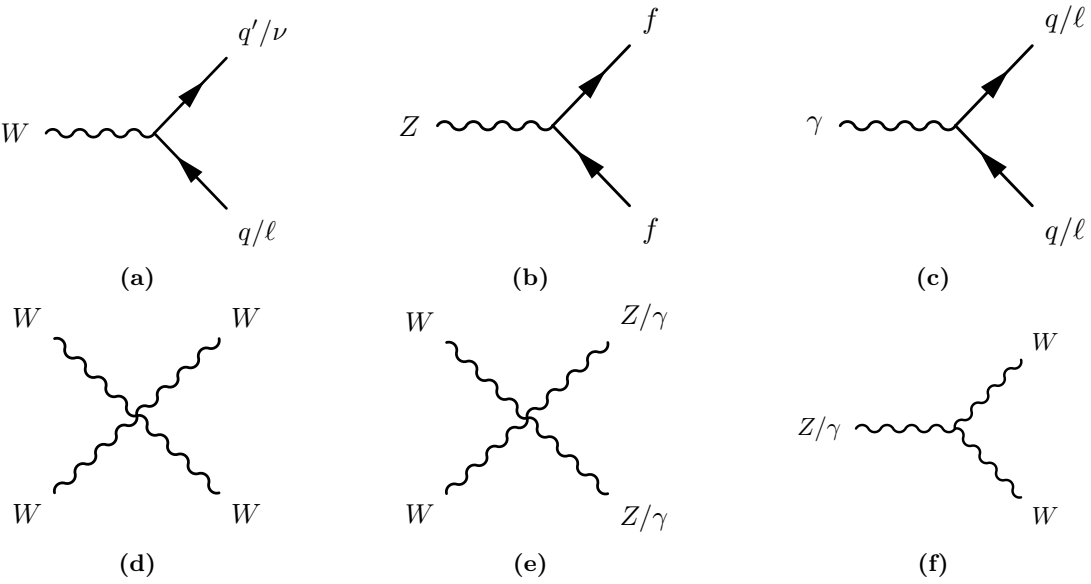


Figure 1.2: Possible vertices in the electroweak interaction.

This is neither invariant under a $SU(2)_L$ transformation of the form $U = \exp(i\alpha^a \frac{\sigma^a}{2})$, nor under a $U(1)_Y$ transformation of the form $\exp(i\alpha \frac{Y}{2})$ [1]. Therefore, the electroweak gauge symmetry is spontaneously broken meaning that the Lagrangian has a symmetry that the vacuum does not have. It is worth noting that the $U(1)_{\text{em}}$ gauge symmetry is not broken as the VEV of ϕ^+ vanishes and ϕ^0 is invariant under $U(1)_{\text{em}}$.

The Higgs doublet can be expressed as excitations around the ground state

$$\Phi(x) = \frac{1}{\sqrt{2}} \begin{pmatrix} \phi_1(x) + i\phi_2(x) \\ v + h(x) + i\chi(x) \end{pmatrix}, \quad (1.36)$$

where h , χ , ϕ_1 and ϕ_2 are real-valued scalar fields with vanishing VEV. The Higgs potential can then be written as

$$V = \mu^2 h^2 + \frac{\mu^2}{v} h(h^2 + \chi^2 + \phi_1^2 + \phi_2^2) + \frac{\mu^2}{4v^2} (h^2 + \chi^2 + \phi_1^2 + \phi_2^2), \quad (1.37)$$

where only h gets a mass term, thus describing an electrically neutral scalar particle with mass $m_h = \sqrt{2}\mu$. The remaining scalar fields remain massless, in accordance with the Nambu-Goldstone theorem [31, 32], stating that every spontaneously broken continuous symmetry generates a massless Goldstone boson. These bosons are unphysical and can be gauged away through a $SU(2)_L$ transformation, such that the expansion around the vacuum from eq. (1.36) involves only the physical scalar $H(x)$,

$$\Phi(x) = \frac{1}{\sqrt{2}} \begin{pmatrix} 0 \\ v + h(x) \end{pmatrix}. \quad (1.38)$$

The gauge transformation bringing eq. (1.36) into the above form is called the *unitary gauge* [1].

In this gauge, the Higgs potential from eq. (1.34) has the form

$$V = \frac{m_h^2}{2} h^2 + \frac{m_h^2}{2v} h^3 + \frac{m_h^2}{8v^2} h^4, \quad (1.39)$$

containing cubic and quartic self-interactions of the Higgs field proportional to m_h^2 . Inserting the excitation around the vacuum state in the kinetic term of \mathcal{L}_h yields mass terms for the vector bosons,

$$\mathcal{L}_h \propto \frac{v^2}{8} g_2^2 (W_\mu^1 W^{1,\mu} + W_\mu^2 W^{2,\mu}) + \frac{v^2}{8} (W_\mu^3 - B_\mu) \begin{pmatrix} g_2^2 & g_1 g_2 \\ g_1 g_2 & g_1^2 \end{pmatrix} \begin{pmatrix} W^{3,\mu} \\ B^\mu \end{pmatrix}. \quad (1.40)$$

Instead of expressing the Lagrangian in terms of the fields W_μ^a and B_μ that make the original gauge invariance manifest, it can also be written in terms of the *physical* fields that correspond to the physical W^\pm , Z and γ bosons in the electroweak theory,

$$\begin{aligned} W_\mu^\pm &= \frac{1}{\sqrt{2}} (W_\mu^1 \mp i W_\mu^2) && \text{with } m_W = \frac{g_2}{2} v, \\ Z_\mu &= \frac{1}{\sqrt{g_1^2 + g_2^2}} (g_2 W_\mu^3 - g_1 B_\mu) && \text{with } m_Z = \frac{\sqrt{g_1^2 + g_2^2}}{2} v, \\ A_\mu &= \frac{1}{\sqrt{g_1^2 + g_2^2}} (g_1 W_\mu^3 + g_2 B_\mu) && \text{with } m_A = 0. \end{aligned}$$

It is worth noting, that the massless photon field A_μ associated with the electromagnetic $U(1)_{\text{em}}$ gauge symmetry is automatically recovered. All possible vertices between fermions and the physical electroweak gauge bosons are shown in fig. 1.2. The change of basis from (W_μ^3, B_μ) to (Z_μ, A_μ) [2] can also be written as a basis rotation with the weak mixing angle θ_W ,

$$\begin{pmatrix} Z_\mu \\ A_\mu \end{pmatrix} = \begin{pmatrix} \cos \theta_W & \sin \theta_W \\ -\sin \theta_W & \cos \theta_W \end{pmatrix} \begin{pmatrix} W_\mu^3 \\ B_\mu \end{pmatrix} \quad \text{with } \cos \theta_W = \frac{g_2}{\sqrt{g_1^2 + g_2^2}} = \frac{m_W}{m_Z}. \quad (1.41)$$

In the SM, not only the W^\pm and Z bosons but also fermions gain their masses through spontaneous breaking of the electroweak gauge symmetry. Fermion fields gain masses through gauge-invariant Yukawa interactions with the Higgs field. For one fermion generation, the respective Yukawa terms in the Lagrangian are

$$\mathcal{L}_{\text{Yukawa,gen}} = -\lambda_\ell \bar{L}_L \Phi \ell_R - \lambda_d \bar{Q}_L \Phi d_R - \lambda_u \bar{Q}_L \Phi^\dagger u_R + \text{h.c.}, \quad (1.42)$$

where λ_f with $f = \ell, d, u$ are the dimensionless Yukawa couplings and $L_L = (\nu_L, \ell_L)^T$ and $Q_L = (u_L, d_L)^T$ are the left-handed lepton and quark doublets, respectively. The VEV of the Higgs field then gives rise to fermion mass terms in the Lagrangian, which, in the unitary gauge, yields for a single fermion generation

$$\mathcal{L}_{\text{Yukawa,gen}} = - \sum_{f=\ell,d,u} \left(m_f \bar{\psi}_f \psi_f + \frac{m_f}{v} H \bar{\psi}_f \psi_f \right) \quad \text{with } m_f = \frac{1}{\sqrt{2}} \lambda_f v. \quad (1.43)$$

Write somewhere
SU2xU1 to
U1 break-down

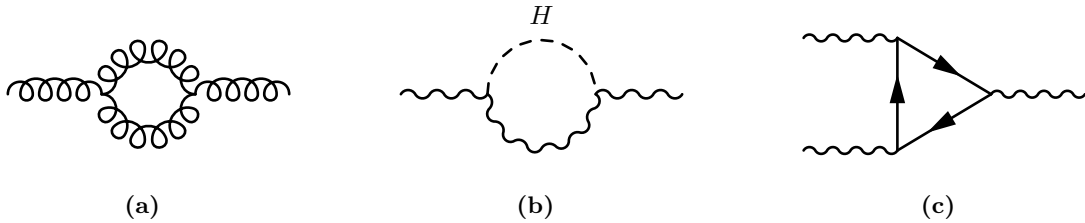


Figure 1.3: Examples of loop corrections to (a) the gluon propagator, (b) the W or Z propagator and (c) the cubic gauge boson vertex.

When introducing all three fermion generations, additional Yukawa terms mixing fermions of different generations appear in the Lagrangian [1]. The terms involving quark fields can be parametrised using the CKM matrix V_{CKM} [10, 11], quantifying the transition probability between quark generations. Since no right-handed neutrinos exist in the SM, no generation mixing in the lepton sector occurs and hence no neutrino mass terms are allowed in the SM. Neutrino oscillations have however been observed experimentally, thus at least one massive neutrino generation needs to exist. Their mixing can then be described with the PMNS matrix [9], allowing neutrinos to acquire mass e.g. through the see-saw mechanism [33].

1.1.3 Renormalisation and divergencies

At lowest order in the perturbative expansion, the momenta of the internal lines in the Feynman diagrams are fixed by the external particles. For higher orders where the diagrams involve loops, the momenta of the internal lines need to be integrated over as they are not fixed by energy-momentum conservation. Some examples of loop corrections to propagators and vertices are shown in fig. 1.3. As each vertex in the Feynman diagrams is associated with a coupling constant that is usually much smaller than 1 (apart from the non-perturbative regime of QCD), higher orders in the perturbative expansion contribute less and less to the total amplitude of the full expansion.

The momentum integrals in loop corrections however lead to *ultraviolet divergencies* for large momenta. In order to eliminate the divergencies, the integrals have to be *regularised*, e.g. by applying a cut-off scale Λ or calculating the integrals in a number $D = 4 - \epsilon$ of dimensions where they converge. The potential divergencies are then absorbed in parameters of the Lagrangian, such as coupling constants and masses, after which the regulator is removed (e.g. $\epsilon \rightarrow 0$) again and a *renormalisation* procedure is applied, replacing the bare parameter values with the physical, measured values [1]. Renormalisation effectively absorbs the effects of quantum fluctuations acting on much smaller scales than the scale of the given problem in the parameters of the theory. As Veltmann and t'Hooft [34, 15] have shown, all Yang-Mills theories with massive gauge fields are renormalisable, making the SM as a whole a renormalisable theory.

Mass dimension needs to be < 4

1.2 Supersymmetry

Among the properties a quantum field theory might possess to make it more mathematically tractable, one specific higher symmetry reveals particularly far-reaching implications; a sym-

metry relating fermions and bosons, known as Supersymmetry (SUSY). The following section introduces the basic concepts of SUSY, a promising class of theories that could solve some of the shortcomings of the SM.

First, a motivation for the need of SUSY is given by highlighting some of the open questions of the SM. This is followed by an introduction to the mathematical description and phenomenological consequences of supersymmetric theories. The following sections are intended to highlight the most important concepts and relations, a much more complete and detailed introduction to SUSY can be found in Refs. [3, 4].

1.2.1 Shortcomings of the Standard Model

Although the SM is a remarkably successful theory able to predict and describe the interactions between elementary particles with unprecedented precision, there are still phenomena in nature that cannot be suitable understood within the theoretical framework of the SM. Those limitations and open questions are the reason for numerous searches looking for new physics beyond the Standard Model (BSM). Some of the aforementioned open questions are described in the following.

Dark Matter

The existence of dark matter (DM), i.e. non-luminous and non-absorbing matter is nowadays well established [7]. Some of the earliest hints for the existence of DM came from the observation that the rotation curves of luminous objects are not consistent with the expected velocities based on the gravitational attraction of the visible objects around them. Zwicky already postulated in 1933 the existence of DM [35] based on rotation curves of galaxies in the Coma cluster. In 1970, Rubin measured rotation curves of spiral galaxies [36], revealing again a significant disagreement with the theoretically expected curves given the visible matter in the galaxies. Based on Newtonian dynamics, the circular velocity of stars outside the bulge of galaxies is expected to fall off with increasing radius as $v(r) \propto 1/\sqrt{r}$ [37]. Rubin's observations however revealed that the velocities of stars outside the bulge stay approximately constant, strongly suggesting the existence of a non-luminous (or *dark*) matter halo around the galaxies. Surveys of galaxy clusters and observations of gravitational lensing effects e.g. in the bullet cluster [38] or the Abell 1689 cluster [39] have since then further consolidated the existence of large accumulations of non-luminous mass in the universe.

The anisotropies in cosmic microwave background (CMB), studied by the COBE [40, 41], WMAP [42, 43] and Planck missions [44] are well described by the Lambda Cold Dark Matter (Λ CDM) model [45], which includes a density for cold dark matter. Planck's latest results [46] suggest that the matter density of the universe is $\Omega_m = 0.3111 \pm 0.0056^\dagger$ and that ordinary baryonic matter only makes up $\sim 4.9\%$ of the universe's matter content, while DM accounts for the remaining $\sim 26.1\%$.

Candidates for non-baryonic DM need to satisfy certain conditions: they have to be stable on cosmological timescales (otherwise they would have decayed by now), they have to couple only very weakly to the electromagnet interaction (if at all, otherwise they would be luminous

[†] The remaining $\sim 69\%$ are taken up by *dark energy*, the nature of which is still an open question.

DM relic density

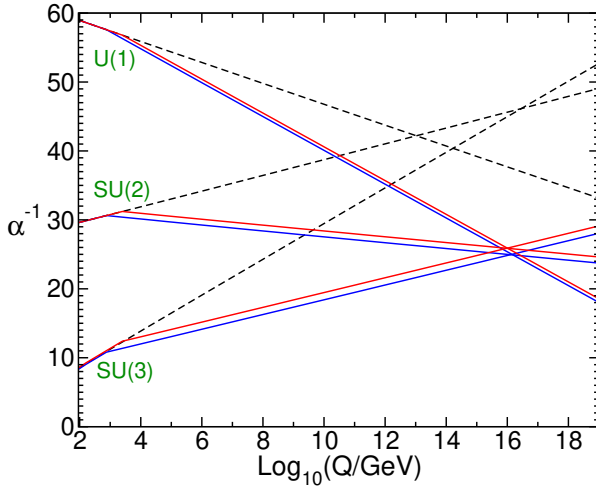


Figure 1.4: Evolution of the inverse coupling constants in the SM (dashed lines) and the MSSM (solid lines) in function of the energy scale Q . In the MSSM, the masses of the supersymmetric particles are treated as common threshold varied between 750 GeV and 2.5 TeV. Figure taken from Ref. [3].

matter) and they need to have the right relic density. Analyses of structure formations in the Universe have furthermore shown that most DM should have been *cold*, i.e. non-relativistic at the beginning of galaxy formation [37]. Candidates for DM particles are e.g. sterile neutrinos, axions, primordial black holes, or weakly interacting massive particles (WIMPs).

In the SM, the only DM candidate particle is the neutrino. Given the upper limits on the neutrino masses, an upper bound on their relic density can be computed, revealing that neutrinos are simply not abundant enough to be a dominant component of DM [37]. Many BSM theories naturally predict new WIMPs with masses in the GeV to TeV range. In many SUSY models with exact R-parity conservation (a quantity introduced in section 1.2.5), the lightest supersymmetric particle is neutral and stable and could be a good candidate for DM.

Unification of forces

Although the SM provides a good description of nature up to the energy scale probed with today's accelerators, some of its peculiar aspects hint to a more fundamental theory. A prominent example is the question why the electric charges of the electrons and the charges of the quarks of the protons and neutrons in the nuclei exactly cancel, making for electrically neutral atoms [1]. Or in other words: why are the charges of all observed particles simple multiples of the fundamental charge? And why are they quantised in the first place?

An explanation to many of these peculiarities comes naturally when describing the SM as a unified theory with a single non-Abelian gauge group, e.g. $SU(5)$ [47]. The larger symmetry group with a single coupling constant is then thought to be spontaneously broken at very high energy, such that the known SM interactions are recovered at the lower energies probed in today's experiments. In such a grand unified theory (GUT), the particles in the SM are arranged in anomaly-free[†] irreducible representations of the gauge group, thereby e.g. naturally ensuring the fractional charges of quarks [2].

In the SM, the coupling constants run towards each other with increasing energy scale, but never exactly meet. In the MSSM with supersymmetric particles at the TeV scale the running

[†] In the sense that loop corrections do not break symmetries the Lagrangian has.

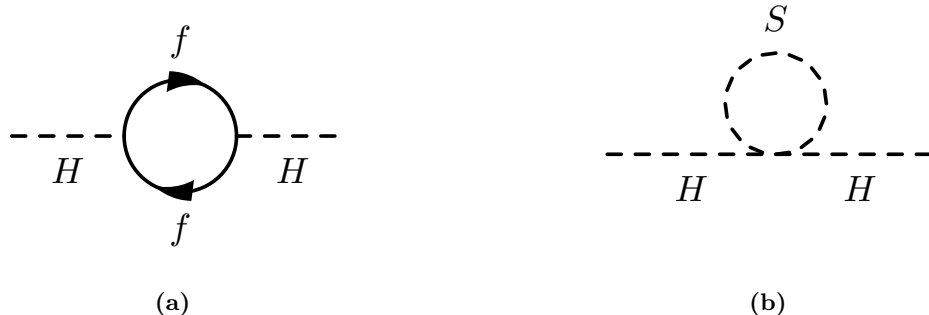


Figure 1.5: A massive fermion (a) and a hypothetical massive scalar particle (b) coupling to the Higgs boson.

couplings meet within their current uncertainties, hinting that a supersymmetric GUT could be a good candidate for describing physics at the unification scale. Figure 1.4 shows the running of the coupling constants in both the SM and the MSSM.

The Hierarchy Problem

As the SM is a renormalisable gauge theory, finite results are obtained for all higher-order loop corrections, making the SM a theory that is in principle well-defined up to infinite energies. In renormalisation terms, this means that the cut-off scale Λ is theoretically allowed to go to arbitrarily high values. It is however clear, that the SM cannot be a complete theory of nature and that at some unknown high-energy scale Λ , *new physics* has to appear. At the very least, a new theoretical framework becomes necessary at the Planck scale $M_P \approx 10^{18} \text{ GeV}$ [3], where quantum gravitational effects can no longer be ignored.

The mass parameters of fermions and massive vector bosons are protected from large quantum corrections by chiral symmetry and gauge symmetry, respectively [48]. The mass parameter of the scalar Higgs field, on the other hand, receives loop corrections proportional at least to the scale at which new physics sets in. The coupling of the Higgs field to a fermion f with mass m_f , depicted in fig. 1.5(a), yields a one-loop correction term to the Higgs square mass [3] given by

$$\Delta m_H^2 = -\frac{|\lambda_f|^2}{8\pi^2} \Lambda^2 + \dots \quad (1.44)$$

Thus, in order to obtain the relatively low value of the Higgs mass in the order of 10^2 GeV , the quantum corrections to the bare Higgs parameter have to be tuned in such a way that they almost cancel. Hence, if there is *any* scale of new physics even only several orders of magnitude higher than the electroweak scale, the resulting large quantum corrections to the Higgs mass immediately lead to a *fine-tuning* problem that is considered to be unnatural.

In SUSY, the Higgs mass is automatically protected from the large quantum corrections by the introduction of two complex scalar partners to each SM fermion. The quantum corrections from a hypothetical heavy complex scalar particle S with mass m_S as in fig. 1.5(b) yields a

one-loop correction [3] given by

$$\Delta m_H^2 = \frac{\lambda_S}{16\pi^2} [\Lambda^2 + 2m_S^2 \log(\Lambda/m_S) + \dots]. \quad (1.45)$$

Interestingly, the corrections in eq. (1.44) and eq. (1.45) enter with opposite signs. Thus, if $\lambda_S = |\lambda_f|^2$, then the large quantum corrections neatly cancel and no excessive fine-tuning is needed. The requirement $\lambda_S = |\lambda_f|^2$ means that the fermions and their supersymmetric bosonic partners would have same masses. Such particles would have been discovered long ago in particle physics experiments, meaning that SUSY must be a broken symmetry (see section 1.2.5 for a discussion on SUSY breaking) such that the supersymmetric particles acquire masses well above those of their SM partners.

Anomalous magnetic moment of the muon

One of the longest standing disagreements between experiment and theory in the SM is the anomalous magnetic moment of the muon [7]. The magnetic moment of the muon $\vec{\mu}_\mu$ is related to its intrinsic spin \vec{S} through the gyromagnetic ratio g_μ by

$$\vec{\mu}_\mu = g_\mu \frac{q}{2m} \vec{S}. \quad (1.46)$$

For a structureless spin-1/2 particle with mass m and charge $q = \pm e$, the gyromagnetic ratio is $g_\mu = 2$ [49]. Loop corrections coupling the muon spin to virtual fields cause small deviations, parameterised by the anomalous magnetic moment

$$a_\mu = \frac{1}{2}(g_\mu - 2). \quad (1.47)$$

The anomalous magnetic moment can be precisely measured as well as predicted within the SM, a comparison between experimental data and theoretical prediction thus directly tests the SM at quantum loop level and may hint to effects from new physics in case of discrepancies [50]. In the SM, the most dominant contribution to a_μ comes from QED corrections involving photon and fermion loops. An exemplary diagram is shown in fig. 1.6(a). Weak contributions involving the heavy W^\pm , Z and Higgs particles are suppressed by their masses [7]. Although the contributions from QCD are relatively small, they give rise to the main theoretical uncertainties as they cannot be calculated from first principles [7].

The E821 experiment at Brookhaven National Lab (BNL) [49] has measured the anomalous magnetic moment of the muon and found a deviation from the SM expectation of

$$\Delta a_\mu = a_\mu^{\text{exp}} - a_\mu^{\text{SM}} = 261(63)(48) \times 10^{-11}, \quad (1.48)$$

where the numbers in parentheses are the uncertainties from experiment and theory, respectively. This represents a deviation of 3.3σ [7] from the SM expectation.

In SUSY, additional Feynman diagrams exist involving the supersymmetric partners of the muon, the muon neutrino and the electroweak gauge bosons, and thus the measured deviation in a_μ can easily be accommodated in many supersymmetric models [51, 52]. Two exemplary lowest-order diagrams involving supersymmetric particles are shown in figs. 1.6(b) and 1.6(c).

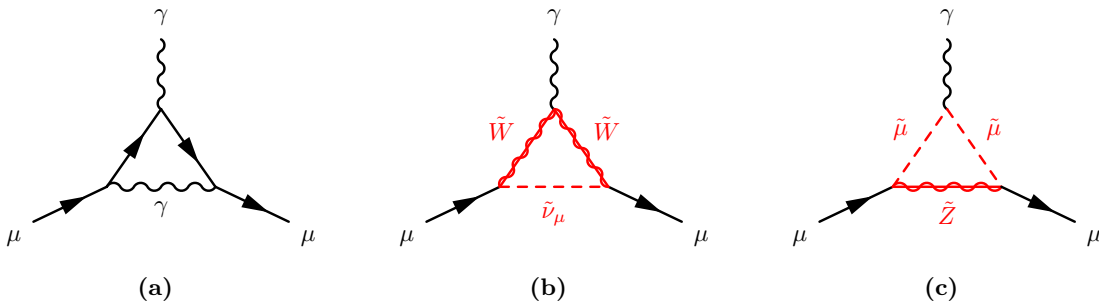


Figure 1.6: Electromagnetic (a) and supersymmetric (b), (c) contributions to a_μ . Adapted from [50].

1.2.2 Supersymmetric Algebra

A generator of supersymmetric transformations is an anti-commuting spinor Q that turns fermionic states $|f\rangle$ into bosonic states $|b\rangle$ and vice-versa.

$$Q|f\rangle = |b\rangle, \quad Q|b\rangle = |f\rangle. \quad (1.49)$$

As spinors are complex objects, Q^\dagger is also a symmetry operator. Both Q and Q^\dagger are necessarily fermionic and thus must carry half-integer spin, in the simplest case spin-1/2, meaning that SUSY must be a spacetime symmetry, i.e. a Poincaré symmetry. The Coleman–Mandula theorem [53] dictates that the symmetry group generating a consistent spacetime QFT must be the direct product of the internal symmetry group with the Poincaré group, which in principle rules out the possibility for SUSY. The Haag–Lopuszanski–Sohnius extension [54] however states that the only possible way of non-trivially combining internal and spacetime symmetry groups is to use a Lie superalgebra and fermionic spin-1/2 generators. Thus, in order to obey the Haag–Lopuszanski–Sohnius theorem and simultaneously allow for parity-violating interactions, the SUSY generators have to satisfy the following algebra of commutation and anti-commutation relations [4],

$$\begin{aligned} \{Q, Q^\dagger\} &= 2\sigma_\mu P^\mu, \\ \{Q, Q\} &= \{Q^\dagger, Q^\dagger\} = 0, \\ [P^\mu, Q] &= [P^\mu, Q^\dagger] = 0, \\ \{M^{\mu\nu}, Q\} &= \sigma^{\mu\nu} Q, \\ \{M^{\mu\nu}, Q^\dagger\} &= \bar{\sigma}^{\mu\nu} Q^\dagger, \end{aligned} \quad (1.50)$$

where P^μ is the four-momentum generator of spacetime translations, $\sigma_\mu = (\mathbb{1}_2, \sigma_i)$, $\bar{\sigma}_\mu = (\mathbb{1}_2, -\sigma_i)$ with $i = 1, 2, 3$ and the Pauli matrices σ_i , and $\sigma^{\mu\nu} = \frac{i}{4}(\sigma^\mu \bar{\sigma}^\nu - \sigma^\nu \bar{\sigma}^\mu)$ as well as $\bar{\sigma}^{\mu\nu} = \frac{i}{4}(\bar{\sigma}^\mu \sigma^\nu - \bar{\sigma}^\nu \sigma^\mu)$. This is the simplest version of SUSY, called $N = 1$ symmetry, as it introduces only one pair of generators. Supersymmetric theories with $N \geq 2$ pairs of generators also exist and generally have some theoretical advantages as e.g. fewer divergencies in the case of $N = 2$ or even no divergencies at all in the case of $N = 4$ [4]. SUSY models with $N \geq 2$ however do not allow for parity violation and thus fail to describe the physics of the SM, disqualifying them from a phenomenological point of view [4].

As both SUSY generators commute with spacetime translations (see eq. (1.50)), they also both commute with the squared mass operator $-P^2$. Consequently, particles related by the generators, called *superpartners*, must have equal eigenvalues under $-P^2$, i.e. they must have equal masses. Furthermore, the SUSY generators also commute with the gauge transformation generators, hence superpartners must have same electric charge, weak isospin and degrees of freedom in colour space [3].

Mention link to gravity

1.2.3 Supermultiplets

The SM and SUSY particles are arranged in irreducible representations of the SUSY algebra, called *supermultiplets*, each containing both fermionic and bosonic states that are superpartners of each other. It can be shown that each supermultiplet has an equal number of fermion and boson degrees of freedom, $n_f = n_b$ [3].

The simplest supermultiplet Ψ that can be constructed contains a single Weyl fermion ψ and two real scalars, described by a single complex field ϕ , called the *sfermion*. The Weyl fermion has two spin helicity states, hence $n_f = 2$, and the complex scalar field has two components with $n_b = 1$ each. An additional complex scalar field F , called *auxiliary field* and not corresponding to a physical particle, has to be introduced in order to allow the SUSY algebra to close off-shell (where the energy-momentum relation does not hold) [3]. The supermultiplet Ψ thus reads

$$\Psi = (\phi, \psi, F). \quad (1.51)$$

Being a pure bookkeeping device, the auxiliary field does not propagate and can be eliminated on-shell with the equations of motion $F = F^* = 0$. This supermultiplet is called a *chiral* or *scalar* supermultiplet [3].

The next-simplest supermultiplet for which $n_f = n_b$ holds, is the *vector* or *gauge* supermultiplet Φ containing a spin-1 gauge boson A_a^μ , where a is the index of the gauge group. In order for the theory to be renormalisable, this gauge boson must be massless before spontaneous breaking of the symmetry. As a massless spin-1 boson has two helicity states, $n_b = 2$, the superpartner, called *gaugino*, must be a massless spin-1/2 Weyl fermion λ_a with two helicity states such that $n_f = 2$ [3]. An auxiliary real bosonic field D_a is needed in order to balance the degrees of freedom off-shell [4], completing the supermultiplet to be

$$\Phi = (\lambda_a, A_a^\mu, D_a). \quad (1.52)$$

Like the chiral auxiliary field, the gauge auxiliary field does not correspond to a physical particle and can be eliminated on-shell through its equations of motion [3].

1.2.4 Supersymmetric Lagrangian

The simplest supersymmetric model that can be shown to realise the superalgebra is the massless, non-interacting Wess–Zumino model [55, 3], given by

$$\begin{aligned} \mathcal{L}_{\text{free}} &= \mathcal{L}_{\text{scalar}} + \mathcal{L}_{\text{fermion}} \\ &= \partial^\mu \phi^* \partial_\mu \phi + i \bar{\psi}^\dagger \bar{\sigma}^\mu \partial_\mu \psi, \end{aligned} \quad (1.53)$$

with a massless complex scalar ϕ and a spin-1/2 fermion ψ , corresponding to a single chiral supermultiplet. As discussed in section 1.2.3, in order for this Lagrangian to satisfy the supersymmetry off-shell where the equations of motion cannot be used, an auxiliary complex scalar field F has to be added. For a collection of i chiral supermultiplets, the free Lagrangian thus reads

$$\begin{aligned}\mathcal{L}_{\text{free}} &= \mathcal{L}_{\text{scalar}} + \mathcal{L}_{\text{fermion}} + \mathcal{L}_{\text{aux}} \\ &= \partial^\mu \phi^{*i} \partial_\mu \phi_i + i \psi^{\dagger i} \bar{\sigma}^\mu \partial_\mu \psi_i + F^{*i} F_i,\end{aligned}\tag{1.54}$$

where the repeated indices i are summed over. The auxiliary Lagrangian term \mathcal{L}_{aux} implies the trivial equations of motion $F = F^* = 0$ which are needed to remove the auxiliary field in the on-shell case. The next step involves adding terms for non-gauge interactions for the chiral supermultiplets. Non-gauge interactions for chiral supermultiplets at most quadratic in the fermion fields can be achieved by introducing the term,

$$\mathcal{L}_{\text{int}} = \frac{1}{2} W^{ij}(\phi, \phi^*) \psi_i \psi_j + V(\phi, \phi^*) + c.c.,\tag{1.55}$$

where W^{ij} is a holomorphic[†] function of the complex scalar fields ϕ_i of the form [4]

$$W^{ij} = \frac{\partial W}{\partial \phi_i \partial \phi_j}.\tag{1.56}$$

Here, W is called the *superpotential*. For the final Lagrangian to be renormalisable, the superpotential can at most be cubic [4], and can thus be written as

$$W = \frac{1}{2} m^{ij} \phi_i \phi_j + \frac{1}{6} y^{ijk} \phi_i \phi_j \phi_k,\tag{1.57}$$

where y^{ij} are the Yukawa couplings between the scalar and the two fermions. Requiring \mathcal{L}_{int} to be invariant under supersymmetry transformations further defines the potential V . The equations of motions of the auxiliary fields F can be written as

$$F_i = \frac{\partial W(\phi)}{\partial \phi^i} = -W_i^*, \quad F^{*i} = -\frac{\partial W(\phi)}{\partial \phi_i} = -W^i,\tag{1.58}$$

which thus yields for the potential $V = W_i^* W^i = F_i F^{*i}$. The full Lagrangian of the Wess-Zumino model [3] with general chiral interactions for i chiral supermultiplets is then given by adding eq. (1.55) with eqs. (1.57) and (1.58) to the free Lagrangian in eq. (1.53). This yields,

$$\mathcal{L} = \partial^\mu \phi^{*i} \partial_\mu \phi_i + i \psi^{\dagger i} \bar{\sigma}^\mu \partial_\mu \psi_i + \frac{1}{2} m^{ij} \psi_i \psi_j + \frac{1}{2} m_{ij}^* \psi^{\dagger i} \psi^{\dagger j} + \frac{1}{2} y^{ijk} \phi_i \psi_j \psi_k + \frac{1}{2} y_{ijk}^* \phi^{*i} \psi^{\dagger j} \psi^{\dagger k} + V(\phi, \phi^*).\tag{1.59}$$

The Lagrangian in eq. (1.59) immediately reveals that, as expected by supersymmetry, the masses of the fermions and bosons in the same supermultiplet are identical. In order to incorporate gauge supermultiplets and consider the interactions between fermions and gauge bosons observed in the SM, the usual minimal coupling rule has to be applied, replacing ∂_μ

[†] A holomorphic function is a complex-valued function in one or more complex variables that is complex differentiable in a neighbourhood for every point of its domain.

with D_μ . This leads to equation of motions for the auxiliary fields D^a

$$D^a = -g(\phi^* T^a \phi), \quad (1.60)$$

where T^a are the generators of the gauge group and g is the coupling constant [3]. The potential then becomes

$$V(\phi, \phi^*) = F^{*i} F_i + \frac{1}{2} \sum_a D^a D^a = W_i^* W^i + \frac{1}{2} \sum_a g_a^2 (\phi^* T^a \phi)^2, \quad (1.61)$$

where a runs over the gauge groups that generally have differing gauge couplings [3, 4].

1.2.5 The Minimal Supersymmetric Standard Model

The MSSM is the simplest $N = 1$ supersymmetrisation of the SM in the sense that it introduces a minimal set of additional particles.

Particle content and interactions

The MSSM arranges all SM particles in one chiral (all the fermions and quarks) and one gauge (all spin-1 bosons) supermultiplet. As supersymmetric partners (*s*partners) have the same quantum numbers apart from spin, none of the SM particles can be spartners of each other. Thus, all spartners have to be new, unseen particles. Table 1.3 summarises the names, notations and spins of all spartners introduced in the MSSM. The naming convention is to prepend the names of the spartners of fermions with an 's' (e.g. *selectron*, *stop*, ...) and append '-ino' to the names of the spartners of the bosons (e.g. *Wino*, *Photino*, ...). Supersymmetric particles (*s*particles) are generally denoted by adding a tilde to the symbol of SM particles (e.g. \tilde{e} , \tilde{u} , \tilde{g}).

An important detail to note is that right-handed and left-handed fermions get their own chiral supermultiplets and thus have distinct spartners, as otherwise the preference of the weak interaction for left-handed particles would be violated. For example, left-handed and right-handed quarks (q_L , q_R) get two different spartners (\tilde{q}_L , \tilde{q}_R), denoted with an index L and R. The index here refers to the handedness of the SM particle as scalar particles have only one helicity state. Additionally, the spartners of the left-handed and right-handed will mix to form physical mass eigenstates.

It is also worth asking why the spartners of SM particles are of lower spin in the first place, as e.g. spin-1 spartners of the SM fermions could also have been considered. The introduction of spin-1 bosons would entail the introduction of new gauge interactions, rendering the MSSM non-minimal [4]. Furthermore, introducing spartners with spin greater than 1 would make the resulting theory non-renormalisable [4].

In the MSSM, two Higgs doublets are needed in order to give masses to the up-type and down-type quarks via Yukawa couplings. A single Higgs field h cannot be used for this as it would require Yukawa terms including the complex conjugate h^* , which is forbidden as the superpotential, being a holomorphic function of the fields, cannot depend on the complex conjugates of the same fields [4]. Additionally, the use of a single Higgs doublet would lead to gauge anomalies in the electroweak gauge symmetry [56]. Instead two complex Higgs doublets

Table 1.3: Particle content of the MSSM. The spin refers to the spin of the spartner. Adapted from [4].

Particle	Spartner 0	Spin
quarks q	squarks \tilde{q}	0
→ top t	stop \tilde{t}	
→ bottom b	sbottom \tilde{b}	
...		
leptons ℓ	sleptons $\tilde{\ell}$	0
→ electron e	selectron \tilde{e}	
→ muon μ	smuon $\tilde{\mu}$	
→ tau τ	stau $\tilde{\tau}$	
→ neutrinos ν_ℓ	stop $\tilde{\nu}_\ell$	
gauge bosons	gauginos	1/2
→ photon γ	photino $\tilde{\gamma}$	
→ boson Z	Zino \tilde{Z}	
→ boson B	Bino \tilde{B}	
→ boson W	Wino \tilde{W}	
→ gluon g	gluino \tilde{g}	
Higgs bosons $H_i^{\pm,0}$	higgsinos $\tilde{H}_i^{\pm,0}$	1/2

with hypercharge $Y = \pm 1/2$ are used in the MSSM. The two Higgs doublets can be written as

$$H_u = \begin{pmatrix} H_u^0 \\ H_u^- \end{pmatrix}, \quad H_d = \begin{pmatrix} H_d^+ \\ H_d^0 \end{pmatrix}, \quad (1.62)$$

As illustrated in section 1.2.4 using the Wess–Zumino model, interactions are introduced using the superpotential. In the MSSM, the superpotential reads

$$W_{\text{MSSM}} = \bar{u} \mathbf{y}_u Q H_u - \bar{d} \mathbf{y}_d Q H_d - \bar{e} \mathbf{y}_e L H_d + \mu H_u H_d, \quad (1.63)$$

where Q and L correspond to the supermultiplets containing the left-handed quarks and leptons as well as their spartners, respectively. Likewise, \bar{u} , \bar{d} , \bar{e} correspond to the supermultiplets containing the right-handed up-type quarks, down-type quarks and leptons as well as their spartners, respectively. The parameters \mathbf{y}_u , \mathbf{y}_d and \mathbf{y}_e are the 3×3 Yukawa coupling matrices. Except for the third generation, the Yukawa couplings are known to be relatively small [3] and are thus not of direct interest for the phenomenology of the theory. Phenomenologically more interesting are the supersymmetric gauge interactions that dominate the production and decay process of spartners in the MSSM [3]. The superpotential in eq. (1.63) illustrates again why two Higgs doublets are needed in the MSSM, since terms like $\bar{u} Q H_d^*$ or $\bar{e} L H_u^*$ are not allowed due to the holomorphism of the superpotential. The term $\mu H_u H_d$ contains the *higgsino mass parameter* μ and is the supersymmetric version of the Higgs mass term in the SM Lagrangian.

Soft supersymmetry breaking

As stated in section 1.2.2, all superpartners must have same quantum numbers apart from their spin. They especially also should have same masses, however such particles would have

been discovered a long time ago and thus SUSY must be broken. Formally, SUSY should thus be an exact symmetry that is spontaneously broken because the Lagrangian has a symmetry under which the vacuum state is not invariant. However, if broken SUSY is still to provide a solution to the Hierarchy problem, i.e. cancel the quadratic divergencies in the loop corrections for the Higgs mass parameter, then the relations between the dimensionless couplings of the SM particles and their superpartners have to be maintained [3]. Hence, only symmetry breaking terms with positive mass dimension are allowed in the Lagrangian, especially also forbidding the presence of dimensionless SUSY-breaking couplings [3]. Such a breaking of SUSY is called *soft* breaking and can be written as

$$\mathcal{L} = \mathcal{L}_{\text{SUSY}} + \mathcal{L}_{\text{soft}}. \quad (1.64)$$

where, $\mathcal{L}_{\text{soft}}$ contains all the symmetry breaking terms while $\mathcal{L}_{\text{SUSY}}$ is the SUSY invariant Lagrangian with all the gauge and Yukawa interactions. In a softly broken SUSY, the loop corrections to the Higgs mass parameter depend quadratically on the largest mass scale associated with the soft terms (m_{soft}). As the fine-tuning problem reappears if m_{soft} becomes too large, superpartners with masses not too far above the TeV scale are generally assumed [3].

A total of 105 new parameters with no counterpart in the SM are introduced through $\mathcal{L}_{\text{soft}}$ [3, 57]:

- gaugino mass parameters M_1 , M_2 and M_3 ,
- trilinear scalar couplings, parametrised by 3×3 matrices in generation space \mathbf{a}_u , \mathbf{a}_d , \mathbf{a}_e , representing Higgs-squark-squark and Higgs-slepton-slepton interactions,
- Hermitian 3×3 matrices in generation space \mathbf{m}_Q^2 , $\mathbf{m}_{\bar{u}}^2$, $\mathbf{m}_{\bar{d}}^2$, \mathbf{m}_L^2 , $\mathbf{m}_{\bar{e}}^2$ that represent the sfermion masses,
- SUSY breaking parameters $m_{H_u}^2$, $m_{H_d}^2$ and b .

The sfermion mass matrices and the trilinear scalar couplings may introduce additional flavour mixing and CP violation, both of which are heavily constrained by experimental results. Flavour mixing in the lepton sector is for example constrained by an upper limit on $\text{BR}(\mu \rightarrow e\gamma) < 4.2 \times 10^{-12}$ [58]. Bounds on additional CP violation as well as squark mixing terms come from measurements of the electron and neutron electric moments and neutral meson systems[†] [?]. Formally, in order to avoid these terms, SUSY breaking can be assumed to be *flavour-blind*, meaning that the mass matrices are approximately diagonal. The large Yukawa couplings for the third generation squarks and sfermions can then be achieved by assuming that the trilinear scalar couplings are proportional to the corresponding Yukawa coupling matrix [3].

As most of the parameters in the MSSM are related to soft SUSY breaking, it is not surprising that the phenomenology of the MSSM strongly depends on the exact breaking mechanism. The breaking is usually introduced to happen in a *hidden sector* and the effects of the breaking are then typically mediated by messenger particles from a messenger field to the *visible sector* containing all the particles of the MSSM. Since the hidden sector is assumed to be only coupled weakly or indirectly to the visible sector, the phenomenology mostly depends on the

[†] While it is theoretically possible to fine-tune the numerous phases in the MSSM such that cancelling contributions are generated, such possibilities will not be discussed in the following.

mechanism mediating the breaking. The two most popular mechanisms are *gravity-mediated* and *gauge-mediated* SUSY breaking.

Mediating SUSY breaking through gravity is an attractive approach, since all particles share gravitational interactions. This makes it easy to imagine gravitational effects to be the only connection between the hidden and the visible sectors. In such models SUSY breaking is mediated through effects of gravitational strength, suppressed by inverse powers of the Planck mass [7]. The mass of the gravitino—the spartner of the hypothetical mediator particle of gravity, called *graviton*—is typically of electroweak scale [59, 60]. Due to its couplings of gravitational strengths, it usually does not play a role in collider physics [7].

In gauge-mediated SUSY breaking (GMSB), additional messenger fields sharing gauge interactions with the MSSM fields are transmitting the breaking from the hidden to the visible sector. In such models, the gravitino is typically the LSP, as its mass ranges from a few eV to a few GeV, making it a candidate for DM [61].

Mass spectrum

In the MSSM, electroweak symmetry breaking is generalised to the two Higgs doublets introduced in eq. (1.62). In total, the two doublets have eight degrees of freedom, three of which are used up to give masses to the W^\pm and Z bosons during the breaking of $SU(2)_L \otimes U(1)_Y$ to $U(1)_{\text{em}}$ (see section 1.1.2). Thus, five physical Higgs bosons appear in the MSSM; two neutral Higgs bosons even under CP transformation, called h^0 and H^0 , one neutral Higgs boson odd under CP transformation, called A^0 , and finally two charged Higgs bosons, called H^\pm . The two Higgs doublets H_u and H_d each get a VEV (v_u and v_d , respectively) that are connected to the VEV v of the SM Higgs field by

$$v_u^2 + v_d^2 = v^2. \quad (1.65)$$

Phenomenologically, the ratio of the two VEVs is usually considered, conventionally called $\tan \beta$,

$$\tan \beta = \frac{v_u}{v_d}. \quad (1.66)$$

Due to electroweak symmetry breaking, the gauginos and higgsinos are not mass eigenstates but mix to form states with definite mass, called *electroweakinos*:

- the two charged higgsinos mix with the two charged winos to form two charged mass eigenstates $\tilde{\chi}_1^\pm, \tilde{\chi}_2^\pm$, called *charginos*,
- the remaining neutral higgsinos mix with the photino, zino and bino to form four neutral mass eigenstates $\tilde{\chi}_1^0, \tilde{\chi}_2^0, \tilde{\chi}_3^0, \tilde{\chi}_4^0$, called *neutralinos*.

Both charginos and neutralinos are by convention labeled in ascending mass order. In the gauge-eigenstate basis $\psi^0 = (\tilde{B}, \tilde{W}^0, \tilde{H}_d^0, \tilde{H}_u^0)$, the neutralino mixing matrix reads [3]

$$M_\chi^0 = \begin{pmatrix} M_1 & 0 & -g_1 v_d / \sqrt{2} & g_1 v_u / \sqrt{2} \\ 0 & M_2 & g_2 v_d / \sqrt{2} & -g_2 v_u / \sqrt{2} \\ -g_1 v_d / \sqrt{2} & g_2 v_d / \sqrt{2} & 0 & -\mu \\ g_1 v_u / \sqrt{2} & -g_2 v_u / \sqrt{2} & -\mu & 0 \end{pmatrix}, \quad (1.67)$$

where M_1 and M_2 stem directly from the soft SUSY breaking terms while the $-\mu$ terms are the higgsino mass terms. Entries with g_1 and g_2 come from Higgs-higgsino-gaugino couplings. The neutralino mixing matrix can be diagonalized to obtain the neutralino masses, which can be expressed in terms of the parameters M_1 , M_2 , μ and $\tan\beta$ [3]. As the exact forms of the mass expressions are relatively complicated [7], they are typically evaluated in limits where one of the mass parameters is significantly smaller than the other two. This is possible because M_1 and M_2 can be chosen to be real and positive through an appropriate phase redefinition of \tilde{B} and \tilde{W}^\dagger . If neutralinos are dominated by the wino, bino or higgsino component, they are called wino-, bino- or higgsino-like, respectively, in the following.

The chargino mixing matrix can be written in a similar fashion. In the gauge-eigenstate $\psi^\pm = (\tilde{W}^\pm, \tilde{H}_u^+, \tilde{W}^-, \tilde{H}_d^-)$, it can be written as

$$\mathbf{M}_{\tilde{\chi}^\pm} = \begin{pmatrix} \mathbb{0}_2 & \mathbf{X}^T \\ \mathbf{X} & \mathbb{0}_2 \end{pmatrix} \quad \text{with} \quad \mathbf{X} = \begin{pmatrix} M_2 & g_2 v_u \\ g_2 v_d & \mu \end{pmatrix}. \quad (1.68)$$

The masses of the charginos are then the eigenvalues of the doubly degenerate 4×4 matrix $\mathbf{M}_{\tilde{\chi}^\pm}^\dagger \mathbf{M}_{\tilde{\chi}^\pm}$ and can be expressed in terms of M_2 , μ and $\sin 2\beta$ [3].

Squarks and sleptons also mix with each other. As in principle any scalars with same electric charge, colour charge and R-parity (see section 1.2.5) can mix with each other, the mass eigenstates of the sleptons and squarks should a priori be obtained through diagonalisation of three 6×6 mixing matrices (one for up-type squarks, one for down-type squarks and one for charged sleptons) and one 3×3 matrix (for sneutrinos). The assumption of flavour-blind soft SUSY breaking terms leads to most of the mixing angles being very small. As opposed to the first and second generation, the third generation sfermions have relatively large Yukawa couplings, therefore the superpartners of the left- and right-handed fermions mix to mass eigenstates $(\tilde{t}_1, \tilde{t}_2)$, $(\tilde{b}_1, \tilde{b}_2)$, $(\tilde{\tau}_1, \tilde{\tau}_2)$, again labeled in ascending mass order. The first and second generation sfermions, on the other hand, having very small Yukawa couplings, end up in nearly mass-degenerate, unmixed pairs.

The gluino, being the only colour octet fermion of the unbroken $SU(3)_C$ gauge group, cannot mix with another fermion and thus is a mass eigenstate with mass $m_{\tilde{g}} = |M_3|$ at tree level [3, 50].

R-parity

The superpotential of the MSSM in principle allows additional gauge-invariant terms that are holomorphic in the chiral superfields but violate either lepton number (L) or baryon number (B). However, L- or B-violating processes have never been observed. Even worse, the L- and B-violating terms would cause a finite lifetime of the proton by allowing for it to decay e.g. via $p \rightarrow e^+ \pi^0$, a process that is heavily constrained to have a lifetime longer than 1.6×10^{34} years [62] as found by the Super-Kamiokande experiment.

In order to avoid these terms, a new symmetry, called *R-parity*, is introduced. R-parity is a multiplicatively conserved quantum number defined to be

$$P_R = (-1)^{3(B-L)+2s}, \quad (1.69)$$

[†] This makes the phase of μ in that convention a physical parameter that can no longer be rotated away through basis rotation.

where s is the spin of the particle. Given this definition, all SM particles and the Higgs bosons have even R-parity ($P_R = +1$) while all sparticles have odd R-parity ($P_R = -1$). Assuming R-parity to be exactly conserved at each vertex in the MSSM leads to a number of interesting phenomenological consequences:

- Sparticles are always produced in pairs.
- Heavier sparticles decay into lighter ones.
- The number of sparticles at each vertex must be even.
- The lightest supersymmetric particle (LSP) must be stable as it cannot decay any further without violating R-parity.

The nature of the LSP can be further constrained by cosmological observations [63]. If it were electrically charged or coupled to the strong interaction, it would have dissipated its energy and mixed with ordinary matter in the galactic disks where it would have formed anomalous heavy isotopes. Upper limits on such supersymmetric relics [64] thus heavily favour an electrically neutral and weakly interacting LSP. This excludes in particular the gluino as an LSP. Another possible LSP, the sneutrino, is ruled out by LEP and direct searches [65–67]. A gravitino LSP is especially attractive in gauge mediated theories.

Another promising option is a neutralino LSP. In large portions of the MSSM parameter space, a neutralino LSP produces a DM relic density that is compatible with the DM relic density measured by Planck [46, 64]. In the following, only R-parity conserving SUSY models with neutralino LSPs are considered.

1.2.6 The phenomenological MSSM

In addition to the 19 parameters of the SM, the MSSM adds a total of 105 additional parameters, too much to allow for a realistic exploration of the MSSM in a meaningful way. However, as already discussed in section 1.2.5, not all values of the 105 additional parameters lead to phenomenologically viable models. By requiring a set of phenomenological constraints, the 105 free parameters can be reduced to only 19 free parameters, spanning a model space called the phenomenological Minimal Supersymmetric Standard Model (pMSSM) [68, 69]. The free parameters in the pMSSM are listed in table 1.4.

The reduction of free parameters is obtained by applying the following constraints on the MSSM:

- No new source of CP violation, as discussed already in section 1.2.5, achieved by assuming all soft breaking parameters to be real.
- Minimal flavour violation, meaning that flavour-changing neutral currents (FCNCs), heavily constrained by experiment, are not allowed and the flavour physics is governed by the CKM matrix.
- First and second sfermion generations are mass-degenerate

Table 1.4: Parameters of the pMSSM.

Parameter	Meaning
$\tan \beta$	ratio of the Higgs doublet VEVs
M_A	mass of the CP-odd Higgs boson
μ	Higgs-higgsino mass parameters
M_1, M_2, M_3	wino, bino and gluino mass parameters
$m_{\tilde{q}}, m_{\tilde{u}_R}, m_{\tilde{d}_R}, m_{\tilde{\ell}}, m_{\tilde{e}_R}$	first and second generation sfermion masses
$m_{\tilde{Q}}, m_{\tilde{t}_R}, m_{\tilde{b}_R}, m_{\tilde{L}}, m_{\tilde{\tau}_R}$	third generation sfermion masses
A_t, A_b, A_τ	third generation trilinear couplings

- The trilinear couplings and Yukawa couplings are negligible for the first and second sfermion generations.

The pMSSM does not make any assumptions on the physics above the TeV scale, and therefore does not assume a specific SUSY breaking mechanism. With its 19 free parameters, and the typical complexity of a search for SUSY, the pMSSM is still computationally extremely challenging to probe. Using appropriate approximations, the computational complexity can be simplified enough for exhaustive scans and comparisons to experimental data to become possible.

1.2.7 Simplified models

In searches for BSM physics at the Large Hadron Collider, it is common to use simplified models [70–72] as a way of reducing the available parameter space to a manageable level. Simplified models do not aim to represent complete supersymmetric models but are mostly defined by the empirical objects and kinematic variables used in the searches, typically allowing only a small number of sparticles to be involved in the decay chain (usually only two or three). Other sparticles are decoupled by setting their masses to be kinematically inaccessible at current collider experiments. The decay chains of the participating sparticles are determined by fixed branching ratios, often set to be 100%. Experimental bounds from non-observation of a given model are then usually presented in function of the physical masses of the sparticles involved in the decay chain. The model space spanned by the free parameters of the simplified model is typically called a *signal grid*, as each set of distinct mass parameter values, called *signal point*, occupies a single point in this space.

Simplified models have the inherent advantage that they circumvent the issue of having to search for SUSY in a vast parameter space where many of the parameters may only have small effects on observables. Their interpretation in terms of limits on individual SUSY production and decay topologies in function of sparticle masses is straightforward and very convenient. The hope is, that simplified models are a reasonable approximation of sizeable regions of parameter space of the more complete model they are embedded in [7]. The obvious downside is however, that the limits obtained in simplified models are not automatically a good approximation of the true underlying constraint on the respective model parameter when interpreted in more complete SUSY models. Often times, for example, the constraints set on sparticle masses in simplified models, significantly overestimate the true constraints obtained in more complex

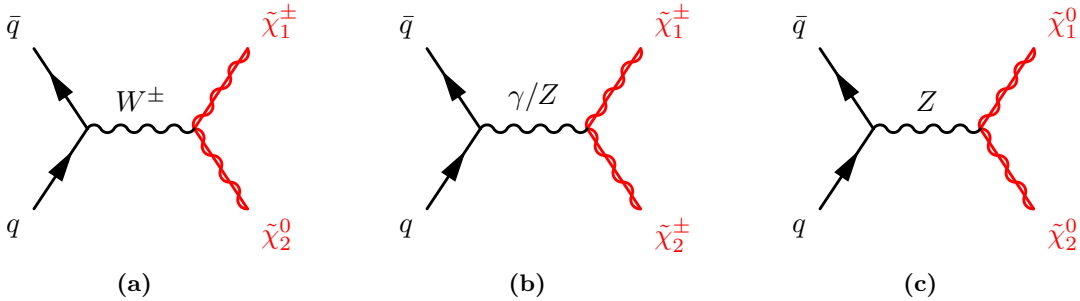


Figure 1.7: Dominant diagrams for production of electroweakino pairs at the Large Hadron Collider. Adapted from Ref. [3]

SUSY spectra, especially when the usual 100% branching fractions are assumed in the simplified models (see e.g. [73, 74]).

One way of circumventing these issues while sticking to the simplified model approach is to ensure that the limits obtained in different simplified models involving different production and decay mechanisms are combined into limits representing more complex SUSY spectra. In such an approach, the simplified model limits can be seen as building blocks for more complete and realistic SUSY models. Another possibility is to perform re-interpretations of SUSY searches—optimised for one or more such simplified models—in more complete SUSY model spaces, like e.g. the pMSSM. This can not only demonstrate the sensitivity of existing SUSY searches beyond simplified models, but also potentially identify blind spots and model regions not covered by current searches. In addition, connections to (in)direct DM searches as well as SM measurements can be explored this way. Recent efforts in this direction include e.g. Refs. [73, 75, 76].

1.3 Search for electroweakinos

While both the ATLAS experiment [77] and CMS experiment [78] at the Large Hadron Collider at CERN set strong limits on the presence of gluinos and squarks at the TeV scale, the limits on electroweakinos are mostly still well below 1 TeV and thus offer ample space for SUSY to hide in. The reason for the relatively low limits on electroweakinos are the low cross-sections of electroweakino production, compared to those of squark and gluino production.

Apart from the electroweakino mass limits set by the current collider experiments, some additional limits from the LEP experiments are still relevant. Combining the results from all four LEP experiments leads to a general lower chargino mass limit of 103.5 GeV, except for corners of the phase space with low sneutrino mass [79]. For small mass splittings between the $\tilde{\chi}_1^\pm$ and the $\tilde{\chi}_1^0$, the lower limit is a little weaker with dedicated searches excluding charginos with $m(\tilde{\chi}_1^\pm) < 91.9$ GeV [79]. For the neutralino, a general lower limit on the lightest neutralino mass comes from limits on the invisible width of the Z boson, excluding $m(\tilde{\chi}_1^0) < 45.5$ GeV[†] [7].

[†] Depending on the coupling between the Z boson and the lightest neutralino.

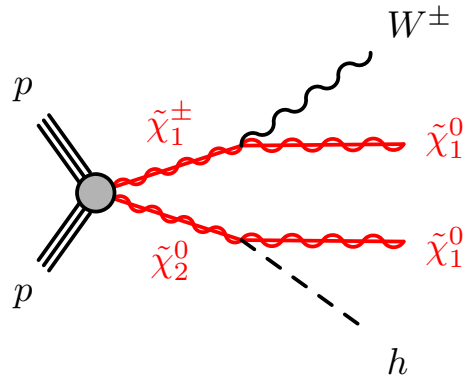


Figure 1.8: Diagram for $\tilde{\chi}_1^\pm \tilde{\chi}_2^0$ pair-production with subsequent decays into $\tilde{\chi}_1^\pm \rightarrow W^\pm \tilde{\chi}_1^0$ and $\tilde{\chi}_2^0 \rightarrow h \tilde{\chi}_1^0$.

1.3.1 Production of electroweakinos at the Large Hadron Collider

If gluinos and squarks are heavier than a few TeV, i.e. too heavy to be within reach of the Large Hadron Collider, the direct production of electroweakinos might be the dominant production mode of SUSY. At hadron colliders, electroweakinos can be pair-produced directly via electroweak processes. The direct production of electroweakino pairs dominantly happens through electroweak gauge bosons from s -channel $q\bar{q}$ annihilation, as shown in fig. 1.7. Contributions from t -channels via squark exchange are typically of less importance [3].

1.3.2 Models used within this work

In SUSY scenarios where the sleptons and charged and pseudoscalar Higgs bosons are heavier than the charginos and neutralinos, a relatively pure wino lightest chargino decays predominantly through $\tilde{\chi}_1^\pm \rightarrow W^\pm \tilde{\chi}_1^0$, while the next-to-lightest neutralino decays via $\tilde{\chi}_2^0 \rightarrow Z/h \tilde{\chi}_1^0$. If, in addition, the higgsinos are much heavier than the wino, and the mass splitting between the two lightest neutralinos is larger than the Higgs boson mass, the decay $\tilde{\chi}_2^0 \rightarrow h \tilde{\chi}_1^0$ is the dominant decay mode of the $\tilde{\chi}_2^0$. In this case, both the $\tilde{\chi}_1^\pm$ and $\tilde{\chi}_2^0$ are wino-like and nearly mass-degenerate.

The main model used in the following is a simplified model considering direct production of a $\tilde{\chi}_1^\pm \tilde{\chi}_2^0$ pair where the lightest chargino decays via $\tilde{\chi}_1^\pm \rightarrow W^\pm \tilde{\chi}_1^0$ and the next-to-lightest neutralino decays via $\tilde{\chi}_2^0 \rightarrow h \tilde{\chi}_1^0$, each with 100% branching ratio. The lightest chargino $\tilde{\chi}_1^\pm$ and the next-to-lightest neutralino $\tilde{\chi}_2^0$ are assumed to be degenerate in mass and pure wino states, while the lightest neutralino $\tilde{\chi}_1^0$ is considered to be a pure bino lightest supersymmetric particle (LSP). The mass parameter hierarchy for this model thus is $|M_1| < |M_2| \ll |\mu|$.

The masses of $\tilde{\chi}_1^\pm/\tilde{\chi}_2^0$ and $\tilde{\chi}_1^0$ are free parameters and are systematically varied, creating a two-dimensional signal grid to be scanned and compared to data. The Higgs boson mass is set to 125 GeV in accordance with the measured value [80, 81] and its branching ratios are the ones from the SM. Figure 1.8 shows an exemplary diagram for this simplified model.

In addition to the simplified model targeted by the SUSY search presented in the following, an additional class of models is considered in the second part of this work. These models are sampled directly from the pMSSM parameter space and are used to re-interpret the aforementioned SUSY search in the pMSSM. In accordance with the simplified model in fig. 1.8, the pMSSM

models are sampled with a focus on electroweakinos, i.e. all electroweak parameters are set to be lighter than 2 TeV while first and second generation squarks are decoupled and set to have mass parameters of 10 TeV. Sleptons are also set to be decoupled with mass parameters fixed at 10 TeV. In order to yield a better rate of surviving models during the sampling without affecting the decays of the electroweakinos too much, third generation squark and gluino mass parameters are varied between 2–5 TeV and 1–5 TeV, respectively. No assumptions are made on the bino, wino or higgsino nature of either charginos or neutralinos. More details on the sampling of the pMSSM models are given in section 10.1.

Reference,
why?

Chapter 2

Experiment

One of Europe’s first joint ventures in science [82], CERN (*Conseil Européen pour la Recherche Nucléaire*) is the largest physics research facility in the world, bringing together more than 12,400 scientists of over 110 nationalities [83] with a common goal of pushing the frontiers of science and technology. Located at the Franco-Swiss border near Geneva, CERN was founded in 1954 and nowadays counts 23 member states [83]. CERN’s main research area is particle physics, hence why the organisation operates a large complex of particle accelerators and detectors.

This chapter introduces the Large Hadron Collider (LHC), CERN’s main particle accelerator, as well as the ATLAS experiment, in which the search for SUSY presented in this work is embedded in.

2.1 The Large Hadron Collider

The LHC [84] is the largest particle accelerator situated at CERN. It is installed in a tunnel with 26.7 km circumference, that was originally constructed from 1984 to 1989 for the LEP accelerator. The tunnel is situated on the Franco-Swiss border and wedged between the Jura mountains and lake Léman. It lies between 45 m (in the limestone of the Jura) and 170 m (in molasse rock) below the surface, resulting in a tilt of 1.4% towards the lake. While proton-proton (pp) collisions are the main operating mode of the LHC, its design also allows it to accelerate and collide heavy ions like lead and xenon. Since data from pp collisions is used in this work, the following sections will mainly focus on this operating mode. As a particle-particle collider, the LHC obviously consists of two rings with counter-rotating beams, as opposed to particle-antiparticle colliders that only need a single ring. With an inner diameter of only 3.7 m, the tunnel however simply too narrow to fit two separate proton rings. Instead the LHC is built in a twin bore design[†], housing two sets of coils and beam channels in a single magnetic and mechanical structure and cryostat [84]. While saving costs, this design has the disadvantage of both beams being magnetically coupled, thereby reducing flexibility of the machine.

Before being injected into the LHC, protons are pre-accelerated by an injection chain built from multiple existing machines in CERN’s accelerator complex, pictured in fig. 2.1. The injection chain consists of predecessor accelerators that have been upgraded in order to be able to handle

[†] Originally proposed by John Blewett at BNL for cost-saving measures of the Colliding Beam Accelerator [84].

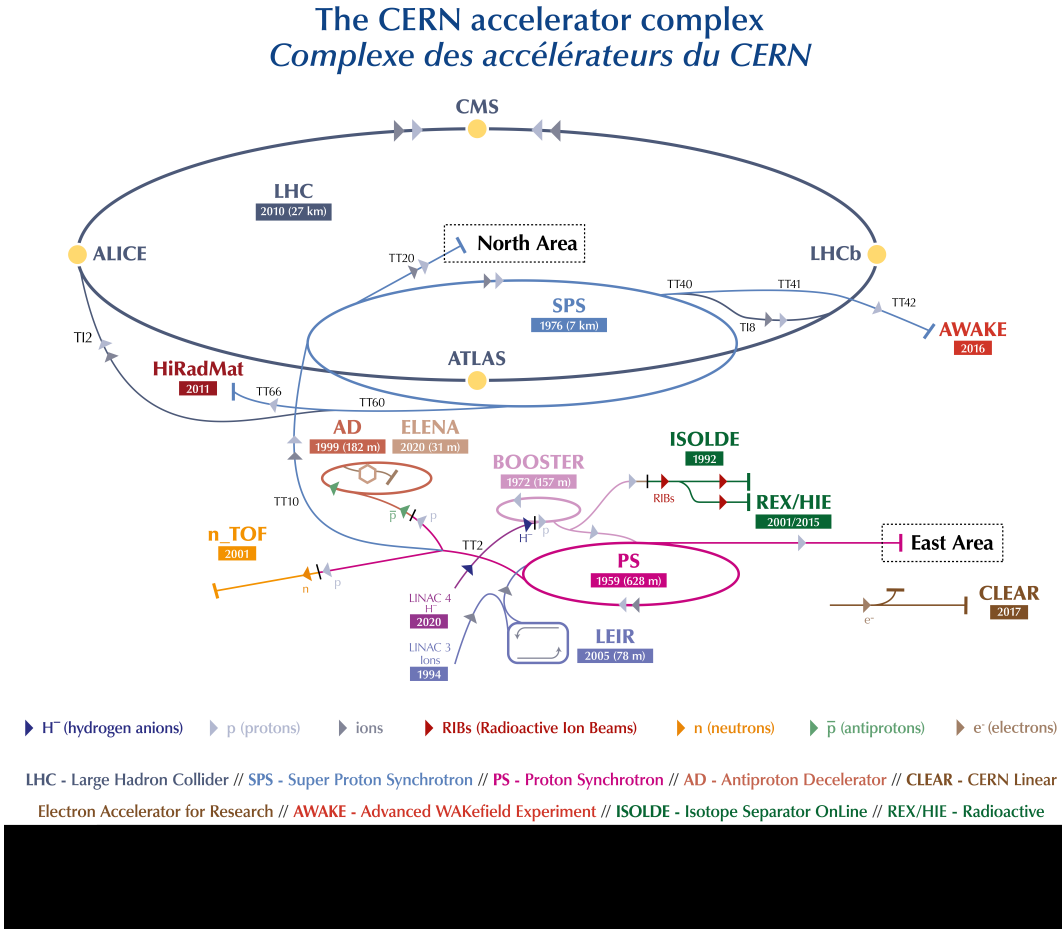


Figure 2.1: CERN accelerator complex as of 2018 [86].

the high luminosity and high energy requirements of the LHC. The protons for the LHC stem from a duoplasmatron source [85], stripping electrons from hydrogen atoms through electric discharges between a hot anode and cathode. The 90 keV protons are then accelerated by a radio frequency (RF) quadrupole to 750 keV before being injected into Linac2[†], a linear accelerator producing a beam of 50 MeV protons through the use of RF cavities. The protons then enter a set of circular accelerators, the Proton Synchrotron Booster, the Proton Synchrotron and the Super Proton Synchrotron, creating a stepwise acceleration up to an energy of 450 GeV, which is the injection energy of the LHC. The LHC finally accelerates the protons up to nominal beam energy before colliding them.

The LHC is composed of eight straight sections and eight arcs. The eight straight sections each serve as interaction points (*Point*), either for particle detectors, or for machine hardware of the collider itself. The Points are labelled clockwise, with IP 1 being closest to the CERN Meyrin site. Four of the eight Points house the main particle physics experiments at the LHC, called ATLAS, CMS, ALICE and LHCb, covering a wide range of fundamental research. The two

[†] Originally built to replace Linac 1 in order to produce higher energetic proton beams, Linac 2 has been replaced by Linac 4 in 2020.

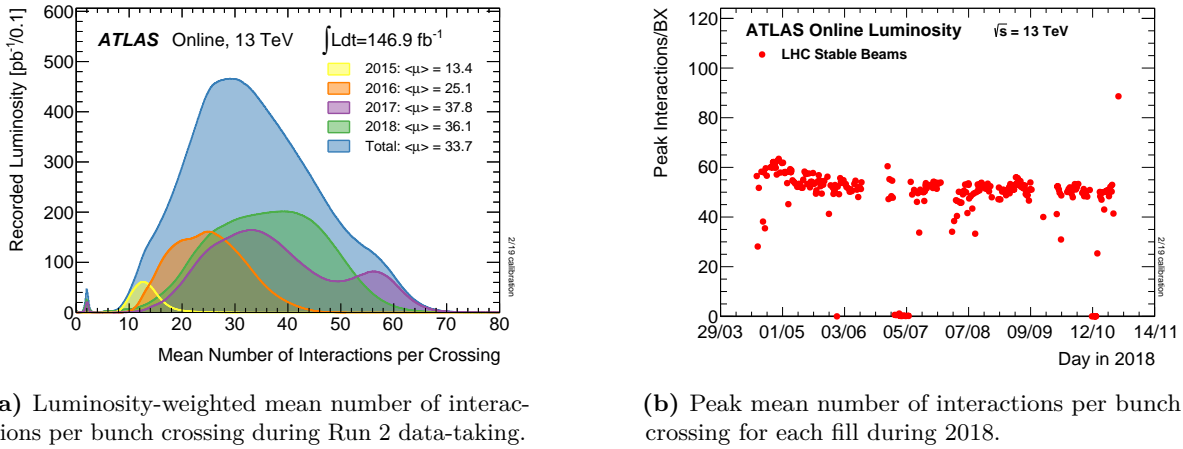
general purpose particle detectors ATLAS [87] and CMS [88] are installed at Point 1 and Point 5, respectively. Both ATLAS and CMS are designed to perform high precision SM measurements including Higgs measurements as well as searches for BSM physics. Being very similar in terms of targeted phase space, ATLAS and CMS can be used to cross-check results of each other. ALICE [89] is situated at Point 2 and specializes on heavy ion physics, studying the physics of quark-gluon plasma at high energy densities. Built in Point 8, LHCb [90] targets B -physics and performs measurements of CP-violation. Apart from the four main experiments, three smaller experiments exist at the LHC: TOTEM, MoEDAL and LHCf. While TOTEM [91] and LHCf [92] study forwards physics close to CMS and ATLAS, respectively, MoEDAL [93] searches for magnetic monopoles.

The remaining four Points house accelerator equipment needed for operation of the LHC. Most of the collimation system is placed at Point 3 and Point 7, performing beam cleaning and machine protection through a series of beam intercepting devices, ensuring that no stray particles from experimental debris or beam halo can reach and damage other machine components. The acceleration of the beam itself is performed at Point 4 with two RF systems, one for each LHC beam. The RF cavities operate at 400 MHz and provide 8 MV during injection and 16 MV during coast [84]. Due to the RF acceleration, the accelerated protons are grouped in packages called *bunches*, each containing roughly 10^{11} protons, with a bunch spacing of 25 ns [84]. Each beam contains a total of 2808 [84] bunches as design value. The remaining Point 6 houses the beam dumping system, allowing to horizontally deflect and fan out both beams into dump absorbers using fast-paced *kicker* magnets. The two nitrogen-cooled dump absorbers each consist of a graphite core contained in a steel cylinder, surrounded by 750 t of concrete and iron shielding [94]. Insertion of the beams from the Super Proton Synchrotron into the LHC happens at Points 2 and 8, close to the ALICE and LHCb experiments.

The eight arcs of the LHC are filled with dipole magnets built from superconducting NbTi Rutherford cables. The electromagnets are responsible for keeping the accelerated particles on their circular trajectory and are the limiting factor of the maximal centre-of-mass energy \sqrt{s} of the LHC. In order to achieve the design energy of $\sqrt{s} = 14$ TeV [94], the magnets have to create a field strength of 8.3 T [84]. In order to sustain the electric currents needed for such high field strengths, the magnets need to be cooled down to 1.9 K [84] using superfluid helium and operated in superconducting state. In addition to the dipole magnets, the arcs contain quadrupole magnets used to shape and focus the beams, as well as multipole magnets correcting and optimizing the beam trajectory. Quadrupole magnets are also used to reduce the beam size before and after the interaction points.

2.1.1 Pile-up

Due to the high number of protons in each bunch, several pp collisions occur at each bunch crossing. This leads to a phenomenon called *pile-up*, where the recorded events not only contain information from the hard-scattering process of interest, but also remnants from additional, often low-energy, pp collisions. During the Run 2 data-taking period, the mean number of inelastic pp collisions per bunch crossing, μ , has varied from roughly 10 to 70, with the majority of bunch crossings having a value of μ around 30. Figure 2.2(a) shows the mean number of interactions per bunch crossing during the Run 2 data-taking period, weighted by luminosity.



(a) Luminosity-weighted mean number of interactions per bunch crossing during Run 2 data-taking.

(b) Peak mean number of interactions per bunch crossing for each fill during 2018.

Figure 2.2: Number of interactions per bunch crossing recorded by the ATLAS detector [95]

The peak number of interactions per bunch crossing μ_{peak} per fill has been consistently around 50 during the 2018 data-taking (cf. fig. 2.2(b)).

Experimentally, pile-up can be divided into five major components [96]:

- *In-time* pile-up: multiple interactions during a single bunch crossing, of which not all will be interesting, as often with relatively low energy. If they can be resolved, the main hard-scattering event can still be isolated and studied.
- *Out-of-time* pile-up: additional collisions occurring in bunch crossings before or after the main event of interest. This happens either due to read-out electronic integrating over longer time frames than the 25 ns bunch spacing, or detector components being sensitive to several bunch crossings.
- *Cavern background*: gas of thermal neutrons and photons that typically fill the experimental caverns during a run of the LHC and tend to cause random hits in detector components.
- *Beam halo events*: protons scraping an up-stream collimator, typically resulting in muons travelling parallel to the beam pip
- *Beam gas events*: collision events that originate from interactions between proton bunches and residual gas inside the beam pipe.

While the effects of cavern background can be mitigated through special pieces of shielding, beam halo and beam gas events leave signatures that can be recognized and removed. Signals from in-time and out-of-time pile-up create irreducible overlap with the events of interest, significantly impacting analyses, and thus need to be simulated [96].

2.1.2 Luminosity and data-taking

Apart from the beam energy, the most important quantity for a collider is the instantaneous luminosity L . For a synchrotron with Gaussian beam distribution, the instantaneous luminosity

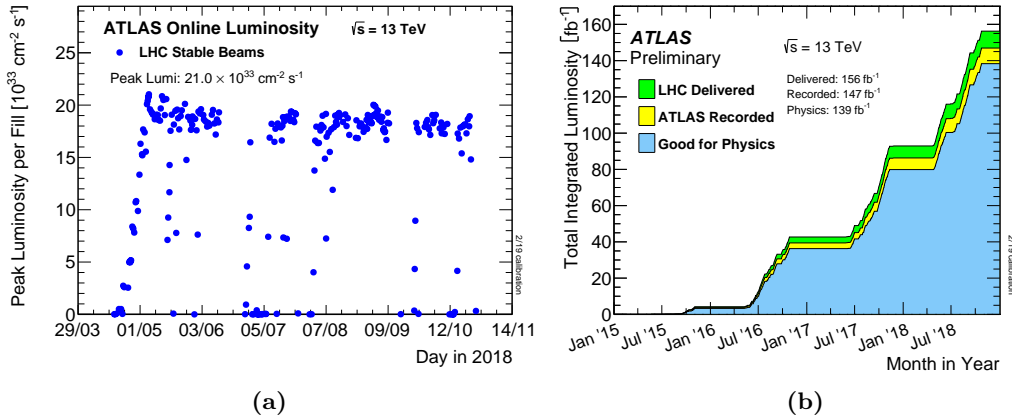


Figure 2.3: Instantaneous and cumulative luminosities in Run 2. Figure (a) shows the peak instantaneous luminosity delivered to ATLAS during pp collision data taking in 2018 as a function of time. Figure (b) shows the cumulative luminosity delivered to ATLAS (green), recorded by ATLAS (yellow) and deemed good for physics analysis (blue) during the entirety of Run 2 [95].

can be written as

$$L = \frac{N_b^2 n_b f_{\text{rev}}}{4\pi\sigma_x\sigma_y} F, \quad (2.1)$$

where n_b is the number of bunches, N_b the number of protons per bunch, f_{rev} the revolution frequency and σ_x and σ_y the transverse beam sizes. The parameters F is a geometrical correction factor accounting for the reduction in instantaneous luminosity due to the beams crossing at a certain crossing angle. While the design instantaneous luminosity of the LHC at the high-luminosity experiments ATLAS and CMS is $L = 10^{34} \text{ cm}^{-2} \text{ s}^{-1}$ [84], the 2017 and 2018 data-taking periods saw a peak luminosity twice as high [97].

The instantaneous luminosity is related to the total number of events N through the cross section σ of the events in question

$$N = \sigma L_{\text{int}} = \sigma \int L dt, \quad (2.2)$$

with L_{int} the total integrated luminosity, a measure for the total amount of collision data produced.

A precise knowledge of the integrated luminosity corresponding to a given dataset is crucial for both SM measurements as well as searches for BSM physics. Searches for SUSY like the one presented in this work rely on precise measurements of the integrated luminosity in order to be able to estimate the contribution from SM background processes. The luminosity measurement for the Run 2 dataset used within this work is described in detail in [98, 99] and relies on a measurement of the bunch luminosity, i.e. the luminosity produced by a single pair of colliding bunches

$$L_b = \frac{\mu f_{\text{rev}}}{\sigma_{\text{inel}}} = \frac{\mu_{\text{vis}} f_{\text{rev}}}{\sigma_{\text{vis}}}, \quad (2.3)$$

with μ the pile-up parameter, σ_{inel} the cross section of inelastic pp collisions, $\mu_{\text{vis}} = \epsilon\mu$ is the fraction ϵ of the pile-up parameter μ visible to the detector and $\sigma_{\text{vis}} = \epsilon\sigma_{\text{inel}}$ the visible inelastic cross section. If σ_{vis} is known, the currently recorded luminosity can be determined

by measuring μ_{vis} . At the ATLAS experiment, the observed number of inelastic interactions per bunch crossing μ_{vis} is measured using dedicated detectors, as for example LUCID-2 [100], a forward Cherenkov-detector using the quartz windows from photomultipliers as Cherenkov medium. In order to use μ_{vis} as luminosity monitor, the respective detectors need to be calibrated through a measurement of the visible inelastic cross section σ_{vis} . This can be done using van der Meer (vdm) scans [101, 102], in which the transverse distribution of protons in the bunches is inferred by measuring the relative interaction rates as a function of the transverse beam separation[†]. The algorithms used to determine the σ_{vis} calibration are described in [98, 99] and the luminosity during the vdm runs can be determined using eq. (2.1). At the LHC, vdm scans are typically performed in special low- μ runs with well-known machine parameters in order to minimise uncertainties [98]. During high- μ physics runs, the luminosity measurement is then an extrapolation from the vdm runs.

The LHC entered operation in 2008, with first beams in September and first collisions by the end of November that same year [103]. Its operation is in general structured into so-called *Runs*, that are spanned by multiple years of data-taking. Run 1 spanned from 2009 to 2013 and delivered roughly 28.5 fb^{-1} of pp collision data to ATLAS, taken at centre-of-mass energies of 7 TeV and 8 TeV [104, 105, 99]. Run 2 lasted from 2015 to 2018 and saw a centre-of-mass energy increase to 13 TeV, delivering approximately 156 fb^{-1} of pp collision data to ATLAS [98]. Run 3 of pp collision data taking with two times design peak luminosity is currently planned to start its physics program in 2022 and last until end of 2024 [106]. Current plans foresee Run 3 to deliver about 150 fb^{-1} of pp collision data with centre-of-mass energies of 13 TeV and 14 TeV. After Run 3, the LHC will be upgraded to the High Luminosity LHC, significantly increasing the peak instantaneous luminosity and delivering up to 3000 fb^{-1} of pp collision data from 2027 until 2040 [106, 107].

This work uses pp collision data taken by ATLAS during Run 2 of the LHC. Of the 156 fb^{-1} delivered to ATLAS, 147 fb^{-1} were recorded, and 139 fb^{-1} were deemed to be good for physics analysis. Figure 2.3 shows the cumulative luminosity delivered to ATLAS during Run 2. Uncertainties on the measurement total recorded luminosity stem from the measurements of μ_{vis} and σ_{vis} , but are dominated by the uncertainties on σ_{vis} as vdm scans can only be done during special runs, while the general conditions during high- μ conditions change continuously. For the full Run 2 dataset, the uncertainties accumulate to $\pm 1.7\%$ [98].

2.2 ATLAS Experiment

The ATLAS experiment is one of two general-purpose detectors at the LHC. Located at Point 1 in a cavern 100 m below the surface, it is approximately 44 m long and 25 m high [87]. The design of the ATLAS experiment is driven by the aim to allow for a diverse research program, including SM precision measurements, Higgs physics and searches for BSM physics, whilst at the same time taking into account the unique and challenging conditions set by the LHC. The various detector technologies used are designed to withstand the high-radiation environment of the LHC, while allowing particle measurements with high spatial and temporal granularity. The general structure of ATLAS is depicted in fig. 2.4, and consists of a central part, called *barrel*, that has a cylindrical shape around the beam pipe, and two discs, called *end-caps*, that

[†] Often called *beam sweeping*.

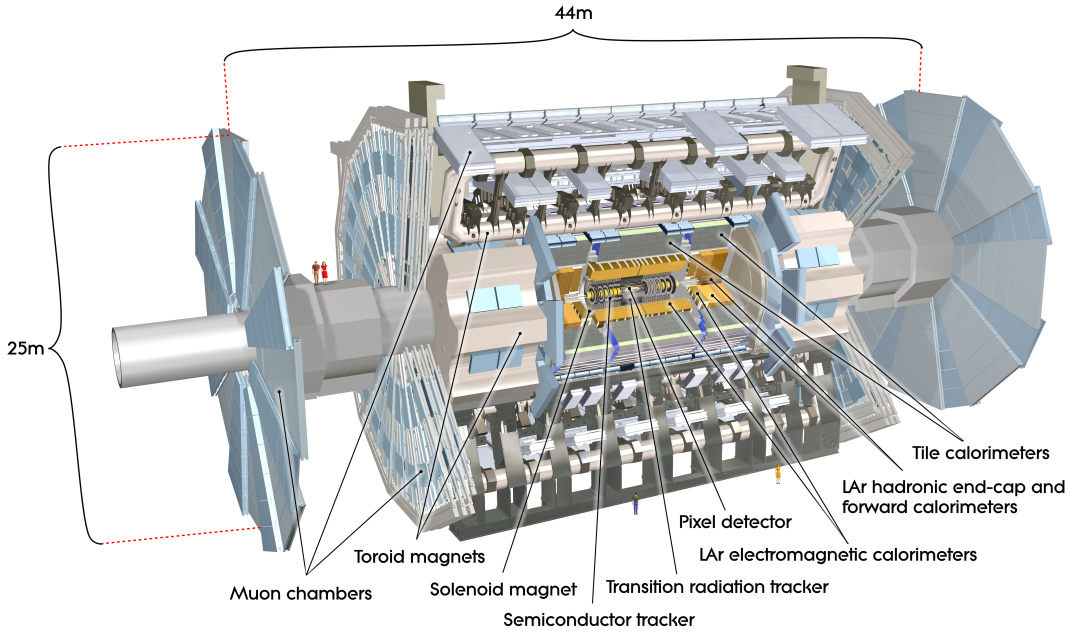


Figure 2.4: Computer generated picture of the ATLAS detector, giving an overview on the various subsystems [108].

close off the barrel on each side. This makes the ATLAS detector forward-backward symmetric and covering nearly the full solid angle of 4π , which is needed in order to measure momentum imbalances caused by particles that only interact weakly with the detector material.

The interface between the ATLAS experiment and the LHC is the beam pipe. In order to be maximally transparent to the particles created in the collisions, but also be able to withstand the forces from the vacuum, the beam pipe is made out of Beryllium close to the interaction point (IP), and stainless-steel further away from the IP [1].

The following sections introduce the working principles of the different detector components used in ATLAS, starting with the innermost component closest to the IP, the inner detector, followed by the calorimeters in the middle and finally the muon spectrometers on the outside. If not otherwise stated, details on the detector components are extracted from [87].

2.2.1 Coordinate system

In order to properly describe collision events in the ATLAS detector, a suitable detector system is needed. The right-handed coordinate system [109] used in ATLAS has its origin at the nominal IP in the centre of the detector. The positive x -axis points towards the centre of the LHC ring, the positive y -axis points upwards to the surface, and the beam pipe is used to define the z -axis. In the $x-y$ plane, called the transverse plane, the azimuthal angle ϕ is the angle around the beam axis, and the polar angle θ is measured from the beam axis. The rapidity [7] is defined as

$$y = \frac{1}{2} \ln \left(\frac{E + p_z}{E - p_z} \right) = \tanh \frac{p_z}{E}^{-1}, \quad (2.4)$$

with E the energy of an object and p_z its momentum in z -direction. As opposed to the polar angle θ , differences in the rapidity are invariant under Lorentz boosts in z -direction.

The pseudorapidity [7] is the high-energy limit ($p \gg m$) of the rapidity, and defined as

$$\eta = -\ln \tan \frac{\theta}{2}, \quad (2.5)$$

with $\cos \theta = p_z/p$. Pseudorapidity and rapidity are approximately equal in the limit where $p \gg m$ and $\theta \gg \frac{1}{\gamma}$. Compared to the rapidity, the pseudorapidity has the advantage of not depending on the energy and momentum calibration of the detected objects. Additionally, it gives a direct correspondence to the polar angle θ through the relation $\tanh \eta = \cos \theta$. Objects travelling along the beam axis have a pseudorapidity of $\eta = \text{inf}$ and objects travelling upwards along the y -axis have $\eta = 0$.

The distance between two objects in the ATLAS detector is given by

$$\Delta R = \sqrt{(\Delta\eta)^2 + (\Delta\phi)^2}. \quad (2.6)$$

The longitudinal momentum of the partons composing the colliding hadrons is only known by means of the Parton Distribution Functions (PDFs), giving the probabilities of the partons to have a certain energy in the direction of the beam. Thus, the total longitudinal energy in each collision is not exactly known, impeding the use of physics quantities in the z -direction. In the $x-y$ plane, however, momentum conservation can be applied, which is why mainly transverse physics quantities are used, indicated by a subscript ‘T’, e.g. E_T or p_T .

2.2.2 Magnet system

In order to perform precise momentum measurements of particles, ATLAS uses a system of magnets, whose magnetic fields force charged particles on curved tracks due to the Lorentz force. Using precise measurements of the tracks taken in the inner detector and the muon spectrometers, the curvature of the tracks can be determined, allowing an inference of the charge-to-momentum ratio q/p of charged particles. ATLAS employs a set of four superconducting magnets, one central solenoid, and three toroids, all operating at a nominal temperature of 4.5 K, achieved through a cryogenic system using liquid helium [87].

The solenoid is aligned on the beam axis and provides a 2 T magnetic field for the inner detector [87]. As it is located in front of the calorimeters (as seen from the IP), it is specially designed to have minimal material thickness in order to avoid influencing the subsequent energy measurements. The solenoid consists of single-layer coils made out of a Nb/Ti conductor and additional aluminum for stability. It operates at a nominal current of 7.73 kA and uses the hadronic calorimeter as return yoke [87].

The toroid magnets consist of a barrel toroid and two end-cap toroids, producing a magnetic field of 0.5 T and 1 T for the muon spectrometers in the barrel and end-caps, respectively[†] [87]. Both barrel and end-cap toroids are made out of Nb/Ti/Cu conductor with aluminum stabilisation, wound into double pancake-shaped coils. The barrel toroid coils are enclosed in eight stainless-

[†] The magnetic field in of the toroid magnets is designed to be higher in the end-caps in order to ensure enough bending power necessary for precise momentum measurements.

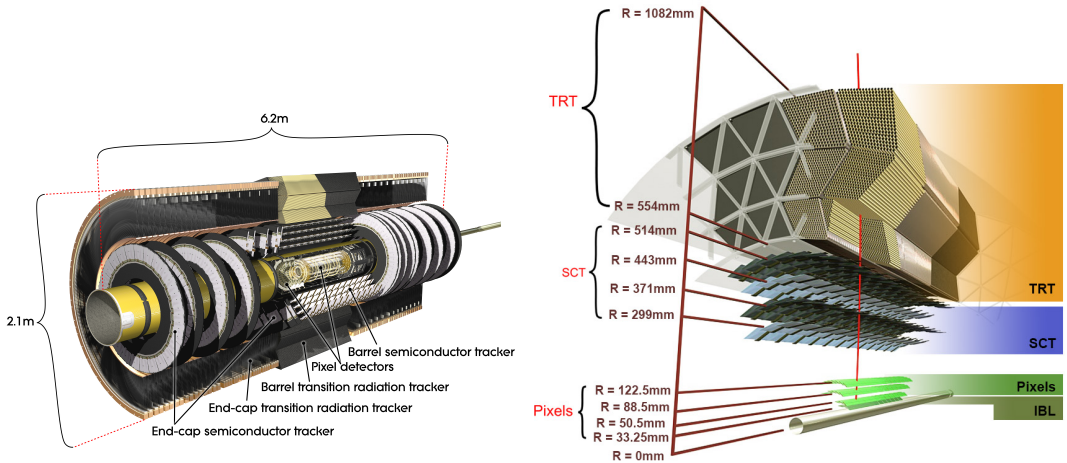


Figure 2.5: Schematic drawing of the ID and its subdetectors. Images adapted from [110, 111].

steel vacuum vessels in a racetrack-shaped configuration and arranged around the barrel calorimeters with an azimuthal symmetry. In order to withstand the Lorentz forces, the end-cap toroid coils are assembled in eight square units, and bolted and glued together with eight wedges, forming rigid structures. Both end-cap and barrel toroids operate at a nominal current of 20.5 kA [87].

2.2.3 Inner detector

Embedded in the magnetic field of the solenoid, the inner detector (ID) measures tracks of charged particles, allowing a determination of their momentum, while also providing crucial information for vertex reconstruction. As the ID is the detector closest to the beam pipe, its components need to be able to withstand the extreme high-radiation environment close to the IP. The ID consists of three subdetectors and uses two different working principles: semiconductor and gaseous detectors. In semiconductor-based tracking detectors, charged particles passing through the detector create a trail of electron-hole pairs that subsequently drift through the semiconductor material and cause electric signals. In gaseous detectors, traversing particles create electron-ion pairs also drift towards metal electrodes and induce electric signals.

Closest to the ID lies the pixel detector, followed by the silicon microstrip tracker (SCT), both of which are made of semiconductors. The SCT is surrounded by the transition radiation tracker (TRT), a gaseous detector. In total, the ID provides tracking and momentum information within $|\eta| < 2.5$ and down to transverse momenta of nominally 0.5 GeV. A schematic illustration of the ID and its subdetectors is shown in fig. 2.5.

Pixel detector

In the high-rate environment directly adjacent to the beam pipe, the only detector technology able to operate and deliver high-precision tracking information are semiconductor detectors segmented into pixels. As opposed to strip detectors, the reduced size of silicon pixel detectors and thus significantly reduced hit rate per readout channel allows pixel detectors to still be

operational in the harsh environment close to the IP. In ATLAS, pixels are hybrids of sensors and readout electronics, and were originally arranged in three layers in the barrel and the end-caps with a typical pixel of $50\text{ }\mu\text{m} \times 400\text{ }\mu\text{m}$, covering pseudorapidities up to $|\eta| < 2.5$. In order to increase robustness and performance in the high-luminosity environment, a new innermost layer, called the insertable B-layer (IBL), was installed together with a new, smaller radius beam pipe between Run 1 and Run 2 [112, 113]. The IBL uses smaller pixels with a size of $50\text{ }\mu\text{m} \times 250\text{ }\mu\text{m}$ and improves the tracking precision as well as vertex identification performance [113]. It also improves the performance of identifying jets originating from b -quarks (called b -tagging). The pixel detector [114]. The tracking precision obtained by the pixel detector is $10\text{ }\mu\text{m}$ in $(R - \phi)$ and $115\text{ }\mu\text{m}$ in (z) for the barrel and (R) for the end-caps.

Silicon microstrip detector

The pixel detector is surrounded by the SCT, consisting of four layers in the barrel and nine disks in the end-caps. In order to provide two-dimensional tracking information, strips are arranged in double-layers with a small crossing angle of 40 mrad and a mean pitch of $80\text{ }\mu\text{m}$ [87]. A charged particle traversing the SCT through the barrel thus creates four space point measurements. In the barrel, one set of strips in each of the four double-layers is oriented in beam direction, thereby measuring $R - \phi$, and in the end-caps, one set of strips in each layer is oriented in radial direction. The SCT has roughly 6.3 million readout channels and provides tracking information up to $|\eta| < 2.5$ [87]. It achieves a precision of $17\text{ }\mu\text{m}$ in $(R - \phi)$ and $580\text{ }\mu\text{m}$ in (z) for the barrel and (R) for the end-caps [87].

Transition radiation tracker

The last and also largest of the three subdetectors of the ID is the TRT, a gaseous detector made of multiple layers of 4 mm diameter drift tubes, surrounding the pixel detector and the SCT. The drift tubes consist of an aluminum cathode coated on a polyimide layer reinforced by carbon fibers and use a gold-plated tungsten wire as anode. The tubes are filled with a Xe-based gas mixture, providing an electric permittivity different from the surrounding material, causing transition radiation when traversed by ultrarelativistic particles. While the 144 cm long tubes in the barrel region are aligned parallel to the beam pipe, the 37 cm long tubes in the end-caps are aligned in radial direction, providing coverage up to $|\eta| < 2.0$ and an intrinsic accuracy of $130\text{ }\mu\text{m}$ in $R - \phi$ [87]. The low accuracy compared to the pixel detector and the SCT is compensated by the large amount of hits (typically 36 per track) and the longer measured track length. As the amount of transition radiation given off by a particle, is proportional to its Lorentz factor γ [7], the TRT is also used to improve electron identification [115]. For the same momentum, electrons will have a higher Lorentz factor than the heavier charged pions, and consequently give off more transition radiation.

2.2.4 Calorimeters

The primary goal of calorimeters is to measure the energies of incoming particles by completely absorbing them. As the energies of neutral particles can not be measured by other means, calorimeters are especially important for jet energy measurements (which contain neutral

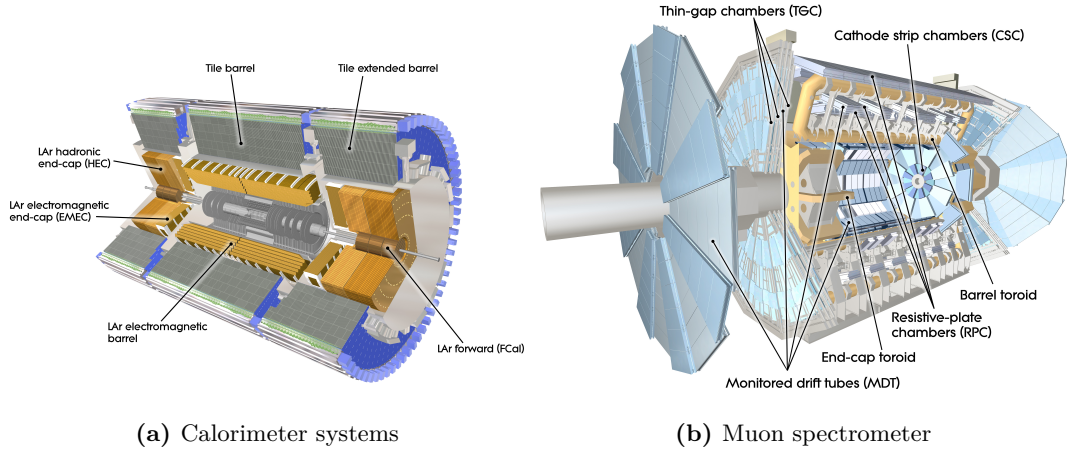


Figure 2.6: Schematic drawing of the calorimeter systems and the muon spectrometer in ATLAS. Images adapted from [116, 117].

hadrons) [1]. Since particles like photons and electrons interact mostly electromagnetically, while hadrons predominantly interact through the strong interaction, two different calorimeter types are needed in ATLAS. For values in η matching the ID, the electromagnetic calorimeter uses a finer granularity designed for precision measurements of electrons and photons. The subsequent hadronic calorimeter uses a coarser granularity sufficient for the requirements of jet reconstruction and missing transverse moment measurements. With a coverage up to $|\eta| < 4.9$, the calorimeter system in ATLAS provides the near hermetic energy measurements needed for the inference of missing transverse momentum created by neutrinos and other weakly interacting neutral particles [87].

Both calorimeters are sampling calorimeters, consisting of alternating layers of active and absorbing material. The absorbing material interacts with the incoming particles, causing them to deposit their energy by creating cascades or *showers* of secondary particles. The active layers are then used to record the shape and intensity of the produced showers. This alternating structure results in reduced material costs but also reduced energy resolution as only part of the particle's energy is sampled. Due to the typically longer cascades in hadronic interactions compared to electromagnetic interactions, and in order to minimise punch-through into the muon system, the hadronic calorimeter requires a greater material depth than the electromagnetic one. The calorimeter systems in ATLAS are schematically illustrated in fig. 2.6(a).

Electromagnetic calorimeter

The Electromagnetic (EM) calorimeter has an accordion-shaped structure and uses liquid argon (LAr) as active material and lead as absorber, providing full ϕ symmetry without azimuthal cracks. It is divided into a barrel part and two end-caps, covering $|\eta| < 1.475$ and $1.375 < |\eta| < 3.2$, respectively, and arranged in a way to provide uniform performance and resolution as a function of ϕ . The barrel EM calorimeter consists of two identical half-barrels with a small gap of 4 cm at $z = 0$. In the end-caps, the EM calorimeter consists of two coaxial wheels, covering the region $1.375 < |\eta| < 2.5$ and $2.5 < |\eta| < 3.2$, respectively. Calorimeter cells in the EM calorimeter are segmented into multiple layers with fine granularity in first layers in

the η region matching the ID, and coarser granularity in the outer layers and for $2.5 < |\eta| < 3.2$. In order to offer good containment of electromagnetic showers, the EM calorimeter has a depth of at least 22 (24) radiation lengths in the barrel (end-caps). A single instrumented LAr layer serves as presampler in the region with $|\eta| < 1.8$, allowing measurements of the energy losses upstream of the EM calorimeter, e.g. in the cryostats [87]. The design energy resolution of the EM calorimeter is $\sigma_E/E = 10\%/\sqrt{E} \oplus 0.7\%$ [87].

Hadronic calorimeter

Placed directly outside the envelope of the EM calorimeter is the hadronic tile calorimeter. It uses steel plates as absorber and polystyrene-based scintillating tiles as active material, and is subdivided into one central barrel and two extended barrels. Each barrel is segmented in three layers in depth with a total thickness of 7.4 interaction lengths. The tiles are oriented radially and perpendicular to the beam pipe and grouped in 64 tile modules per barrel, resulting in a near hermetic azimuthal coverage. Wavelength shifting fibres are used to shift the ultraviolet light produced in the scintillator to visible light and guide it into photomultipliers located at the radially far end of each module. The tile calorimeter covers a region with $|\eta| < 1.7$ and has a granularity of $\Delta\eta \times \Delta\phi = 0.1 \times 0.1$ except for the outermost layer which has a slightly coarser granularity in η . The design energy resolution of the tile calorimeter is $\sigma_E/E = 56.4\%/\sqrt{E} \oplus 5.5\%$ [87].

Hadronic calorimetry in the end-caps is provided by two independent calorimeter wheels per end-cap, situated directly behind the electromagnetic end-cap calorimeter (EMEC). Similar to the EMEC, the hadronic end-cap calorimeter (HEC) also uses LAr calorimeter as active material, allowing both calorimeter systems to share a single cryostat per end-cap. Instead of lead, the HEC however uses copper as absorber, which not only drastically reduces the mass of a calorimeter with a given interaction length, but also improves the linearity of low-energy hadronic signals [118]. Each of the four wheels of the HEC is comprised of 32 wedge-shaped modules, divided into two layers in depth. The HEC provides coverage in the region with $1.5 < |\eta| < 3.2$, slightly overlapping with the tile calorimeter and thus reducing the drop in material density in the transition region. While the granularity in the precision region with $1.5 < |\eta| < 2.5$ is the same as for the tile calorimeter, more forward regions with large $|\eta|$ have a granularity of $\Delta\eta \times \Delta\phi = 0.2 \times 0.2$ [87]. The design resolution of the HEC is $\sigma_E/E = 70.6\%/\sqrt{E} \oplus 5.8\%$ [87].

The forward region with $3.1 < |\eta| < 4.9$ is covered by the LAr forward calorimeter (FCal), which is integrated into the end-cap cryostats. This hermetic design not only minimises energy losses in cracks between the calorimeter systems, but also reduces the amount of background reaching the muon system in the outer shell of the ATLAS experiment. In order to limit the amount of neutrons reflected into the ID, the FCal is recessed by about 1.2 m with respect to the EM calorimeter, motivating a high-density design due to space constraints. The FCal in each end-cap consists of three layers with a total depth of 10 interaction lengths. While the first layer uses copper as absorber and is optimised for electromagnetic measurements, the remaining two layers are made of tungsten and cover hadronic interactions. The metals comprising each layer are arranged in a matrix structure with electrodes consisting of rods and tubes parallel to the beam pipe filling out regular channels. The small gaps (0.25 mm in the first layer) between the rods and tubes of the electrodes are filled with LAr as active material.

2.2.5 Muon spectrometer

Muons, being minimum ionising particles, are the only charged particles that consistently pass through the entire detector including the calorimeter system. Providing one of the cleanest signatures for BSM physics [1], muonic final states are measured with a dedicated detector system on the outermost layer of the ATLAS experiment. Embedded in the magnetic field of the toroid magnets, the muon spectrometer (MS) consists of three concentric cylindrical layers in the barrel region, and three wheels in each end-cap, and provides momentum measurements up to $|\eta| < 2.7$ [87]. It is designed to deliver a transverse momentum resolution of 10% for 1 TeV tracks and be able to measure muon momenta down to roughly 3 GeV.

The MS uses two high-precision gaseous detector chamber types, Monitoring Drift Tube (MDT) chambers and Cathode Strip Chamber (CSC). As both the MDT and CSC are drift chambers relying on charges drifting to an anode or cathode, the maximum response times of 700 ns and 50 ns, respectively, are slow compared to the bunch-spacing of 25 ns. ATLAS therefore uses Resistive Plate Chamber (RPC) in the barrel and Thin Gap Chamber (TGC) in the end-caps as triggers in order to associate measurements to the right bunch-crossing.

Monitored drift tubes

The MDT chambers are the main subcomponent providing precision measurements of the muon tracks up to $|\eta| < 2.7$, except in the innermost end-cap layer where their coverage only extends to $|\eta| < 2.0$. The MDT are made of 3–4 layers of ~ 30 mm diameter drift tubes operated with Ar/CO₂ gas[†] pressurised to 3 bar. Charged particles traversing the drift tubes ionise the gas, creating electrons that drift towards a central tungsten-rhenium anode wire with a diameter of 50 μm . Following the symmetry of the barrel toroid magnet, the MDT chambers are arranged as octets around the calorimeters with the drift tubes in ϕ direction, i.e. tangential to circles around the beam pipe. In order to be able to correct for potential chamber deformations due to varying thermal gradients, each MDT chamber is equipped with an internal optical alignment system. Apart from the regular chambers in the barrel and the end-cap wheels, special modules are installed in order to minimise the acceptance losses due to the ATLAS support structure (the *feet* of the experiment).

Cathode strip chambers

In the region with $|\eta| > 2.0$ in the first layer of the end-caps, the particle flux is too high to allow for safe operation of MDT chambers. Instead, CSC, multiwire proportional chambers, are used for precision measurements in this region. The gold-plated tungsten-rhenium anode wires in the CSC have a diameter of 30 μm and are oriented in radial direction. The wires are enclosed on both sides by cathode planes, one segmented perpendicular to the wires (thus providing the precision coordinate), the other parallel to the wires. Each chamber is filled with an Ar/CO₂ gas mixture and consists of four wire planes, resulting in four measurements of η and ϕ for each track. In addition to the chamber-internal alignment sensors, ATLAS also employs an optical alignment system in order to align the precision chambers to each other [87].

[†] With a small admixture of 300 ppm of water to improve high voltage stability.

Resistive plate chambers

RPC are gaseous parallel electrode-plate chambers that use two resistive plastic laminate plates kept 2 mm apart by insulating spacers. Due to an electric field of roughly 4.9 kV mm^{-1} between the plates, charged particles traversing the chamber cause avalanches of charges that can be read out through capacitive coupling to metallic strips mounted on the outside of the resistive plates. In order to provide tracking information in both coordinates, each RPC consists of two rectangular units each containing two gas volumes with a total of four pairwise orthogonal sets of readout strips. The three concentric cylindrical layers of RPC in the barrel region thus provide six measurements of η and ϕ and cover $|\eta| < 1.05$

Thin gap chambers

The TGC are not only necessary for triggering in the end-cap MS but also provide measurements of a second coordinate, orthogonal to the measurements of the MDT. TGC are multi-wire proportional chambers enclosed by two cathode planes and a wire-to-wire gap of 1.8 mm. The gas mixture of CO_2 and n-pentane allows for a quasi-saturated operation mode resulting in a relatively low gas gain. Each TGC unit is built from a doublet or triplet of such chambers, separated by a supporting honeycomb structure. In each unit, the azimuthal coordinate is measured by radial copper readout strips, while the bending coordinate is provided by the wire groups. The TGC are mounted in two concentric disks in each end-cap, one covering the rapidity range $1.05 < |\eta| < 1.92$ and one covering the more forward region $1.92 < |\eta| < 2.4$.

2.2.6 Forward detectors

Apart from the relative luminosity monitor LUCID-2 [100] (introduced in section 2.1.2) located at $\pm 17 \text{ m}$ from the IP, ATLAS uses three additional small detectors in the forward region. At $\pm 140 \text{ m}$ from the IP, immediately behind the location where the straight beam pipe splits back into two separate beam pipes, lies the Zero-Degree Calorimeter (ZDC) [119]. The ZDC is embedded in an absorber for neutrals mainly measures forward neutrons with $|\eta| > 8.3$ in heavy-ion collisions. Even further out from the IP at $\pm 240 \text{ m}$, lies the Absolute Luminosity for ATLAS (ALFA) detector [120], consisting of scintillating fibre trackers placed in Roman pots [121] measuring the absolute luminosity through small scattering angles of $3 \mu\text{rad}$ (necessitating the special beam conditions also used for the LUCID-2 calibrations). The last of the forward detectors is the ATLAS Forward Proton (AFP) [122] detector, installed at the end of 2016 and operational since early 2017, is situated $\pm 205 \text{ m}$ and $\pm 217 \text{ m}$ from the IP and consists of Roman pots containing silicon trackers and time-of-flight detectors. The AFP detectors aims to study very forward protons from elastic and diffractive scattering.

2.2.7 Trigger and data acquisition system

With a nominal bunch spacing of 25 ns, the bunch crossing rate within ATLAS is 40 MHz. Even with only a single pp collision event per bunch crossing, a mean event size of $\sim 1.6 \text{ MB}$ results in a data volume of more than 60 TB s^{-1} , which is impossible to process and write to disk with current technology. In addition, interesting physics events will often only occur at

relatively low rates, and generally be hidden in vast amounts of QCD processes that have much higher cross-sections. In order to reduce the event rate written to disk and focus on interesting signatures worth studying, ATLAS used a two-level trigger system during the Run 2 data-taking period [123].

The Level 1 (L1) trigger [124] is hardware-based and uses only coarse granularity calorimeter and muon detector information as inputs in order to define Regions of Interest (ROIs), i.e. regions in η and ϕ with interesting features. With a decision time of only 2.5 μ s per event, the L1 trigger reduces the event rate from the bunch-crossing rate of 40 MHz to 100 kHz. The ROIs generated by the L1 trigger are subsequently processed by the High Level Trigger (HLT) [125], a software-based trigger running on a computing farm. The HLT has access to the full detector granularity in the ROIs as well as the entire event and runs reconstruction algorithms similar to those used in offline analysis, allowing to significantly refine the decisions from the L1 trigger. The HLT reduces the event rate from 100 kHz to 1 kHz, matching the data storage constraints. Data flow from the detectors to the storage elements and between the L1 and HLT trigger elements is handled by the Data Acquisition System (DAQ) [125].

2.2.8 Monte Carlo simulation

Monte Carlo (MC) methods play a crucial role for simulating physics events in ATLAS. MC simulations are computational algorithms using repeated random sampling to solve complex problems, often the estimation of multi-dimensional integrals for which analytical solutions are not known. According to the law of large numbers the numerical approximations obtained by such a stochastic method become more accurate, the larger the sample size is. In addition, the central limit theorem also allows to state an uncertainty on the estimation of an expected value. This method can in principle be used for any problem with a probabilistic interpretation and is therefore well suited for particle physics where many aspects are inherently connected to Probability Density Functions (pdfs).

is this true?

In the ATLAS experiment, MC methods are not only used in physics analysis to estimate contributions from various physics processes in different phase space regions, but also to simulate particle interactions with the detector material and even finds ample applications in detector design and optimisation as well as physics objects reconstruction techniques. All of these applications rely on the MC simulations being as precise as possible, i.e. correctly describing the physics processes and detector responses underlying the data recorded by the ATLAS experiment. For reasons of more efficient computing resource utilisation and easier software validation, the ATLAS simulation infrastructure [126] can be divided into three main steps:

- (i) Event generation,
- (ii) Detector simulation,
- (iii) Digitisation,

producing an output format identical to that of the DAQ for recorded pp collision events, such that the same trigger and reconstruction algorithms can be run over simulated data.

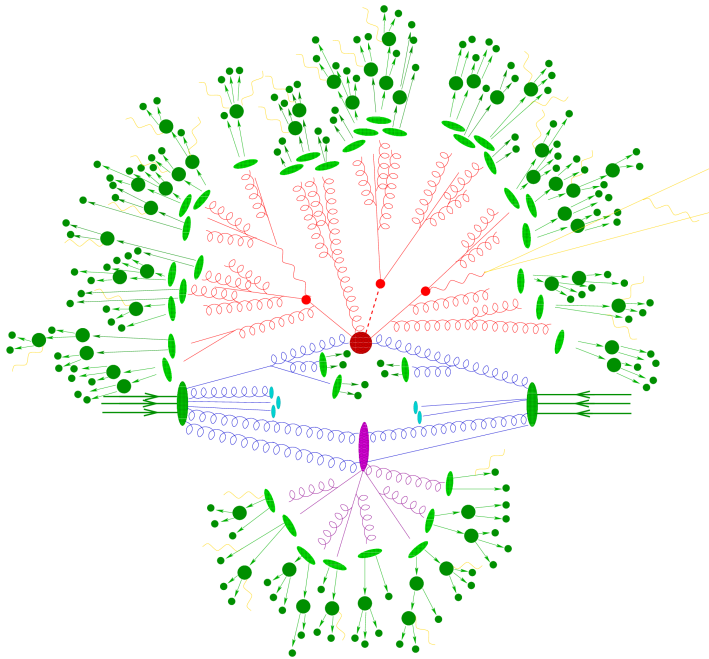


Figure 2.7: Pictorial representation of a $t\bar{t} + H$ event simulated by a MC event generator. The hard interaction (big red blob) is followed by the decay of the two top quarks and the Higgs boson (small red blobs). ISR and FSR are shown as curly blue and red lines, respectively. A second interaction is simulated (purple blob) and contributions from the underlying event are modelled (purple lines). The hadronisation of final-state partons (light green blobs) is followed by the decays of unstable hadrons (dark green blobs). QED radiation (yellow lines) is added at each stage of the event simulation. Figure adapted from [127].

Event generation

The majority of pp collisions are not interesting for particle physicists in the sense that they only involve soft hadrons travelling along the beam axis. Only a few events actually involve an *hard-scattering* event with high-momentum transfer, rendering them interesting for particle physicists to study. Generating and understanding the final states of these pp collision events is an enormously challenging problem as it typically involves hundreds of particles with energies spanning many orders of magnitude [128]. This makes the matrix elements connected to these processes too complicated to be computed beyond the first few orders of perturbation theory. The treatment of divergences and the integration over large phase-spaces further complicates the calculation of experimental observables.

It is not surprising that the simulation of the hard-scatter interaction is at the heart of any MC event generator. Due to the high-momentum transfer scale, the cross section of this process can be calculated perturbatively using collinear factorisation [128],

$$\sigma = \sum_{a,b} \int_0^1 dx_a dx_b \int d\Phi_n f_a^{h_1}(x_a, \mu_F) f_b^{h_2}(x_b, \mu_F) \times \frac{1}{2x_a x_b s} |\mathcal{M}_{ab \rightarrow n}|^2(\Phi_n; \mu_F, \mu_R), \quad (2.7)$$

with x_a and x_b the momentum fractions of the partons a and b with respect to their parent hadrons h_1 and h_2 , μ_F and μ_R are the unphysical factorisation and the renormalisation scales, respectively and $d\Phi_n$ is the differential final state phase-space element. The phase space integration is typically done using MC sampling methods. The choices for μ_R and μ_F are to some degree arbitrary, but are typically chosen to be in accordance with the logarithmic structure of QCD, such that the matrix elements can be combined with the subsequent parton showers [128]. The Matrix Element (ME) $|\mathcal{M}_{ab \rightarrow n}|^2$ can be calculated using different methods [128], with most MC generators employing leading order (LO) computations. As LO matrix elements are only reliable for the shapes of the distributions, an additional *K-factor* correcting the normalisation

simulation tools allow to plugin any Lagrangian and get events at detector level

of the cross section to next-to-leading order (NLO) is typically used. The probability of finding a parton with momentum fractions x in a hadron h , is given by the PDF $f_a^h(x, \mu_F)$ and depends on the probed factorisation scale μ_F . The PDFs depend on non-perturbative aspects of the proton wave function and can thus not be calculated from first principles. Instead, they are extracted from measurements in deep inelastic scattering experiments (see e.g. [129, 130]). The variety of PDFs provided by different groups, is accessible in a common format through a unified interface implemented by the LHAPDF library [131]. In MC generators, the choice of PDFs not only play a crucial role for the simulation of the hard process, but also in the subsequent parton showers and multiple parton interactions, thus influencing both cross sections and event shapes.

Fixed-order matrix elements work well for describing separated, hard partons but is not sufficient to describe soft and collinear partons. Higher order effects from gluon radiation can be simulated using a Parton Shower (PS) algorithm. The emitted gluons will radiate additional gluons or split into quark–antiquark pairs which can in turn undergo gluon radiation. The PS thus describes an evolutionary process in momentum transfer scales from the scale of the hard scatter interaction down to the infrared scale $\mathcal{O}(1\text{ GeV})$ where QCD becomes non-perturbative and partons are confined into hadrons. Both ISR and FSR are simulated through the PS. As opposed to ME calculations, PSs offer poor modelling of few hard partons, but excel in the simulation of collinear and soft multi-parton states.

In order to avoid double counting, the hard partons described by the calculation of the ME and the soft collinear emissions of the PS have to be connected to each other. This is done either through *matching* or *merging*. ME matching approaches [132] integrate higher-order corrections to an inclusive process with the PS [128]. Merging techniques like the CKKW [133] or CKKW-L [134] methods define an unphysical merging scale which can be understood as a jet resolution scale such that higher order ME corrections are only calculated for jets above that scale (while jets below that scale are modelled with the PS).

Next, additional activity in the event not directly associated to the hard process is simulated. The underlying event is typically defined to be all additional activity after ISR and FSR off the hard process has been taken into account [128]. Furthermore, *multiple interactions* can occur in a single pp collision. The modelling of multiple interactions involves multiple hard scatter processes per pp collision as well as multiple soft interactions in addition to the hard scatter process.

Once the PS reaches energies of $\mathcal{O}(1\text{ GeV})$, entering the non-perturbative regime of QCD, the coloured objects need to be transformed into colourless states. This so-called *hadronisation* step cannot be calculated from first principles but has to be modelled, typically with either a *string* or a *cluster* model. The most advanced of the string models is the *Lund* model [135, 136]. It starts from linear confinement and considers a linear potential between a $q\bar{q}$ pair, that can be thought of as a uniform colour flux tube stretching between the q and \bar{q} , with a transverse dimension of the order of typical hadronic size (i.e. around 1 fm). As the $q\bar{q}$ pair moves apart, the flux tube stretches in length, leading to an increase in potential energy, finally breaking apart once enough energy is available to create a new $q'\bar{q}'$ pair, resulting in two colourless quark pairs $q\bar{q}'$ and $q'\bar{q}$. The new quark pairs can again move apart and break up further, leading to quark anti-quark pairs with low relative momentum, forming the final hadrons. The cluster model is based on the preconfinement property of PSs [137], stating that the colourless clusters of partons can be formed at any evolution scale Q_0 of the PS, and result in universal invariant mass distributions that depend only on Q_0 and the QCD scale Λ , but not on the energy scale

Q or nature of the hard process at the origin of the PS [128]. The universal invariant mass distribution holds in the asymptotic limit where $Q_0 \ll Q$. If further $Q_0 \gg \Lambda$, then the mass, momentum and multiplicity distributions of the colourless clusters can even be calculated perturbatively [128]. Cluster models start with non-perturbative splitting of gluons and $q\bar{q}$ pairs, followed by the formation of clusters from colour-connected pairs. Clusters further split up until the Q_0 scale is reached, where they form the final mesons.

As not all hadrons formed in the hadronisation process are stable, the affected hadrons need to be decayed until they form resonances stable enough to reach the detector material. In addition QED radiation, that can happen at any time during the event, needs to be simulated. This is typically done with algorithms similar to the ones used for the PS.

The simulation steps that cannot be performed from first principles but rely on phenomenological models (underlying event, PS, hadronisation) introduce free parameters that need to be derived or *tuned* from parameter optimisations against experimental data. In ATLAS, the output of MC event generators is stored in so-called EVNT data format containing HepMC [138] event records. Although only the stable final-state particles are propagated to the detector simulation, the HepMC event record contains the entire connected tree as so-called *Monte Carlo truth*.

Detector simulation

Only the final-state particles generated by the MC event generator are read into the detector simulation. In ATLAS, the full detector simulation is handled GEANT4 [139], a toolkit providing detailed models for physics processes and an infrastructure for particle transportation through a geometry. GEANT4 has knowledge about the full detector geometry as well as the materials used in the subdetectors and is able to compute the energy deposits (so-called *hits*) from single particles in the different sensitive portions of the detector components. The GEANT4 simulation adds information to the Monte Carlo truth content created during the event generation, including however only the most relevant tracks (mostly from the ID) due to size constraints [126].

The complicated detector geometry and the detailed description of physics processes requires large computing resources for the full detector simulation using GEANT4, rendering it inaccessible for many physics studies requiring large statistics. Several varieties of fast simulations are available to this end. One of the most-used ones is ATLFAST-II [126], a fast simulation that uses the GEANT4 full simulation only for the ID and MS. The slow simulation in the calorimeters—that takes about 80% of the full simulation time—is replaced with FASTCALOSIM [140], using parameterised electromagnetic and hadronic showers. Compared to the $\mathcal{O}(10^3)$ s simulation time per event in the full simulation, the ATLFAST-II detector simulation only takes $\mathcal{O}(10^2)$ s [126].

Digitisation

During the digitisation step, the hits from the detector simulation are converted into detector responses, so-called *digits* that are typically produced when currents or voltages in the respective readout channels rise above a certain threshold in a given time window. The digitisation considers a modelling of the peculiarities of each detector component, including electronic noise and cross-talk [126]. The effects from out-of-time and in-time pile-up are also considered by reading in multiple events and overlaying their hits. In order to match the true pile-up distribution in

data, the number of events to overlay per bunch crossing can be set at run time. As described in section 2.1.1, effects from cavern background, beam halo and beam gas can either be mitigated or removed at analysis level and are therefore typically not simulated.

Chapter 3

Statistical data analysis

Statistical models are used in order to quantify the correspondence between theoretical predictions and the experimental observations in searches for SUSY. This chapter introduces the statistical concepts, methods and formulae used in this work for statistical inference. A frequentist approach to statistics is employed, interpreting probabilities as the frequencies of the outcomes of repeatable experiments that may either be real, based on computer simulations, or mathematical abstraction [7, 141]. The ensuing description largely follows [141, 142].

3.1 The likelihood function

In measurements in high energy physics, a *statistical model* $f(\mathbf{x}|\phi)$ is a parametric family of Probability Density Functions (pdfs) describing the probability of observing data \mathbf{x} given a set of model parameters ϕ that typically describe parameters of the physical theory or unknown detector effects. The *likelihood function* $L(\phi)$ is then numerically equivalent to $f(\mathbf{x}|\phi)$ with \mathbf{x} fixed. As opposed to the pdf $f(\mathbf{x})$ which describes the value of f as a function of \mathbf{x} given a fixed set of parameters ϕ , the likelihood refers to the value of f as a function of ϕ given a fixed value of \mathbf{x} .

Searches for BSM physics are typically centred around the measurement of several disjoint binned distributions (called *channels* c) that are each associated with different event selection criteria (as opposed to different scattering processes) yielding observed event counts \mathbf{n} . In such counting experiments where each event is independently drawn from the same underlying distribution, each bin is fundamentally described by a Poisson term. The Poisson probability to observe n events with a expectation of ν events, is given by

$$\text{Pois}(n|\nu) = \frac{\nu^n}{n!} e^{-\nu}. \quad (3.1)$$

The expectation ν_{cb} in each channel c and bin b is a sum over the set of physics processes considered (called *samples*). The sample-wise rates are in general a function of the the model parameters ϕ , that can either be *free parameters* η or *constrained parameters* χ . Free parameters directly determined by the Poisson terms for the data observations are called *normalisation factors*. The constrained parameters represent the systematic uncertainties considered in the

model. The degree to which they cause a deviation of the expected event rates from the nominal event rates is limited through *constraint terms* $c_\chi(a_\chi|\chi)$ that can be viewed as *auxiliary measurements* with global observed data \mathbf{a} .

For a given observation $\mathbf{x} = (\mathbf{n}, \mathbf{a})$ of observed events \mathbf{n} and auxiliary data \mathbf{a} , the likelihood then reads

$$L(\boldsymbol{\eta}, \chi) = \prod_{c \in \text{channels}} \prod_{b \in \text{bins}_c} \text{Pois}(n_{cb}|\nu_{cb}(\boldsymbol{\eta}, \chi)) \prod_{\chi \in \chi} c_\chi(a_\chi|\chi), \quad (3.2)$$

where, given a certain integrated luminosity, n_{cb} and ν_{cb} refer to the corresponding observed and expected rate of events, respectively [143]. Most of the systematic uncertainties are so-called *interpolation parameters* α representing either normalisation uncertainties or correlated shape uncertainties. Their constraint terms $c_\alpha(a_\alpha|\alpha)$ are parametrised by a Gaussian with mean $a = 0|\alpha$ and variance $\sigma = 1$, with $\alpha = 0$ representing the nominal value. The *up* and *down* variations are then given by $\alpha = \pm 1$, thus representing $\pm 1\sigma$ variations. The impact of any given value of the parameter on the event rates is then evaluated through polynomial interpolation and exponential extrapolation, a method that avoids discontinuous first and second derivatives at $\alpha = 0$ and ensures positive values for the predicted event rates [144].

Sample rates derived from theory calculations (i.e. MC simulation), are scaled to the integrated luminosity corresponding to the observed data. The integrated luminosity is itself a measurement that is subject to uncertainties. Therefore, an additional constraint term in the likelihood is needed. It is parametrised by a Gaussian with mean corresponding to the nominal integrated luminosity measurement and variance equal to the integrated luminosity measurement uncertainty.

Uncertainties arising from the finite size of the MC datasets often used to derive estimated event rates are modelled by bin-wise scale factors γ_b . The constraint terms are Gaussian distributions with central value equal to unity and variances calculated from the individual uncertainties of the samples defined in the respective channel.

As the event rate in a given bin can depend on multiple parameters, and, likewise, a single parameter can affect the expected event rate in multiple bins, correlations between the model parameters ϕ can occur.

The above prescription for building binned likelihoods is called the HISTFACTORY template [144]. In this work, two independent implementations of the HISTFACTORY template are used. The first implementation uses RooFIT [145] and RooSTATS [146] for fitting (using Minuit [147] and implemented within the ROOT framework [148, 149]), and HISTFITTER [150] as interface for steering fits and hypothesis tests and bookkeeping of results. The second implementation uses pyhf [151, 152], a pure-python implementation of HISTFACTORY that is independent from ROOT and uses computational graph libraries like PYTORCH [153], TENSORFLOW [154] and JAX [155] to speed up the minimisation process.

Apart from separating the model parameter set into free and constrained parameters $\phi = (\boldsymbol{\eta}, \chi)$, a separate partition $\phi = (\psi, \theta)$ is frequently used in the context of hypothesis testing. Here, $\boldsymbol{\eta}$ are so-called *parameters of interests* of the model for which hypothesis tests are performed, and θ are *nuisance parameters* that are not of immediate interest but need to be accounted for to correctly model the data. In the search presented in this work, the only Parameter of Interest (POI) is the *signal strength* parameter μ , representing the ratio of the signal process cross section to its reference cross section as expected from theory. The expectation ν_i in each

Explain
this fur-
ther

bin i can be parametrised through

$$\nu_b = \mu S_b + B_b, \quad (3.3)$$

where S_b and B_b are the bin-wise expected signal and background rates, respectively. Fixing $\mu = 0$ thus yields an expected event rate containing only SM processes (thus called *background-only*), while $\mu = 1$ represents a *signal-plus-background* description at nominal signal cross section. Scanning multiple values of μ allows to set limits on the visible cross sections of the signal models considered in the search.

3.2 Parameter estimation

Given a likelihood $L(\mu, \phi)$ for a fixed set of observations \mathbf{x} , a measurement can be understood as a parameter estimation. In general, an estimator $\hat{\phi}$ is a function of the observed data used to estimate the true value of the model parameter ϕ .

In particle physics, the most commonly used estimator is the Maximum Likelihood Estimator (MLE). The MLEs for the model parameters $\hat{\phi}$ are defined to be the parameter values that maximise $L(\phi)$, or, equivalently maximise $\ln L(\phi)$ and minimises $-\ln L(\phi)$. The logarithm of the likelihood is used for computational reasons, as it not only reduces the computational complexity by avoiding exponentials and products, but also avoids problems of running out of floating point precision. As the logarithm is a monotonically increasing function, $\ln L(\phi)$ has maxima at the same parameter values as $L(\phi)$.

The MLE $\hat{\phi}$ can thus be found by solving

$$\frac{\partial \ln L}{\partial \phi_i} = 0, \quad (3.4)$$

where the index i runs over all parameters. The solution typically needs to be found numerically using minimisation algorithms. In the following, the parameter estimation is referred to as a *fit* of the model to data, and the maximum likelihood estimates of the parameters are consequently called *best-fit values*.

3.3 Statistical tests

In addition to estimating the values of model parameters, searches for SUSY are naturally interested in claiming discovery (or alternatively exclusion) of hypothesised signal models. In the frequentist approach, this can be formulated in terms of hypothesis tests, evaluating a *null hypothesis* H_0 against an *alternative hypothesis* H_1 , with the goal of rejecting the null hypothesis. For discovering a new signal process, H_0 is defined to describe only known SM processes (called *background-only* hypothesis), while H_1 describes both SM background processes as well as the signal process (called *signal plus background hypothesis*). When excluding a signal model the signal plus background hypothesis takes over the role of H_0 and is tested against the background-only hypothesis.

The degree of agreement of observed data with a certain hypothesis H is quantified by computing a *p*-value, representing the probability of finding data of greater or more extreme incompatibility

under assumption of H . The hypothesis can then be considered as excluded if its observed p -value is below a specified threshold. It is common to convert the p -value into a *significance* Z , defined in such a way that a Gaussian distributed observable with measured value Z standard deviations above its mean gives a one-sided upper tail probability equal to p . This yields the expression

$$Z = \Phi^{-1}(1 - p), \quad (3.5)$$

where Φ^{-1} is the quantile of the standard Gaussian. Discovery of a signal then conventionally requires a significance of at least $Z = 5$, while exclusion of a signal hypothesis at 95% confidence level requires a p -value of 0.05, i.e. $Z = 1.64$ [142].

The p -values are calculated using a *test statistic* that parameterises the compatibility between the hypothesis and data in a single value. At the LHC experiments, the test statistics used for hypothesis testing are based on the *profile likelihood ratio*

$$\lambda(\mu) = \frac{L(\mu, \hat{\theta}(\mu))}{L(\hat{\mu}, \hat{\theta})}, \quad (3.6)$$

where the *conditional maximum likelihood estimates* $\hat{\theta}$ are the values of θ that maximise the likelihood with μ fixed. The profile likelihood ratio depends explicitly on μ , and implicitly on $\mathbf{x} = (\mathbf{n}, \mathbf{a})$, but is asymptotically (i.e. in the limit of a large number of events) independent of the nuisance parameters θ^\dagger . The asymptotic independence from θ follows from Wald's and Wilks' theorems [156, 157] and is one of the main motivations for using the profile likelihood ratio, as it avoids the problem of having to compute p -values for all possible values of θ . The profile likelihood ratio takes values between 0 and 1, with $\lambda(\mu) = 1$ corresponding to cases where the tested value of μ is in good agreement with the observed data.

As the rate of signal processes considered in this work is non-negative, an estimator for μ must satisfy $\hat{\mu} \geq 0$. In order to avoid the formal complications of having a boundary at $\mu = 0$, it is convenient to consider an effective estimator $\hat{\mu}$ that is allowed to become negative, provided that the respective Poisson terms for $\mu S_b + B_b$ remain positive. By imposing the constraint $\mu \geq 0$ on the test statistic itself, it is possible to avoid the formal problems of having a boundary at $\mu = 0$. This leads to the definition of

$$\tilde{\lambda}(\mu) = \begin{cases} \frac{L(\mu, \hat{\theta}(\mu))}{L(\hat{\mu}, \hat{\theta})}, & \hat{\mu} \geq 0, \\ \frac{L(\mu, \hat{\theta}(\mu))}{L(0, \hat{\theta}(0))}, & \hat{\mu} < 0, \end{cases} \quad (3.7)$$

where $\hat{\theta}(0)$ and $\hat{\theta}(\mu)$ are the conditional MLEs of θ given a signal strength parameter of 0 and μ , respectively.

[†] Eliminated by choosing specific values of the nuisance parameters for a given \mathbf{x} and μ , often referred to as *profiling*.

Discovery

For the important special case where $\mu = 0$ is tested in a model with $\mu \geq 0$, i.e. discovery of a non-negative signal (rejection of the $\mu = 0$ hypothesis), the test statistic in eq. (3.7) becomes

$$q_0 = \tilde{t}_0 = \begin{cases} -\ln \lambda(0), & \hat{\mu} \geq 0, \\ 0, & \hat{\mu} < 0. \end{cases} \quad (3.8)$$

This definition ensures that the $\mu = 0$ hypothesis is not rejected due to a downward fluctuation in data, causing $\hat{\mu} < 0$. In case more events are seen in data than expected based on the background-only hypothesis, eq. (3.8) produces increasingly large values of q_0 , corresponding to an increasing incompatibility between data and the background-only hypothesis. The p -value quantifying the disagreement between the $\mu = 0$ hypothesis and data can then be computed using

$$p_0 = \int_{q_0,\text{obs}}^{\infty} f(q_0|0) dq, \quad (3.9)$$

with q_0,obs the observed value of the test statistic q_0 in data and $f(q_0|0)$ the pdf of q_0 under assumption of the $\mu = 0$ hypothesis. In the asymptotic limit with a single POI, the test statistic q_0 can be written as

$$q_0 = \begin{cases} \hat{\mu}^2/\sigma^2, & \hat{\mu} \geq 0, \\ 0, & \hat{\mu} < 0, \end{cases} \quad (3.10)$$

where $\hat{\mu}$ has a Gaussian distribution with mean μ' and variance σ^2 . In the case where $\mu' = 0$, the pdf of q_0 has the form of a half chi-square distribution with one degree of freedom, and its cumulative distribution is $F(q_0|0) = \Phi(\sqrt{q_0})$. Using eq. (3.5), the p -value obtained with eq. (3.9) can be expressed with the significance Z_0 as

$$Z_0 = \sqrt{q_0}. \quad (3.11)$$

Exclusion and upper limits

If the background-only ($\mu = 0$) hypothesis cannot be rejected, the hypotheses can be switched around and instead the signal plus background hypothesis can be tested. For excluding the signal plus background ($\mu = 1$) hypothesis and setting upper limits on the signal strength μ , the test statistic is defined as

$$\tilde{q}_{\mu} = \begin{cases} -2 \ln \tilde{\lambda}(\mu), & \hat{\mu} \geq 0, \\ 0, & \hat{\mu} < 0. \end{cases} = \begin{cases} -2 \ln \frac{L(\mu, \hat{\theta}(\mu))}{L(\hat{\mu}, \hat{\theta})}, & \hat{\mu} \geq 0, \\ -2 \ln \frac{L(\mu, \hat{\theta}(\mu))}{L(0, \hat{\theta}(0))}, & 0 \leq \hat{\mu} \leq \mu, \\ 0 & \hat{\mu} > \mu. \end{cases} \quad (3.12)$$

Setting $\tilde{q}_{\mu} = 0$ in the case where $\hat{\mu} > \mu$ ensures that an overfluctuation of data is not considered as evidence against the signal hypothesis. This is opposed to the definition of q_0 , where an underfluctuation of data ($\hat{\mu} < \mu$) is not regarded to be evidence against the background-only hypothesis. The p -value, quantifying the level of agreement between data and the tested value

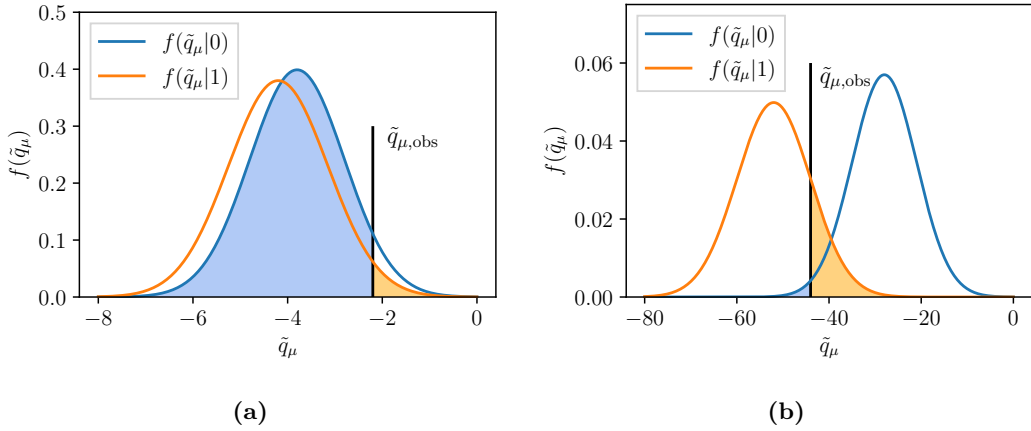


Figure 3.1: Distribution of the pdfs of the signal plus background (in orange) and background-only (in blue) models. The coloured areas represent the p_{s+b} and p_b values, respectively. Figure (a) shows a case where both pdfs are close together, while figure (b) shows a case where both are well separated. Adapted from [158].

of μ is then given by

$$p_\mu = \int_{\tilde{q}_{\mu,\text{obs}}}^{\infty} f(\tilde{q}_\mu|\mu) d\tilde{q}_\mu, \quad (3.13)$$

where, as before, $\tilde{q}_{\mu,\text{obs}}$ is the observed value of the test statistic in data and $f(\tilde{q}_\mu|\mu)$ is the pdf of \tilde{q}_μ given the hypothesis μ . In the asymptotic limit, the test statistic \tilde{q}_μ can be written as

$$\tilde{q}_\mu = \begin{cases} \mu^2\sigma^2 - 2\mu\hat{\mu}/\sigma^2, & \hat{\mu} \geq 0, \\ (\mu - \hat{\mu})^2\sigma^2, & 0 \leq \hat{\mu} \leq \mu, \\ 0 & \hat{\mu} > \mu, \end{cases} \quad (3.14)$$

which yields for the significance Z_μ the expression

$$Z_\mu = \begin{cases} \sqrt{\tilde{q}_\mu}, & 0 < \tilde{q}_\mu \leq \mu^2/\sigma^2 \\ \frac{\tilde{q}_\mu + \mu^2/\sigma^2}{2\mu/\sigma}, & \tilde{q}_\mu > \mu^2/\sigma^2. \end{cases} \quad (3.15)$$

3.4 CL_s approach

In the CL_{s+b} method, a signal plus background model is excluded if $p_{s+b} < \alpha$, where α is defined by the desired confidence level, typically $CL = 1 - \alpha = 95\%$, and p_{s+b} can be calculated using the test statistic \tilde{q}_μ (with $\mu = 1$) introduced before. If the experiment has very low sensitivity to a specific signal plus background model, e.g. because the production cross section is too low, the test statistic of the signal plus background model will be very close to that of the background-only model. In case of an underfluctuation in data, the $\mu = 1$ model can then falsely be excluded, even though no sensitivity is expected. Figure 3.1 illustrates this with a simple example. In fact, the exclusion of models to which the experiment has no sensitivity has a probability of at least α [158].

This problem can be remedied by adopting the CL_s method [159], altering the threshold for excluding a model in a way to avoid exclusion of models to which the experiment has very low sensitivity. The CL_s value is defined as

$$CL_s = \frac{p_{s+b}}{1 - p_b}, \quad (3.16)$$

where p_b is the p -value of the background-only hypothesis. If the distributions of the test statistics for the signal plus background and the background-only models are close a small value of p_{s+b} due to an underfluctuation in data will entail a large value of p_b . Consequently, in the calculation of the CL_s value, p_{s+b} will be penalised by $1 - p_b$ (that will be close to 0), resulting in $CL_s > p_{s+b}$, preventing the exclusion of the signal plus background model. Conversely, in the case where the two test statistics are well-separated and $p_{s+b} < \alpha$, then p_b will also be small and thus CL_s will be close to p_{s+b} obtained by the frequentist approach.

3.5 Sensitivity estimation

When designing search regions for an analysis, it is necessary to achieve an optimal signal-to-background separation power. A significance metric is needed in order to quantify the separation power and have a metric to optimise for. In the following, the expected discovery significance introduced in Ref. [160] is used. As the full statistical model is in general not yet known when designing the search regions, appropriate assumptions have to be made. In a *cut-and-count* selection where only the total number of events after a selection are relevant (and not e.g. their distribution), the significance is determined by the total number of signal events S , the total number of background events B and the uncertainty on the expected number of background events ΔB . This can be modelled as a so-called *on/off* problem [160, 161], where the cut-and-count experiment uses two bins, a signal region (SR) enriched in signal events, and a control region (CR) containing only background events. The parameter $\tau = n_{\text{CR}}/n_{\text{SR}}$ then denotes the ratio between the event rate in the CR, n_{CR} , to the event rate in the SR, n_{SR} .

If τ is known, then the likelihood of this simple configuration can be written in terms of the expected background event rate

$$L(\mu, B) = \text{Pois}(n_{\text{SR}}|\mu S + B) \cdot \text{Pois}(n_{\text{CR}}|\tau B), \quad (3.17)$$

with μ the signal strength parameter. The relative background uncertainty can thus be treated as coming from a Poisson-distributed auxiliary measurement containing only background (i.e. in the CR) with corresponding uncertainty $\sqrt{\tau B}$, leading to the approximation

$$\tau = \frac{B}{\Delta B^2}. \quad (3.18)$$

As n_{SR} and n_{CR} are each drawn from a Poisson probability with unknown means ν_{SR} and ν_{CR} , the background-only hypothesis corresponds exactly to the case where the ratio of Poisson means $\lambda = \nu_{\text{CR}}/\nu_{\text{SR}}$ is equal to τ [160]. The two Poisson terms can then be written as the product of a single Poisson term with mean $n_{\text{tot}} = n_{\text{SR}} + n_{\text{CR}}$ and the binomial probability of picking n_{SR} events out of n_{tot} with probability $\rho = \nu_{\text{SR}}/\nu_{\text{tot}} = 1/(1 + \lambda)$, yielding for the

likelihood

$$\begin{aligned} L(\mu, B) &= \text{Pois}(n_{\text{tot}}|\lambda_{\text{tot}}) \cdot B(n_{\text{SR}}|\rho, n_{\text{tot}}) \\ &= \frac{e^{-\lambda_{\text{tot}}} \lambda_{\text{tot}}^{n_{\text{tot}}}}{n_{\text{tot}}!} \cdot \binom{n_{\text{tot}}}{n_{\text{SR}}} \rho^{\lambda_{\text{tot}}} (1-\rho)^{n_{\text{tot}}-n_{\text{SR}}}. \end{aligned} \quad (3.19)$$

Since the background-only hypothesis can not only be expressed as $\mu = 0$, $\nu_{\text{SR}} = \nu_B$, or $\lambda = \tau$, but especially also as $\rho = 1/(1 + \tau)$ [160], its p -value can be calculated using the well-known frequentist binomial test,

$$p_B = \sum_{j=n_{\text{SR}}}^{n_{\text{tot}}} B(j|n_{\text{tot}}, \rho). \quad (3.20)$$

The significance corresponding to p_B can be derived using eq. (3.5) is computable in a numerically fast way using the incomplete beta function. The algorithm used for calculating Z_B in this work is implemented in the `RooStats::NumberCountingUtils` methods in ROOT.

Part II

The 1-lepton analysis

Chapter 4

Analysis overview

This chapter aims to give an introduction to the search for electroweakinos presented in this work. First, the targeted final state, the 1-lepton final state, is introduced and motivated, followed by the SM background processes that need to be considered when doing searches for SUSY in this final state. Next the reconstruction and identification of physics objects as well as the event selection requirements are described.

4.1 Search for electroweakinos in the 1-lepton final state

In the search for electroweakinos presented herein, the simplified model introduced in section 1.3.2 is interpreted in final states with one lepton, two b -jets and high missing transverse momentum. This final state can occur when the W boson decays through $W^\pm \rightarrow \ell^\pm \nu_\ell$, while the Higgs boson decays into $h \rightarrow b\bar{b}$. Although a final state without leptons would benefit from the higher branching fraction of the $W^\pm \rightarrow q'\bar{q}$ decay, due to the QCD couplings these final states are largely dominated by QCD multi-jet background processes that are omnipresent at hadron colliders like the LHC. Final states with exactly one lepton have lower cross sections but allow to reject a majority of the QCD background, as pure QCD multi-jet events can only appear in the 1-lepton final state through false reconstruction of a jet as a lepton (so-called *fake* leptons).

Targeting the decay of the Higgs boson into a pair of b quarks benefits from the high branching ratio of 58.3% and allows a full reconstruction of Higgs candidates, a procedure that will be used to achieve a high signal-to-background ratio. Figure 4.1 shows the full signal model targeted in this search, including the considered decays of the W and Higgs bosons.

Previous searches for electroweakinos in this final state have been performed by the ATLAS [162, 163] and CMS [164] collaborations, excluding $\tilde{\chi}_1^\pm \tilde{\chi}_2^0$ masses up to 540 GeV and 490 GeV, respectively, for massless $\tilde{\chi}_1^0$. The two previous ATLAS searches used 20.3 fb^{-1} of $\sqrt{s} = 8 \text{ TeV}$ and 36.1 fb^{-1} of $\sqrt{s} = 13 \text{ TeV}$ pp collision data, respectively. As opposed to this, the search presented in the following uses the full dataset available from the Run 2 data taking period, amounting to an unprecedented 139 fb^{-1} of pp collision data at $\sqrt{s} = 13 \text{ TeV}$.

refer to observables

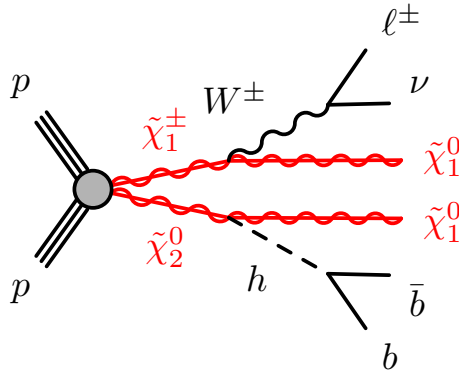


Figure 4.1: Diagram for the simplified model used in this work including the decays $W^\pm \rightarrow \ell^\pm \nu_\ell$ and $h \rightarrow b\bar{b}$.

4.2 Standard Model backgrounds

Although the requirement of exactly one lepton isolated from surrounding hadronic activity significantly reduces the contribution from QCD multi-jet background, numerous SM processes can result in final states with exactly one isolated lepton, multiple jets and missing transverse momentum. Background sources are generally classified into *reducible* and *irreducible* backgrounds. Irreducible backgrounds are processes that have a physical phase space that is indistinguishable from the final state of the signal process considered. Reducible backgrounds, on the other hand, result from partially misreconstructed processes as well as mismeasurements. Examples of reducible processes are events where a lepton originates from a heavy flavour (HF) decay, photon conversions or misreconstructed jets. SM processes that result in final states with an isolated lepton, multiple jets and missing transverse momentum typically involve a W boson decaying into a lepton–neutrino pair (a so-called *leptonic decay*). The neutrino will contribute to the total missing transverse momentum in the event, while additional jets can appear in the final state through QCD radiation or other branches of the decay chain.

By far the largest SM background contributions stem from the production of top quarks, predominantly through top quark pair $t\bar{t}$ production, where both top quarks decay into a W boson and a b quark. Final states with one isolated lepton can occur through leptonic decay of one of the W bosons. Figure 4.2(a) shows a diagram depicting an exemplary decay of a $t\bar{t}$ system into a final state with one lepton, multiple jets (two of which originate from b quarks) and missing transverse momentum. In addition to $t\bar{t}$, single top production (s -channel, t -channel or tW -channel) can also result in similar final states as the SUSY signal and thus constitutes a significant SM background process. An exemplary decay is shown in fig. 4.2(b).

Apart from processes involving top quarks, the production of a W boson in association with multiple jets ($W + \text{jets}$) is the third major background considered in the analysis. If the W boson undergoes a leptonic decay and two of the produced jets are tagged as originating from b quarks, the signature of this process is similar to that of signal events. An exemplary diagram for a $W + \text{jets}$ event is shown in fig. 4.2(c).

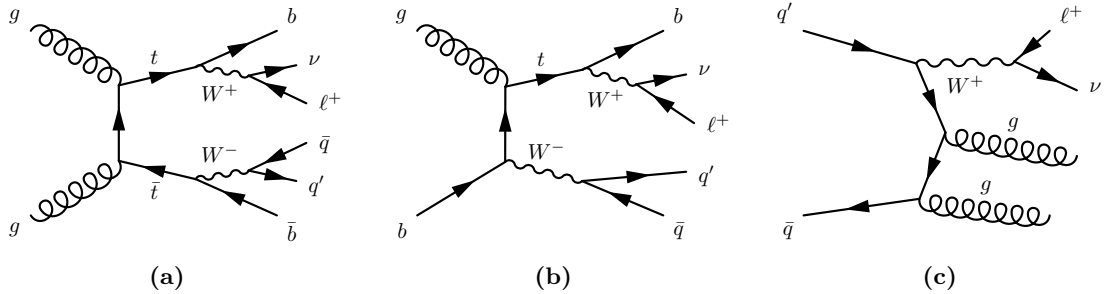


Figure 4.2: Exemplary Feynman diagrams showing the dominant processes (a) $t\bar{t}$, (b) single top and (c) $W + \text{jets}$ production with subsequent decays.

Production of multiple vector bosons V ($= W, Z$)—although not a dominant background due to low cross sections—can still result in the same final state as the signal process. In the following, diboson VV and multibosons VVV processes are considered.

Other SM backgrounds with small contributions in the phases spaces targeted by the analysis include $Z + \text{jets}$ production, $t\bar{t} + V$ production, as well as various processes involving Higgs bosons. $Z + \text{jets}$ plays only a minor role, as the only irreducible component is $Z(\rightarrow \tau\tau) + \text{jets}$, where one τ -lepton undergoes a leptonic decay and the other one a hadronic decay. Production of $t\bar{t} + V$ has a similar topology as ordinary $t\bar{t}$ processes but with lower cross section and additional objects in the final state. Higgs processes considered in the following include single Higgs production through vector boson fusion (VBF) or gluon–gluon fusion (ggF) as well as $h + V$ and $h + t\bar{t}$ processes. In the following, these backgrounds are simply labelled *other*.

Pure QCD multi-jet events can only appear in the 1-lepton final state through false reconstruction of a jet as a lepton (so-called *fake* leptons) and mismeasurement of E_T^{miss} . As it has been shown that this background is negligible in all selections relevant to this search, no estimation for QCD contribution is considered in the following [165].

4.3 Monte Carlo samples

Table 4.1 summarises all MC generators and software versions used for the simulated events used in the following. Further details are given in the relevant ATLAS simulation notes [166–169].

4.3.1 Signal samples

The $\tilde{\chi}_1^\pm/\tilde{\chi}_2^0$ pair production signal samples were generated at LO using MADGRAPH5_AMC@NLO 2.6.2 [170, 171] with up to two additional partons in the ME. MADGRAPH5_AMC@NLO is interfaced with PYTHIA8 [172] for the PS, hadronisation and underlying event, using the CKKW-L [173] scheme for matching the PS to the MEs. The NNPDF 2.3 LO [174] PDF set and the A14 set of tuned parameters [175] are used. For modelling the decay of HF quarks, EVTGEN [176] v1.6 is used.

As the $\tilde{\chi}_1^\pm/\tilde{\chi}_2^0$ and $\tilde{\chi}_1^0$ masses are free parameters of the signal model, they are systematically scanned, resulting in a set of 164 distinct evenly distributed in the two-dimensional grid spanned

by the mass parameters. In the following the two-dimensional grid will be referred to as *signal grid*, while the distinct signal scenarios (each with a unique set of mass parameter values) will be referred to as *signal point*. The generated signal grid covers $\tilde{\chi}_1^\pm/\tilde{\chi}_2^0$ masses from 150 GeV to 1.1 TeV and $\tilde{\chi}_1^0$ masses from 0 GeV to 550 GeV, avoiding the kinematically forbidden region with $m(\tilde{\chi}_1^\pm/\tilde{\chi}_2^0) < m(\tilde{\chi}_1^0) + m(h)$.

Signal samples well within the expected sensitivity range of the analysis (with relatively low $\tilde{\chi}_1^\pm/\tilde{\chi}_2^0$ and $\tilde{\chi}_1^0$ masses) are generated using the ATLFast-II detector simulation, while the full detector simulation using GEANT4 is used for the remaining model points for maximum accuracy. In order to account for pileup effects, all signal samples are overlaid with simulated minimum bias events generated using PYTHIA8 and the A3 tune [177], reweighted to match the pileup distribution measured in data.

The cross sections for chargino pair production have been calculated using RESUMMINO [178] at NLO in the strong coupling constant and including next-to-leading logarithm (NLL) terms in the soft gluon resummation [179, 180].

4.3.2 Background samples

Top pair production and single top processes were generated using POWHEG-Box v2 [181], implementing the POWHEG method [182, 183] for merging NLO MEs with the PSs. The PS, hadronisation and underlying event were simulated using PYTHIA8 with the A14 tune. Production of $t\bar{t}$ in association with a vector boson $t\bar{t} + V$ are generated using MADGRAPH5_AMC@NLO 2.3.3, interfaced with PYTHIA8 for the PS. The set of PDFs used for simulation of $t\bar{t}$, single top, and $t\bar{t} + V$ is the NNPDF2.3LO set.

Production of a vector boson V with additional jets ($V + \text{jets}$) is simulated using SHERPA 2.2.1 [127, 184], allowing up to two (four) additional parton emissions at NLO (LO) accuracy. The CKKW ME+PS matching and merging scheme [185, 133], extended to NLO accuracy [186]. Diboson (VV) and multiboson (VVV) is simulated using SHERPA 2.2.1 and 2.2.2. The PDFs used are provided by the NNPDF3.0NNLO set [187] and the generator tune is the default SHERPA tune.

All Higgs processes are simulated using POWHEG-Box v2 for the ME calculations and PYTHIA8 for the PS, underlying event and hadronisation. While the generation of $h + t\bar{t}$ uses the A14 tune and the NNPDF2.3LO set, $h + V$ and single Higgs production are simulated using the NNPDF 3.0 NNLO set and the AZNLO [188] set of tuned generator parameters.

The detector simulation for all MC background samples was performed using the full detector simulation based on GEANT4, introduced in section 2.2.8. Except for the MC samples generated using SHERPA, all background samples use EVTGEN v1.2 or v1.6 to model the decay of HF quarks. Similar to the signal models, all background samples are mixed with simulated minimum bias events generated with PYTHIA8 and the A3 tune.

4.4 Object definitions

The reconstruction of physics objects requires the combination of data from multiple detector components. Due to finite detector resolutions, and the sheer amount of particles produced

Table 4.1: Overview of configuration of MC generators used for simulating the various signal and SM background processes.

Process	Matrix element	Parton shower	PDF set	Cross section	Tune
Signal	MADGRAPH5_AMC@NLO 2.6.2	PYTHIA 8.230	NNPDF 2.3 LO	NLO+NLL [178–180]	A14
$t\bar{t}$	POWHEG-BOX	PYTHIA 8.230	NNPDF2.3LO	NNLO+NNLL [189, 190]	A14
t (s-channel)	POWHEG-BOX	PYTHIA 8.230	NNPDF2.3LO	NLO [191]	A14
t (t-channel)	POWHEG-BOX	PYTHIA 8.230	NNPDF2.3LO	NLO [191]	A14
$t + W$	POWHEG-BOX	PYTHIA 8.230	NNPDF2.3LO	NNLO [191? , 192]	A14
$t\bar{t} + V$	MADGRAPH5_AMC@NLO 2.3.3	PYTHIA 8.210	NNPDF2.3LO	NLO [193, 194]	A14
$V + \text{jets}$	SHERPA 2.2.1		NNPDF3.0NNLO	NNLO [195]	SHERPA default
VV	SHERPA 2.2.1/2.2.2		NNPDF3.0NNLO	NLO [169]	SHERPA default
VVV	SHERPA 2.2.1/2.2.2		NNPDF3.0NNLO	NLO [169]	SHERPA default
$h + t\bar{t}$	POWHEG-BOX	PYTHIA 8.230	NNPDF2.3LO	NLO [196]	A14
$h + V$	POWHEG-BOX	PYTHIA 8.212	NNPDF3.0NNLO	NNLO [196]	AZNLO
h (ggF)	POWHEG-BOX	PYTHIA 8.212	NNPDF3.0NNLO	$N^3\text{LO}+N^3\text{LL}$ [196]	AZNLO
h (VBF)	POWHEG-BOX	PYTHIA 8.212	NNPDF3.0NNLO	NNLO [196]	AZNLO

in each collision, this process does not always work without flaws. Sometimes, objects are falsely reconstructed or not reconstructed at all. In order to minimise reconstruction errors, different identification and reconstruction criteria are introduced for each physics object category. Electrons and muons are categorised into *baseline* and *signal* objects. Baseline objects have a smaller purity but a higher acceptance which is e.g. useful for the reconstruction of the missing transverse momentum. Stricter identification and isolation criteria are required for signal objects, resulting in lower acceptances but also lower reconstruction errors. In this analysis, signal-type objects are used as the physical objects. Table 4.2 gives a comprehensive summary of the object definitions introduced in the following.

4.4.1 Tracks and vertices

The reconstruction of tracks of charged particles starts with the formation of clusters from the raw data recorded in the Pixel and SCT detectors. Clusters are formed by grouping together adjacent pixels and strips with energy deposits above threshold and are subsequently used to create three-dimensional space-points, representing the points where charged particles traversed the active ID material [197]. Sets of three space-points form track seeds that serve as inputs for a combinatorial Kalman filtering technique [198] that includes additional space-points from the remaining pixel and SCT layers to extend the preliminary trajectory. A χ^2 track fit is performed at each step of the extension. Multiple track candidates are formed from seeds that can be extended by more than one compatible space-point in one layer. Ambiguities are resolved by assigning track candidates a score taking into account basic track properties like the χ^2 of the track fit, or its associated p_T [197]. The ambiguity solver requires track candidates to contain a minimum of 7 pixel and SCT clusters, have a maximum of one shared pixel cluster and two shared SCT clusters on the same layer and have no more than two holes[†] of which only one is allowed to be in the pixel detector. Track candidates also need to have $p_T > 400$ MeV, $|\eta| < 2.5$ and have longitudinal (z_0) and transversal (d_0) impact parameters with respect to their associated vertex satisfying $|z_0 \sin \theta| < 3.0$ mm and $|d_0| < 2.0$ mm, where θ is the polar angle of the track. Track candidates surviving the ambiguity solver are extended by compatible

[†] Holes are intersections of the track trajectory with sensitive detector material not containing a cluster.

hits in the TRT [199] and subject to a global high-resolution track fit before being added to the final track collection [197].

Vertex reconstruction uses a selection of tracks satisfying a set of quality requirements [200] to fit the best vertex position in a procedure iteratively downweighting less compatible tracks [201]. Once the vertex position has been determined, incompatible tracks with small weights are removed and can be reused for the reconstruction of additional vertices [201]. All reconstructed vertices with at least two associated tracks are kept as valid primary vertex candidates. In events with multiple candidates, the primary vertex is defined to be the one with the highest $\sum p_T^2$ of its associated tracks.

4.4.2 Electrons and Photons

Electron and photon candidates are reconstructed from energy deposits in topologically connected cells in the electromagnetic and hadronic calorimeters. The reconstruction algorithm starts with the preparation of the energy deposits into so-called *topo-clusters* [202]. These are formed by calorimeter cells containing energy deposits above a certain noise threshold, so-called *seed* cells, including their neighbouring cells which can, in turn, also act as seed cells. All cell signals are measured at the electromagnetic scale, assuming that energy deposits stem only from electromagnetic interactions. Although the topo-clustering algorithm starts with cells from both calorimeters, only cells from the EM calorimeter are used in the subsequent electron and photon reconstruction steps. Using only EM topo-clusters with a certain threshold ratio of the EM energy to the total cluster energy significantly reduces contamination from pileup clusters [203]. The EM topo-clusters are then loosely matched to ID tracks that are re-fitted in order to account for energy losses through bremsstrahlung [203]. Vertices from photon conversions are reconstructed from tracks matched to fixed-size clusters [204] and also matched to the EM topo-clusters. In the final step of the reconstruction algorithm, EM topo-clusters are sorted according to descending E_T and tested as seed clusters for dynamic, variable-size *superclusters*, with different seed requirements for electrons and photons [203]. Clusters near seed candidates can be added as satellites cluster candidates, originating e.g. from bremsstrahlung. Electrons and photons are then finally built from the reconstructed superclusters and their energies are calibrated using $Z \rightarrow ee$ decays [205].

The identification of prompt electrons relies on a likelihood discriminant built from quantities measured in the ID and calorimeters. The quantities are chosen according to their ability of discriminating prompt isolated electrons from non-prompt leptons originating in HF decays, from photon conversions or from jets. They include the properties of the electron track, the shape of the EM shower and the quality of the match between the electron track and the calorimeter clusters [206]. Photon identification, on the other hand, relies on a cut-based selection exploiting the shape of the EM shower.

In this analysis, electrons are required to satisfy $p_T > 7 \text{ GeV}$ and $|\eta| < 2.47$. Baseline electrons are identified using the *LooseAndBLayer* requirement on the identification likelihood, requiring a hit in the innermost layer of the pixel detector, at least two additional hits in the remaining layers of the pixel detector and seven hits in the pixel and SCT detectors combined [206]. In addition, the longitudinal impact parameter z_0 of baseline electrons needs to satisfy $\Delta z_0 \sin \theta < 0.5 \text{ mm}$ with respect to the primary vertex. Signal electrons are a subset of baseline electrons and need to satisfy the *Tight* likelihood identification, yielding an efficiency of 80% for prompt electrons

with $E_T = 40 \text{ GeV}$ [206]. In addition to the longitudinal impact parameter, signal leptons also need to satisfy $d_0/\sigma_{d_0} < 5$, where the transverse impact parameter d_0 and its uncertainty σ_{d_0} are measured with respect to the beam line.

Finally, electrons need to be *isolated*, meaning that the vicinity of electrons needs to be clear of additional significant detector activity. Requiring electrons to be isolated prevents the selection of non-prompt electrons originating e.g. from HF decays or misidentifications of light hadrons. Isolation is quantified using two observables, one using tracking information and the other one using calorimeter data. The track based isolation variable $p_T^{\text{varcone}20}$ is the sum of all track momenta above 1 GeV, (excluding the electrons track itself) in a cone around the electron. The size of the cone is $\Delta R = \min(10 \text{ GeV}/p_T, 0.2)$, i.e. shrinking with increasing electrons p_T . The calorimeter based variable $E_T^{\text{cone}20}$ corresponds to the sum of the transverse energies in topo-clusters (excluding the electrons itself and after correcting for pileup effects) in a cone with $\Delta R = 0.2$ around the electrons. In this analysis, both baseline and signal electrons are required to satisfy the *Loose* working point [203], corresponding to the requirements $p_T^{\text{varcone}20}/p_T < 0.2$ and $E_T^{\text{cone}20} < 0.15$. In order improve the rejection of non-prompt electrons at high transverse momenta, electrons with $p_T > 200 \text{ GeV}$ need to satisfy the *HighPtCaloOnly* working point, applying the tighter requirement $E_T^{\text{cone}20} < \max(0.015 \cdot p_T, 3.5 \text{ GeV})$.

Photons are required to have $p_T > 13 \text{ GeV}$ and $|\eta| < 2.37$ and need to satisfy the *tight* identification and *FixedCutTight* isolation requirements [203]. In this analysis, photons are only used in the calculation of the missing transverse momentum.

4.4.3 Muons

The reconstruction of muons uses primarily data from the ID and MS and is based on the fact that muons are minimum ionising particles. Muon candidates are independently reconstructed in the ID and the MS as muon tracks and only then combined to a muon candidate that can be used by physics analysis [207, 208]. The track reconstruction in the ID follows the same procedure used for other charged-particle tracks, described in section 4.4.1. In the MS, the muon track reconstruction starts with the identification of short straight-line track segments. Segments from different MS layers are combined into preliminary muon track candidates if they are loosely compatible with the IP and match a first-order approximation of the parabolic trajectory describing the muon track in the magnetic field. Track candidates are then fitted in a global χ^2 fit, taking into account possible MS chamber misalignments as well as interactions with the detector material [208]. In order to increase the reconstruction performance, MS muon tracks are subsequently combined with the ID tracks using five different reconstruction strategies, described in detail in [208]. Only two of these strategies are relevant for this analysis:

- *combined muons*, which are formed by combining the ID and MS tracks through a global fit, taking into account the energy loss in the calorimeters,
- *MS extrapolated muons*, which are built using MS muon tracks only, but extrapolating the tracks back to the IP and requiring them to be loosely compatible with the IP. Extrapolated muons are mainly used for providing acceptance in the region $2.5 < |\eta| < 2.7$, which is beyond the coverage provided by the ID.

After resolving the overlaps between the different muon types, the muon objects used for physics analysis are subject to a momentum calibration using data from $J/\Psi \rightarrow \mu\mu$ and $Z \rightarrow \mu\mu$ decays [207, 208].

Identification of muons is performed using quality requirements designed to suppress non-prompt muons originating from pion and kaon decays and allow a robust momentum measurement. Muons in this analysis are built using combined and extrapolated muons that satisfy the *Medium* identification requirements [207]. Combined muons need to have at least three hits in at least two MDT layers, except for the region with $|\eta| < 0.1$, where a single MDT layer is enough, as long as there is no more than one MDT hole layer. Extrapolated muons need to have at least three hits in at least three MDT and CSC layers. In addition, all muons need to have a significance of the ratio of the measured charge and momentum of the muons satisfying $\sigma(q/p) < 7$.

Muons in this analysis also need to satisfy $p_T > 6 \text{ GeV}$ as well as $|\eta| < 2.7$ or $|\eta| < 2.5$ for baseline or signal muons, respectively. The longitudinal impact parameter of baseline muons is required to be $\Delta z_0 \sin \theta < 0.5 \text{ mm}$ with respect to the primary vertex. Signal muons additionally need to have a transverse impact parameter satisfying $d_0/\sigma_{d_0} < 3$. Similar to electrons, muons also need to be isolated, using the same variables. Both signal and baseline muons need to conform to the *Loose* working point, requiring $p_T^{\text{varcone}20}/p_T < 0.3$ and $E_T^{\text{cone}20} < 0.15$ [208].

4.4.4 Jets

Jets are reconstructed at the EM scale using the anti- k_t algorithm [209] with a radius parameter $R = 0.4$, implemented in the FASTJET [210, 211] package. The inputs to the anti- k_t algorithm are topo-clusters [212], built using the same procedure introduced in section 4.4.2. Tracks with $p_T > 500 \text{ MeV}$ and an association to the primary vertex are assigned to jets using *ghost association* [213], a method treating them as particles with infinitesimal momentum such that

truth jets

the properties of the calorimeter-based jets are not changed.

Reconstructed jets undergo a jet energy scale (JES) calibration, correcting the four-momentum and scaling the energy and mass [212]. In a first step, energy contributions from in-time and out-of-time pileup are removed using a data-driven jet-by-jet approach based on jet areas and pileup p_T density as well as a residual correction derived from MC simulation and parameterised by the number of mean interactions per bunch crossing and the number of reconstructed primary vertices [212, 213]. The reconstructed jet four-momentum is corrected to the particle-level energy scale through an absolute JES and η calibration. In order to reduce the dependence of the jet response (i.e. the ratio between the measured jet energy and the true jet energy) on the flavour and energy distribution of its constituents, a series of multiplicative corrections, called global sequential calibration (GSC) [214], is applied. The GSC improves the jet energy resolution (JER) and is based on data from the calorimeters, jet-related tracking information as well as MS information. Differences between the jet response in data and MC simulation, caused by imperfect detector and physics simulations, are corrected using so-called *in situ* calibrations [212]. The jet response in data and MC simulations is measured separately, allowing to derive a correction factor that is applied on data. Similar to the JES, the JER is also calibrated. The JER is measured in dijet events through p_T asymmetry [215].

Even after the subtraction of pileup effects, some pileup jets still remain. The jet vertex tagger (JVT) [216], a multivariate discriminant, can be used to suppress pileup jets. It is based on variables that describe the fraction of the total jet momentum corresponding to tracks associated to the primary vertex. In this analysis, jets with $p_T < 120 \text{ GeV}$ and $|\eta| < 2.5$ need to be associated to the primary vertex using the *medium* working point, achieving an average 92% efficiency for jets originating from the hard scatter interaction [212].

Baseline jets in this analysis are required to have $p_T > 20 \text{ GeV}$ and $|\eta| < 4.5$. Analysis variables built using jets use signal jets with $p_T > 30 \text{ GeV}$ and $|\eta| < 2.8$.

4.4.5 Flavour tagging

As can be easily seen through the CKM matrix, b -quarks primarily decay through $b \rightarrow Wc$. However, since the small coupling constant proportional to the corresponding CKM matrix element V_{cb} (corresponding to the $b \leftrightarrow c$ transition), b -hadrons have relatively long lifetimes of the order of 1.5 ps ($\langle c\tau \rangle \approx 450 \mu\text{m}$) [7]. In the typical momentum ranges, b -hadrons can have a measurable flight length before decaying, leading to secondary vertices that are displaced from the hard-scatter interaction point. In order to exploit this, ATLAS uses a collection of algorithms designed to discern HF jets containing b -hadrons from light-flavour jets by exploiting either the impact parameters or reconstructing the displaced vertices. A multivariate classifier, called MV2 [217] combines the outputs of the different taggers using a boosted decision tree (BDT) algorithm that is trained on $t\bar{t} + Z'$ MC samples.

Due to the Higgs decay $h \rightarrow b\bar{b}$ in the targeted signal model, b -jets play a crucial role in the analysis. Baseline jets with $|\eta| < 2.5$ are used as input to the MV2c10 b -tagging algorithm, an implementation of the MV2 discriminant using a c -jet fraction of 7% during the BDT training [218, 219]. The working point chosen for the MV2c10 tagger achieves a b -tagging efficiency of 77% with a rejection rates of 4.9, 15, and 110 for c -jets, τ -jets and light-flavour jets, respectively, measured in simulated $t\bar{t}$ events [218].

4.4.6 Missing transverse momentum

Momentum conservation in the transverse plane implies that the sum of the transverse momenta of all objects in a pp collision should vanish. Particles escaping the detector without being measured thus lead to a momentum imbalance, in the following referred to as missing transverse momentum $\mathbf{p}_T^{\text{miss}}$ with magnitude E_T^{miss} . The missing transverse momentum in each event is computed using all reconstructed objects and takes into account tracks associated to the primary vertex but not used for any reconstructed objects [220], yielding

$$\mathbf{p}_T^{\text{miss}} = - \sum \mathbf{p}_T^e - \sum \mathbf{p}_T^\gamma - \sum \mathbf{p}_T^\mu - \sum \mathbf{p}_T^{\text{jet}} - \sum \mathbf{p}_T^{\text{track}}. \quad (4.1)$$

While terms originating from the reconstructed, calibrated objects are collectively referred to as the *hard term*, the remaining track term is referred to as *soft term*. As τ -leptons are not explicitly reconstructed in this analysis, no corresponding term is included in eq. (4.1). Hadronic decays of τ -leptons are, however, included in the jet term as they are, in general, reconstructed as jets. The computation of E_T^{miss} uses all baseline objects introduced in the previous sections. Ambiguities between objects are resolved using an overlap removal procedure

Table 4.2: Overview of the object definitions used in the analysis.

Property	Baseline type	Signal type
Electrons		
Kinematic	$p_T > 7 \text{ GeV}$, $ \eta < 2.47$	$p_T > 7 \text{ GeV}$, $ \eta < 2.47$
Identification	<i>LooseAndBLayer</i> [206]	<i>Tight</i> [206]
Impact parameters	$\Delta z_0 \sin \theta < 0.5 \text{ mm}$	$\Delta z_0 \sin \theta < 0.5 \text{ mm}$, $d_0/\sigma_{d_0} < 5$
Isolation	–	<i>Loose</i> [203] ($p_T \leq 200 \text{ GeV}$) <i>HighPtCaloOnly</i> [203] ($p_T > 200 \text{ GeV}$)
Muons		
Kinematic	$p_T > 6 \text{ GeV}$, $ \eta < 2.7$	$p_T > 6 \text{ GeV}$, $ \eta < 2.5$
Identification	<i>Medium</i> [207]	<i>Medium</i> [207]
Impact parameters	$\Delta z_0 \sin \theta < 0.5 \text{ mm}$	$\Delta z_0 \sin \theta < 0.5 \text{ mm}$, $d_0/\sigma_{d_0} < 3$
Isolation	–	<i>Loose</i> [208]
Jets		
Kinematic	$p_T > 20 \text{ GeV}$, $ \eta < 4.5$	$p_T > 30 \text{ GeV}$, $ \eta < 2.8$
JVT	–	<i>Medium</i> [212], $p_T < 120 \text{ GeV}$, $ \eta < 2.5$
<i>b</i> -jets		
Kinematic	$p_T > 20 \text{ GeV}$, $ \eta < 4.5$	$p_T > 30 \text{ GeV}$, $ \eta < 2.5$
JVT	–	<i>Medium</i> [212], $p_T < 120 \text{ GeV}$, $ \eta < 2.5$
<i>b</i> -tagging	–	<i>MV2c10</i> [218] with 85% efficiency

that is separate and independent from the procedure described in section 4.5 [220]. In order to reduce effects from pileup, the E_T^{miss} is computed using the *tight* working point described in Ref. [221], excluding forward jets with $|\eta| > 2.4$ and $p_T < 30 \text{ GeV}$.

Events without any true E_T^{miss} can have non-zero reconstructed E_T^{miss} due to residual pileup effects, object mismeasurements are particles escaping through uninstrumentalised regions of the detector. Such *fake* E_T^{miss} allows events without any real E_T^{miss} (e.g. $Z(\rightarrow ee) + \text{jets}$) to pass the event selection criteria and end up in the regions of interest even after requiring a certain threshold value of E_T^{miss} .

4.5 Overlap removal

As the reconstruction procedure runs independently for each object type, it may happen that the same tracks or energy deposits in the calorimeters are used for the reconstruction of two different objects. For example electrons tend to cluster as well as jets and are therefore often also reconstructed as electron-seeded jets [222]. In order to resolve ambiguities and prevent double-counting, an overlap removal procedure using the distance parameter $\Delta R_y = \sqrt{(\Delta y)^2 + (\Delta\phi)^2}$ is performed. The procedure sequentially runs the following steps on baseline objects, with only surviving objects participating in subsequent steps:

1. Electrons sharing an ID track with a muon are removed, preventing duplication of muons via bremsstrahlung with subsequent photon conversion [222].

2. Jets within $\Delta R_y < 0.2$ of an electron are rejected, preventing the pure duplication of electrons as electron-seeded jets [222].
3. Electrons overlapping with remaining jets within $\Delta R_y = \min(0.4, 0.04 + 10 \text{ GeV}/p_T)$ are removed, resolving the regime where hadronic jets lose a fraction of their energy to electron-seeded jets [222]. The shrinking cone size avoids unnecessary rejection of electrons originating from decays of boosted particles together with jets.
4. Jets with less than three associated tracks, within $\Delta R_y < 0.2$ of a muon or where the muon has been matched to the jet through ghost association [223] are removed. This resolves for example scenarios where a muon is reconstructed as a jet due to bremsstrahlung or FSR with subsequent photon conversion reconstructed both as electron and jet [222].
5. Muons overlapping with a remaining jet are removed. The same shrinking cone size as for electrons is used. This predominantly removes non-prompt muons produced in light meson decays, or HF decays, together with jets [222].

4.6 Analysis variables

In order to separate supersymmetric signal events from SM processes, it is necessary to apply requirements on different discriminating observables, creating so-called *signal regions* enriched in signal events. In addition these variables are also used to construct regions enriched in SM background events, in the following used for the background estimation in the signal regions. The distributions of all discriminating variables are illustrated in fig. 4.3, showing signal and SM background distributions, each normalised to unity. Most observables depend on the absolute mass scale of the supersymmetric particles, as well as the mass difference between $\tilde{\chi}_1^\pm/\tilde{\chi}_2^0$ and $\tilde{\chi}_1^0$.

Number of jets

The simplified model depicted in fig. 4.1 features two b -jets in the final state, originating from the decay of the Higgs boson. In the following, all events are required to have exactly two b -jets in the final state, significantly reducing contributions from $W + \text{jets}$ processes that have a very low probability of producing two b -jets. In order to avoid rejecting signal events with ISR or FSR, a third, light-flavour jet is allowed in the final state.

Invariant mass of the b -tagged jets

The invariant mass of the two b -jets $m_{b\bar{b}}$ is defined as

$$m_{b\bar{b}} = \sqrt{(\mathbf{p}_{b_1} + \mathbf{p}_{b_2})^2}, \quad (4.2)$$

where \mathbf{p}_{b_1} and \mathbf{p}_{b_2} are the four-vector momenta of the leading and subleading b -jets, respectively. The term *leading* henceforth refers to the object with the largest p_T in its object category. In

the high-relativistic limit $E \gg m$, the invariant mass of the two b -jets can be written as

$$m_{b\bar{b}} = \sqrt{2p_T^{b_1} p_T^{b_2} (\cosh \Delta\eta - \cos \Delta\phi)}. \quad (4.3)$$

As the two b -jets originate from the Higgs decay $h \rightarrow b\bar{b}$, their measured invariant mass will in general be close to the measured Higgs mass of around 125 GeV [7], leading to a peak in the $m_{b\bar{b}}$ distribution, as can clearly be seen in fig. 4.3(d). In most SM background processes, on the other hand, the b -jets do not originate from a Higgs decay, and thus their $m_{b\bar{b}}$ distribution does not exhibit the same peak-like structure. In order to enrich signal events in a selection, a requirement of $100 \text{ GeV} < m_{b\bar{b}} < 140 \text{ GeV}$ is used in the following.

Missing transverse energy

The missing transverse energy E_T^{miss} is an observable finding widespread usage in searches for SUSY at the LHC. In SM processes, E_T^{miss} only stems from neutrinos and fake E_T^{miss} arising e.g. from mismeasurements or imperfect detector hermeticity. In the case of the SUSY scenario considered in the following, two LSPs escape the detector, leaving a considerable amount of missing transverse momentum, such that a lower requirement on E_T^{miss} allows to separate signal and background processes. Figure 4.3(c) shows the E_T^{miss} distribution, illustrating the fact that signal models with high absolute sparticle masses as well as high mass differences tend to have the largest E_T^{miss} .

Transverse mass

The transverse mass m_T [224, 225] is one of the most important observables considered in this analysis. It aims to reconstruct the mass of a heavy particle decaying into two daughter particles subject to a co-linear boost in the laboratory transverse plane. In SUSY searches targeting the 1-lepton final state, m_T is commonly used to reconstruct the transverse mass of the W boson decaying into a lepton–neutrino pair, and is therefore defined as

$$m_T = \sqrt{2p_T^\ell E_T^{\text{miss}} (1 - \cos[\Delta\phi(\mathbf{p}_T^\ell, \mathbf{p}_T^{\text{miss}})])}, \quad (4.4)$$

where \mathbf{p}_T^ℓ is the momentum three-vector of the lepton in the event. As additional leptons are vetoed, the vast majority of the leptons in background processes stem from leptonic decays of W bosons. In background events where the neutrino from $W \rightarrow \ell\nu$ is the only source of E_T^{miss} , the transverse mass has a theoretical kinematic endpoint at the W boson mass,

$$m_T^{\text{max}} = m_W \approx 80 \text{ GeV}. \quad (4.5)$$

Due to finite detector resolution, mismeasurements or additional E_T^{miss} in the event, background events can sometimes have $m_T > m_W$, leading to a kinematic endpoint at m_W that is not infinitely sharp.

In the signal scenarios considered in the analysis, the LSPs constitute a majority of the E_T^{miss} in an event, which typically leads to a m_T distribution that is significantly broader than that of background processes and does not present the same kinematic endpoint. A lower requirement on the transverse mass slightly above the W boson mass thus allows to reject a majority of the

SM background events while keeping most of the signal events. As can be seen in fig. 4.3(c), the broadness of the m_T distribution depends on the scale of the mass parameters, with increasing mass differences leading to increasingly broad distributions. For this reason, different signal regions with varying requirements on m_T can be constructed, targeting different kinematic regimes in the signal grid.

Contransverse mass

The contransverse mass m_{CT} [226] is designed to have a kinematic endpoint for pair produced heavy particles decaying into invisible and visible particles subject to a contra-linear boost. In the following, m_{CT} is defined as

$$m_{CT} = \sqrt{2p_T^{b_1} p_T^{b_2} (1 + \cos \Delta\phi_{bb})}, \quad (4.6)$$

where $p_T^{b_1}$ and $p_T^{b_2}$ are the transverse momenta of the two b -jets in the final state. Although m_{CT} is invariant under co-linear boosts in the beam direction[†], it is not invariant under transverse boosts, e.g. due to ISR jets, such that m_{CT} as well as its kinematic endpoint depend on the size and direction of the transverse boost. For this reason, a boost-corrected version of the contransverse mass is used in the following, using a procedure described in detail in Ref. [227].

For $t\bar{t}$ events where each top quark decays via $t \rightarrow bW$, the two b -jets used for calculating m_{CT} stem from each of the two decay branches of the $t\bar{t}$ system. It can be shown that, in this case, the boost-corrected contransverse mass has a kinematic endpoint at [227]

$$m_{CT}^{\max} = \frac{m^2(t) - m^2(W)}{m(t)} \approx 135 \text{ GeV}. \quad (4.7)$$

In signal events, the two input b -jets originate from the same Higgs boson, and thus m_{CT} does not present a clear kinematic endpoint but rather tends to take much higher values. Figure 4.3(b) clearly illustrates the kinematic endpoint for $t\bar{t}$ backgrounds and further shows that signal distributions take on much higher values depending on their mass parameter scales. Similar as for the transverse mass, varying lower bounds on m_{CT} will be used to define signal regions optimised to different kinematic regimes.

Invariant mass of the lepton and leading b -jet

The invariant mass of the lepton and the leading b -jet $m_{\ell b_1}$ is designed to offer high rejection power towards $t\bar{t}$ and single top processes. In events where the lepton and leading b -jet originate from the same top quark decay $t \rightarrow bW \rightarrow b\ell\nu$, the $m_{\ell b_1}$ distribution has a kinematic endpoint at

$$m_{\ell b_1}^{\max} = \sqrt{m^2(t) - m^2(W)} \approx 153 \text{ GeV} \quad (4.8)$$

In signal events, the lepton and leading b -jet originate from the decay chains of the $\tilde{\chi}_1^\pm$ and $\tilde{\chi}_2^0$, respectively and thus the $m_{\ell b_1}$ distribution depends on the mass scale of the SUSY particles, yielding good discriminative power especially for signal scenarios with high $\tilde{\chi}_1^\pm/\tilde{\chi}_2^0$ masses.

[†] This is by construction the case, as only transverse quantities are used.

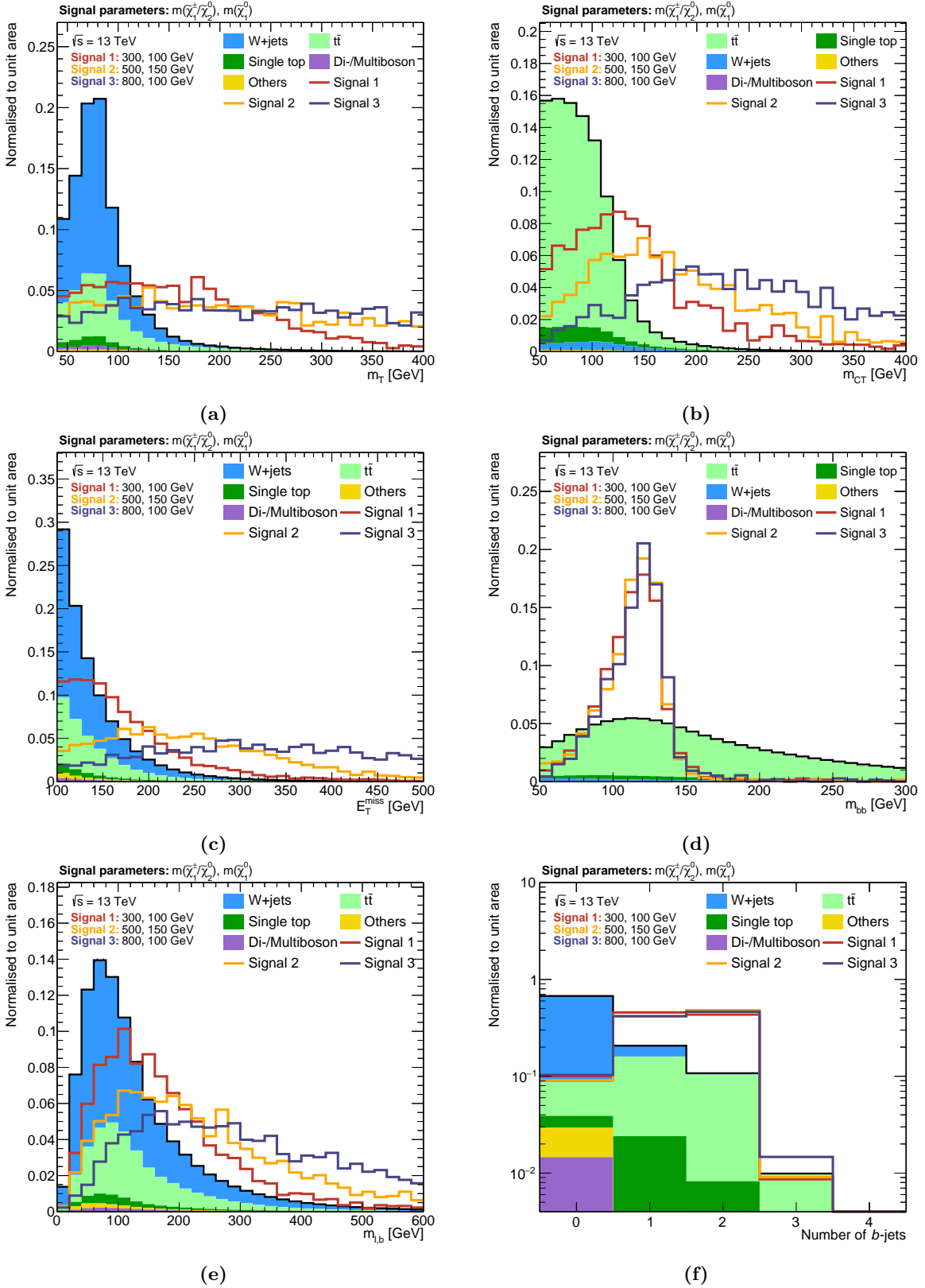


Figure 4.3: Distributions of the most important observables used in the analysis. The simulated SM backgrounds are stacked on top of each other, and distributions from exemplary signal models with the quoted mass parameters are overlaid. In order to emphasise the shape differences, both background and signal distributions are normalised to unity. A preselection of exactly one lepton (signal and baseline), at least two light jets and $E_T^{\text{miss}} > 100 \text{ GeV}$ is applied.

4.7 Trigger strategy

The trigger strategy of an analysis is crucial to select pp events worth investigating, and typically relies on triggers sensitive to physics objects that are important to the considered signal scenarios. The data used in this analysis have been recorded with E_T^{miss} triggers. Selecting events with invisible particles is inherently difficult precisely because these particles do not leave a trace in the detector. As described in section 2.2.7, the L1 trigger uses only parts of the instrumented regions, a technique that is not well suited for momentum imbalance triggers that rely on a sum of momenta over the full solid angle [228]. In addition, the significant increase in luminosity in Run 2 of the LHC degrades the E_T^{miss} resolution in the calorimeters, the only detector component used for the E_T^{miss} triggers [228]. The L1 triggers used in this analysis employed a threshold of $E_T^{\text{miss}} > 50 \text{ GeV}$, before feeding passing events to the HLT for further analysis.

Two different types of E_T^{miss} triggers are used by the HLT, one based on jets (`mht` algorithm), and one implementing local pile-up suppression (`pufit` algorithm). As hadronic jets dominate the visible momentum in most interesting events, using them for E_T^{miss} computation and triggering is well-motivated. The `mht` algorithm was used during the 2015–2016 data taking period and computes the E_T^{miss} from the negative vectorial sum of the transverse momenta of all jets with a transverse momentum $p_T > 7 \text{ GeV}$ before calibration [228]. The HLT jets are reconstructed and calibrated using a similar procedure as for offline analysis, and are thus corrected for pile-up effects [229]. The `pufit` algorithm was used during the 2017–2018 data taking period and takes as input topo clusters formed using the method described in section 4.4.2. The clusters are subsequently combined into η - ϕ patches of approximately jet size and corrected for pile-up effects based on the distribution of the energy deposits in the calorimeter. The `pufit` algorithm assumes that high transverse energy deposits stem from the hard-scatter events, while low transverse energy deposits originate mainly from pile-up effects [228]. The online E_T^{miss} threshold used increased from 70 GeV to 110 GeV in order to keep the trigger rate more or less stable under rising instant luminosities during the different data-taking periods.

Since the online reconstruction techniques used by the triggers are slightly different[†] than those used in offline analysis, the performance of triggers is in general not a simple step function but a so-called *turn-on curve* with rising efficiency, followed by a *plateau region* with constant efficiency. In order to achieve the same trigger selection in MC as in data, the MC events are each assigned a random run number that are distributed according to the respective integrated luminosities of each data taking period. Using the run numbers, the same triggers used for data taking during each run can be applied for MC events.

Figure 4.4 shows the combined E_T^{miss} trigger efficiencies for the electron and muon channel separately. In the following, an offline requirement of $E_T^{\text{miss}} > 240 \text{ GeV}$ is applied for all analysis regions, selecting events where the E_T^{miss} triggers are fully efficient and show no significant difference between MC and data. Thus, no efficiency correction is considered in the following. A statistical uncertainty of 2% is taken to account for the difference between data and MC in the trigger plateaus.

[†] This is necessary to be able to handle the data streams caused by the pp collisions.

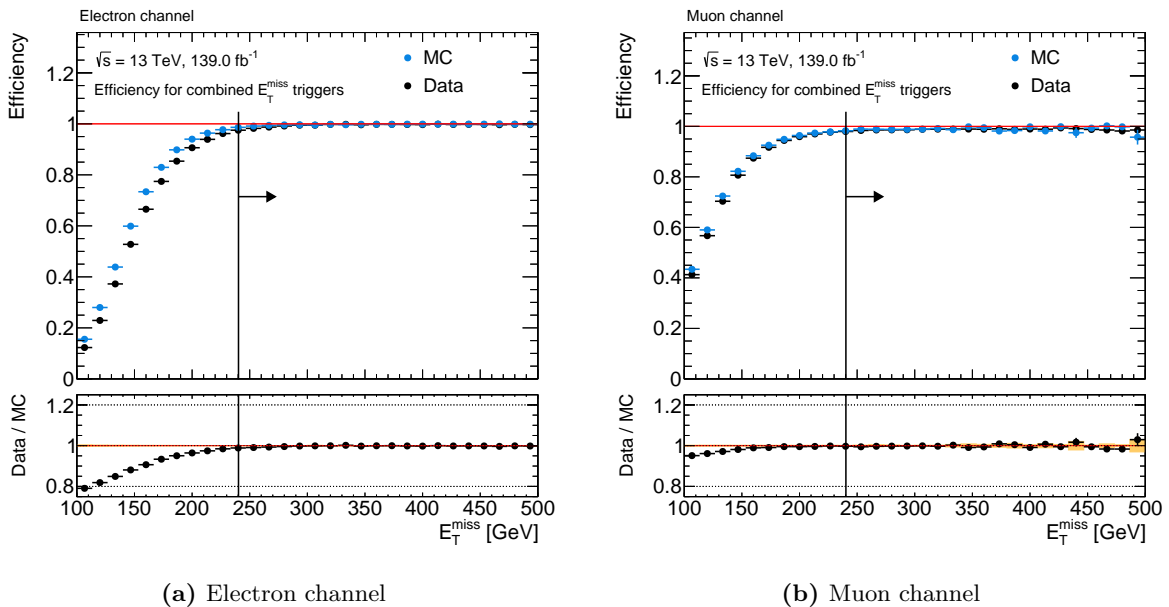


Figure 4.4: Efficiencies of the combined E_T^{miss} triggers in data and MC events, triggered by single lepton triggers in the (a) electron and (b) muon channels. A preselection requiring exactly one lepton (baseline and signal), at least two jets, and $E_T^{\text{miss}} > 100 \text{ GeV}$ is applied. The arrow indicates the offline E_T^{miss} requirement applied on all selections in the analysis.

4.8 Event cleaning

Before being considered for analysis, events need to pass a series of quality requirements. Data events need to be certified to be good for physics analysis by the data quality system [230], requiring that no transient detector issues have compromised the quality of the data events recorded. This could happen due to e.g. sudden noise bursts in detector electronics, or high-voltage trips in detector components. Only data events where all detector components were flagged as being operational, a process that is performed at the granularity of a *luminosity block*, a time period of roughly 60 s of data-taking where the instantaneous luminosity, detector and trigger configuration are considered to be constant.

A second series of quality requirements is applied on both data and MC events. To be considered in any subsequent analysis step, events need to have at least one reconstructed primary vertex with a minimum of two tracks with $p_T > 500$ MeV associated to it. Events are discarded where a jet is tagged as originating from a non-collision background process. The **Loose** working point described in Ref. [231] is used to tag such jets, and has an efficiency of 99.5% for jets from pp collision events with $p_T > 20$ GeV. Similarly, events are rejected if they contain a *bad* muons with a significantly worse than usual momentum resolution that can affect many variables in the entire event and therefore may have non-negligible effects on the analysis. In the following, muons are flagged as *bad* if the relative error on the combined q/p measurement is either larger than 0.2 or worse than the one from the ID and MS track fits. Events are also rejected if a reconstructed muon is flagged to originate from cosmic radiation, using thresholds on the transverse and longitudinal impact parameters of $d_0 > 0.2$ mm and $z_0 > 1$ mm with respect to the primary vertex.

Chapter 5

Signal region optimisation

In order to discover the rare signals predicted by the SUSY models considered, dedicated kinematic regions enriched in signal events, so called signal region (SR) are constructed. They are optimised to be able to discover a maximum number of the signal models considered in the analysis. In this chapter, the SR optimisation procedures leading to the final SRs are introduced and discussed.

5.1 Optimisation methods

All optimisation methods used in the following need a figure of merit that should be maximised in order to define the best performing setup. While the multidimensional cut scan in section 5.1.1 and the N-1 plots approach in section 5.1.2 use the binomial discovery significance Z_B introduced in section 3.5, the fit scan procedure in section 5.1.3 aims to maximise the area of the expected exclusion contour.

5.1.1 Multidimensional cut scan

The first optimisation method used for designing the SRs is an N -dimensional cut scan using N observables. For each unique combination of requirements on the set of considered observables, the expected signal and background rate as well as the statistical uncertainty on the background rate is determined from the MC samples. As this takes a non-negligible amount of time, it is crucial to restrict the amount of cut combinations. By comparing with distributions at preselection level as e.g. shown in fig. 4.3, a set of discrete cuts can be defined for each observable. In practice, a total number of $\mathcal{O}(10^7 - 10^8)$ cut combinations can still be tested on a single machine with a reasonable turnaround time.

After determining the expected event rates and statistical uncertainties, the different cut combinations are binned into a predefined number of signal efficiency bins. For each bin, the background rejection is subsequently maximised, i.e. the cut combination with the highest background is chosen as a candidate combination for the respective signal efficiency bin. Cut combination candidates maximising the background rejection are assumed to also maximise the discovery significance. With the significance definition used herein, this is in general a valid

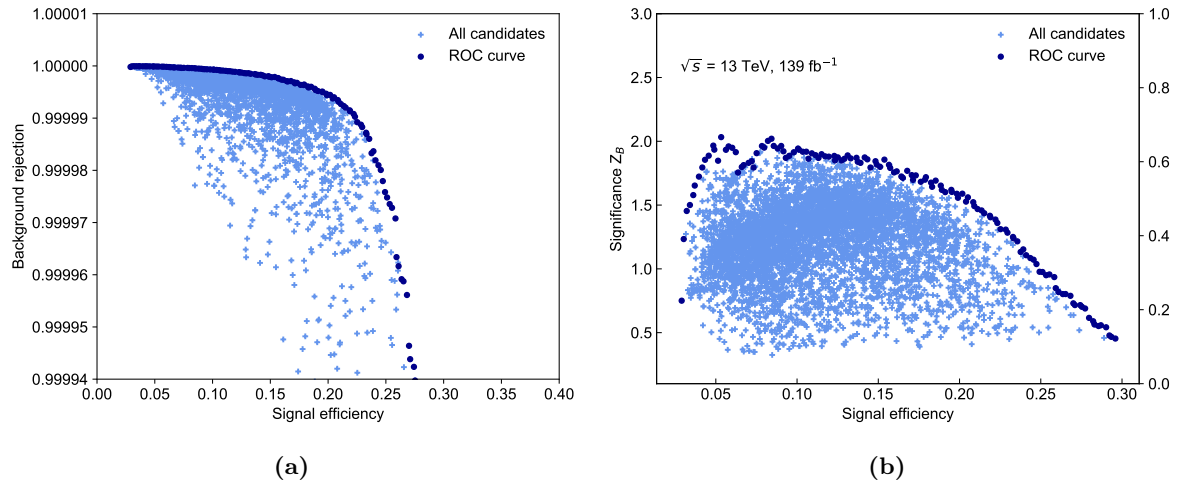


Figure 5.1: Small N -dimensional cut scan using 10^4 unique cut combinations, illustrating the approach of (a) generating a ROC curve from the scanned cut combinations in order to (b) reduce the number of candidates used in computationally expensive significance calculations. In (b), the significance Z_B includes the MC statistical uncertainty on the expected background rate.

assumption is it tends to monotonically increase with decreasing background rate, even when the statistical uncertainty on the background estimation increases due to tighter requirements and less available MC statistics. This procedure effectively generates a receiver operating characteristic (ROC) curve. As only a small subset of all tested cut combinations are selected as candidates and lie on the ROC curve, more computationally intensive calculations can be performed, as e.g. calculating the discovery significance. This is illustrated in a small scan using 10^4 cut combinations in fig. 5.1.

A common problem of N -dimensional scans is the concept of *overtightening* the selections given the available MC statistics. Since the cross sections of the considered SUSY process are many orders of magnitude smaller than those of most of the SM processes, it is necessary to apply tight requirements on the kinematic observables in order to achieve a significant signal-to-background separation. However, due to the finite amount of MC statistics available, many of the more extreme cut combinations select kinematic regions where not enough MC statistics are available for a reasonable estimation of the background rates. Thus, by maximising the background rejection, it may occur that cut combinations are selected where the mere lack of MC statistics to properly estimate the background rates causes a high significance value. As the significance values obtained for such configurations are naturally not trustworthy, they need to be avoided.

In the N -dimensional cut scan implementation used herein, the available MC datasets are split in two statistically independent, equally sized subsets. This allows to compute two independent values for the discovery significance for each cut combination candidate, as well as having two ROC curves for each scan. A large difference in either the significance values or the ROC curves then is a clear indication that too tight cuts are applied for the available MC statistics. In addition, requirements on the minimum number of raw MC events for different background processes, as well as the maximum allowed statistical uncertainty on a given process, are applied. In the following, the N -dimensional cut scan implementation provided by `ahoi` [232] is used.

5.1.2 $N - 1$ plots

Instead of performing a brute-force scan of a large set of cut combinations, a more manual approach, using repeated one-dimensional scans can be employed. In so-called $N - 1$ plots, the variable distributions of the background components as well as exemplary signal processes are plotted together with the significance achieved by applying a cut on each value on the x -axis of the plotted distribution. All other selection cuts except the one on the plotted variable are applied. This allows to investigate the impact that a cut on a single observable has on the overall significance value. By repeating this process for each variable considered, it is possible to iteratively approach a cut combination yielding results comparable to a brute-force cut scan. Especially when considering a sizeable set of variables, this manual approach quickly becomes very cumbersome and runs into the risk of missing optimal cut combinations an N -dimensional cut scan would have found.

For this reason, $N - 1$ plots are used in the following to verify and fine-tune the results from N -dimensional cut scans.

5.1.3 Fit scans

The last of the optimisation methods used in the following relies on simplified fit setups in order to compute the expected exclusion limits for various signal region candidates obtained using the previous methods. The simplified fit setups estimate the background contribution purely from MC and considers a systematic uncertainty on the background estimate of 30%, correlated over all signal region bins. Statistical uncertainties on the background estimation from the limited MC statistics are included for each bin. Similar to the previous methods, many different configurations can be tested, aiming to maximise the size of the expected exclusion contour.

Although being a very simple fit configuration, the statistical inference can take a significant amount of computation time. In order to keep the number of configurations to be tested at a manageable level, the signal region candidates obtained from the previous methods are only varied to a limited degree, assuming that they were already close to optimal in terms of expected exclusion area.

5.2 Optimisation procedure

The optimisation of the SRs uses experience from past analyses investigating the same signal model in the same final state [162, 163], all the while exploring new observables and SR configurations optimised for the full Run 2 dataset.

5.2.1 Benchmark signal points

A total of six so-called *benchmark* signal points representative for the entire signal grid are chosen for the first step of the optimisation procedure involving N -dimensional cut scans and $N - 1$ plots. Apart from the variables introduced in section 4.6, a set of additional, potentially discriminative observables are considered in the N -dimensional cut scan[†]:

Need pre-sel plots for these

Table 5.1: List of observables and cut ranges used in the N -dimensional cut scan. All cut ranges, except for N_{jet} and $N_{b\text{-jet}}$, are allowed not to be applied at all.

Observable	Cut values
$E_{\text{T}}^{\text{miss}}$ [GeV]	$>$ $\in \{200, 220, 240, 260, 280, 300, 320, 340\}$
$E_{\text{T}}^{\text{miss}}$ significance	$>$ $\in \{5, 10, 15\}$
m_{T} [GeV]	$>$ $\in \{100, 120, 140, 160, 180, 200, 220, 240, 260, 280, 300\}$
m_{CT} [GeV]	$>$ $\in \{100, 120, 140, 160, 180, 200, 220, 240, 260, 280, 300\}$
m_{bb} lower [GeV]	$>$ $\in \{85, 90, 95, 100, 105, 110, 115\}$
m_{bb} upper [GeV]	$<$ $\in \{130, 135, 140, 145, 150\}$
p_{T}^{ℓ} [GeV]	$>$ $\in \{20, 40, 60, 80\}$
$p_{\text{T}}^{\text{jet}1}$ [GeV]	$>$ $\in \{50, 100, 150\}$
$p_{\text{T}}^{\text{jet}2}$ [GeV]	$>$ $\in \{50, 75, 100\}$
ΔR_{jj}	$<$ $\in \{0.8, 1.0, 1.2, 2.0\}$
ΔR_{bb}	$<$ $\in \{0.8, 1.0, 1.2, 2.0\}$
N_{jet}	\leq $\in \{2, 3, 4\}$
$\Delta\phi(E_{\text{T}}^{\text{miss}}, p_{\text{T}}^{\ell})$ [rad]	$>$ $\in \{0.5, 1.0, 2.0, 2.5\}$

- Transverse momenta of the two leading jets as well as the lepton. Especially for signal models with high mass differences between the $\tilde{\chi}_1^\pm/\tilde{\chi}_2^0$ and the $\tilde{\chi}_1^0$, the transverse momenta of the lepton and the jets tend to be higher than in background processes.
- Object-based $E_{\text{T}}^{\text{miss}}$ significance S [233], a quantity designed to offer good discrimination against fake $E_{\text{T}}^{\text{miss}}$ caused by mismeasurements or the non-hermeticity of the detector. Events with a large share of fake $E_{\text{T}}^{\text{miss}}$ accumulate at low values of S , while events with mostly real $E_{\text{T}}^{\text{miss}}$ tend to have large values of S .
- The distance between the two leading jets ΔR_{jj} as well as the two b -jets ΔR_{bb} . As the two b -jets originating from the Higgs decay in the signal scenario tend to be close together and the highest- p_{T} jets in an event, both ΔR_{jj} and ΔR_{bb} tend to have small values for signal events. In background processes, the two leading (b -)jets often do not originate from the same object and thus tend to be further apart.
- The azimuthal distance between the lepton p_{T} and the missing transverse momentum, $\Delta\phi(p_{\text{T}}^{\ell}, p_{\text{T}}^{\text{miss}})$. This observable exploits the fact that the lepton and the $E_{\text{T}}^{\text{miss}}$ tend to have a more back-to-back configuration in signal events than in many background processes where the lepton and the neutrino (often responsible for most of the $E_{\text{T}}^{\text{miss}}$ in an event) often originate from the same W boson.

In order to avoid selecting cut combination candidates with overtightened selection criteria compared to the available MC statistics, constraints on the relative statistical uncertainty on the background and on the raw number of MC events passing the cut combination candidates are applied. Cut combinations are only considered if they result in less than 50% relative statistical uncertainty on the total background. In addition, all cut combinations need to result in at least 5 raw MC events for each of the major backgrounds, $t\bar{t}$, single top and $W + \text{jets}$.

[†] These variables will turn out not to be used for the final signal regions and are only introduced here for completeness of the optimisation procedure description.

is this
conf up-
to-date?

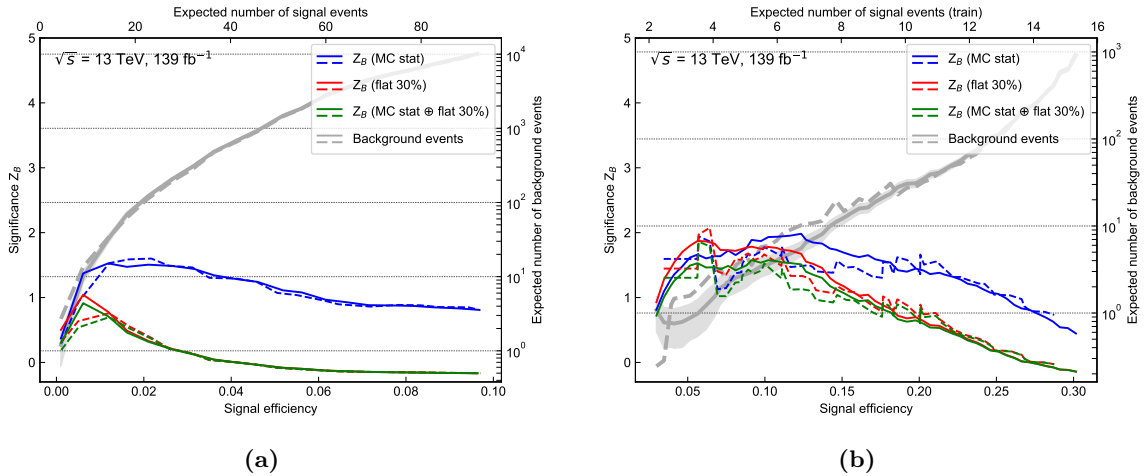


Figure 5.2: Results of the N -dimensional cut scan for two exemplary benchmark points. The binomial discovery significance Z_B is plotted against the signal efficiency for varying uncertainty configurations. Additionally, the expected SM background rates are shown, including statistical uncertainty for one of the two statistically independent samples (shaded area). The solid and dashed lines represent the two statistically independent subsets that the MC samples are split into.

The discrete selection possibilities for each of the observables are shown in table 5.1. A preselection of one lepton and exactly two b -jets (and thus at least two jets overall in the event) is always applied. Requirements on the different observables in table 5.1 are optional and do not need to be applied by the optimisation algorithm. The results of the brute-force N -dimensional cut scans for each benchmark signal point can be visualised by plotting the expected discovery significance Z_B against the signal efficiency. Figure 5.2 shows the cut scan results for two of the benchmark signal points, the corresponding plots for the remaining benchmark points can be found in fig. A.1. In these figures, the binomial significance is calculated for different uncertainty configurations for each of the two statistically independent subsets. In addition, the expected background rate is shown for each of the two sample subsets. As such, these figures allow to pick a cut combination with high achieved significance while avoiding statistical fluctuations and overtightening. The cut combinations chosen for each benchmark point, after a round of $N - 1$ plots, are shown in table 5.2. The $N - 1$ plots, shown in figs. A.2 to A.7, are used to validate and fine-tune the cut values obtained through the cut scan and allows to remove cuts on observables that do not contribute significantly to the achieved Z_B value. From the initially 12 considered observables, only six (excluding the b -jet multiplicity technically not part of the scan) are part of the chosen cut combination candidates. The remaining observables turned out not to significantly improve the sensitivity.

5.2.2 Towards the final signal regions

The optimal cut combinations obtained for the benchmark signal points, shown in table 5.2, subsequently need to be consolidated into a finite set of SRs. From table 5.2, it can easily be seen that all benchmark points favour a baseline selection including exactly two b -jets, possibly one additional light jet, a Higgs mass window requirement of roughly $m_{bb} \in [100, 140]$ GeV, and $E_T^{\text{miss}} > 240$ GeV. The requirements on m_T , m_{CT} and $m_{\ell b_1}$ are however not easily consolidated

Table 5.2: Optimal cut combination for each benchmark signal point obtained with a brute force cut scan and a round of N-1 plots. The significance is computed for 139 fb^{-1} with the binomial discovery significance Z_B and includes MC statistical uncertainty as well as a flat 30% systematic uncertainty.

Observable	(300, 150)	(400, 200)	(600, 300)	(800, 250)	(800, 150)	(800, 0)
$N_{b\text{-jet}}$	2	2	2	2	2	2
N_{jet}	2	2	2 – 3	2 – 3	2 – 3	2 – 3
$m_{b\bar{b}}$ [GeV]	[105 – 135]	[100 – 140]	[100 – 140]	[95 – 145]	[95 – 145]	[95 – 145]
E_T^{miss} [GeV]	> 240	> 240	> 240	> 240	> 240	> 240
m_{CT} [GeV]	> 200	> 240	> 260	> 260	> 260	> 280
m_T [GeV]	> 100	> 120	> 140	> 200	> 240	> 240
$m_{\ell b_1}$ [GeV]	–	–	> 150	> 120	> 120	> 120
$Z_B [\sigma]$	0.8	1.9	2.1	1.8	2.2	2.3

into a single signal region, as they vastly differ depending on the model space represented by each benchmark point.

From the normalised distributions in fig. 4.3, it can already be seen that signal points from different kinematic regimes in the parameter space would in principle prefer different requirements on all three of these observables. Designing a single signal region that is optimised for the entire parameter space is thus not possible. Instead, a more generalised configuration is chosen, defining multiple signal region bins orthogonal to each other through their requirement on m_T and the m_{CT} , effectively creating a two-dimensional shape fit in these observables as the different SR bins can be fit simultaneously. Such a shape-fit configuration allows to exploit the differences in shape between signal and background distributions, and is able to accommodate the varying shapes of signal points from different regions in the parameter space.

The optimal number of bins as well as values of the individual bin edges in both distributions depends on the available MC statistics and is determined using the simplified fit scans introduced in section 5.1.3. The MC statistical uncertainty as well as a systematic uncertainty of 30%, correlated over all bins, is considered in each scanned configuration. The number of bins are varied in each direction (m_T and m_{CT}) between two and five, each time with varying bin edge values. As configurations with more bins could benefit from the additional MC statistics resulting from looser selection criteria on the remaining variables, the previously consolidated baseline selection is also allowed to vary to some extent. Configurations with multiple orthogonal SR bins in the E_T^{miss} or $m_{b\bar{b}}$ are also included in the scan. A subset of the investigated SR candidates are shown in fig. 5.3, only showing the nominal expected exclusion limit at 95% without uncertainty bands.

As expected already from table 5.2, the best performing configurations define multiple signal region bins in the m_T and m_{CT} distributions, while keeping a constant baseline selection on the remaining observables. Figure 5.4(a) shows a comparison of the expected exclusion contour for exemplary two-dimensional shape-fit configurations, using signal regions binned in (m_T, E_T^{miss}) , $(m_T, m_{b\bar{b}})$ and (m_T, m_{CT}) . The setup using a two-dimensional shape-fit in m_T and m_{CT} clearly maximises the expected excluded area. In addition, this configuration also leads to optimal sensitivity within the expected limit, as can be seen in fig. A.8(a). Finally, applying a

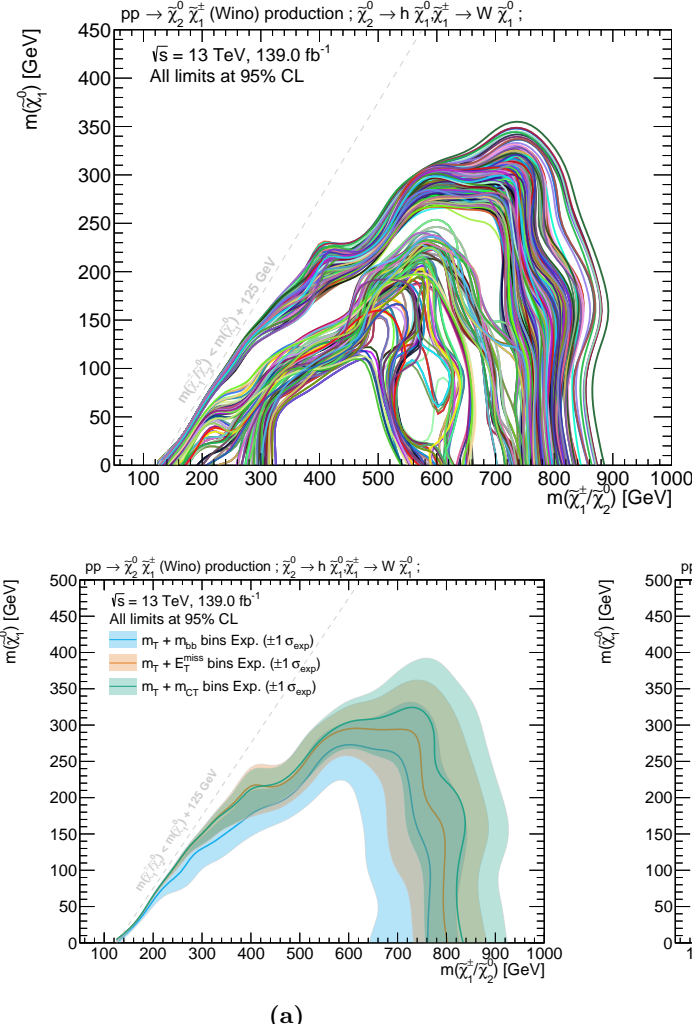


Figure 5.3: Expected exclusion contours obtained from a subset of the signal region candidates. The background estimation is taken directly from MC and includes MC statistical uncertainty as well as an uncorrelated shape uncertainty of 30%. For the sake of visibility, only the nominal contours are shown (without uncertainty bands).

Figure 5.4

requirement on high values of $m_{\ell b_1}$ in the highest m_T bins has been shown (see fig. A.8(b)) to significantly improve sensitivity to signal models with high mass differences.

5.3 Signal region definitions

An overview of the final signal region definitions is provided in table 5.3. Based on the previously discussed results, three signal regions bins in m_T are defined, optimised for the low (SRLM), medium (SRMM), and high (SRHM) mass difference regimes. While SRLM targets the smallest values of m_T , SRMM and SRHM target progressively increasing values of m_T . All three signal regions are further divided into three m_{CT} bins each, resulting in a total of nine disjoint SR bins. The signal region with the highest requirement on m_T (SRHM) also requires $m_{\ell b_1} > 120 \text{ GeV}$, for the reason explained previously. All three SRs otherwise share a common set of requirements

Table 5.3: Overview of the selection criteria for the signal regions. *Exclusion* SRs are defined for model-dependent limits, and *discovery* SRs are defined for model-independent limits. Each of the three exclusion SRs is binned in three m_{CT} regions for a total of nine exclusion bins.

	SRLM	SRMM	SRHM
N_{lepton}		$= 1$	
p_T^ℓ [GeV]		$> 7(6)$ for $e(\mu)$	
N_{jet}		$= 2$ or 3	
$N_{b\text{-jet}}$		$= 2$	
E_T^{miss} [GeV]		> 240	
$m_{b\bar{b}}$ [GeV]		$\in [100, 140]$	
$m(\ell, b_1)$ [GeV]	–	–	> 120
m_T [GeV] (excl.)	$\in [100, 160]$	$\in [160, 240]$	> 240
m_{CT} [GeV] (excl.)	$\{ \in [180, 230], \in [230, 280], > 280 \}$		
m_T [GeV] (disc.)	> 100	> 160	> 240
m_{CT} [GeV] (disc.)		> 180	

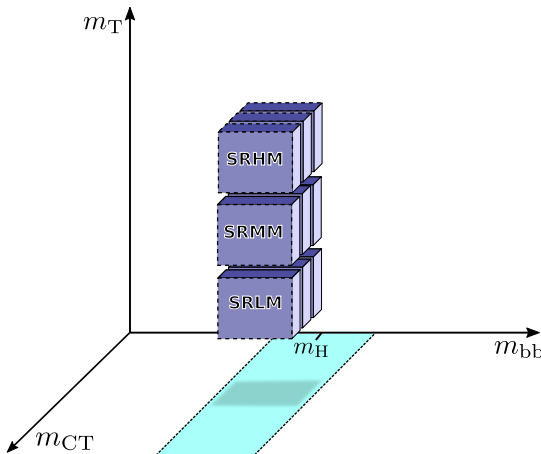


Figure 5.5: Configuration of the exclusion signal regions. Nine signal region bins are defined on m_T and m_{CT} within the Higgs mass window, resulting in a two-dimensional shape-fit.

on the number of jets, E_T^{miss} and $m_{b\bar{b}}$. As shape-fits are by construction highly model-dependent[†], these SRs will be used for deriving model-dependent limits in the case where no significant excess compared to the expected SM background rate is seen in data. For this reason, the shape-fit regions will be referred to as *exclusion* regions in the following. A graphical representation of the nine exclusion signal region bins is shown in fig. 5.5.

For evaluating a potential excess in data compared to the expected background rate, a second set of signal regions is derived from the optimised shape-fit setup. For each of the three bins in the transverse mass (SRLM, SRMM, and SRHM), the three m_{CT} bins are summed up and the upper bound on m_T is removed (if present). This results in three cut-and-count signal regions that make minimal model assumptions and can be interpreted in any signal model as long as the predicted signal rates are known. In case of no significant excess over the SM expectation, these so-called *discovery* SRs can be used to derive model-independent limits.

[†] The signal shapes need to be known in order to estimate the expected signal rates in multiple, disjoint signal region bins.

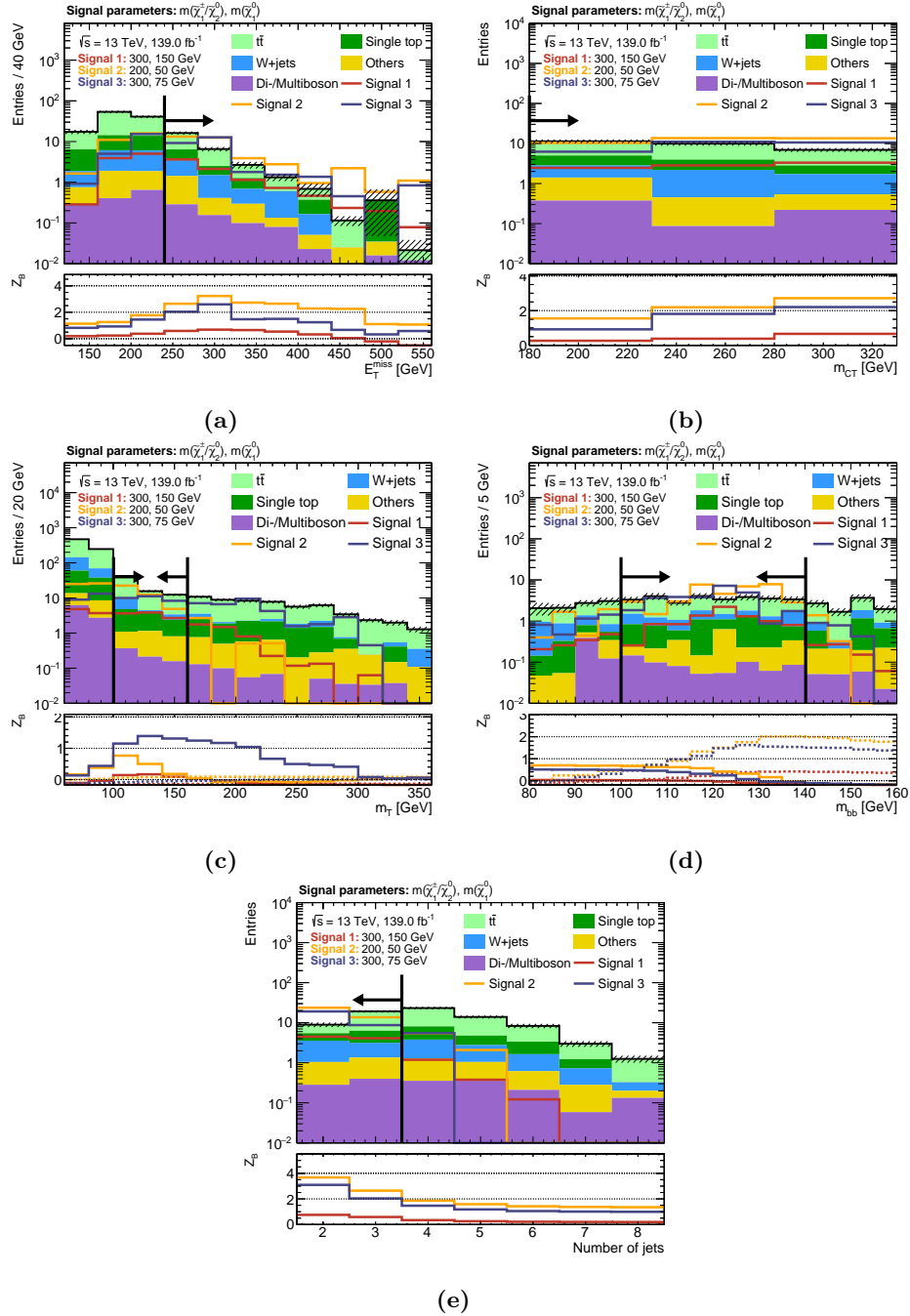


Figure 5.6: $N - 1$ plots for SRLM, with exemplary signal points and all m_{CT} bins included. The dashed area represents MC statistical uncertainty on the background. In all figures except fig. (b), the significance in the lower pad is obtained by summing up all the events in the direction of the cut arrow and includes 30% uncertainty as well as MC statistical uncertainty. In fig. (b) the significance is only computed on a bin-by-bin basis, i.e. not summing up all events in the direction of the cut arrow.

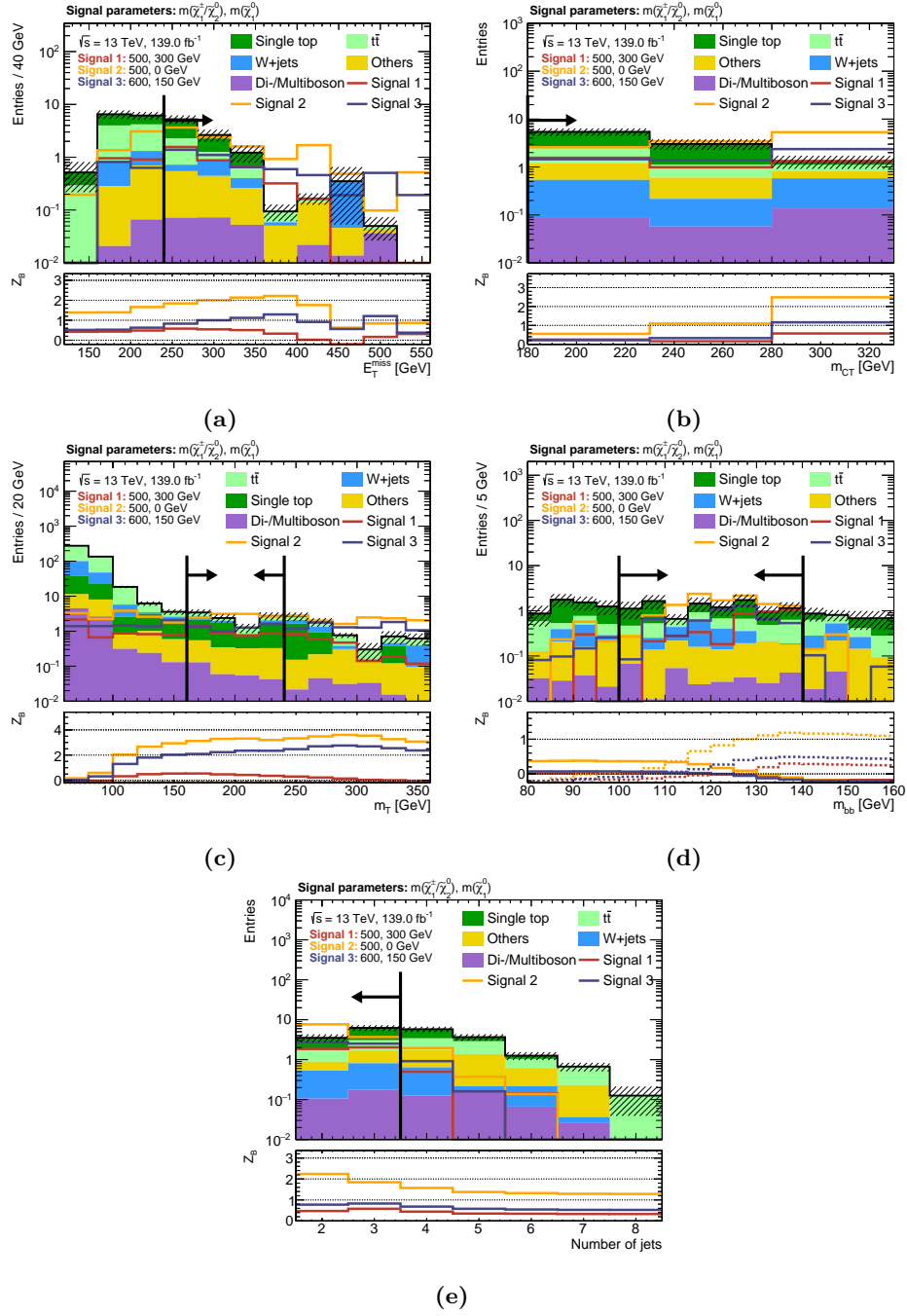


Figure 5.7: $N - 1$ plots for SRMM, with exemplary signal points and all m_{CT} bins included. The dashed area represents MC statistical uncertainty on the background. In all figures except fig. (b), the significance in the lower pad is obtained by summing up all the events in the direction of the cut arrow and includes 30% uncertainty as well as MC statistical uncertainty. In fig. (b) the significance is only computed on a bin-by-bin basis, i.e. not summing up all events in the direction of the cut arrow.

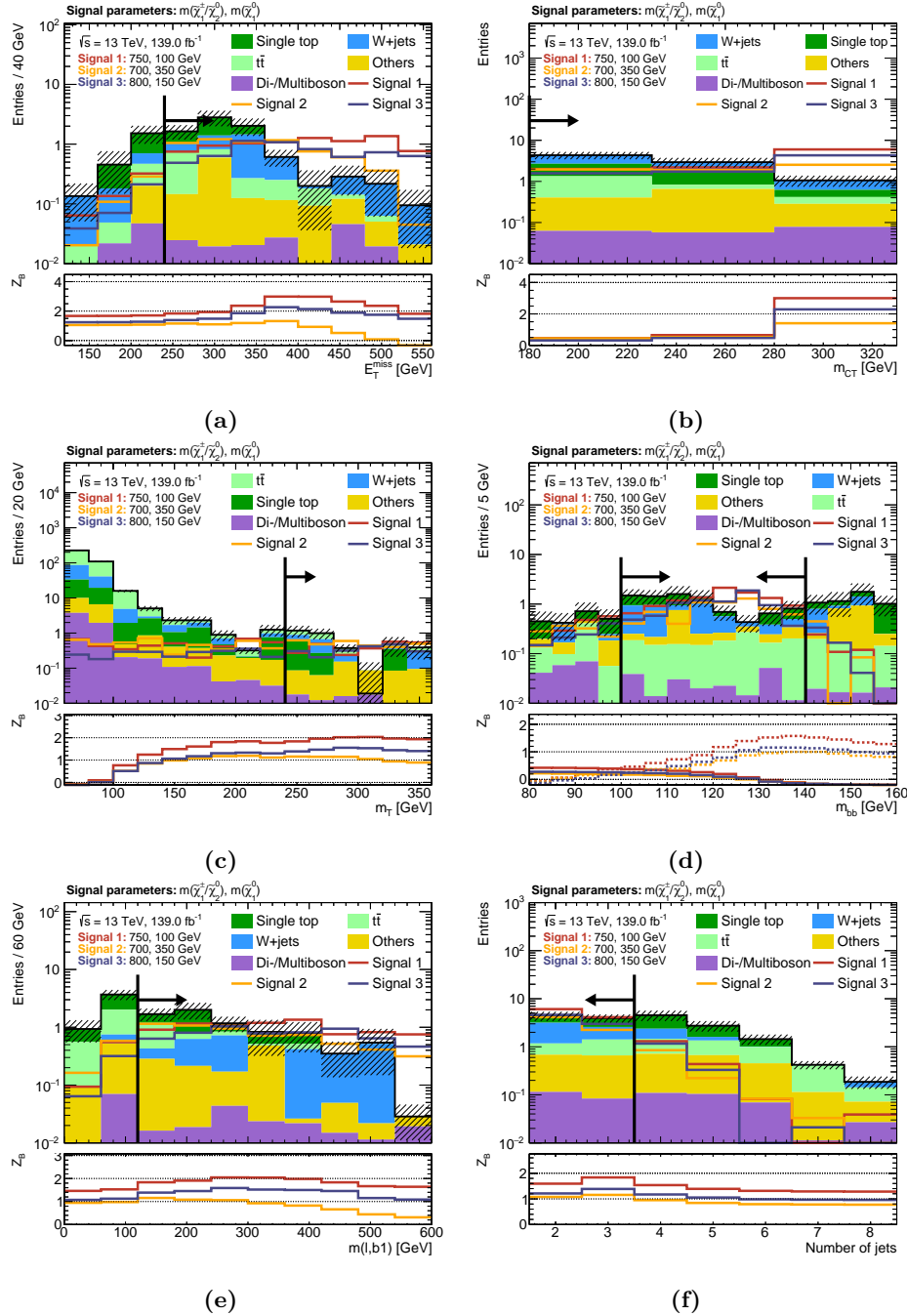


Figure 5.8: $N - 1$ plots for SRHM, with exemplary signal points and all m_{CT} bins included. The dashed area represents MC statistical uncertainty on the background. In all figures except fig. (b), the significance in the lower pad is obtained by summing up all the events in the direction of the cut arrow and includes 30% uncertainty as well as MC statistical uncertainty. In fig. (b) the significance is only computed on a bin-by-bin basis, i.e. not summing up all events in the direction of the cut arrow.

Chapter 6

Background estimation

A reliable estimation of the expected SM background rates in the SRs is crucial for exercising the statistical machinery laid out in chapter 3 and making conclusive statistical statements. The background estimation approaches used in the following either rely on semi-data-driven techniques or on MC-only estimations. As estimating backgrounds only from MC simulation is often problematic due to e.g. mis-modelings in the phase space regions targeted not appropriately covered by the uncertainties, a (semi)-data-driven approach is often favoured. In the following, the major backgrounds $t\bar{t}$, single top and $W + \text{jets}$ are estimated using a semi-data-driven approach, while the expected rates from the remaining smaller backgrounds rely purely on MC simulations and are normalised to their theoretical cross section.

6.1 General strategy

6.1.1 Transfer factor approach

Estimating background contributions in SRs in a semi-data-driven approach, usually involves the introduction of so-called control regions (CRs) used to control dominant background processes by comparing their expected event rates to data. The CRs are designed to be enriched in events of a given background process (or type) while being approximately free of signal contamination. If $N_p^{\text{MC}}(\text{SR})$ and $N_p^{\text{MC}}(\text{CR})$ are the expected rates for a given background process p from MC simulation in a given SR and CR, respectively, then the transfer factor $N_p^{\text{MC}}(\text{SR})/N_p^{\text{MC}}(\text{CR})$ allows to convert the number of observed background events in the CRs, $N_p^{\text{obs.}}(\text{CR})$ into a background estimate in the SRs, $N_p^{\text{est.}}(\text{SR})$, through

$$N_p^{\text{est.}}(\text{SR}) = N_p^{\text{obs.}}(\text{CR}) \frac{N_p^{\text{MC}}(\text{SR})}{N_p^{\text{MC}}(\text{CR})} = \mu_p N_p^{\text{MC}}(\text{SR}). \quad (6.1)$$

An important benefit of this approach is that the impact of systematic uncertainties on the estimated background rates can be evaluated on the transfer factors, that are ratios of MC estimates. As such, systematic uncertainties can be canceled in the extrapolation to the SR. The uncertainty on the background estimate is then a combination of statistical uncertainties in the CR and remaining uncertainties affecting the extrapolation. For this reason, CRs are

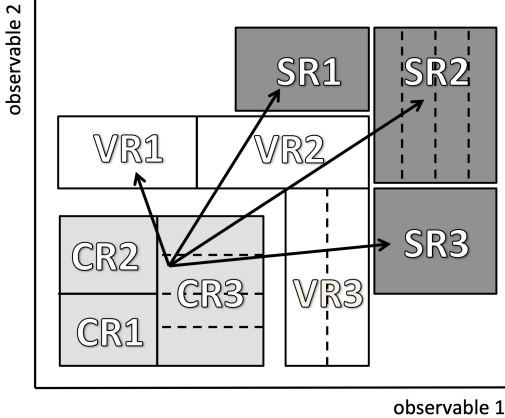


Figure 6.1: Schematic view of an analysis strategy including multiple control, validation and signal regions with one or multiple bins each. Extrapolations from the control regions into the signal regions can be verified in the validation regions lying in the phase space extrapolated over. Figure adapted from [150].

usually deliberately chosen to have large statistics, effectively reducing the uncertainties on the extrapolation to the SRs.

As indicated in eq. (6.1), the transfer factor approach is formally equivalent to using the process-specific normalisation factor introduced in section 3.1, effectively *normalising* the number of background events expected from MC in the CR to the number of observed events. In the profile likelihood fit setups used in the following, implemented using HISTFITTER [150], the normalisation factor μ_b is fitted to data instead of background as expected from MC simulation. In the following, multiple disjoint CRs are used to simultaneously normalise multiple background processes to data in a combined fit. In order not to have an underdetermined minimisation problem, at least the same number of CRs as normalisation factors needs to be used. Two different profile likelihood fit configurations are used in the following, a *background-only* fit configuration assuming no signal contribution and typically only including the CRs, and a *model-dependent* fit configuration with nominal signal contribution using CRs as well as SR.

In order to verify the quality of the extrapolation from the CRs to the SRs, so-called validation region (VR) are defined. VRs do not participate in the actual fit of the model parameters to data, but serve as intermediate regions to verify the extrapolation. For this reason, VRs are typically placed in the region between the CRs and SRs that is extrapolated over. A schematic view of an analysis strategy using all three types of regions is shown in fig. 6.1. All three types of regions can have more than one bin and are separated using suitable observables that are extrapolated over.

6.1.2 Analysis blinding

An important concept in the design phase of searches for new physics is the idea of *blinding* regions of interest [234], meaning that measured data are not looked at in these regions. This avoids issues of *experimenter's bias*, i.e. unintended influences on the design of the analysis based on the observed data. If data were already known when designing the signal regions (and therefore the outcome of the analysis would be known to some extent), experimenter's bias could for example occur during the selection of the final signal region definitions.

During the design of a search for new physics, signal regions are generally kept blinded until the complete analysis strategy is fixed. Once the SRs have been designed, the next step is to develop suitable CRs with negligible signal contamination. This is followed by design of VRs that can be unblinded once the CRs are fixed. The SRs are only unblinded after the extrapolation from the CRs has been verified in the VRs, allowing to either quantify potential excesses in data or set limits on model parameters.

6.1.3 Data versus Monte Carlo plots

In this chapter, all plots comparing data versus MC are *pre-fit*, meaning that no background-only fit has been run in order to determine the normalisation factors and total systematic uncertainties for the background estimate. The contributions from the dominant backgrounds $t\bar{t}$, $W + \text{jets}$ and single top are normalised simultaneously in the control regions by solving the system of i equations

$$n_{\text{data}}^{\text{CR}_i} = \mu_{t\bar{t}} B_{t\bar{t}}^{\text{CR}_i} + \mu_W B_W^{\text{CR}_i} + \mu_{\text{ST}} B_{\text{ST}}^{\text{CR}_i} + B_{\text{other}}^{\text{CR}_i}, \quad (6.2)$$

where i runs over the list of CRs introduced in section 6.2 and $\mu_{t\bar{t}}$, μ_W and μ_{ST} are the normalisation factors of the $t\bar{t}$, $W + \text{jets}$ and single top backgrounds, respectively, that are to be determined. $B_{t\bar{t}}^{\text{CR}_i}$, $B_W^{\text{CR}_i}$, $B_{\text{ST}}^{\text{CR}_i}$ and $B_{\text{other}}^{\text{CR}_i}$ are the background rates expected from MC simulation in the i -th CR. Normalisation factors obtained are 0.96 for $t\bar{t}$, 1.24 for $W + \text{jets}$ and 0.73 for single top. As will be shown in section 8.1, the normalisation factors obtained using the full statistical procedure will be close to these values.

Additionally, the uncertainty bands on the background estimation include only MC statistical uncertainty as well as experimental uncertainties. The variations of the experimental uncertainties are normalised to the nominal background estimate in the case of $t\bar{t}$, $W + \text{jets}$ and single top, such that only the shapes of the dominant backgrounds are affected. For the remaining minor backgrounds, the experimental uncertainties can affect both normalisation and shape. All experimental uncertainties are assumed to be fully correlated over all processes and bins, allowing them to be added together in quadrature. The uncertainty bars on the data points correspond to the 68% confidence interval, assuming data to be Poisson distributed.

6.2 Control regions

The contributions from $t\bar{t}$, $W + \text{jets}$ production and single top processes are normalised to data in dedicated CRs. Other processes like $Z + \text{jets}$, diboson and multiboson, $t\bar{t} + V$, $t\bar{t} + h$ and $V + h$ are estimated directly from MC simulation and normalised to their theoretical cross sections. All CRs are designed to be kinematically as close as possible to the respective SRs, such that the normalisation factors derived in the CRs are also valid in the SRs. The CRs are mutually exclusive and made orthogonal to the SRs through their requirements on m_T , m_{CT} and $m_{b\bar{b}}$. Apart from the requirements on these three observables as well as the requirement on $m_{\ell b_1}$ (removed altogether in the CRs), the CRs share the same set of cuts as the SRs. Figure 6.4(a) illustrates the configuration of all CRs, especially highlighting the fact that all CRs are located in sideband regions off the $m_{b\bar{b}}$ window, significantly reducing signal contamination. Table 6.1

Table 6.1: Overview of the CR and VR definitions. All regions partially share the same selection as the SR for all variables except $m_{\ell b_1}$, which is not used in the CR and VR definitions.

CR	TR-LM	TR-MM	TR-HM	WR	STR	
$m_{b\bar{b}}$ [GeV]		<100 or >140		$\in [50, 80]$	>195	
m_T [GeV]	$\in [100, 160]$	$\in [160, 240]$	>240	$\in [50, 100]$	>100	
m_{CT} [GeV]		<180		>180	>180	
VR	VR-onLM	VR-onMM	VR-onHM	VR-offLM	VR-offMM	VR-offHM
$m_{b\bar{b}}$ [GeV]		$\in [100, 140]$		$\in [50, 80] \cup [160, 195]$	$\in [50, 80] \cup [160, 195]$	$\in [50, 75] \cup [165, 195]$
m_T [GeV]	$\in [100, 160]$	$\in [160, 240]$	>240	$\in [100, 160]$	$\in [160, 240]$	>240
m_{CT} [GeV]		<180			>180	

summarises the kinematic requirements separating the CRs from other regions of interest in the analysis.

Control regions for $t\bar{t}$

As events from $t\bar{t}$ processes constitute the dominant SM background in all SRs, it is necessary to have a precise and reliable estimation of their contributions. Three CRs are defined for $t\bar{t}$, following the same binning in m_T , and thus called TRLM, TRMM and TRHM in the following. A good purity of $t\bar{t}$ processes as well as the necessary high MC are achieved by inverting the requirements on $m_{b\bar{b}}$ and m_{CT} . The achieved $t\bar{t}$ purities are 79.6% in TRLM, 85.9% in TRMM and 84.1% in TRHM. The composition of the different $t\bar{t}$ decay modes in each CR is found to be similar as in the respective SR. The maximum signal contamination over the entire signal grid is 0.8%, 1.1% and 1.9% for TRLM, TRMM and TRHM, respectively, and thus negligible. Figures 6.3(a) to 6.3(c) show the signal contamination over the entire signal grid.

Control region for $W + \text{jets}$

Events from $W + \text{jets}$ production represent the second largest contribution of SM background events in the SRs. A single $W + \text{jets}$ CR (WR) is defined by replacing the requirements on m_T and $m_{b\bar{b}}$ with $50 \text{ GeV} < m_T < 100 \text{ GeV}$ and $50 \text{ GeV} < m_{b\bar{b}} < 80 \text{ GeV}$, respectively. No bins in m_{CT} are defined for WR. As for the $t\bar{t}$ control regions, moving WR off the Higgs mass peak allows to achieve a tolerable maximum signal contamination of about 2.4% (with most signal points having significantly less than 1% signal contamination in WR), as shown in fig. 6.3(d). Applying a low requirement on m_T allows to predominantly select events in front of the kinematic endpoint of the transverse mass of the W boson, resulting in a high statistics control region with a $W + \text{jets}$ purity of roughly 52.5%.

Control region for single top

Single top processes result in significant background contributions in some SRs, necessitating a proper semi-data-driven estimation. A single top CR (STR) is defined by replacing the Higgs mass window cut on $m_{b\bar{b}}$ with $m_{b\bar{b}} > 195 \text{ GeV}$ and removing the bins in m_{CT} . Off the Higgs mass peak guarantees a low maximum signal contamination of roughly 0.8% and a high purity

of single top processes of about 51.7%. The signal contamination across the entire signal grid is shown in fig. 6.3(e).

6.3 Validation regions

Two sets of VRs regions are introduced in order to verify the extrapolation over the different distributions. The first set, called VRon is situated on the Higgs boson mass peak but with the m_{CT} requirement inverted to $m_{\text{CT}} < 180 \text{ GeV}$, allowing it to be used for validating the extrapolation in m_{CT} . The second set of VRs is located on both sides off the Higgs boson mass peak at same values in m_{CT} than the SRs. This set of off-peak VRs, called VRoff, can be used to validate the extrapolation in $m_{b\bar{b}}$. All VRs use the same binning in m_{T} as the SRs such that the extrapolation into their respective associated SR can be validated. The different bins are consequently called VRonLM, VRonMM VRonHM and VRoffLM, VRoffMM, VRoffHM. The selections defining the VRs are summarised in table 6.1.

prefit plots
of VR?

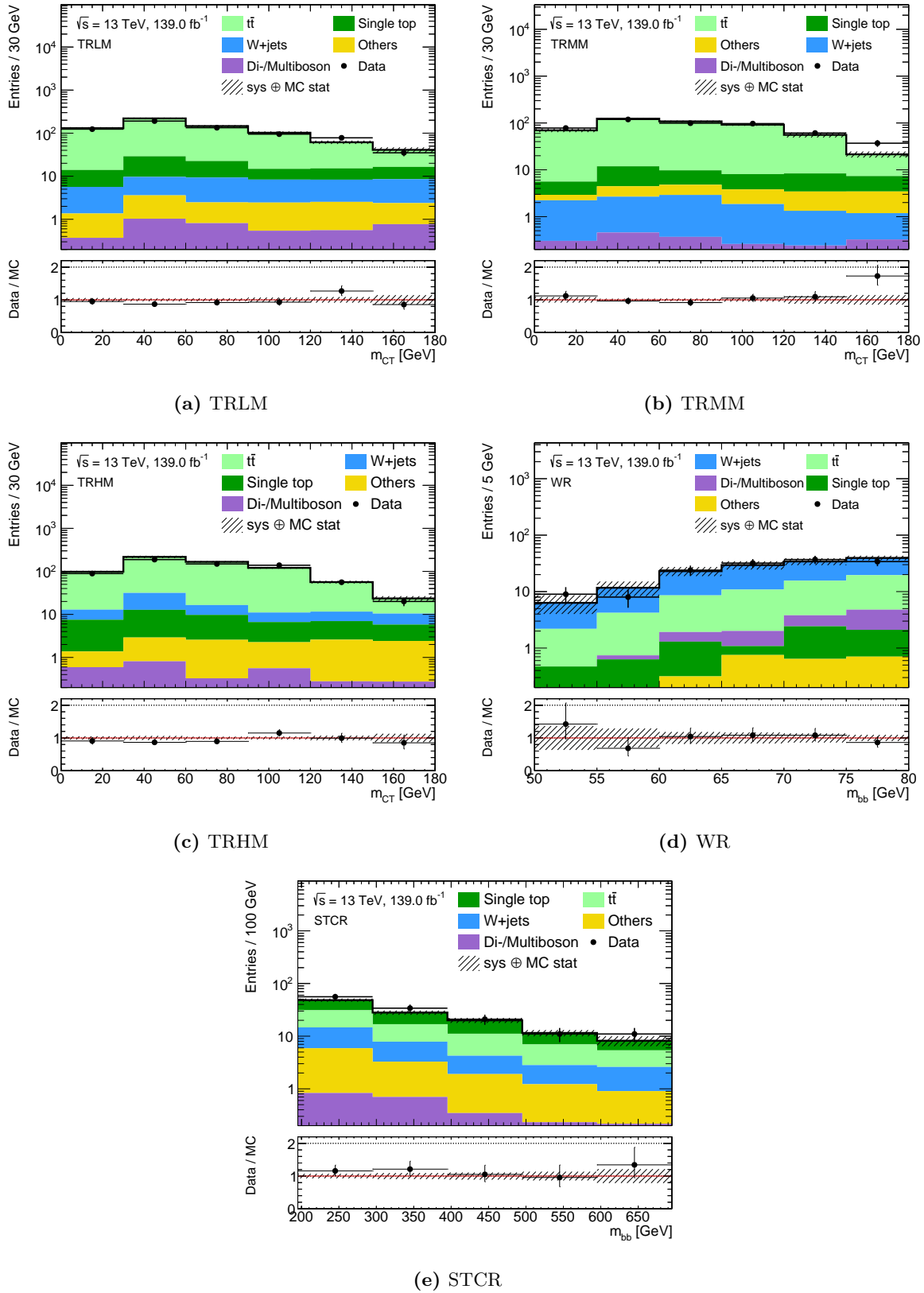


Figure 6.2: Exemplary distribution shown in each control region. As laid out in the beginning of this chapter, the shaded region includes MC statistical uncertainty as well as experimental uncertainties, added in quadrature. A good agreement between MC expectation and data is observed in all CRs.

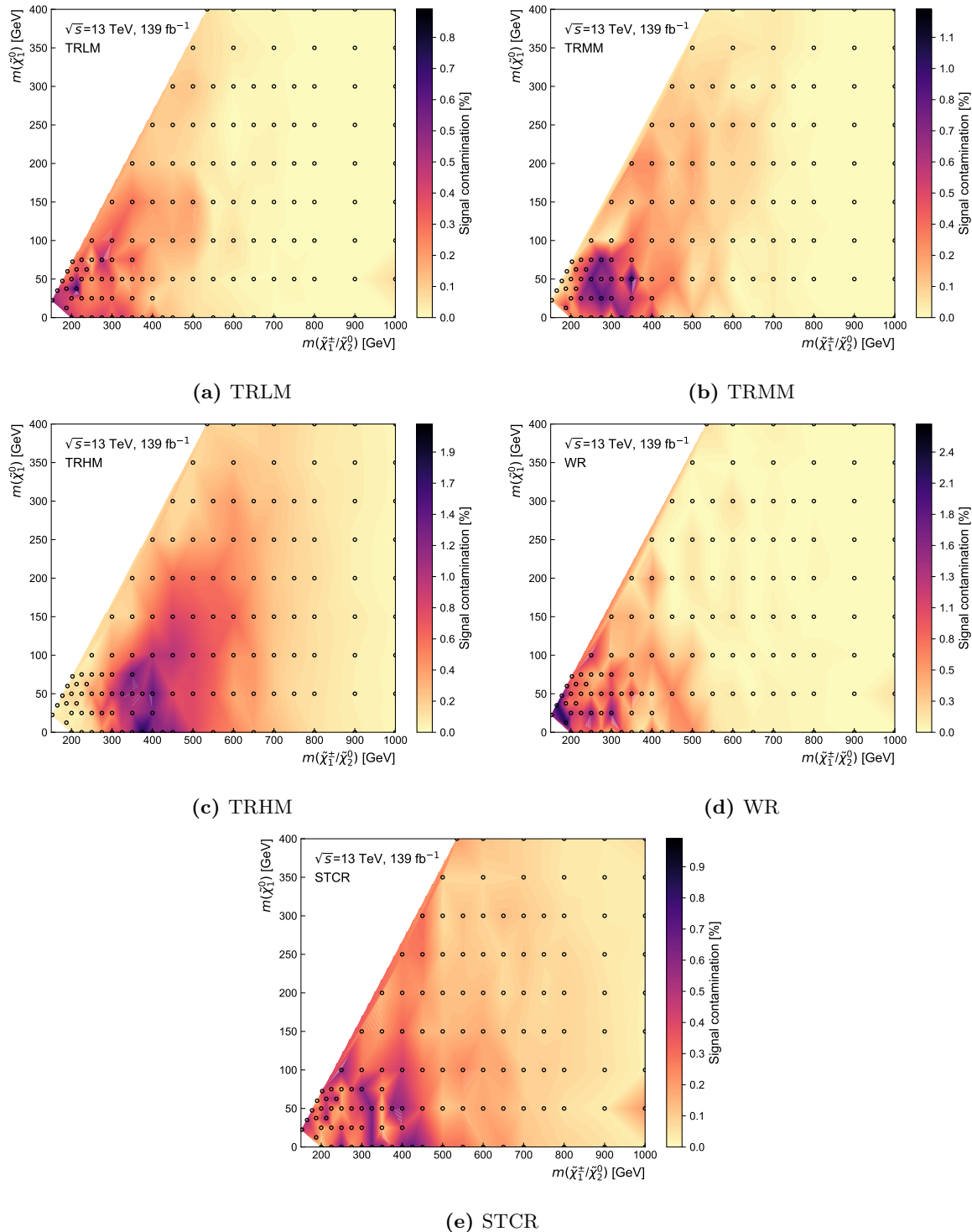


Figure 6.3: Signal contamination (shown on the z -axis) for all CRs throughout the signal grid. The space between the signal points (indicated by the black circles) is interpolated using Delaunay triangles.

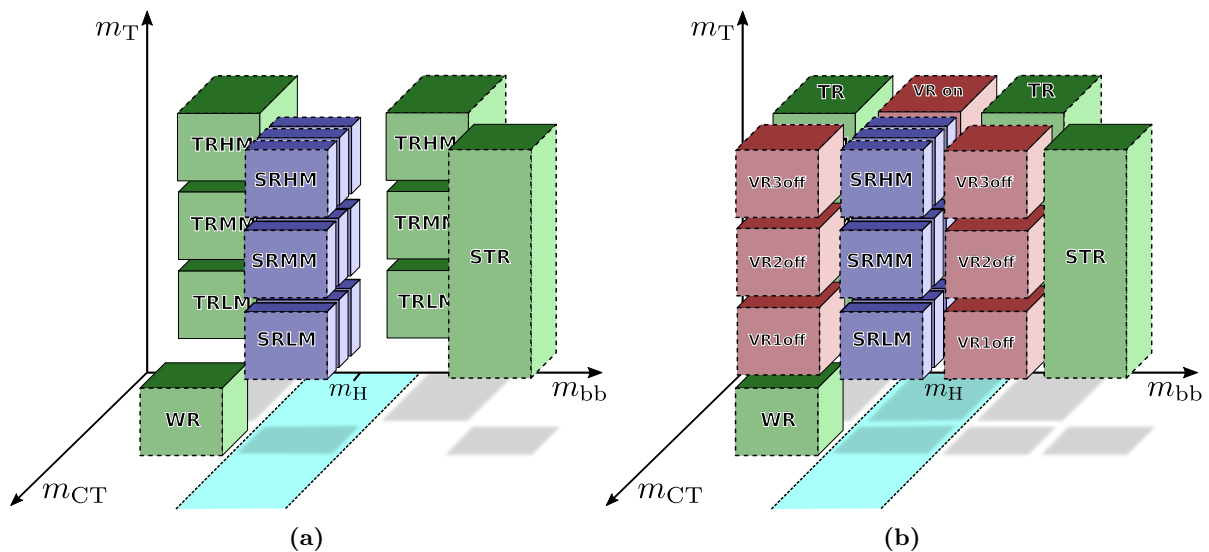


Figure 6.4: Configuration of (a) the control regions placed around the signal regions off the $m_{b\bar{b}}$ window as well as (b) the validation regions in the phase space between the CRs and SRs. The VRs are arranged such that each of the extrapolations can be validated.

Chapter 7

Systematic uncertainties

Several sources of systematic uncertainties need to be considered in the following. As laid out in chapter 3, they enter the likelihood as nuisance parameters and can be interpreted as a loss of information on the signal strength parameter. In the following, they are separated into experimental uncertainties arising from finite detector resolution and object reconstruction and theoretical uncertainties due to modelling of the physics processes during simulation.

7.1 Experimental uncertainties

Experimental uncertainties arise from the experimental methods used to derive the signal and background rate estimations. They are evaluated using up and down variations provided either as variational weights in the case of efficiency uncertainties, or as additional variational samples derived by performing the object reconstruction with varied parameters.

7.1.1 Pile-up reweighting and luminosity

The MC events were largely already generated before the full data was taken, and therefore before the full pileup profile in data was known. For this reason, the number of average interactions $\langle\mu\rangle$ per bunch crossing in MC is in general not identical to that in data, necessitating a reweighting procedure in MC. In order to account for differences in the measured inelastic pp cross sections and the one obtained from MC simulation, a scale factor of 1.03 is applied before the reweighting procedure. As MC samples are generated with integer of $\langle\mu\rangle$ only, the scale factor is applied to data instead. The uncertainty on the pileup reweighting is evaluated by varying the data scale factor by ± 0.04 and deriving variational pileup weights.

As detailed in section 2.1.2, the total integrated luminosity relies on the measurement of the bunch luminosity which in turn needs precise measurements of the visible inelastic cross section σ_{vis} as well as the visible pile-up parameter μ_{vis} . Uncertainties on the measurement of the total recorded cross section are dominated by the uncertainties on σ_{vis} that is measured during special vdM scans. For the full Run 2 dataset, an overall luminosity uncertainty of $\pm 1.7\%$, is considered for all MC processes not normalised to data using a CR, derived using the methods described in Ref. [98].

7.1.2 Triggers

As all selections considered in the analysis apply a minimum E_T^{miss} requirement of 240 GeV where the E_T^{miss} triggers are fully efficient (see section 4.7), a 2% normalisation uncertainty correlated over all bins is considered.

7.1.3 Leptons

A large number of uncertainties on electrons arises from energy scale and resolution measurements [203, 206]. They are assumed to be fully correlated in η and are summed in quadrature, resulting in one nuisance parameter for the energy scale and one for the resolution. Similarly, uncertainties on muons arise from calibrations of the muon momentum scale and resolution [207]. They are evaluated using variations in the smearing of the ID and MS tracks as well as the momentum scale, resulting in a total of five nuisance parameters entering the likelihood. Additional lepton uncertainties considered in the following originate from reconstruction, identification and isolation efficiencies, as well as track-to-vertex association and bad muon identification efficiencies. The latter two are only considered for muons.

7.1.4 Jets

The calibration of the jets to the absolute JES is subject uncertainties arising e.g. from the *in situ* measurements, pile-up effects or flavour-dependence [212], encoded in a large set of 125 parameters. The full detail contained in the complete set of uncertainty components offers far greater statistical precision than needed for the following analysis. As the majority of the parameters (a total of 98) stems from *in situ* measurements, an eigenvector decomposition is performed on the covariance matrix of these components [235], allowing to determine the 15 principal orthogonal components (including a residual term adding the remaining terms in quadrature), with minimal loss in bin-by-bin correlation information. Five additional parameters evaluating uncertainties arising from *in situ* η -intercalibrations of forward jets with respect to central jets are kept separate due to their two-dimensional dependence on p_T and η [212]. Effects from pile-up are described by four nuisance parameters. Uncertainties arising from differing detector responses to gluon- and quark-initiated jets as well as flavour-related differences are accounted for by two more nuisance parameters. Uncertainties from jets that are not contained in the calorimeters and *punch-through* into the MS are evaluated with an additional parameter. A last parameter encodes the uncertainty arising from the calibration of MC samples reconstructed using ATLFAST-II instead of the full detector simulation.

Systematic uncertainties on the JER arise from measured differences between data and MC simulation, noise from pile-up, and *in situ* measurements of the jet p_T imbalance. A similar eigenvector decomposition as for part of the JES uncertainties is used, reducing the set of nuisance parameters considered in the following to 13 [212]. Finally, uncertainties related to the efficiency of jet vertex tagging are evaluated using a weight systematic.

7.1.5 Flavour tagging

Uncertainties on the flavour tagging efficiency originate e.g. from modelling uncertainties as well as uncertainties on the reconstruction of physics objects. As for the JER and JES the full set of nuisance parameters that would in principle need to be included in order to consider the full bin-by-bin correlations and p_T and η dependence of the uncertainties, is reduced to a more manageable size using an eigenvector decomposition. This leads to a total of five nuisance parameters encoding uncertainties on the b -tagging efficiency, c -jet and light-jet mistagging rate as well as the extrapolation to high- p_T jets [218, 219].

7.1.6 Missing transverse energy

The uncertainties on E_T^{miss} are evaluated using the systematic variations of all calibrated objects as inputs to the E_T^{miss} calculation. Additional uncertainties arise from the calculation of the track soft term. In the following, uncertainties on the soft term scale and resolution are considered, resulting in one nuisance parameter for the soft term scale and two nuisance parameters (corresponding to the perpendicular and parallel components) for the soft term resolution uncertainty. All track soft term uncertainties are derived by comparing simulation to $Z \rightarrow \mu\mu$ events [220]. Contributions to the JES uncertainty due to pile-up is considered

7.2 Theoretical uncertainties

As discussed in section 2.2.8, due to finite order calculations, the different steps of the MC simulation generally introduces a certain number of unphysical scales and parameters. In order to quantify the uncertainties arising from the ad-hoc values of these, the MC simulation generally needs to be re-run with systematically varied parameter values. Since varied MC simulation parameters affect the event kinematics even before reconstruction and calibration, it is computationally very expensive to produce a full set of variations for each MC sample used in the nominal analysis.

In the following, multiple approaches are used to derive the theory uncertainties. For some of the variational samples, the full MC simulation chain was run with reduced statistics or different samples produced with a different set of MC generators and tunes were available. For others, variations were already processed during the initial MC simulation of the nominal sample and subsequently stored as variational weights. Finally, some of the variational samples were simulated at truth-level (i.e. without detector simulation). The latter approach was used especially in the case of SUSY signal samples, where theory uncertainties are expected to only have a minor impact and a full simulation of all parameter variations would be computationally unfeasible.

For background processes that are normalised to data in a dedicated CR, the theory uncertainties are evaluated on the transfer factors. For a process p , a control region CR_i , and a destination region R_j (either a SR or a VR), the transfer factor reads

$$f_p(\text{CR}_i \rightarrow \text{R}_j) = \frac{N_p^{\text{MC}}(\text{R}_j)}{N_p^{\text{MC}}(\text{CR}_i)}, \quad (7.1)$$

where $N_p^{\text{MC}}(\text{R}_j)$ and $N_p^{\text{MC}}(\text{CR}_i)$ are the expected event rates for the process p in CR_i and R_j , respectively. The systematic uncertainty on the transfer factor is then given by

$$\Delta f_p^{\text{syst}} = \frac{f_p^{\text{variation}}}{f_p^{\text{nominal}}} - 1, \quad (7.2)$$

with $f_p^{\text{variation}}$ and f_p^{nominal} the transfer factors from the variational and nominal samples, respectively. If the MC samples used for deriving the variational and nominal transfer factors are statistically independent, a statistical component of the uncertainty is derived using the individual statistical uncertainties on the background estimate,

$$\Delta f_p^{\text{stat}} = (\Delta f_p^{\text{syst}} + 1) \sqrt{\sum_{n \in N} \left(\frac{\sigma_n}{n} \right)^2}, \quad (7.3)$$

where n runs over the set of expected event rates and σ_n is the absolute MC statistical uncertainty associated to each expected event rate n . In the following the control region used to evaluate the uncertainties on the transfer factors is taken to be the sum of all CRs introduced in section 6.2. This not only significantly improves the statistics in the region used for normalisation, but also results in a consistent treatment across all theoretical uncertainties on all relevant processes.

For other backgrounds directly estimated from MC simulation, the systematic uncertainty on the expected event rate in each region R_i is given by

$$\Delta n_p^{\text{syst}}(\text{R}_i) = \frac{n_p^{\text{syst}}(\text{R}_i)n_p^{\text{nominal}}(\text{P})}{n_p^{\text{nominal}}(\text{R}_i)n_p^{\text{syst}}(\text{P})} - 1, \quad (7.4)$$

where the region P is a so-called *loose preselection* with minimal analysis selection criteria used for normalisation of the event rates to be compared. If not otherwise indicated the loose preselection used for normalisation requires exactly one isolated lepton, 2–3 jets of which at least one is b -tagged, $E_{\text{T}}^{\text{miss}} > 220 \text{ GeV}$ and $m_{\text{T}} > 50 \text{ GeV}$.

Apart from the hard scattering and parton showering uncertainties on top processes, all other theoretical uncertainties enter the likelihood as asymmetric correlated shape uncertainties. The hard scattering and parton showering uncertainties on top processes described below are estimated using MC generator comparisons and thus need to be symmetrised. The shape information is however still kept, i.e. the uncertainties are not one-sided.

7.2.1 Background

$t\bar{t}$ and single top

Theory uncertainties on the estimate of $t\bar{t}$ and single top processes arise for example from the simulation of the hard scattering between the interacting partons. These are evaluated by comparing the nominal MC samples generated using POWHEG and PYTHIA8 with alternative samples generated using MADGRAPH_AMC@NLO and PYTHIA8. An uncertainty resulting from the hadronisation and fragmentation scheme chosen in PYTHIA8 is estimated by comparison to a MC sample generated using POWHEG and HERWIG++ [236]. Uncertainties arising from ISR are evaluated at full reconstruction level by varying up and down by a factor of two the

unphysical renormalisation μ_R and factorisation μ_F scales as well as the parameters controlling the showering and ME+PS matching [237]. Likewise, uncertainties arising from simulation of FSR are estimated by varying the effective coupling α_s^{FSR} [237].

Uncertainties also originate from the PDF set used when simulating the nominal MC sample. As detailed in table 4.1, the NNPDF3.0NLO is used for the simulation of both $t\bar{t}$ and single top processes. An envelope around the variational expected event rates obtained from the NNPDF3.0NLO uncertainties are used to compute an uncertainty on the transfer factor.

Beyond LO single top production diagrams, interference appears between Wt and $t\bar{t}$ production. Two approaches are commonly used to try and isolate the Wt channel: diagram removal (DR) and diagram subtraction (DS) [238]. While the former removes all diagrams in the NLO Wt amplitude that are doubly resonant (meaning that they involve an intermediate t quark that can be on-shell), the latter introduces subtraction terms in the NLO Wt cross section cancelling the $t\bar{t}$ contribution [238]. As the DR scheme is used for estimating the event rate of the Wt channel in the analysis, a comparison with an estimation using the DS scheme allows to derive an uncertainty associated to the interference.

$W/Z + \text{jets}$

For $W/Z + \text{jets}$ processes, simulated using SHERPA 2.2.1, four different unphysical scales can be varied in order to investigate uncertainties on the modelling. The renormalisation μ_R and factorisation μ_F scales are both independently and together varied up and down by a factor of two, resulting in a total of seven combined variations. Three envelopes are determined from varying only μ_R , only μ_F or μ_R and μ_F together, allowing to determine three separate uncertainties. The CKKW ME+PS matching scheme also uses an unphysical scale for determining the overlap between jets from the ME and the PS. The nominal value of 20 GeV for the merging scale is varied to 30 GeV and 15 GeV for the up and down systematic variations, respectively. Finally, the scale used for resummation of soft gluon emission, μ_{QSF} is varied up and down by a factor of two.

An additional uncertainty arises from the choice of PDF set used for simulating $W/Z + \text{jets}$. It is evaluated by propagating the PDF error set (containing slightly different parameterisations of the PDF) to the analysis observables. Uncertainties due to the choice of $\alpha_s = 0.118$ for fitting the PDFs are estimated by comparing with variations using $\alpha_s(m_Z) = 0.119$ and $\alpha_s(m_Z) = 0.117$, and added in quadrature to the previous PDF uncertainty.

As $Z + \text{jets}$ is not normalised to data in a dedicated CR but to its nominal SM cross section, an additional normalisation uncertainty corresponding to the uncertainty on the cross section is thus considered.

Other backgrounds

For diboson, multiboson and $t\bar{t} + V$ processes, uncertainties arising from the unphysical scales μ_F , μ_R as well as μ_{QSF} and the CKKW ME+PS matching scale are considered using the same prescription described above for $W/Z + \text{jets}$. For these three processes as well as for the other minor backgrounds $V + h$ and $t\bar{t} + h$, an additional uncertainty on the SM cross section used for normalisation is considered.

7.2.2 Signal

Theoretical uncertainties on the SUSY signal processes arise from the unphysical factorisation, renormalisation and CKKW-L ME+PS merging scales. These are evaluated using a similar procedure as for background processes, varying the different scales up and down by a factor of two and comparing the expected signal rates. An additional uncertainty on PS originating from the chosen PYTHIA8 tune is estimated by varying up and down the chosen value for α_s^{ISR} .

As detailed in section 4.3.1, the cross section of electroweakino pair production is calculated using RESUMMINO. A theoretical uncertainty on the cross section is considered in the following, but does not enter the statistical fit procedure as nuisance parameter. Instead, in addition to the set of observed CL_s values using the nominal cross section, two additional *variational* sets are derived using signal cross sections fixed at their $\pm 1\sigma$ variations. This allows to draw a cross section uncertainty band on the observed exclusion contour.

Due to the large number of MC samples, all theory uncertainties on SUSY signal processes are evaluated at truth-level only. As the VRs typically have relatively low signal contamination and thus low signal MC statistics available for evaluating theory uncertainties, requirements on observables with negligible impact on the shapes of the theoretical uncertainties are loosened. In the on-peak VRs, the requirements loosened are $m_T > 60 \text{ GeV}$ and $E_T^{\text{miss}} > 140 \text{ GeV}$. The same loosened selection is applied in SRs in cases where MC statistical uncertainty is too high for a reliable estimation of the theoretical uncertainties. In the off-peak VRs, the requirements loosened are $m_T > 60 \text{ GeV}$ and $E_T^{\text{miss}} > 60 \text{ GeV}$ and $m_{\text{CT}} > 60 \text{ GeV}$. Overall, the theoretical uncertainties on the expected signal rate range from about 10% in phase space regions with large mass splitting between $\tilde{\chi}_1^\pm/\tilde{\chi}_2^0$ and $\tilde{\chi}_1^0$ to about 25% in regions with small mass splittings.

Plots from
HF numbers?

7.3 Impact on signal regions

Table 7.1 shows a breakdown of the dominant systematic uncertainties on the background prediction in the SRs, obtained after a background-only fit in the CRs with subsequent extrapolation to the SRs. The total uncertainty in the SRs amounts to 15% in SRLM and increases to 25% in SRMM and 34% in SRHM. Theoretical uncertainties have the largest contribution to the total uncertainty. For SRLM, the largest uncertainty originates from the $t\bar{t}$ parton shower uncertainty (10%), while for SRMM (SRHM) the single top generator uncertainties are the largest ones with 10% (21%). Theoretical uncertainties on $W + \text{jets}$ and other minor backgrounds have only small to negligible effects. The experimental uncertainties in general have less impact on the total uncertainty than the theoretical ones, with the largest experimental uncertainties contributing only 5–10% depending on the SR. The dominant experimental uncertainties arise from the JES and JER as well as E_T^{miss} modelling and pile-up. The MS statistical uncertainties contribute 5–18% depending on the SR.

Table 7.1: Breakdown of the dominant systematic uncertainties in background estimates in the various exclusion signal regions (m_{CT} bins summed up). As the individual uncertainties can be correlated, they do not necessarily add up in quadrature to the total background uncertainty. The percentages show the size of the uncertainty relative to the total expected background. Table adapted from Ref. [165].

Signal Region	SRLM	SRMM	SRHM
Total background expectation	27	8.6	8.1
Total uncertainty	± 4 [15%]	± 2.2 [25%]	± 2.7 [34%]
Theoretical systematic uncertainties			
$t\bar{t}$	± 2.6 [10%]	± 0.6 [7%]	± 0.33 [4%]
Single top	± 0.8 [2.7%]	± 1.1 [12%]	± 1.9 [23%]
$W + \text{jets}$	± 0.23 [0.9%]	± 0.07 [0.8%]	± 0.19 [2.3%]
Other backgrounds	± 0.13 [0.5%]	± 0.15 [1.7%]	± 0.08 [1.0%]
MC statistical uncertainties			
MC statistics	± 1.7 [6%]	± 1.1 [13%]	± 1.2 [14%]
Uncertainties in the background normalisation			
Normalisation of dominant backgrounds	± 1.3 [5%]	± 1.6 [18%]	± 1.3 [16%]
Experimental systematic uncertainties			
$E_T^{\text{miss}}/\text{JVT}/\text{pile-up}/\text{trigger}$	± 1.8 [7%]	± 0.4 [4%]	± 0.4 [5%]
Jet energy resolution	± 1.6 [6%]	± 0.5 [6%]	± 0.4 [5%]
b -tagging	± 1.1 [4%]	± 0.29 [3.4%]	± 0.13 [1.5%]
Jet energy scale	± 0.9 [3.2%]	± 0.9 [10%]	± 0.29 [4%]
Lepton uncertainties	± 0.32 [1.2%]	± 0.09 [1.0%]	± 0.19 [2.3%]

Chapter 8

Results

This chapter discusses the results of the different fit configurations and hypothesis tests performed in the analysis. After the background estimation obtained through a background-only fit in the CRs is validated in the VRs, the SRs are unblinded and the observed data is compared to the SM background expectation.

8.1 Background-only fit results

8.1.1 Results in the control regions

As all CRs are mutually exclusive, a background-only fit simultaneously using information from all CRs can be run. Only the terms for the CRs enter the likelihood as channels and any signal contamination present in the CRs is neglected. This allows to fit the dominant backgrounds to data, and thus by construction leads to a good agreement between observed data and the total fitted background estimate in all CRs. The free normalisation parameters for $t\bar{t}$ (μ_T), single top (μ_{ST}) and $W + \text{jets}$ (μ_W) are fitted to be

$$\begin{aligned}\mu_T &= 1.02^{+0.07}_{-0.09}, \\ \mu_{ST} &= 0.6^{+0.5}_{-0.25}, \\ \mu_W &= 1.22^{+0.26}_{-0.24}.\end{aligned}\tag{8.1}$$

While the dominant $t\bar{t}$ background stays roughly at its nominal expectation with respect to MC simulation, $W + \text{jets}$ processes are scaled up. The single top expectation, on the other hand, is scaled down. The high uncertainty on μ_{ST} can be attributed to the relatively low MC statistics as well as the comparably low purity of single top events in STR.

Table 8.1 summarises the fitted background estimate including all uncertainties for all control regions. As discussed in chapter 6, $t\bar{t}$ is the most dominant in all control regions except WR where $W + \text{jets}$ is the largest background, followed by single top and $W + \text{jets}$ processes. Small contributions come from diboson, multiboson as well as other backgrounds like $t\bar{t} + V$, $t\bar{t} + h$ and $V + h$. All processes estimated directly from MC simulation cumulatively account for only 10%, 5.5% and a maximum of 2.6% in the single top, $W + \text{jets}$ and $t\bar{t}$ control regions, respectively.

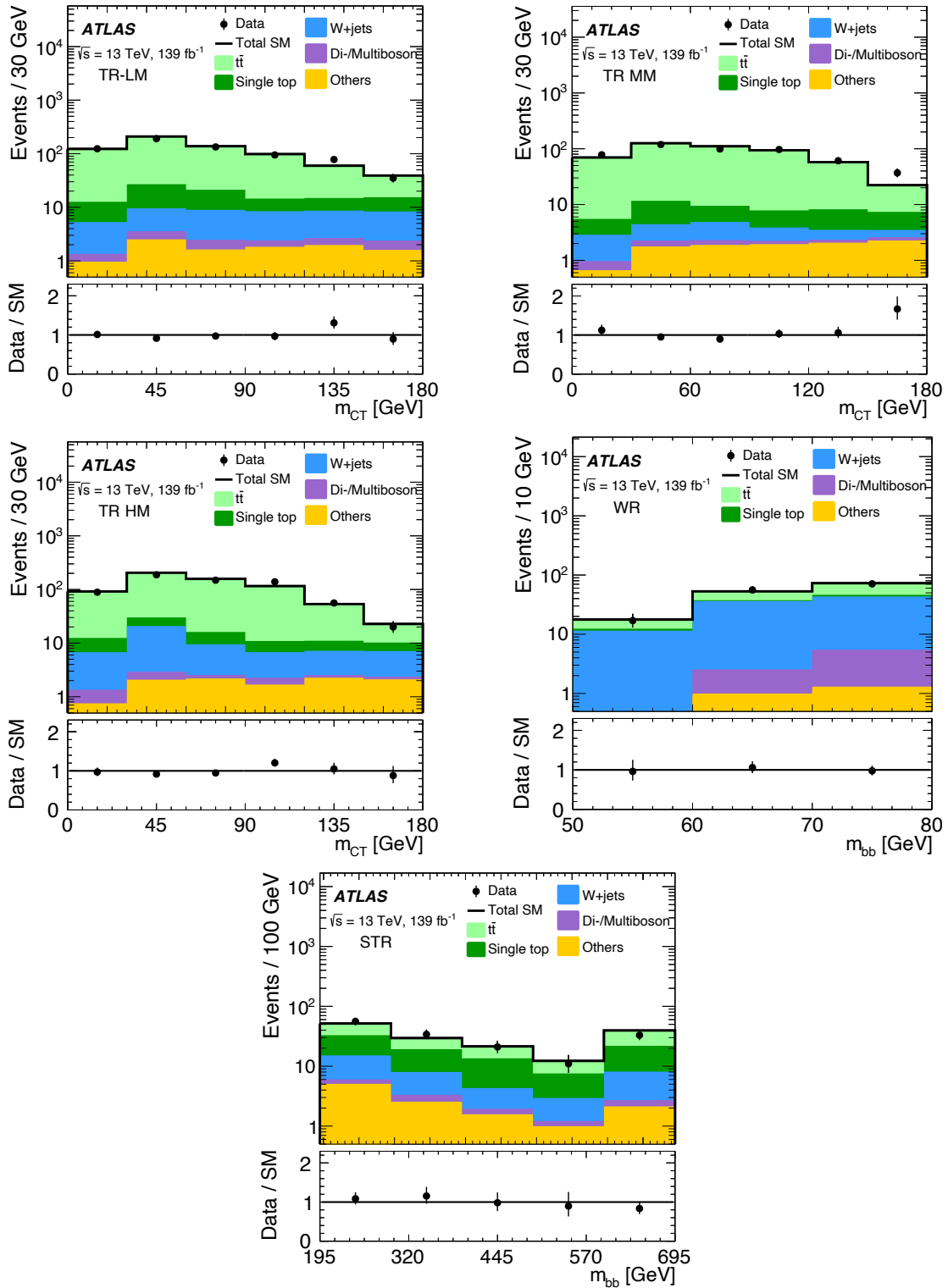


Figure 8.1: Exemplary distribution shown in each control region after the background-only fit. The shaded region includes all systematic uncertainties (including correlations) as well as MC statistical uncertainty. The $t\bar{t}$, single top and $W + \text{jets}$ are normalised simultaneously in all CRs. A good agreement between MC expectation and data is observed in all CRs.

Table 8.1

Region	TRLM	TRMM	TRHM	WR	STCR
Observed events	657	491	641	144	155
Fitted SM events	666 ± 25	480 ± 21	645 ± 26	143 ± 12	154 ± 15
$t\bar{t}$	560 ± 40	430 ± 33	550 ± 40	47 ± 9	59 ± 12
Single top	60 ± 40	27 ± 23	33 ± 27	5 ± 4	57 ± 22
$W + \text{jets}$	34 ± 8	10.5 ± 2.8	44 ± 11	83 ± 16	23 ± 6
Di-/Multiboson	4.3 ± 1.2	2.0 ± 0.5	2.8 ± 0.5	5.7 ± 1.0	2.8 ± 0.9
Other	10.5 ± 1.3	10.6 ± 1.4	11.1 ± 1.4	2.4 ± 0.4	12.3 ± 1.5
MC exp. SM events	720 ± 80	474 ± 33	680 ± 50	130 ± 13	180 ± 50
$t\bar{t}$	570 ± 70	407 ± 30	570 ± 40	46 ± 10	52 ± 10
Single top	102 ± 18	46 ± 13	58 ± 16	9 ± 6	90 ± 40
$W + \text{jets}$	29 ± 4	8.4 ± 1.2	36.1 ± 3.1	67 ± 5	19.0 ± 2.0
Di-/Multiboson	4.1 ± 1.1	2.0 ± 0.5	2.8 ± 0.5	5.6 ± 1.0	2.8 ± 0.9
Other	10.6 ± 1.3	10.6 ± 1.4	11.2 ± 1.4	2.5 ± 0.4	12.4 ± 1.5

Exemplary distributions in the CRs after the background-only fit are shown in fig. 8.1, revealing a good agreement between observed data and the SM background estimate throughout the distributions shown.

8.1.2 Results in the validation regions

In order to validate the extrapolations from the CRs to the SRs, the results of the background-only fit in are extrapolated into the VRs. Table 8.2 details the observed data and background estimation before and after the fit in the different VR bins.

In the on-peak VRs, $t\bar{t}$ is by far the dominant background. Contributions from single top and $W + \text{jets}$ each amount to only 1–5%, depending on validation region bin. Diboson, multiboson and other SM processes result in minor contributions of the level of not more than 3% of the total background estimate. As the total uncertainties on the background estimate in the on-peak regions are dominated by the $t\bar{t}$ uncertainties, the large uncertainties on the $W + \text{jets}$ and single top estimate due to relatively limited MC statistics do not have a significant impact. In the off-peak VRs, $t\bar{t}$ is the dominant process in the low mass regime, while contribution from single top and $W + \text{jets}$ are subdominant. In the medium and high mass regimes, $t\bar{t}$, single top and $W + \text{jets}$ all result in similar contributions. Diboson, multiboson and other SM processes are only minor backgrounds in all off-peak regions, cumulatively amounting to only 10–14% of the total background estimate depending on the mass regime. Exemplary N-1 distributions in the validation regions after the results from the background-only fit are extrapolated are shown in fig. 8.2.

The agreement between data and the background estimate is summarised in ???. The background estimates agree within 1.5σ with the observed data in all validation regions, except for the VR-
onMM where the agreement is within 1.9σ . Thus, the overall agreement in the validation regions

quote exact numbers

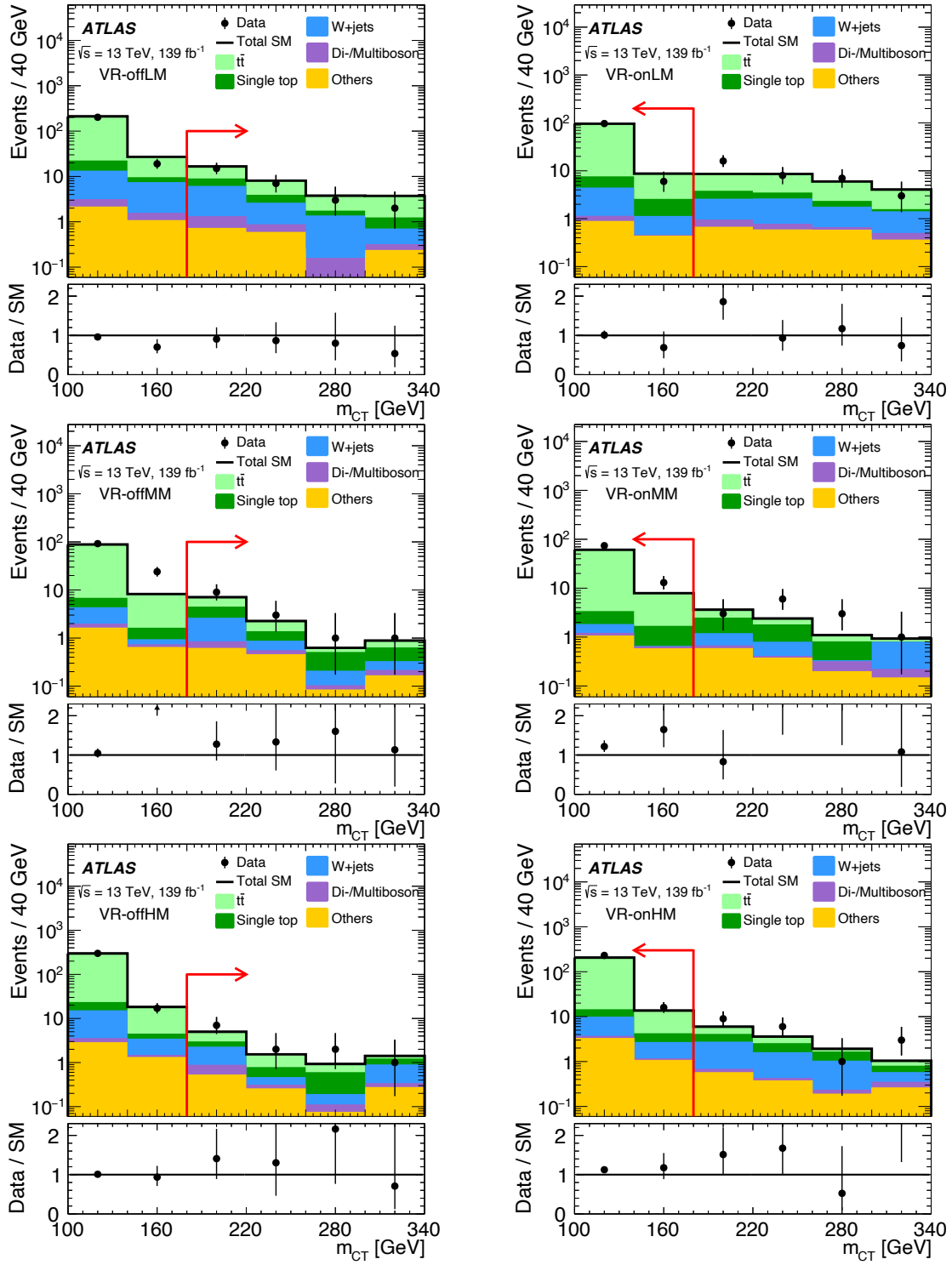


Figure 8.2: Exemplary distributions shown in each validation region after the background-only fit with subsequent extrapolation to the VRs. All selection cuts except for the requirement on m_{CT} (indicated using the red arrow) are applied. The shaded region includes all systematic uncertainties as well as MC statistical uncertainty.

Table 8.2

Region	VR-onLM	VR-onMM	VR-onHM	VR-offLM	VR-offMM	VR-offHM
Observed events	103	87	247	27	14	12
Fitted SM events	100 ± 19	64 ± 9	215 ± 18	34 ± 6	9.5 ± 2.7	7.5 ± 2.6
$t\bar{t}$	90 ± 19	59 ± 9	196 ± 19	18 ± 4	2.4 ± 1.4	1.8 ± 1.8
Single top	5^{+5}_{-5}	$2.6^{+2.9}_{-2.6}$	6 ± 6	5 ± 4	3.0 ± 1.8	1.8 ± 1.5
$W + \text{jets}$	4 ± 4	0.6 ± 0.5	7.9 ± 2.1	8.2 ± 2.6	2.3 ± 0.8	2.2 ± 0.6
Di-/Multiboson	0.24 ± 0.08	0.19 ± 0.08	0.54 ± 0.19	1.07 ± 0.27	0.39 ± 0.11	0.51 ± 0.14
Other	1.34 ± 0.22	1.67 ± 0.28	4.4 ± 2.0	1.6 ± 0.5	1.34 ± 0.25	1.15 ± 0.24
MC exp. SM events	110 ± 40	69 ± 17	218 ± 22	34 ± 7	12.8 ± 3.4	9.7 ± 3.3
$t\bar{t}$	92 ± 35	62 ± 17	196 ± 21	16 ± 5	3.8 ± 2.2	3.1 ± 1.9
Single top	8 ± 5	4.5 ± 3.4	11 ± 6	9 ± 4	5.3 ± 2.2	3.1 ± 2.5
$W + \text{jets}$	2.8 ± 2.3	0.5 ± 0.5	6.5 ± 1.2	6.5 ± 1.6	2.0 ± 0.5	1.80 ± 0.34
Di-/Multiboson	0.24 ± 0.07	0.19 ± 0.08	0.50 ± 0.17	1.07 ± 0.28	0.37 ± 0.10	0.50 ± 0.15
Other	1.35 ± 0.23	1.70 ± 0.28	4.4 ± 0.9	1.6 ± 0.5	1.36 ± 0.25	1.16 ± 0.24

is considered to be acceptable, paving the way for further extrapolation of the background estimate into the SRs.

8.1.3 Results in the signal regions

By extrapolating the results from the background-only fit in the control regions, the background estimate in the signal regions can be obtained. Table 8.3 compares the background estimate with the observed data for all discovery signal regions. In the low mass discovery signal region, $t\bar{t}$ is the dominant background, followed by $W + \text{jets}$ and single top. In the medium mass discovery signal region, all three main backgrounds contribute at roughly equal parts. In the high mass signal region, $W + \text{jets}$ is the largest SM background, followed by single top and $t\bar{t}$. In all discovery signal regions, diboson, multiboson and other SM backgrounds yield only minor contributions. The results in the exclusion signal regions are shown in table 8.4. As for the discovery signal regions, $t\bar{t}$ is the dominant background in the low mass signal region bins, while $W + \text{jets}$ slightly dominates in the high mass signal region bins. The m_{CT} distribution in all three exclusion SRs are shown in ??.

None of the exclusion or discovery signal regions reveal a significant deviation from the SM background estimate in data, meaning that all observations are compatible with the SM. Consequently, the signal regions will be used in the following to derive model-dependent as well as model-independent limits. A slight overfluctuation of data in the discovery SRs (that are not mutually exclusive) is quantified to be within 2σ , resulting in weaker model-independent limits than expected. Some of the exclusion signal region bins also exhibit slight overfluctuations in data, all well within 2σ of the SM background estimate. Thus, the observed model-dependent exclusion limit derived in section 8.2 is slightly weaker than expected. Figure 8.4 summarises for all regions the observed data, SM background estimate as well as the significances of any deviations.

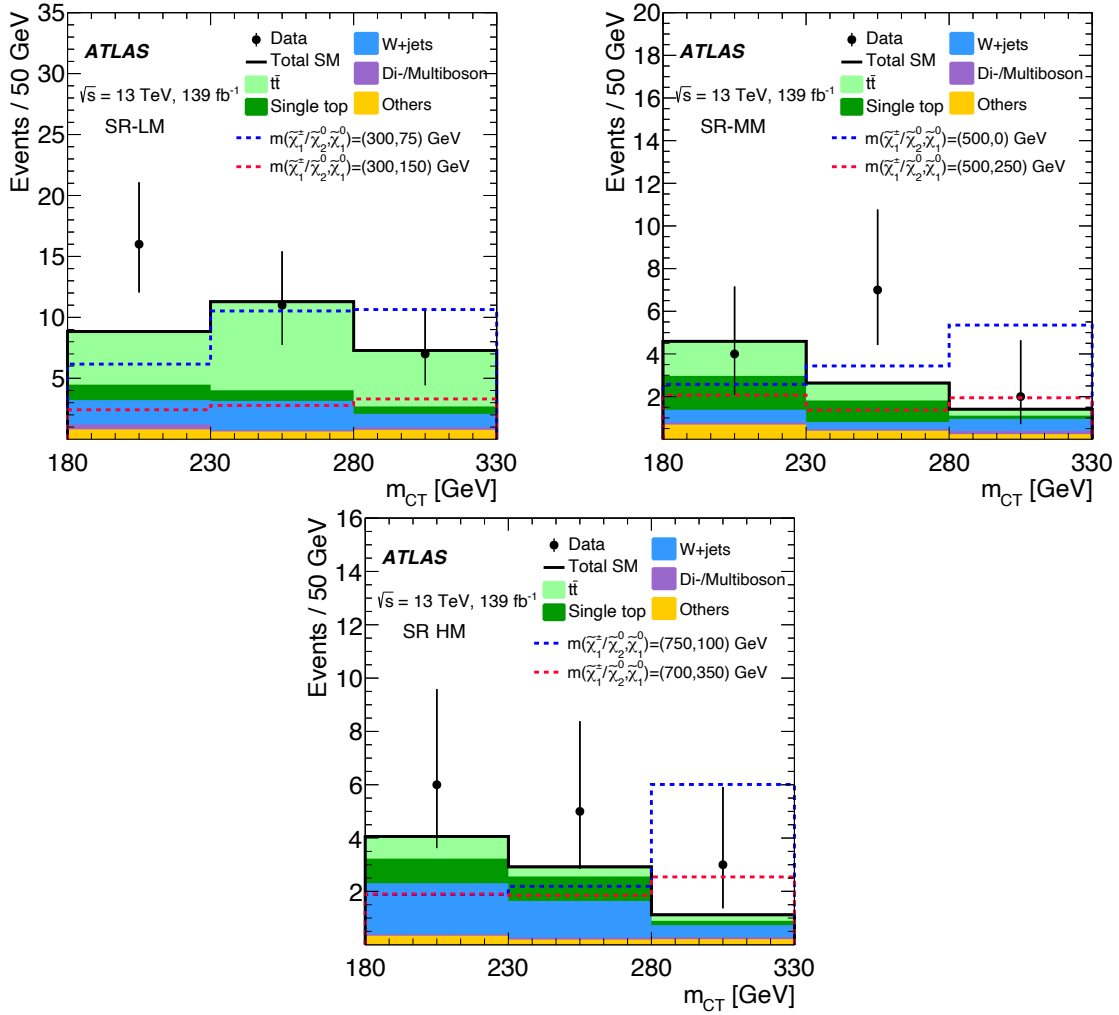


Figure 8.3: Exemplary distribution shown in each exclusion signal region after the background-only fit. The shaded region includes all systematic uncertainties (including correlations) as well as MC statistical uncertainty.

Table 8.3

Region	SR-LM (disc.)	SR-MM (disc.)	SR-HM (disc.)
Observed events	66	32	14
Fitted SM events	47 ± 6	21 ± 5	8.6 ± 2.8
Fitted ttbar events	22 ± 4	5.9 ± 1.9	1.9 ± 0.7
Fitted singletop events	9 ± 6	6 ± 5	$2.0^{+2.4}_{-2.0}$
Fitted wjets events	11.1 ± 2.9	5.6 ± 1.4	3.7 ± 1.0
Fitted diboson events	1.23 ± 0.24	0.56 ± 0.11	0.21 ± 0.06
Fitted Z+jets events	4.8 ± 0.5	2.6 ± 0.4	0.74 ± 0.16
MC exp. SM events	50 ± 7	22 ± 5	8 ± 4
MC exp. ttbar events	21 ± 5	4.9 ± 1.6	1.2 ± 0.6
MC exp. singletop events	14 ± 4	9 ± 5	$2.9^{+3.5}_{-2.9}$
MC exp. wjets events	9.1 ± 1.3	4.5 ± 0.7	3.0 ± 0.6
MC exp. diboson events	1.20 ± 0.23	0.56 ± 0.11	0.21 ± 0.06
MC exp. Z+jets events	4.8 ± 0.5	2.6 ± 0.4	0.74 ± 0.16

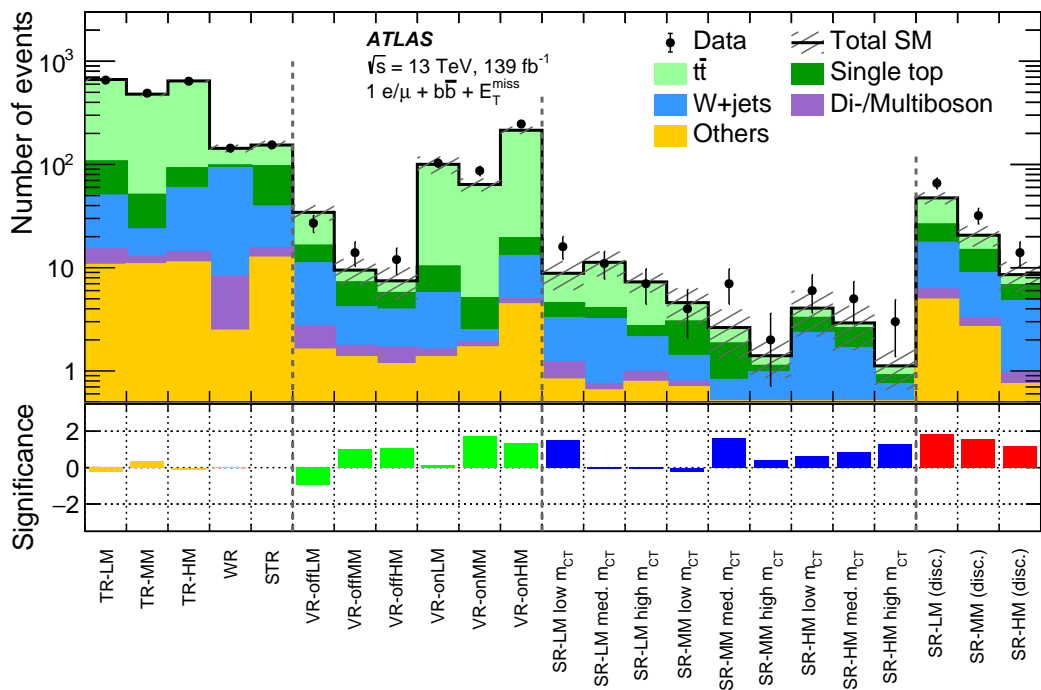
**Figure 8.4**

Table 8.4: Background fit results for the exclusion SR regions. The errors shown are the statistical plus systematic uncertainties. Uncertainties in the fitted yields are symmetric by construction, except where the negative error is truncated at an event yield of zero.

SR-LM	All m_{CT} bins	Low m_{CT}	Medium m_{CT}	High m_{CT}
Observed	34	16	11	7
Expected	27 ± 4	8.8 ± 2.8	11.3 ± 3.1	7.3 ± 1.5
$t\bar{t}$	16.2 ± 3.4	4.4 ± 2.2	7.3 ± 2.5	4.6 ± 1.2
Single top	2.7 ± 1.8	1.3 ± 1.1	$0.9^{+1.0}_{-0.9}$	0.6 ± 0.6
$W+jets$	5.5 ± 2.0	2.0 ± 0.9	2.4 ± 1.3	1.1 ± 0.5
Di-/Multiboson	0.67 ± 0.19	0.39 ± 0.13	$0.09^{+0.11}_{-0.09}$	0.18 ± 0.04
Others	2.23 ± 0.29	0.81 ± 0.25	0.64 ± 0.15	0.77 ± 0.12
SR-MM	All m_{CT} bins	Low m_{CT}	Medium m_{CT}	High m_{CT}
Observed	13	4	7	2
Expected	8.6 ± 2.2	4.6 ± 1.7	2.6 ± 1.3	1.4 ± 0.6
$t\bar{t}$	2.7 ± 1.4	1.6 ± 0.9	0.8 ± 0.7	0.30 ± 0.24
Single top	2.7 ± 1.9	1.6 ± 1.5	$1.0^{+1.1}_{-1.0}$	$0.15^{+0.19}_{-0.15}$
$W+jets$	1.5 ± 0.7	0.6 ± 0.4	$0.3^{+0.4}_{-0.3}$	0.57 ± 0.26
Di-/Multiboson	0.29 ± 0.08	0.09 ± 0.04	0.065 ± 0.028	0.14 ± 0.06
Others	1.33 ± 0.27	0.69 ± 0.20	0.40 ± 0.13	0.24 ± 0.09
SR-HM	All m_{CT} bins	Low m_{CT}	Medium m_{CT}	High m_{CT}
Observed	14	6	5	3
Expected	8.1 ± 2.7	4.1 ± 1.9	2.9 ± 1.3	1.1 ± 0.5
$t\bar{t}$	1.4 ± 0.5	0.8 ± 0.4	0.36 ± 0.25	0.22 ± 0.15
Single top	$2.0^{+2.4}_{-2.0}$	$0.9^{+1.5}_{-0.9}$	0.9 ± 0.9	$0.16^{+0.26}_{-0.16}$
$W+jets$	3.7 ± 1.0	1.9 ± 0.8	1.4 ± 0.8	0.45 ± 0.19
Di-/Multiboson	0.21 ± 0.06	0.057 ± 0.025	0.075 ± 0.027	0.08 ± 0.04
Others	0.74 ± 0.16	0.34 ± 0.09	0.19 ± 0.08	0.21 ± 0.08

8.2 Interpretation

As no significant excess of data is observed in any of the signal regions, model-independent as well as model-dependent limits are computed.

8.2.1 Model-independent upper limits

Model-independent upper limits on the visible cross section of new physics are derived using the discovery SRs. For this, a likelihood containing terms for the CRs and the discovery SRs is used. Since the discovery SRs are not mutually exclusive, only one discovery SR enters the likelihood at a time. This results in three distinct fit configurations in which the signal strength μ is the POI and no signal contamination is assumed in the control regions. The POI is subsequently scanned in distinct steps from 0 to high[†] values, followed by a hypothesis test at each scan step. The upper limit on the number of observed signal events S_{obs}^{95} is then given by the value of μ for which the corresponding CL_s value drops below 0.05. An upper limit on the visible cross section $\langle \epsilon\sigma \rangle_{\text{obs}}^{95}$ is then obtained by dividing S_{obs}^{95} by the integrated luminosity of 139 fb^{-1} . In addition to the upper limits on $\langle \epsilon\sigma \rangle_{\text{obs}}^{95}$ and S_{obs}^{95} , table 8.5 also gives the p -values (and corresponding significances) for rejecting the background-only hypothesis in favour of the signal-plus-background hypothesis. As all significances are below 1.88σ for all SRs, no indication for physics beyond the SM is seen.

8.2.2 Model-dependent exclusion limits

For each signal point in the signal grid considered, a separate *exclusion* fit is run in the CRs and the exclusion SRs. As all exclusion signal region bins are disjoint, a likelihood containing terms for all bins can be constructed, effectively creating a shape-fit in the binned variables m_T and m_{CT} . As opposed to the background-only fit, the exclusion fits allow for signal contribution in all regions considered, and considers the signal strength μ to be a free parameter. For each point in the signal grid, the expected and observed CL_s value is calculated as discussed in section 3.4. Expected (observed) contour lines can then be drawn at expected (observed) $\text{CL}_s = 0.05$. Signal points inside the contour are excluded at 95% CL. Figure 8.5 shows the exclusion contours obtained in the $\tilde{\chi}_1^\pm \tilde{\chi}_2^0$ signal grid considered in the analysis. The dashed line

[†] The signal strength is in principle allowed to exceed unity in order to find an 95% CL upper limit

Table 8.5: Left to right: 95% CL upper limits on the visible cross-section ($\langle \epsilon\sigma \rangle_{\text{obs}}^{95}$) and on the number of signal events (S_{obs}^{95}). The third column (S_{exp}^{95}) shows the expected 95% CL upper limit (and its $\pm 1\sigma$ excursions) on the number of signal events if no BSM signal is present. The last three columns indicate the CL_B value, i.e. the confidence level observed for the background-only hypothesis, the discovery p -value (p_0) and the significance Z [?].

Signal Region	$\langle \epsilon\sigma \rangle_{\text{obs}}^{95} [\text{fb}]$	S_{obs}^{95}	S_{exp}^{95}	CL_B	p_0	Z
SR-LM (disc.)	0.26	36.8	$20.0^{+8.0}_{-5.4}$	0.97	0.03	1.88
SR-MM (disc.)	0.18	24.8	$15.3^{+6.2}_{-4.6}$	0.94	0.06	1.54
SR-HM (disc.)	0.11	14.7	$9.7^{+3.3}_{-2.7}$	0.89	0.10	1.30

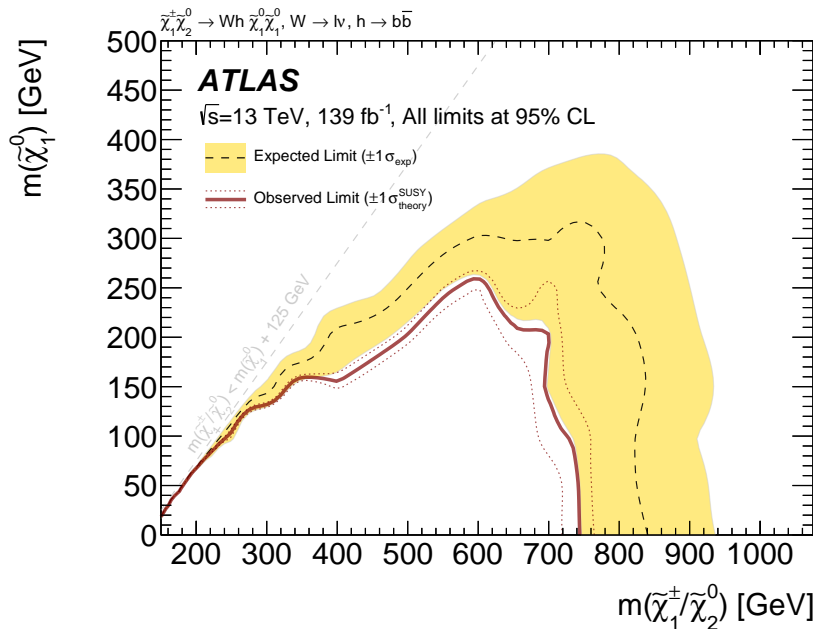


Figure 8.5

corresponds to the expected exclusion contour, obtained using the Asimov dataset. The yellow uncertainty band represents the interval containing 68% of all exclusion contours obtained for observations distributed according to the background-only hypothesis. The solid red line represents the observed exclusion limit obtained using the data recorded by ATLAS. As discussed in section 7.2.2, the dashed red lines are obtained by varying the signal cross sections up and down by 1σ .

Due to the slight overfluctuations of data observed in some of the exclusion signal region bins, the observed limit is slightly weaker than the expected one. The observed exclusion limit extends to about 740 GeV in $m(\tilde{\chi}_1^\pm/\tilde{\chi}_2^0)$ for massless $\tilde{\chi}_1^0$, and up to 600 GeV for $m(\tilde{\chi}_1^0) = 250$ GeV. This extends the previous limit set by ATLAS in this simplified model and decay channel by more than 200 GeV in $m(\tilde{\chi}_1^\pm/\tilde{\chi}_2^0)$ for massless $\tilde{\chi}_1^0$, an improvement made possible not only by the increase in integrated luminosity but also the introduction of a two-dimensional shape fit in the analysis strategy.

8.3 Discussion

At the time of writing, the limits derived in this analysis constitute the most stringent limits on the $\tilde{\chi}_1^\pm \tilde{\chi}_2^0 \rightarrow Wh\tilde{\chi}_1^0\tilde{\chi}_1^0$ simplified model set by ATLAS. Although this is ultimately bound to change with new searches extending these limits even further,

Part III

Reinterpretation

Chapter 9

Simplified likelihoods

Chapter 10

Reinterpretation in the pMSSM

10.1 Sampling

Part IV

Summary and Outlook

Chapter 11

Summary

Here be dragons/

Part V

Appendix

Appendix A

A.1 N-1 plots for cut-scan results

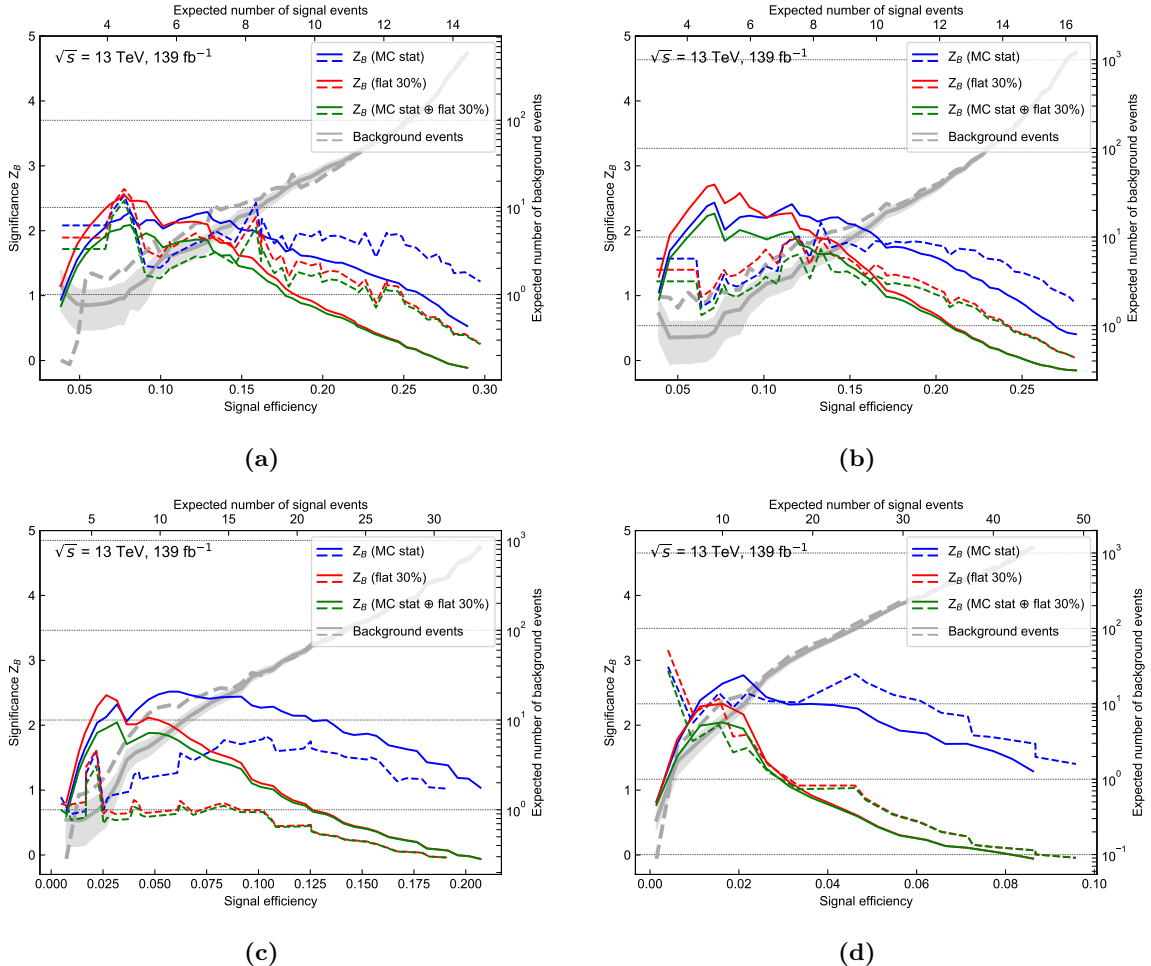


Figure A.1: Results of the N -dimensional cut scan for two exemplary benchmark points. The binomial discovery significance Z_B is plotted against the signal efficiency for varying uncertainty configurations. Additionally, the expected SM background rates are shown, including statistical uncertainty for one of the two statistically independent samples (shaded area). The solid and dashed lines represent the two statistically independent subset that the MC samples are split into.

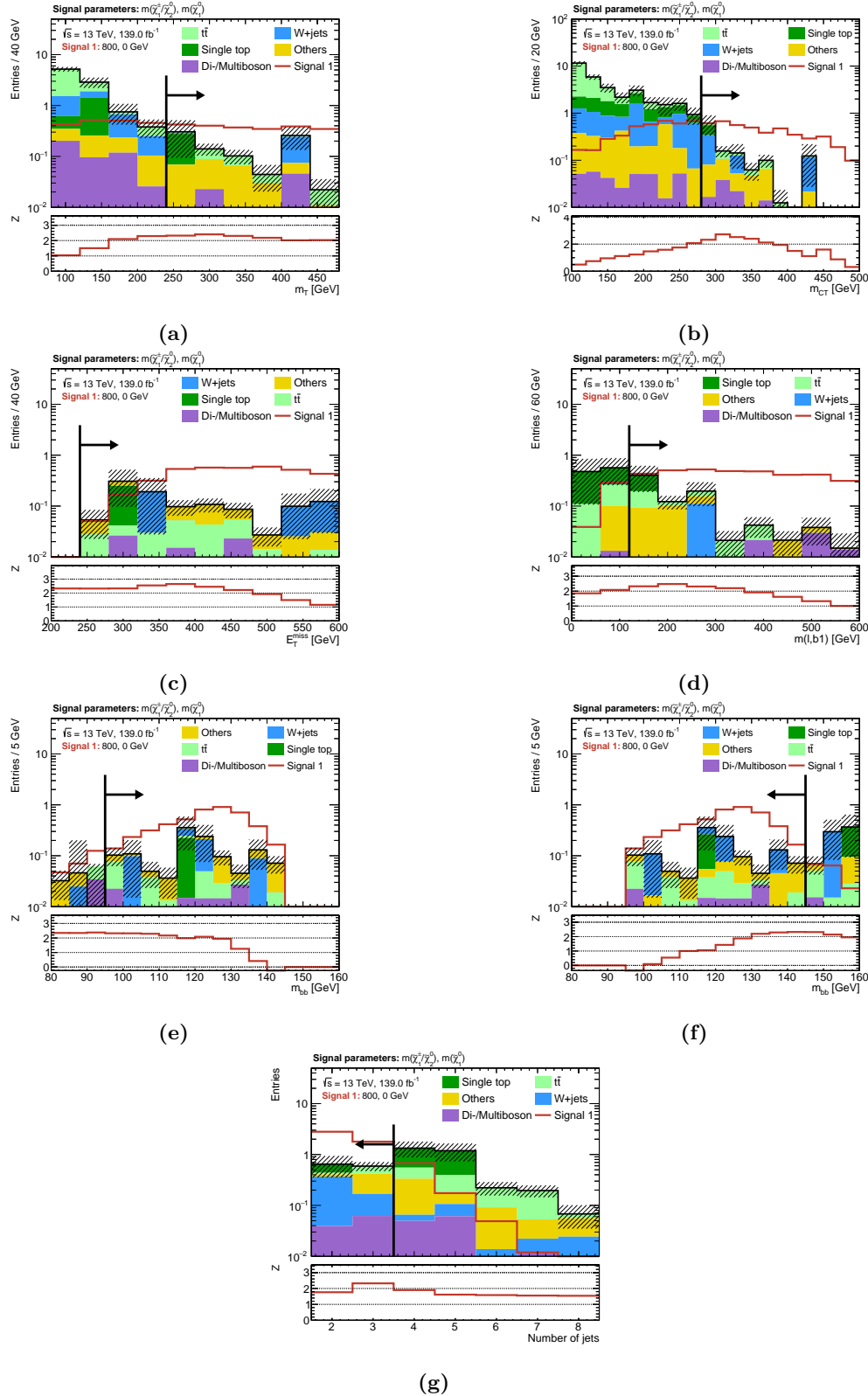


Figure A.2: N-1 plots for the chosen cut combination for the $(m(\tilde{\chi}_1^\pm/\tilde{\chi}_2^0), m(\tilde{\chi}_1^0)) = (800 \text{ GeV}, 0 \text{ GeV})$ signal point. The shaded region includes MC statistical uncertainty as well as 30% systematic uncertainty (added quadratically) on the background. The significance is computed using the binomial discovery significance using the uncertainty on the background.

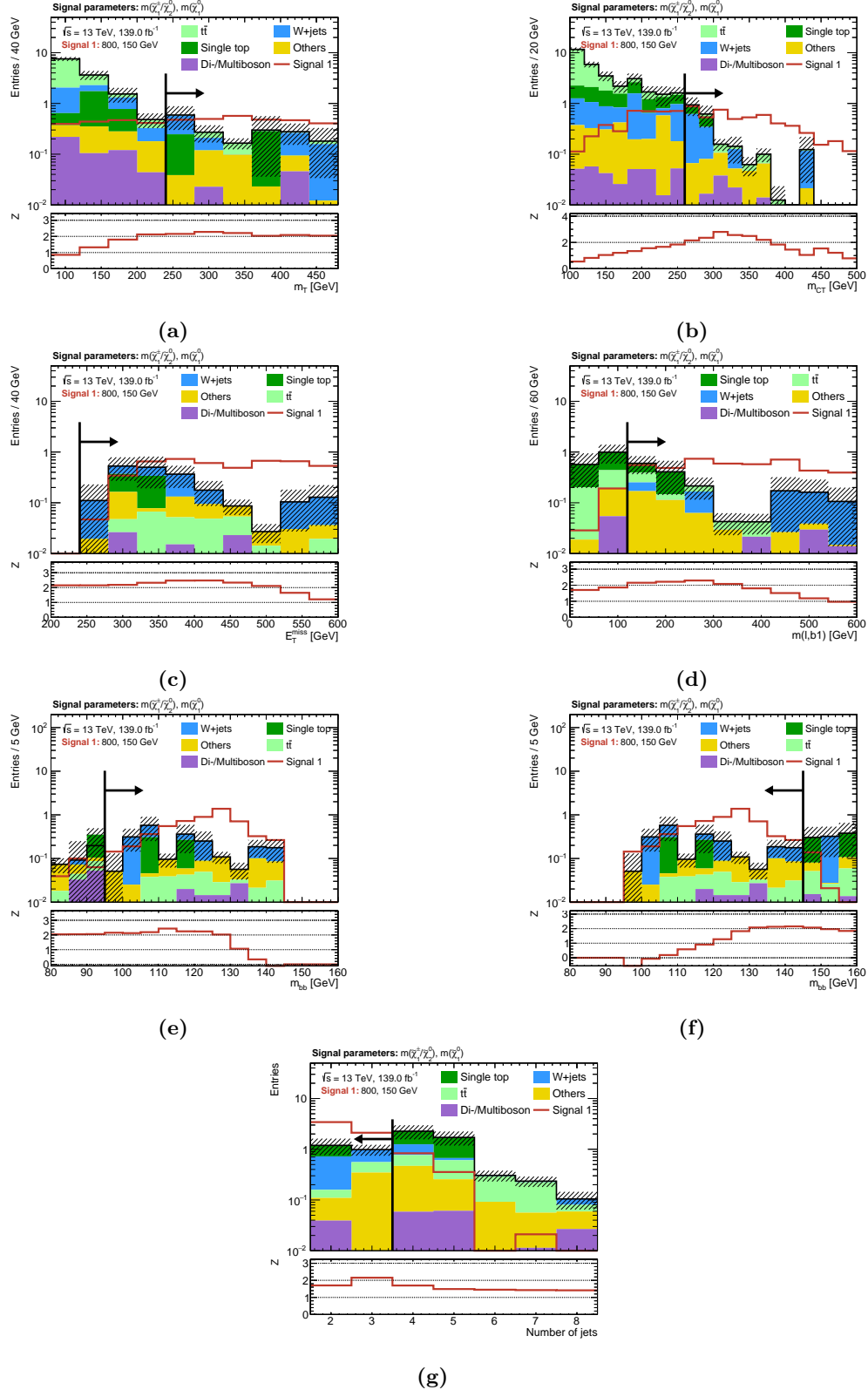


Figure A.3: N-1 plots for the chosen cut combination for the $(m(\tilde{\chi}_1^\pm/\tilde{\chi}_2^0), m(\tilde{\chi}_1^0)) = (800 \text{ GeV}, 150 \text{ GeV})$ signal point. The shaded region includes MC statistical uncertainty as well as 30% systematic uncertainty (added quadratically) on the background. The significance is computed using the binomial discovery significance using the uncertainty on the background.

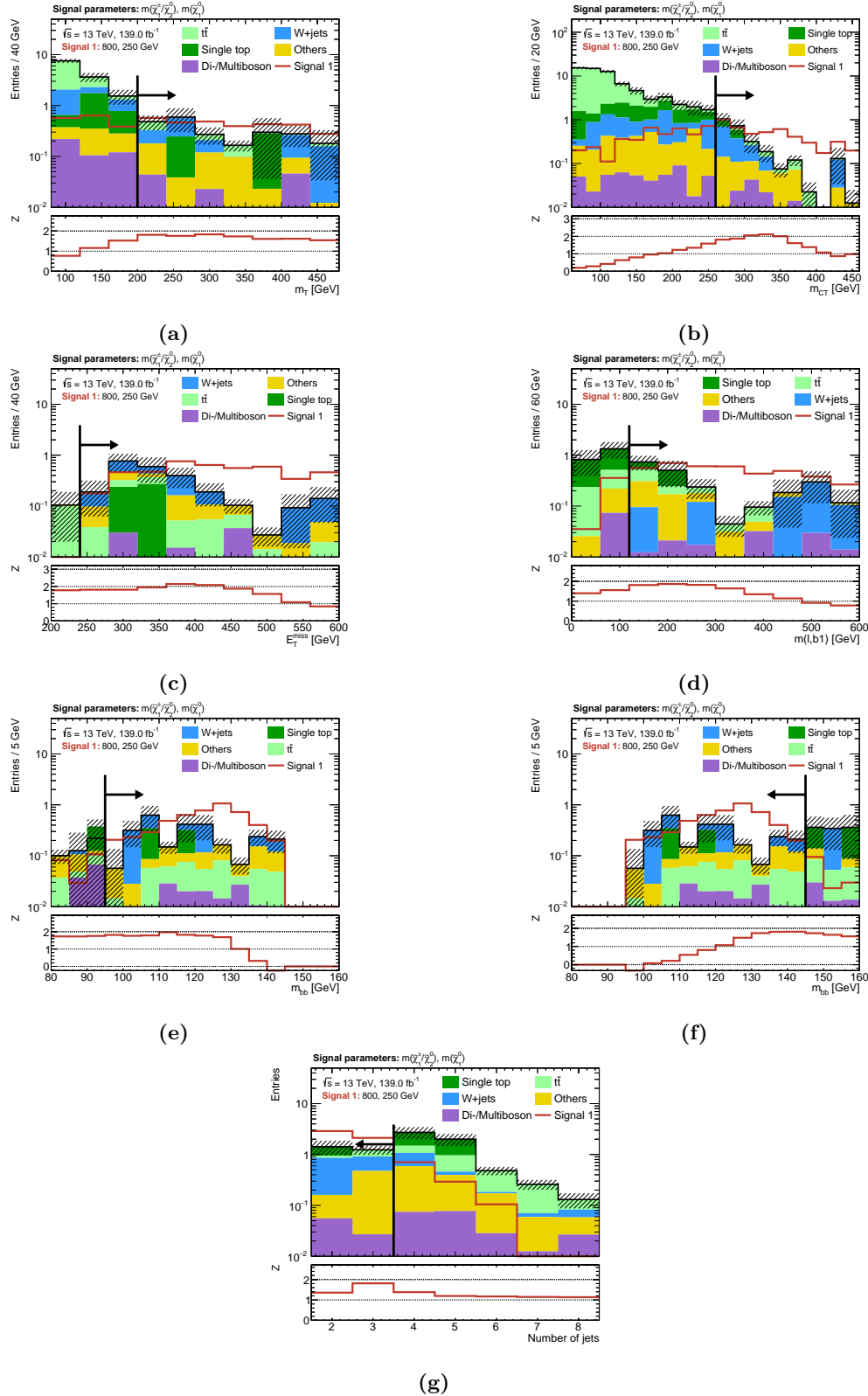


Figure A.4: N-1 plots for the chosen cut combination for the $(m(\tilde{\chi}_1^\pm/\tilde{\chi}_2^0), m(\tilde{\chi}_1^0)) = (800 \text{ GeV}, 250 \text{ GeV})$ signal point. The shaded region includes MC statistical uncertainty as well as 30% systematic uncertainty (added quadratically) on the background. The significance is computed using the binomial discovery significance using the uncertainty on the background.

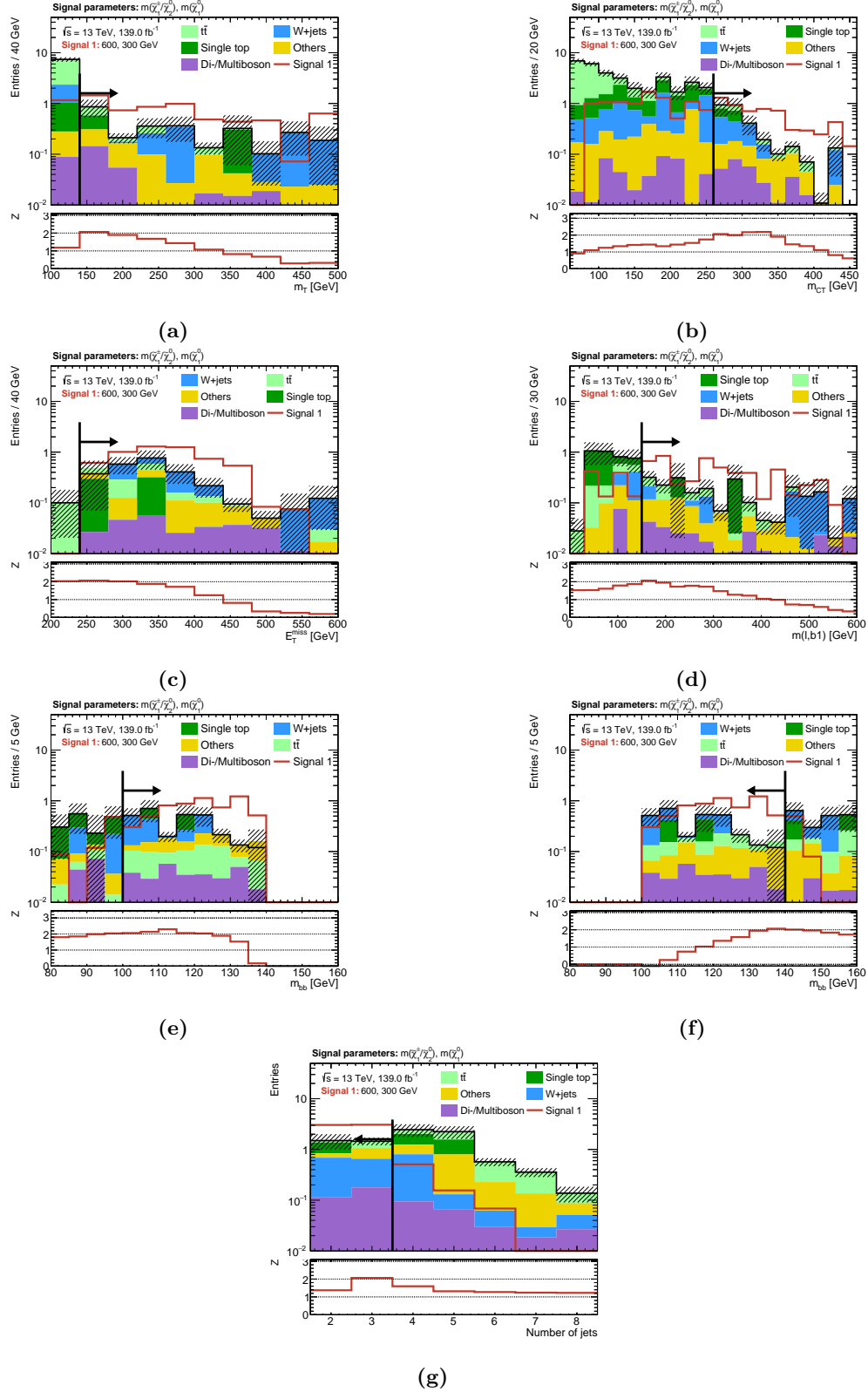


Figure A.5: N-1 plots for the chosen cut combination for the $(m(\tilde{\chi}_1^\pm/\tilde{\chi}_2^0), m(\tilde{\chi}_1^0)) = (600 \text{ GeV}, 300 \text{ GeV})$ signal point. The shaded region includes MC statistical uncertainty as well as 30% systematic uncertainty (added quadratically) on the background. The significance is computed using the binomial discovery significance using the uncertainty on the background.

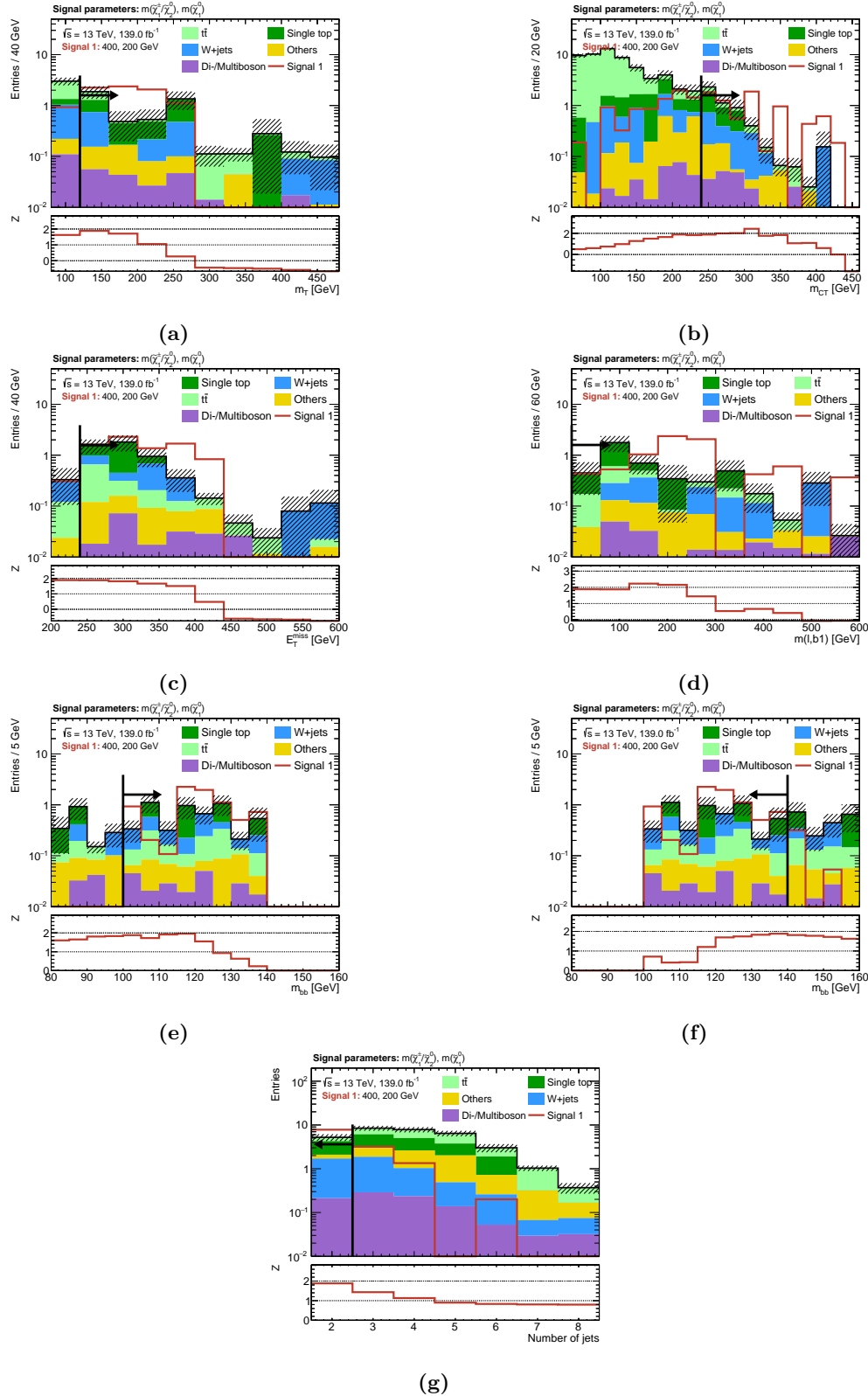


Figure A.6: N-1 plots for the chosen cut combination for the $(m(\tilde{\chi}_1^\pm/\tilde{\chi}_2^0), m(\tilde{\chi}_1^0)) = (400 \text{ GeV}, 200 \text{ GeV})$ signal point. The shaded region includes MC statistical uncertainty as well as 30% systematic uncertainty (added quadratically) on the background. The significance is computed using the binomial discovery significance using the uncertainty on the background.

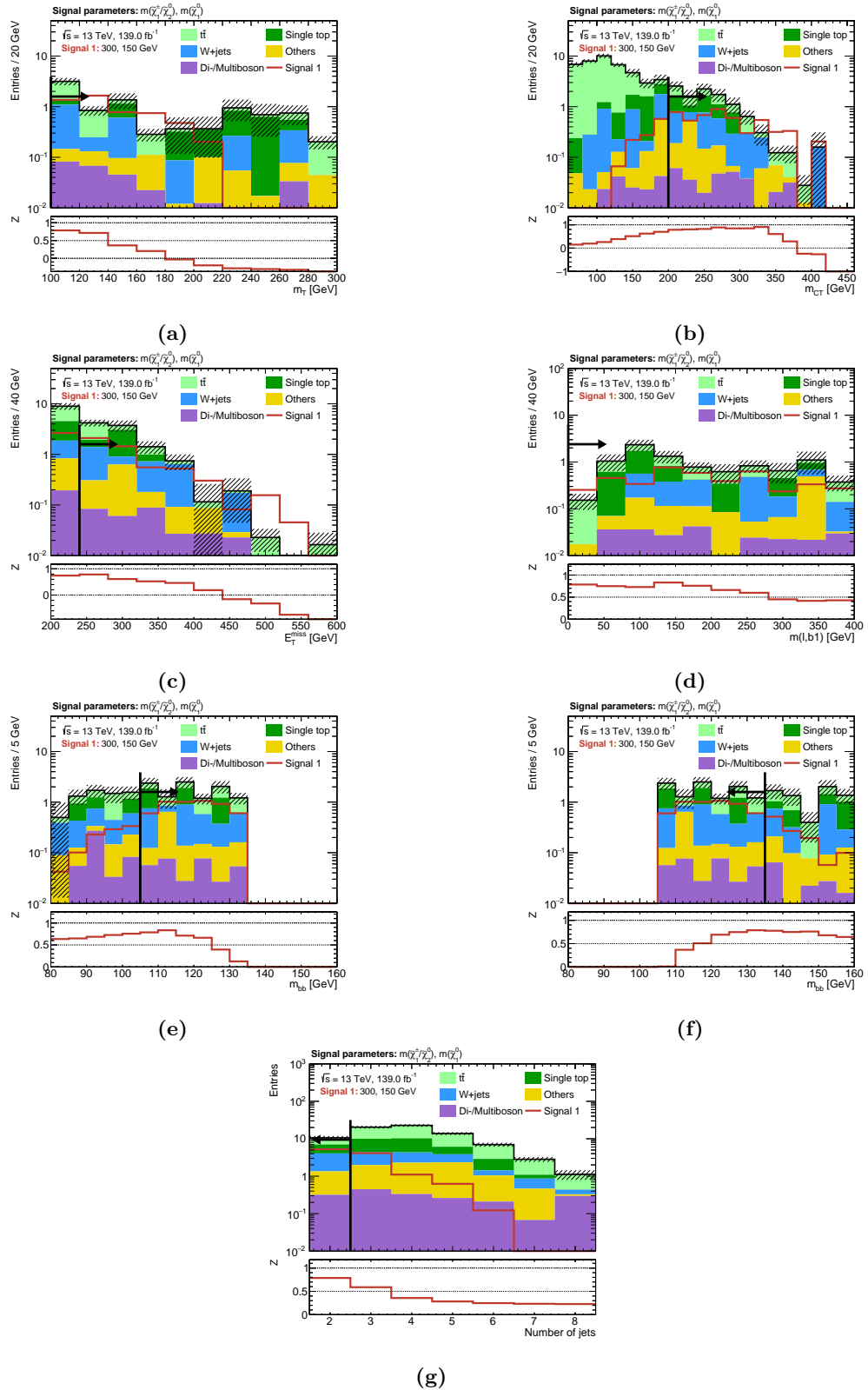


Figure A.7: N-1 plots for the chosen cut combination for the $(m(\tilde{\chi}_1^\pm/\tilde{\chi}_2^0), m(\tilde{\chi}_1^0)) = (300 \text{ GeV}, 150 \text{ GeV})$ signal point. The shaded region includes MC statistical uncertainty as well as 30% systematic uncertainty (added quadratically) on the background. The significance is computed using the binomial discovery significance using the uncertainty on the background.

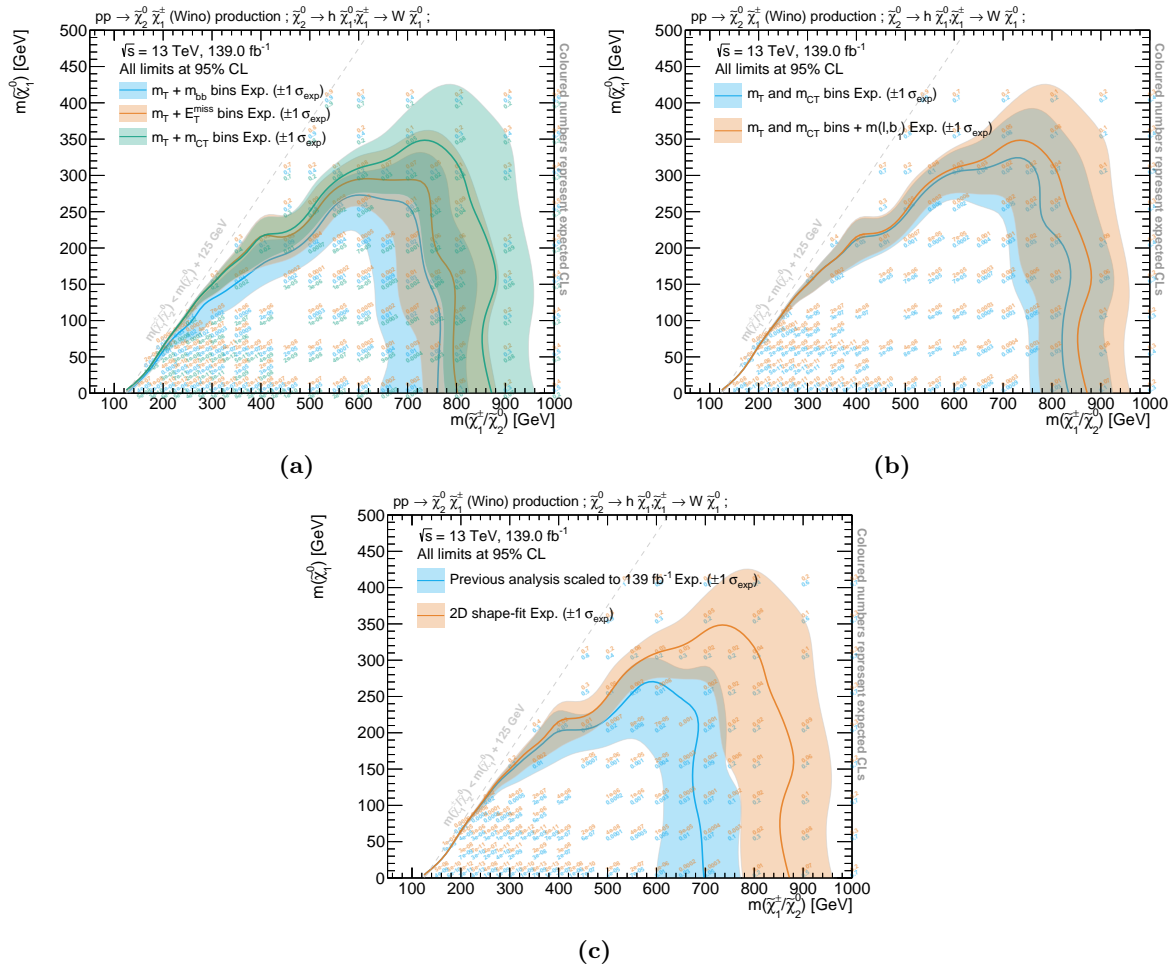


Figure A.8

Appendix B

B.1 Background estimation

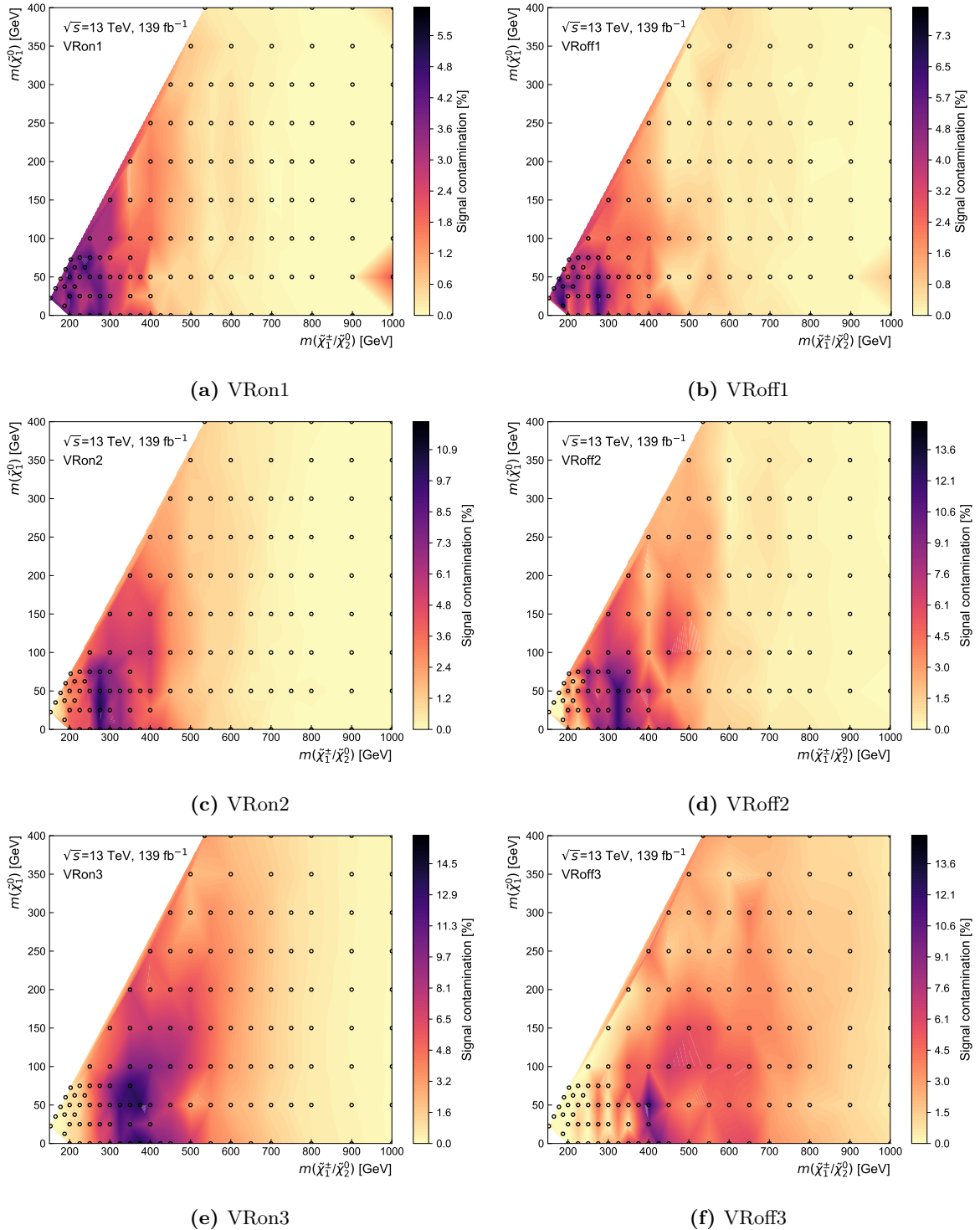


Figure B.1: Signal contamination (shown on the z -axis) for all VRs throughout the signal grid. The space between the signal points (indicated by the black circles) is interpolated using Delaunay triangles.

Abbreviations

- Λ CDM** Lambda Cold Dark Matter. 20
- AFP** ATLAS Forward Proton. 50
- ALFA** Absolute Luminosity for ATLAS. 50
- BDT** boosted decision tree. 75
- BSM** beyond the Standard Model. 20, 21, 41, 42, 49, 57
- CKM** Cabibbo–Kobayashi–Maskawa. 8, 19, 32, 75
- CMB** cosmic microwave background. 20
- CR** control region. 63, 95–98, 100–103, 105–108, 111–113, 119
- CSC** Cathode Strip Chamber. 49, 74
- DAQ** Data Acquisition System. 51
- DM** dark matter. 20, 21, 30, 32, 34
- DR** diagram removal. 107
- DS** diagram subtraction. 107
- EM** Electromagnetic. 47, 48, 72, 74
- EMEC** electromagnetic end-cap calorimeter. 48
- EWK** electroweak. 7
- FCal** forward calorimeter. 48
- FCNC** flavour-changing neutral current. 32
- FSR** Final State Radiation. 52, 53, 77, 107
- ggF** gluon–gluon fusion. 69

- GSC** global sequential calibration. 74
- GUT** grand unified theory. 21, 22
- HEC** hadronic end-cap calorimeter. 48
- HF** heavy flavour. 68–70, 72, 73, 75, 77
- HLT** High Level Trigger. 51, 81
- IBL** insertable B-layer. 46
- ID** inner detector. 45–48, 54, 71–73, 76, 82, 104
- IP** interaction point. 43–45, 50, 73
- ISR** Initial State Radiation. 52, 53, 77, 79, 106
- JER** jet energy resolution. 74, 104, 105, 108
- JES** jet energy scale. 74, 104, 105, 108
- JVT** jet vertex tagger. 75, 76
- L1** Level 1. 51, 81
- LAr** liquid argon. 47, 48
- LEP** Large Electron Positron. 7, 32, 37
- LHC** Large Hadron Collider. 37–39, 41–43, 67, 78
- LO** leading order. 52, 69, 107
- LSP** lightest supersymmetric particle. 35, 78
- MC** Monte Carlo. 51–54, 58, 69–71, 74, 75, 81–89, 91–93, 95–98, 100, 103–108, 111–114, 116, 134–140
- MDT** Monitoring Drift Tube. 49, 50, 74
- ME** Matrix Element. 52, 53, 69, 70, 107, 108
- MLE** Maximum Likelihood Estimator. 59, 60
- MS** muon spectrometer. 49, 50, 54, 73, 74, 82, 104, 108
- MSSM** Minimal Supersymmetric Standard Model. 21, 22, 27–32
- NLL** next-to-leading logarithm. 70
- NLO** next-to-leading order. 53, 70, 107

- PDF** Parton Distribution Function. 44, 53, 69, 70, 107
- pdf** Probability Density Function. 51, 57, 61, 62
- PMNS** Pontecorvo–Maki–Nakagawa–Sakata. 8, 19
- pMSSM** phenomenological Minimal Supersymmetric Standard Model. 32–36
- POI** Parameter of Interest. 58, 61, 119
- PS** Parton Shower. 53, 54, 69, 70, 107, 108
- QCD** quantum chromodynamics. 10, 13–15, 19, 23, 52, 53, 67–69
- QED** quantum electrodynamics. 7, 11–14, 16, 23, 52, 54
- QFT** quantum field theory. 9, 10, 24
- RF** radio frequency. 38, 39
- ROC** receiver operating characteristic. 84
- ROIs** Regions of Interest. 51
- RPC** Resistive Plate Chamber. 49, 50
- SCT** silicon microstrip tracker. 45, 46, 71, 72
- SM** Standard Model of Particle Physics. 7, 8, 10, 16, 19–23, 25, 27, 34, 35, 59, 67–69, 71, 77–80, 84, 87, 90, 95, 98, 107, 111, 113, 115, 119, 134
- SR** signal region. 63, 83, 85, 87–90, 95–99, 102, 105, 108, 111, 113, 115, 119
- SUSY** Supersymmetry. 20, 23, 25, 37, 41, 57, 59, 67, 68, 78, 79, 83, 84, 105, 108
- TGC** Thin Gap Chamber. 49, 50
- TRT** transition radiation tracker. 45, 46, 72
- VBF** vector boson fusion. 69
- vdm** van der Meer. 42, 103
- VEV** vacuum expectation value. 16–18, 30, 33
- VR** validation region. 96, 97, 99, 102, 105, 108, 111, 113, 114, 144
- WIMP** weakly interacting massive particle. 21
- ZDC** Zero-Degree Calorimeter. 50

Bibliography

- [1] I. C. Brock and T. Schorner-Sadenius, *Physics at the terascale*. Wiley, Weinheim, 2011. <https://cds.cern.ch/record/1354959>.
- [2] M. E. Peskin and D. V. Schroeder, *An Introduction to quantum field theory*. Addison-Wesley, Reading, USA, 1995. <http://www.slac.stanford.edu/~mpeskin/QFT.html>.
- [3] S. P. Martin, “A Supersymmetry primer,” [arXiv:hep-ph/9709356 \[hep-ph\]](https://arxiv.org/abs/hep-ph/9709356). [Adv. Ser. Direct. High Energy Phys.18,1(1998)].
- [4] M. Bustamante, L. Cieri, and J. Ellis, “Beyond the Standard Model for Montaneros,” in *5th CERN - Latin American School of High-Energy Physics*. 11, 2009. [arXiv:0911.4409 \[hep-ph\]](https://arxiv.org/abs/0911.4409).
- [5] L. Brown, *The Birth of particle physics*. Cambridge University Press, Cambridge Cambridgeshire New York, 1986.
- [6] P. J. Mohr, D. B. Newell, and B. N. Taylor, “CODATA Recommended Values of the Fundamental Physical Constants: 2014,” *Rev. Mod. Phys.* **88** no. 3, (2016) 035009, [arXiv:1507.07956 \[physics.atom-ph\]](https://arxiv.org/abs/1507.07956).
- [7] P. D. Group, “Review of Particle Physics,” *Progress of Theoretical and Experimental Physics* **2020** no. 8, (08, 2020), <https://academic.oup.com/ptep/article-pdf/2020/8/083C01/34673722/ptaa104.pdf>. <https://doi.org/10.1093/ptep/ptaa104>. 083C01.
- [8] **Super-Kamiokande** Collaboration, Y. Fukuda *et al.*, “Evidence for oscillation of atmospheric neutrinos,” *Phys. Rev. Lett.* **81** (1998) 1562–1567, [arXiv:hep-ex/9807003 \[hep-ex\]](https://arxiv.org/abs/hep-ex/9807003).
- [9] Z. Maki, M. Nakagawa, and S. Sakata, “Remarks on the unified model of elementary particles,” *Prog. Theor. Phys.* **28** (1962) 870–880. [,34(1962)].
- [10] N. Cabibbo, “Unitary symmetry and leptonic decays,” *Phys. Rev. Lett.* **10** (Jun, 1963) 531–533. <https://link.aps.org/doi/10.1103/PhysRevLett.10.531>.
- [11] M. Kobayashi and T. Maskawa, “CP Violation in the Renormalizable Theory of Weak Interaction,” *Prog. Theor. Phys.* **49** (1973) 652–657.
- [12] E. Noether and M. A. Tavel, “Invariant variation problems,” [arXiv:physics/0503066](https://arxiv.org/abs/physics/0503066).
- [13] J. C. Ward, “An identity in quantum electrodynamics,” *Phys. Rev.* **78** (Apr, 1950) 182–182. <https://link.aps.org/doi/10.1103/PhysRev.78.182>.

- [14] Y. Takahashi, “On the generalized ward identity,” *Il Nuovo Cimento (1955-1965)* **6** no. 2, (Aug, 1957) 371–375. <https://doi.org/10.1007/BF02832514>.
- [15] G. ’tHooft, “Renormalization of massless yang-mills fields,” *Nuclear Physics B* **33** no. 1, (1971) 173 – 199. <http://www.sciencedirect.com/science/article/pii/0550321371903956>.
- [16] J. Taylor, “Ward identities and charge renormalization of the yang-mills field,” *Nuclear Physics B* **33** no. 2, (1971) 436 – 444. <http://www.sciencedirect.com/science/article/pii/0550321371902975>.
- [17] A. A. Slavnov, “Ward identities in gauge theories,” *Theoretical and Mathematical Physics* **10** no. 2, (Feb, 1972) 99–104. <https://doi.org/10.1007/BF01090719>.
- [18] C. N. Yang and R. L. Mills, “Conservation of isotopic spin and isotopic gauge invariance,” *Phys. Rev.* **96** (Oct, 1954) 191–195. <https://link.aps.org/doi/10.1103/PhysRev.96.191>.
- [19] K. G. Wilson, “Confinement of quarks,” *Phys. Rev. D* **10** (Oct, 1974) 2445–2459. <https://link.aps.org/doi/10.1103/PhysRevD.10.2445>.
- [20] T. DeGrand and C. DeTar, *Lattice Methods for Quantum Chromodynamics*. World Scientific, Singapore, 2006. <https://cds.cern.ch/record/1055545>.
- [21] S. L. Glashow, “Partial-symmetries of weak interactions,” *Nuclear Physics* **22** no. 4, (1961) 579 – 588. <http://www.sciencedirect.com/science/article/pii/0029558261904692>.
- [22] S. Weinberg, “A model of leptons,” *Phys. Rev. Lett.* **19** (Nov, 1967) 1264–1266. <https://link.aps.org/doi/10.1103/PhysRevLett.19.1264>.
- [23] A. Salam and J. C. Ward, “Weak and electromagnetic interactions,” *Il Nuovo Cimento (1955-1965)* **11** no. 4, (Feb, 1959) 568–577. <https://doi.org/10.1007/BF02726525>.
- [24] C. S. Wu, E. Ambler, R. W. Hayward, D. D. Hoppes, and R. P. Hudson, “Experimental test of parity conservation in beta decay,” *Phys. Rev.* **105** (Feb, 1957) 1413–1415. <https://link.aps.org/doi/10.1103/PhysRev.105.1413>.
- [25] M. Gell-Mann, “The interpretation of the new particles as displaced charge multiplets,” *Il Nuovo Cimento (1955-1965)* **4** no. 2, (Apr, 1956) 848–866. <https://doi.org/10.1007/BF02748000>.
- [26] K. Nishijima, “Charge Independence Theory of V Particles*,” *Progress of Theoretical Physics* **13** no. 3, (03, 1955) 285–304, <https://academic.oup.com/ptp/article-pdf/13/3/285/5425869/13-3-285.pdf>. <https://doi.org/10.1143/PTP.13.285>.
- [27] T. Nakano and K. Nishijima, “Charge Independence for V-particles*,” *Progress of Theoretical Physics* **10** no. 5, (11, 1953) 581–582, <https://academic.oup.com/ptp/article-pdf/10/5/581/5364926/10-5-581.pdf>. <https://doi.org/10.1143/PTP.10.581>.
- [28] F. Englert and R. Brout, “Broken symmetry and the mass of gauge vector mesons,” *Phys. Rev. Lett.* **13** (Aug, 1964) 321–323. <https://link.aps.org/doi/10.1103/PhysRevLett.13.321>.
- [29] P. W. Higgs, “Broken symmetries and the masses of gauge bosons,” *Phys. Rev. Lett.* **13** (Oct, 1964) 508–509. <https://link.aps.org/doi/10.1103/PhysRevLett.13.508>.

- [30] P. W. Higgs, “Spontaneous symmetry breakdown without massless bosons,” *Phys. Rev.* **145** (May, 1966) 1156–1163. <https://link.aps.org/doi/10.1103/PhysRev.145.1156>.
- [31] Y. Nambu, “Quasiparticles and Gauge Invariance in the Theory of Superconductivity,” *Phys. Rev.* **117** (1960) 648–663. [[132\(1960\)](#)].
- [32] J. Goldstone, “Field Theories with Superconductor Solutions,” *Nuovo Cim.* **19** (1961) 154–164.
- [33] V. Brdar, A. J. Helmboldt, S. Iwamoto, and K. Schmitz, “Type-I Seesaw as the Common Origin of Neutrino Mass, Baryon Asymmetry, and the Electroweak Scale,” *Phys. Rev. D* **100** (2019) 075029, [arXiv:1905.12634 \[hep-ph\]](https://arxiv.org/abs/1905.12634).
- [34] G. ’t Hooft and M. Veltman, “Regularization and renormalization of gauge fields,” *Nuclear Physics B* **44** no. 1, (1972) 189 – 213. <http://www.sciencedirect.com/science/article/pii/0550321372902799>.
- [35] F. Zwicky, “Die Rotverschiebung von extragalaktischen Nebeln,” *Helv. Phys. Acta* **6** (1933) 110–127. <https://cds.cern.ch/record/437297>.
- [36] V. C. Rubin and W. K. Ford, Jr., “Rotation of the Andromeda Nebula from a Spectroscopic Survey of Emission Regions,” *Astrophys. J.* **159** (1970) 379–403.
- [37] G. Bertone, D. Hooper, and J. Silk, “Particle dark matter: Evidence, candidates and constraints,” *Phys. Rept.* **405** (2005) 279–390, [arXiv:hep-ph/0404175](https://arxiv.org/abs/hep-ph/0404175).
- [38] D. Clowe, M. Bradac, A. H. Gonzalez, M. Markevitch, S. W. Randall, C. Jones, and D. Zaritsky, “A direct empirical proof of the existence of dark matter,” *Astrophys. J.* **648** (2006) L109–L113, [arXiv:astro-ph/0608407 \[astro-ph\]](https://arxiv.org/abs/astro-ph/0608407).
- [39] A. Taylor, S. Dye, T. J. Broadhurst, N. Benitez, and E. van Kampen, “Gravitational lens magnification and the mass of abell 1689,” *Astrophys. J.* **501** (1998) 539, [arXiv:astro-ph/9801158](https://arxiv.org/abs/astro-ph/9801158).
- [40] C. Bennett *et al.*, “Four year COBE DMR cosmic microwave background observations: Maps and basic results,” *Astrophys. J. Lett.* **464** (1996) L1–L4, [arXiv:astro-ph/9601067](https://arxiv.org/abs/astro-ph/9601067).
- [41] G. F. Smoot *et al.*, “Structure in the COBE Differential Microwave Radiometer First-Year Maps,” *ApJS* **396** (September, 1992) L1.
- [42] **WMAP** Collaboration, “Nine-year Wilkinson Microwave Anisotropy Probe (WMAP) Observations: Final Maps and Results,” *ApJS* **208** no. 2, (October, 2013) 20, [arXiv:1212.5225 \[astro-ph.CO\]](https://arxiv.org/abs/1212.5225).
- [43] **WMAP** Collaboration, “Nine-year Wilkinson Microwave Anisotropy Probe (WMAP) Observations: Cosmological Parameter Results,” *ApJS* **208** no. 2, (October, 2013) 19, [arXiv:1212.5226 \[astro-ph.CO\]](https://arxiv.org/abs/1212.5226).
- [44] **Planck** Collaboration, “Planck 2018 results. I. Overview and the cosmological legacy of Planck,” *Astron. Astrophys.* **641** (2020) A1, [arXiv:1807.06205 \[astro-ph.CO\]](https://arxiv.org/abs/1807.06205).
- [45] A. Liddle, *An introduction to modern cosmology; 3rd ed.* Wiley, Chichester, Mar, 2015. <https://cds.cern.ch/record/1976476>.
- [46] **Planck** Collaboration, “Planck 2018 results. VI. Cosmological parameters,” *Astron. Astrophys.* **641** (2020) A6, [arXiv:1807.06209 \[astro-ph.CO\]](https://arxiv.org/abs/1807.06209).

- [47] H. Georgi and S. L. Glashow, “Unity of all elementary-particle forces,” *Phys. Rev. Lett.* **32** (Feb, 1974) 438–441. <https://link.aps.org/doi/10.1103/PhysRevLett.32.438>.
- [48] I. Aitchison, *Supersymmetry in Particle Physics. An Elementary Introduction*. Cambridge University Press, Cambridge, 2007.
- [49] **Muon g-2** Collaboration, G. Bennett *et al.*, “Final Report of the Muon E821 Anomalous Magnetic Moment Measurement at BNL,” *Phys. Rev. D* **73** (2006) 072003, [arXiv:hep-ex/0602035](https://arxiv.org/abs/hep-ex/0602035).
- [50] H. Baer and X. Tata, *Weak Scale Supersymmetry: From Superfields to Scattering Events*. Cambridge University Press, 2006.
- [51] A. Czarnecki and W. J. Marciano, “The Muon anomalous magnetic moment: A Harbinger for ‘new physics’,” *Phys. Rev. D* **64** (2001) 013014, [arXiv:hep-ph/0102122](https://arxiv.org/abs/hep-ph/0102122).
- [52] J. L. Feng and K. T. Matchev, “Supersymmetry and the anomalous magnetic moment of the muon,” *Phys. Rev. Lett.* **86** (2001) 3480–3483, [arXiv:hep-ph/0102146](https://arxiv.org/abs/hep-ph/0102146).
- [53] S. Coleman and J. Mandula, “All possible symmetries of the s matrix,” *Phys. Rev.* **159** (Jul, 1967) 1251–1256. <https://link.aps.org/doi/10.1103/PhysRev.159.1251>.
- [54] R. Haag, J. T. Lopuszanski, and M. Sohnius, “All Possible Generators of Supersymmetries of the s Matrix,” *Nucl. Phys.* **B88** (1975) 257. [,257(1974)].
- [55] J. Wess and B. Zumino, “Supergauge transformations in four dimensions,” *Nuclear Physics B* **70** no. 1, (1974) 39 – 50.
<http://www.sciencedirect.com/science/article/pii/0550321374903551>.
- [56] H. Georgi and S. L. Glashow, “Gauge theories without anomalies,” *Phys. Rev. D* **6** (Jul, 1972) 429–431. <https://link.aps.org/doi/10.1103/PhysRevD.6.429>.
- [57] S. Dimopoulos and D. W. Sutter, “The Supersymmetric flavor problem,” *Nucl. Phys. B* **452** (1995) 496–512, [arXiv:hep-ph/9504415](https://arxiv.org/abs/hep-ph/9504415).
- [58] **MEG** Collaboration, T. Mori, “Final Results of the MEG Experiment,” *Nuovo Cim. C* **39** no. 4, (2017) 325, [arXiv:1606.08168 \[hep-ex\]](https://arxiv.org/abs/1606.08168).
- [59] H. P. Nilles, “Supersymmetry, Supergravity and Particle Physics,” *Phys. Rept.* **110** (1984) 1–162.
- [60] A. Lahanas and D. Nanopoulos, “The road to no-scale supergravity,” *Physics Reports* **145** no. 1, (1987) 1 – 139.
<http://www.sciencedirect.com/science/article/pii/0370157387900342>.
- [61] J. L. Feng, A. Rajaraman, and F. Takayama, “Superweakly interacting massive particles,” *Phys. Rev. Lett.* **91** (2003) 011302, [arXiv:hep-ph/0302215](https://arxiv.org/abs/hep-ph/0302215).
- [62] **Super-Kamiokande** Collaboration, K. Abe *et al.*, “Search for proton decay via $p \rightarrow e^+ \pi^0$ and $p \rightarrow \mu^+ \pi^0$ in 0.31 megaton-years exposure of the Super-Kamiokande water Cherenkov detector,” *Phys. Rev. D* **95** no. 1, (2017) 012004, [arXiv:1610.03597 \[hep-ex\]](https://arxiv.org/abs/1610.03597).
- [63] J. R. Ellis, “Beyond the standard model for hill walkers,” in *1998 European School of High-Energy Physics*, pp. 133–196. 8, 1998. [arXiv:hep-ph/9812235](https://arxiv.org/abs/hep-ph/9812235).

- [64] J. R. Ellis, J. Hagelin, D. V. Nanopoulos, K. A. Olive, and M. Srednicki, “Supersymmetric Relics from the Big Bang,” *Nucl. Phys. B* **238** (1984) 453–476.
- [65] D. O. Caldwell, R. M. Eisberg, D. M. Grumm, M. S. Witherell, B. Sadoulet, F. S. Goulding, and A. R. Smith, “Laboratory limits on galactic cold dark matter,” *Phys. Rev. Lett.* **61** (Aug, 1988) 510–513. <https://link.aps.org/doi/10.1103/PhysRevLett.61.510>.
- [66] M. Mori, M. M. Nojiri, K. S. Hirata, K. Kihara, Y. Oyama, A. Suzuki, K. Takahashi, M. Yamada, H. Takei, M. Koga, K. Miyano, H. Miyata, Y. Fukuda, T. Hayakawa, K. Inoue, T. Ishida, T. Kajita, Y. Koshio, M. Nakahata, K. Nakamura, A. Sakai, N. Sato, M. Shiozawa, J. Suzuki, Y. Suzuki, Y. Totsuka, M. Koshiba, K. Nishijima, T. Kajimura, T. Suda, A. T. Suzuki, T. Hara, Y. Nagashima, M. Takita, H. Yokoyama, A. Yoshimoto, K. Kaneyuki, Y. Takeuchi, T. Tanimori, S. Tasaka, and K. Nishikawa, “Search for neutralino dark matter heavier than the w boson at kamiokande,” *Phys. Rev. D* **48** (Dec, 1993) 5505–5518. <https://link.aps.org/doi/10.1103/PhysRevD.48.5505>.
- [67] **CDMS** Collaboration, D. S. Akerib *et al.*, “Exclusion limits on the WIMP-nucleon cross section from the first run of the Cryogenic Dark Matter Search in the Soudan Underground Laboratory,” *Phys. Rev. D* **72** (2005) 052009, [arXiv:astro-ph/0507190](https://arxiv.org/abs/astro-ph/0507190).
- [68] A. Djouadi, J.-L. Kneur, and G. Moultaka, “SuSpect: A Fortran code for the supersymmetric and Higgs particle spectrum in the MSSM,” *Comput. Phys. Commun.* **176** (2007) 426–455, [arXiv:hep-ph/0211331](https://arxiv.org/abs/hep-ph/0211331).
- [69] C. F. Berger, J. S. Gainer, J. L. Hewett, and T. G. Rizzo, “Supersymmetry without prejudice,” *Journal of High Energy Physics* **2009** no. 02, (Feb, 2009) 023–023. <http://dx.doi.org/10.1088/1126-6708/2009/02/023>.
- [70] J. Alwall, P. Schuster, and N. Toro, “Simplified Models for a First Characterization of New Physics at the LHC,” *Phys. Rev. D* **79** (2009) 075020, [arXiv:0810.3921 \[hep-ph\]](https://arxiv.org/abs/0810.3921).
- [71] **LHC New Physics Working Group** Collaboration, D. Alves, “Simplified Models for LHC New Physics Searches,” *J. Phys. G* **39** (2012) 105005, [arXiv:1105.2838 \[hep-ph\]](https://arxiv.org/abs/1105.2838).
- [72] D. S. Alves, E. Izaguirre, and J. G. Wacker, “Where the Sidewalk Ends: Jets and Missing Energy Search Strategies for the 7 TeV LHC,” *JHEP* **10** (2011) 012, [arXiv:1102.5338 \[hep-ph\]](https://arxiv.org/abs/1102.5338).
- [73] F. Ambrogi, S. Kraml, S. Kulkarni, U. Laa, A. Lessa, and W. Waltenberger, “On the coverage of the pMSSM by simplified model results,” *Eur. Phys. J. C* **78** no. 3, (2018) 215, [arXiv:1707.09036 \[hep-ph\]](https://arxiv.org/abs/1707.09036).
- [74] O. Buchmueller and J. Marrouche, “Universal mass limits on gluino and third-generation squarks in the context of Natural-like SUSY spectra,” *Int. J. Mod. Phys. A* **29** no. 06, (2014) 1450032, [arXiv:1304.2185 \[hep-ph\]](https://arxiv.org/abs/1304.2185).
- [75] **ATLAS** Collaboration, M. Aaboud *et al.*, “Dark matter interpretations of ATLAS searches for the electroweak production of supersymmetric particles in $\sqrt{s} = 8$ TeV proton-proton collisions,” *JHEP* **09** (2016) 175, [arXiv:1608.00872 \[hep-ex\]](https://arxiv.org/abs/1608.00872).
- [76] **ATLAS** Collaboration, “Summary of the ATLAS experiment’s sensitivity to supersymmetry after LHC Run 1 — interpreted in the phenomenological MSSM,” *JHEP* **10** (2015) 134, [arXiv:1508.06608 \[hep-ex\]](https://arxiv.org/abs/1508.06608).

- [77] **ATLAS** Collaboration, “Mass reach of the atlas searches for supersymmetry.” https://atlas.web.cern.ch/Atlas/GROUPS/PHYSICS/PUBNOTES/ATL-PHYS-PUB-2020-020/fig_23.png, 2020.
- [78] **CMS** Collaboration, “Summary plot moriond 2017.” https://twiki.cern.ch/twiki/pub/CMSPublic/SUSYSummary2017/Moriond2017_BarPlot.pdf, 2017.
- [79] L. S. W. Group, “Notes lepsusywg/02-04.1 and lepsusywg/01-03.1.” <http://lepsusy.web.cern.ch/lepsusy/>, 2004. Accessed: 2021-02-11.
- [80] **ATLAS** Collaboration, G. Aad *et al.*, “Observation of a new particle in the search for the Standard Model Higgs boson with the ATLAS detector at the LHC,” *Phys. Lett. B* **716** (2012) 1–29, [arXiv:1207.7214 \[hep-ex\]](https://arxiv.org/abs/1207.7214).
- [81] **CMS** Collaboration, S. Chatrchyan *et al.*, “Observation of a New Boson at a Mass of 125 GeV with the CMS Experiment at the LHC,” *Phys. Lett. B* **716** (2012) 30–61, [arXiv:1207.7235 \[hep-ex\]](https://arxiv.org/abs/1207.7235).
- [82] CERN, “About cern.” <https://home.cern/about>. Accessed: 2021-01-21.
- [83] CERN, “CERN Annual report 2019,” tech. rep., CERN, Geneva, 2020. <https://cds.cern.ch/record/2723123>.
- [84] L. R. Evans and P. Bryant, “LHC Machine,” *JINST* **3** (2008) S08001. 164 p. [http://cds.cern.ch/record/1129806](https://cds.cern.ch/record/1129806). This report is an abridged version of the LHC Design Report (CERN-2004-003).
- [85] R. Scrivens, M. Kronberger, D. Küchler, J. Lettry, C. Mastrostefano, O. Midttun, M. O’Neil, H. Pereira, and C. Schmitzer, “Overview of the status and developments on primary ion sources at CERN*.” <https://cds.cern.ch/record/1382102>.
- [86] E. Mobs, “The CERN accelerator complex - 2019. Complexe des accélérateurs du CERN - 2019.” <https://cds.cern.ch/record/2684277>. General Photo.
- [87] **ATLAS** Collaboration, “The ATLAS Experiment at the CERN Large Hadron Collider,” *JINST* **3** (2008) S08003.
- [88] **CMS** Collaboration, S. Chatrchyan *et al.*, “The CMS Experiment at the CERN LHC,” *JINST* **3** (2008) S08004.
- [89] **ALICE** Collaboration, K. Aamodt *et al.*, “The ALICE experiment at the CERN LHC,” *JINST* **3** (2008) S08002.
- [90] **LHCb** Collaboration, J. Alves, A. Augusto *et al.*, “The LHCb Detector at the LHC,” *JINST* **3** (2008) S08005.
- [91] **TOTEM** Collaboration, G. Anelli *et al.*, “The TOTEM experiment at the CERN Large Hadron Collider,” *JINST* **3** (2008) S08007.
- [92] **LHCf** Collaboration, O. Adriani *et al.*, “Technical design report of the LHCf experiment: Measurement of photons and neutral pions in the very forward region of LHC.”
- [93] **MoEDAL** Collaboration, J. Pinfold *et al.*, “Technical Design Report of the MoEDAL Experiment.”

- [94] O. S. Bruning, P. Collier, P. Lebrun, S. Myers, R. Ostojic, J. Poole, and P. Proudlock, *LHC Design Report*. CERN Yellow Reports: Monographs. CERN, Geneva, 2004.
<https://cds.cern.ch/record/782076>.
- [95] **ATLAS** Collaboration, “ATLAS Public Results - Luminosity Public Results Run 2.”
<https://twiki.cern.ch/twiki/bin/view/AtlasPublic/LuminosityPublicResultsRun2>. Accessed: 2021-01-17.
- [96] **ATLAS** Collaboration, Z. Marshall, “Simulation of Pile-up in the ATLAS Experiment,” *J. Phys. Conf. Ser.* **513** (2014) 022024.
- [97] “First beam in the LHC - accelerating science.”
<https://home.cern/news/news/accelerators/record-luminosity-well-done-lhc>. Accessed: 2021-01-10.
- [98] **ATLAS Collaboration** Collaboration, “Luminosity determination in pp collisions at $\sqrt{s} = 13$ TeV using the ATLAS detector at the LHC,” Tech. Rep. ATLAS-CONF-2019-021, CERN, Geneva, Jun, 2019.
<https://cds.cern.ch/record/2677054>.
- [99] **ATLAS** Collaboration, M. Aaboud *et al.*, “Luminosity determination in pp collisions at $\sqrt{s} = 8$ TeV using the ATLAS detector at the LHC,” *Eur. Phys. J. C* **76** no. 12, (2016) 653, [arXiv:1608.03953 \[hep-ex\]](https://arxiv.org/abs/1608.03953).
- [100] G. Avoni, M. Bruschi, G. Cabras, D. Caforio, N. Dehghanian, A. Floderus, B. Giacobbe, F. Giannuzzi, F. Giorgi, P. Grafström, V. Hedberg, F. L. Manghi, S. Meneghini, J. Pinfold, E. Richards, C. Sbarra, N. S. Cesari, A. Sbrizzi, R. Soluk, G. Ucchielli, S. Valentinetto, O. Viazlo, M. Villa, C. Vittori, R. Vuillermet, and A. Zoccoli, “The new LUCID-2 detector for luminosity measurement and monitoring in ATLAS,” *Journal of Instrumentation* **13** no. 07, (Jul, 2018) P07017–P07017.
<https://doi.org/10.1088/1748-0221/13/07/p07017>.
- [101] S. van der Meer, “Calibration of the effective beam height in the ISR,” Tech. Rep. CERN-ISR-PO-68-31. ISR-PO-68-31, CERN, Geneva, 1968.
<https://cds.cern.ch/record/296752>.
- [102] P. Grafström and W. Kozanecki, “Luminosity determination at proton colliders,” *Progress in Particle and Nuclear Physics* **81** (2015) 97 – 148.
<http://www.sciencedirect.com/science/article/pii/S0146641014000878>.
- [103] “New schedule for CERN’s accelerators and experiments.”
<https://home.cern/news/press-release/cern/first-beam-lhc-accelerating-science>. Accessed: 2021-01-10.
- [104] **ATLAS** Collaboration, G. Aad *et al.*, “Luminosity Determination in pp Collisions at $\sqrt{s} = 7$ TeV Using the ATLAS Detector at the LHC,” *Eur. Phys. J. C* **71** (2011) 1630, [arXiv:1101.2185 \[hep-ex\]](https://arxiv.org/abs/1101.2185).
- [105] **ATLAS Collaboration** Collaboration, G. Aad *et al.*, “Improved luminosity determination in pp collisions at $\sqrt{s} = 7$ TeV using the ATLAS detector at the LHC. Improved luminosity determination in pp collisions at $\sqrt{s} = 7$ TeV using the ATLAS detector at the LHC,” *Eur. Phys. J. C* **73** no. CERN-PH-EP-2013-026. CERN-PH-EP-2013-026, (Feb, 2013) 2518. 27 p. <https://cds.cern.ch/record/1517411>. Comments: 26 pages plus author list (39 pages total), 17 figures, 9 tables, submitted to EPJC, All figures are available at <a href=

- [106] “Record luminosity: well done LHC.”. <https://home.cern/news/news/accelerators/new-schedule-cerns-accelerators-and-experiments>. Accessed: 2021-01-10.
- [107] A. G., B. A. I., B. O., F. P., L. M., R. L., and T. L., *High-Luminosity Large Hadron Collider (HL-LHC): Technical Design Report V. 0.1*. CERN Yellow Reports: Monographs. CERN, Geneva, 2017. <https://cds.cern.ch/record/2284929>.
- [108] J. Pequenao, “Computer generated image of the whole ATLAS detector.” Mar, 2008.
- [109] **ATLAS** Collaboration, “ATLAS: Detector and physics performance technical design report. Volume 1.”.
- [110] J. Pequenao, “Computer generated image of the ATLAS inner detector.” Mar, 2008.
- [111] **ATLAS Collaboration** Collaboration, K. Potamianos, “The upgraded Pixel detector and the commissioning of the Inner Detector tracking of the ATLAS experiment for Run-2 at the Large Hadron Collider,” Tech. Rep. ATL-PHYS-PROC-2016-104, CERN, Geneva, Aug, 2016. <https://cds.cern.ch/record/2209070>. 15 pages, EPS-HEP 2015 Proceedings.
- [112] **ATLAS IBL** Collaboration, B. Abbott *et al.*, “Production and Integration of the ATLAS Insertable B-Layer,” *JINST* **13** no. 05, (2018) T05008, [arXiv:1803.00844 \[physics.ins-det\]](https://arxiv.org/abs/1803.00844).
- [113] **ATLAS** Collaboration, “ATLAS Insertable B-Layer Technical Design Report,” Tech. Rep. CERN-LHCC-2010-013. ATLAS-TDR-19, Sep, 2010. <http://cds.cern.ch/record/1291633>.
- [114] **ATLAS** Collaboration, G. Aad *et al.*, “ATLAS b-jet identification performance and efficiency measurement with $t\bar{t}$ events in pp collisions at $\sqrt{s} = 13$ TeV,” *Eur. Phys. J. C* **79** no. 11, (2019) 970, [arXiv:1907.05120 \[hep-ex\]](https://arxiv.org/abs/1907.05120).
- [115] ATLAS Collaboration, “Particle Identification Performance of the ATLAS Transition Radiation Tracker.” ATLAS-CONF-2011-128, 2011. <https://cds.cern.ch/record/1383793>.
- [116] J. Pequenao, “Computer Generated image of the ATLAS calorimeter.” Mar, 2008.
- [117] J. Pequenao, “Computer generated image of the ATLAS Muons subsystem.” Mar, 2008.
- [118] S. Lee, M. Livan, and R. Wigmans, “Dual-Readout Calorimetry,” *Rev. Mod. Phys.* **90** no. arXiv:1712.05494. 2, (Dec, 2017) 025002. 40 p. <https://cds.cern.ch/record/2637852>. 44 pages, 53 figures, accepted for publication in Review of Modern Physics.
- [119] M. Leite, “Performance of the ATLAS Zero Degree Calorimeter,” Tech. Rep. ATL-FWD-PROC-2013-001, CERN, Geneva, Nov, 2013. <https://cds.cern.ch/record/1628749>.
- [120] S. Abdel Khalek *et al.*, “The ALFA Roman Pot Detectors of ATLAS,” *JINST* **11** no. 11, (2016) P11013, [arXiv:1609.00249 \[physics.ins-det\]](https://arxiv.org/abs/1609.00249).
- [121] U. Amaldi, G. Cocconi, A. Diddens, R. Dobinson, J. Dorenbosch, W. Duinker, D. Gustavson, J. Meyer, K. Potter, A. Wetherell, A. Baroncelli, and C. Bosio, “The real part of the forward proton proton scattering amplitude measured at the cern intersecting storage rings,” *Physics Letters B* **66** no. 4, (1977) 390 – 394. <http://www.sciencedirect.com/science/article/pii/0370269377900223>.

- [122] L. Adamczyk, E. Banaś, A. Brandt, M. Bruschi, S. Grinstein, J. Lange, M. Rijssenbeek, P. Sicho, R. Staszewski, T. Sykora, M. Trzebiński, J. Chwastowski, and K. Korcyl, “Technical Design Report for the ATLAS Forward Proton Detector,” Tech. Rep. CERN-LHCC-2015-009. ATLAS-TDR-024, May, 2015.
<https://cds.cern.ch/record/2017378>.
- [123] **ATLAS** Collaboration, A. R. Martínez, “The Run-2 ATLAS Trigger System,” *J. Phys. Conf. Ser.* **762** no. 1, (2016) 012003.
- [124] **ATLAS Collaboration** Collaboration, *ATLAS level-1 trigger: Technical Design Report*. Technical Design Report ATLAS. CERN, Geneva, 1998.
<https://cds.cern.ch/record/381429>.
- [125] **ATLAS Collaboration** Collaboration, P. Jenni, M. Nessi, M. Nordberg, and K. Smith, *ATLAS high-level trigger, data-acquisition and controls: Technical Design Report*. Technical Design Report ATLAS. CERN, Geneva, 2003.
<https://cds.cern.ch/record/616089>.
- [126] **ATLAS** Collaboration, G. Aad *et al.*, “The ATLAS Simulation Infrastructure,” *Eur. Phys. J. C* **70** (2010) 823–874, [arXiv:1005.4568 \[physics.ins-det\]](https://arxiv.org/abs/1005.4568).
- [127] T. Gleisberg, S. Hoeche, F. Krauss, M. Schonherr, S. Schumann, F. Siegert, and J. Winter, “Event generation with SHERPA 1.1,” *JHEP* **02** (2009) 007, [arXiv:0811.4622 \[hep-ph\]](https://arxiv.org/abs/0811.4622).
- [128] A. Buckley *et al.*, “General-purpose event generators for LHC physics,” *Phys. Rept.* **504** (2011) 145–233, [arXiv:1101.2599 \[hep-ph\]](https://arxiv.org/abs/1101.2599).
- [129] V. N. Gribov and L. N. Lipatov, “Deep inelastic e p scattering in perturbation theory,” *Sov. J. Nucl. Phys.* **15** (1972) 438–450.
- [130] J. Blumlein, T. Doyle, F. Hautmann, M. Klein, and A. Vogt, “Structure functions in deep inelastic scattering at HERA,” in *Workshop on Future Physics at HERA (To be followed by meetings 7-9 Feb and 30-31 May 1996 at DESY)*. 9, 1996. [arXiv:hep-ph/9609425](https://arxiv.org/abs/hep-ph/9609425).
- [131] A. Buckley, J. Ferrando, S. Lloyd, K. Nordström, B. Page, M. Rüfenacht, M. Schönher, and G. Watt, “LHAPDF6: parton density access in the LHC precision era,” *Eur. Phys. J. C* **75** (2015) 132, [arXiv:1412.7420 \[hep-ph\]](https://arxiv.org/abs/1412.7420).
- [132] M. Bengtsson and T. Sjostrand, “Coherent Parton Showers Versus Matrix Elements: Implications of PETRA - PEP Data,” *Phys. Lett. B* **185** (1987) 435.
- [133] S. Catani, F. Krauss, R. Kuhn, and B. R. Webber, “QCD matrix elements + parton showers,” *JHEP* **11** (2001) 063, [arXiv:hep-ph/0109231](https://arxiv.org/abs/hep-ph/0109231).
- [134] L. Lonnblad, “Correcting the color dipole cascade model with fixed order matrix elements,” *JHEP* **05** (2002) 046, [arXiv:hep-ph/0112284](https://arxiv.org/abs/hep-ph/0112284).
- [135] B. Andersson, G. Gustafson, G. Ingelman, and T. Sjostrand, “Parton Fragmentation and String Dynamics,” *Phys. Rept.* **97** (1983) 31–145.
- [136] B. Andersson, *The Lund Model*. Cambridge Monographs on Particle Physics, Nuclear Physics and Cosmology. Cambridge University Press, 1998.
- [137] D. Amati and G. Veneziano, “Preconfinement as a Property of Perturbative QCD,” *Phys. Lett. B* **83** (1979) 87–92.

- [138] M. Dobbs and J. B. Hansen, “The HepMC C++ Monte Carlo event record for High Energy Physics,” *Comput. Phys. Commun.* **134** (2001) 41–46.
- [139] **GEANT4** Collaboration, S. Agostinelli *et al.*, “GEANT4: A Simulation toolkit,” *Nucl. Instrum. Meth. A* **506** (2003) 250–303.
- [140] **ATLAS Collaboration** Collaboration, “The new Fast Calorimeter Simulation in ATLAS,” Tech. Rep. ATL-SOFT-PUB-2018-002, CERN, Geneva, Jul, 2018. <https://cds.cern.ch/record/2630434>.
- [141] K. Cranmer, “Practical Statistics for the LHC,” in *2011 European School of High-Energy Physics*, pp. 267–308. 2014. [arXiv:1503.07622 \[physics.data-an\]](https://arxiv.org/abs/1503.07622).
- [142] G. Cowan, K. Cranmer, E. Gross, and O. Vitells, “Asymptotic formulae for likelihood-based tests of new physics,” *Eur. Phys. J. C* **71** (2011) 1554, [arXiv:1007.1727 \[physics.data-an\]](https://arxiv.org/abs/1007.1727). [Erratum: Eur. Phys. J.C73,2501(2013)].
- [143] ATLAS Collaboration, “Reproduction searches for new physics with the ATLAS experiment through publication of full statistical likelihoods.” ATL-PHYS-PUB-2019-029, 2019. <https://cds.cern.ch/record/2684863>.
- [144] **ROOT Collaboration** Collaboration, K. Cranmer, G. Lewis, L. Moneta, A. Shibata, and W. Verkerke, “HistFactory: A tool for creating statistical models for use with RooFit and RooStats,” Tech. Rep. CERN-OPEN-2012-016, New York U., New York, Jan, 2012. <https://cds.cern.ch/record/1456844>.
- [145] W. Verkerke and D. P. Kirkby, “The RooFit toolkit for data modeling,” *eConf C0303241* (2003) MOLT007, [arXiv:physics/0306116 \[physics\]](https://arxiv.org/abs/physics/0306116). [,186(2003)].
- [146] L. Moneta, K. Belasco, K. S. Cranmer, S. Kreiss, A. Lazzaro, D. Piparo, G. Schott, W. Verkerke, and M. Wolf, “The RooStats Project,” *PoS ACAT2010* (2010) 057, [arXiv:1009.1003 \[physics.data-an\]](https://arxiv.org/abs/1009.1003).
- [147] F. James and M. Roos, “MINUIT: a system for function minimization and analysis of the parameter errors and corrections,” *Comput. Phys. Commun.* **10** no. CERN-DD-75-20, (Jul, 1975) 343–367. 38 p. <https://cds.cern.ch/record/310399>.
- [148] R. Brun and F. Rademakers, “ROOT: An object oriented data analysis framework,” *Nucl. Instrum. Meth. A* **389** (1997) 81–86.
- [149] I. Antcheva *et al.*, “Root — a c++ framework for petabyte data storage, statistical analysis and visualization,” *Computer Physics Communications* **182** no. 6, (2011) 1384 – 1385. <http://www.sciencedirect.com/science/article/pii/S0010465511000701>.
- [150] M. Baak, G. J. Besjes, D. Côte, A. Koutsman, J. Lorenz, and D. Short, “HistFitter software framework for statistical data analysis,” *Eur. Phys. J. C* **75** (2015) 153, [arXiv:1410.1280 \[hep-ex\]](https://arxiv.org/abs/1410.1280).
- [151] L. Heinrich, M. Feickert, G. Stark, and K. Cranmer, “pyhf: pure-python implementation of histfactory statistical models,” *Journal of Open Source Software* **6** no. 58, (2021) 2823. <https://doi.org/10.21105/joss.02823>.
- [152] L. Heinrich, M. Feickert, and G. Stark, “pyhf: v0.6.0.” <https://github.com/scikit-hep/pyhf>.

- [153] A. Paszke, S. Gross, F. Massa, A. Lerer, J. Bradbury, G. Chanan, T. Killeen, Z. Lin, N. Gimelshein, L. Antiga, A. Desmaison, A. Kopf, E. Yang, Z. DeVito, M. Raison, A. Tejani, S. Chilamkurthy, B. Steiner, L. Fang, J. Bai, and S. Chintala, “Pytorch: An imperative style, high-performance deep learning library,” in *Advances in Neural Information Processing Systems 32*, H. Wallach, H. Larochelle, A. Beygelzimer, F. d’Alché-Buc, E. Fox, and R. Garnett, eds., pp. 8024–8035. Curran Associates, Inc., 2019. <http://papers.neurips.cc/paper/9015-pytorch-an-imperative-style-high-performance-deep-learning-library.pdf>.
- [154] M. Abadi, A. Agarwal, P. Barham, E. Brevdo, Z. Chen, C. Citro, G. S. Corrado, A. Davis, J. Dean, M. Devin, S. Ghemawat, I. Goodfellow, A. Harp, G. Irving, M. Isard, Y. Jia, R. Jozefowicz, L. Kaiser, M. Kudlur, J. Levenberg, D. Mané, R. Monga, S. Moore, D. Murray, C. Olah, M. Schuster, J. Shlens, B. Steiner, I. Sutskever, K. Talwar, P. Tucker, V. Vanhoucke, V. Vasudevan, F. Viégas, O. Vinyals, P. Warden, M. Wattenberg, M. Wicke, Y. Yu, and X. Zheng, “TensorFlow: Large-scale machine learning on heterogeneous systems,” 2015. <https://www.tensorflow.org/>. Software available from tensorflow.org.
- [155] J. Bradbury, R. Frostig, P. Hawkins, M. J. Johnson, C. Leary, D. Maclaurin, and S. Wanderman-Milne, “JAX: composable transformations of Python+NumPy programs,” 2018. <http://github.com/google/jax>.
- [156] A. Wald, “Tests of statistical hypotheses concerning several parameters when the number of observations is large,” *Transactions of the American Mathematical Society* **54** no. 3, (1943) 426–482. <https://doi.org/10.1090/S0002-9947-1943-0012401-3>.
- [157] S. S. Wilks, “The large-sample distribution of the likelihood ratio for testing composite hypotheses,” *Ann. Math. Statist.* **9** no. 1, (03, 1938) 60–62. <https://doi.org/10.1214/aoms/1177732360>.
- [158] G. Cowan, “Statistics for Searches at the LHC,” in *69th Scottish Universities Summer School in Physics: LHC Physics*, pp. 321–355. 7, 2013. [arXiv:1307.2487 \[hep-ex\]](https://arxiv.org/abs/1307.2487).
- [159] A. L. Read, “Presentation of search results: the CL_S technique,” *J. Phys. G* **28** (2002) 2693.
- [160] R. D. Cousins, J. T. Linnemann, and J. Tucker, “Evaluation of three methods for calculating statistical significance when incorporating a systematic uncertainty into a test of the background-only hypothesis for a Poisson process,” *Nucl. Instrum. Meth. A* **595** no. 2, (2008) 480, [arXiv:physics/0702156 \[physics.data-an\]](https://arxiv.org/abs/physics/0702156).
- [161] K. CRANMER, “Statistical challenges for searches for new physics at the lhc,” *Statistical Problems in Particle Physics, Astrophysics and Cosmology* (May, 2006) . http://dx.doi.org/10.1142/9781860948985_0026.
- [162] ATLAS Collaboration, “Search for direct pair production of a chargino and a neutralino decaying to the 125 GeV Higgs boson in $\sqrt{s} = 8$ TeV pp collisions with the ATLAS detector,” *Eur. Phys. J. C* **75** (2015) 208, [arXiv:1501.07110 \[hep-ex\]](https://arxiv.org/abs/1501.07110).
- [163] ATLAS Collaboration, “Search for chargino and neutralino production in final states with a Higgs boson and missing transverse momentum at $\sqrt{s} = 13$ TeV with the ATLAS detector,” *Phys. Rev. D* **100** (2019) 012006, [arXiv:1812.09432 \[hep-ex\]](https://arxiv.org/abs/1812.09432).
- [164] CMS Collaboration, “Search for electroweak production of charginos and neutralinos in WH events in proton–proton collisions at $\sqrt{s} = 13$ TeV,” *JHEP* **11** (2017) 029, [arXiv:1706.09933 \[hep-ex\]](https://arxiv.org/abs/1706.09933).

- [165] ATLAS Collaboration, “Search for direct production of electroweakinos in final states with one lepton, missing transverse momentum and a Higgs boson decaying into two b -jets in pp collisions at $\sqrt{s} = 13$ TeV with the ATLAS detector,” *Eur. Phys. J. C* **80** (2020) 691, [arXiv:1909.09226 \[hep-ex\]](https://arxiv.org/abs/1909.09226).
- [166] ATLAS Collaboration, “Improvements in $t\bar{t}$ modelling using NLO+PS Monte Carlo generators for Run 2.” ATL-PHYS-PUB-2018-009, 2018. <https://cds.cern.ch/record/2630327>.
- [167] ATLAS Collaboration, “Modelling of the $t\bar{t}H$ and $t\bar{t}V(V = W, Z)$ processes for $\sqrt{s} = 13$ TeV ATLAS analyses.” ATL-PHYS-PUB-2016-005, 2016. <https://cds.cern.ch/record/2120826>.
- [168] ATLAS Collaboration, “ATLAS simulation of boson plus jets processes in Run 2.” ATL-PHYS-PUB-2017-006, 2017. <https://cds.cern.ch/record/2261937>.
- [169] ATLAS Collaboration, “Multi-Boson Simulation for 13 TeV ATLAS Analyses.” ATL-PHYS-PUB-2017-005, 2017. <https://cds.cern.ch/record/2261933>.
- [170] J. Alwall, R. Frederix, S. Frixione, V. Hirschi, F. Maltoni, O. Mattelaer, H. S. Shao, T. Stelzer, P. Torrielli, and M. Zaro, “The automated computation of tree-level and next-to-leading order differential cross sections, and their matching to parton shower simulations,” *JHEP* **07** (2014) 079, [arXiv:1405.0301 \[hep-ph\]](https://arxiv.org/abs/1405.0301).
- [171] R. Frederix and S. Frixione, “Merging meets matching in MC@NLO,” *JHEP* **12** (2012) 061, [arXiv:1209.6215 \[hep-ph\]](https://arxiv.org/abs/1209.6215).
- [172] T. Sjöstrand, S. Ask, J. R. Christiansen, R. Corke, N. Desai, P. Ilten, S. Mrenna, S. Prestel, C. O. Rasmussen, and P. Z. Skands, “An Introduction to PYTHIA 8.2,” *Comput. Phys. Commun.* **191** (2015) 159–177, [arXiv:1410.3012 \[hep-ph\]](https://arxiv.org/abs/1410.3012).
- [173] L. Lönnblad and S. Prestel, “Matching tree-level matrix elements with interleaved showers,” *JHEP* **03** (2012) 019, [arXiv:1109.4829 \[hep-ph\]](https://arxiv.org/abs/1109.4829).
- [174] R. D. Ball *et al.*, “Parton distributions with LHC data,” *Nucl. Phys. B* **867** (2013) 244, [arXiv:1207.1303 \[hep-ph\]](https://arxiv.org/abs/1207.1303).
- [175] ATLAS Collaboration, “ATLAS Pythia 8 tunes to 7 TeV data.” ATL-PHYS-PUB-2014-021, 2014. <https://cds.cern.ch/record/1966419>.
- [176] D. J. Lange, “The EvtGen particle decay simulation package,” *Nucl. Instrum. Meth. A* **462** (2001) 152.
- [177] ATLAS Collaboration, “The Pythia 8 A3 tune description of ATLAS minimum bias and inelastic measurements incorporating the Donnachie–Landshoff diffractive model.” ATL-PHYS-PUB-2016-017, 2016. <https://cds.cern.ch/record/2206965>.
- [178] B. Fuks, M. Klasen, D. R. Lamprea, and M. Rothberg, “Precision predictions for electroweak superpartner production at hadron colliders with RESUMMINO,” *Eur. Phys. J. C* **73** (2013) 2480, [arXiv:1304.0790 \[hep-ph\]](https://arxiv.org/abs/1304.0790).
- [179] J. Fiaschi and M. Klasen, “Neutralino-chargino pair production at NLO+NLL with resummation-improved parton density functions for LHC Run II,” *Phys. Rev. D* **98** no. 5, (2018) 055014, [arXiv:1805.11322 \[hep-ph\]](https://arxiv.org/abs/1805.11322).

- [180] B. Fuks, M. Klasen, D. R. Lamprea, and M. Rothering, “Gaugino production in proton-proton collisions at a center-of-mass energy of 8 TeV,” *JHEP* **10** (2012) 081, [arXiv:1207.2159 \[hep-ph\]](https://arxiv.org/abs/1207.2159).
- [181] S. Alioli, P. Nason, C. Oleari, and E. Re, “A general framework for implementing NLO calculations in shower Monte Carlo programs: the POWHEG BOX,” *JHEP* **06** (2010) 043, [arXiv:1002.2581 \[hep-ph\]](https://arxiv.org/abs/1002.2581).
- [182] S. Frixione, P. Nason, and G. Ridolfi, “A Positive-weight next-to-leading-order Monte Carlo for heavy flavour hadroproduction,” *JHEP* **09** (2007) 126, [arXiv:0707.3088 \[hep-ph\]](https://arxiv.org/abs/0707.3088).
- [183] P. Nason, “A New method for combining NLO QCD with shower Monte Carlo algorithms,” *JHEP* **11** (2004) 040, [arXiv:hep-ph/0409146](https://arxiv.org/abs/hep-ph/0409146).
- [184] E. Bothmann *et al.*, “Event generation with Sherpa 2.2,” *SciPost Phys.* **7** no. 3, (2019) 034, [arXiv:1905.09127 \[hep-ph\]](https://arxiv.org/abs/1905.09127).
- [185] S. Höche, F. Krauss, S. Schumann, and F. Siegert, “QCD matrix elements and truncated showers,” *JHEP* **05** (2009) 053, [arXiv:0903.1219 \[hep-ph\]](https://arxiv.org/abs/0903.1219).
- [186] S. Höche, F. Krauss, M. Schönherr, and F. Siegert, “QCD matrix elements + parton showers. The NLO case,” *JHEP* **04** (2013) 027, [arXiv:1207.5030 \[hep-ph\]](https://arxiv.org/abs/1207.5030).
- [187] NNPDF Collaboration, R. D. Ball *et al.*, “Parton distributions for the LHC run II,” *JHEP* **04** (2015) 040, [arXiv:1410.8849 \[hep-ph\]](https://arxiv.org/abs/1410.8849).
- [188] ATLAS Collaboration, “Example ATLAS tunes of PYTHIA8, PYTHIA6 and POWHEG to an observable sensitive to Z boson transverse momentum.” ATL-PHYS-PUB-2013-017, 2013. <https://cds.cern.ch/record/1629317>.
- [189] M. Czakon and A. Mitov, “Top++: A program for the calculation of the top-pair cross-section at hadron colliders,” *Comput. Phys. Commun.* **185** (2014) 2930, [arXiv:1112.5675 \[hep-ph\]](https://arxiv.org/abs/1112.5675).
- [190] M. Cacciari, M. Czakon, M. Mangano, A. Mitov, and P. Nason, “Top-pair production at hadron colliders with next-to-next-to-leading logarithmic soft-gluon resummation,” *Phys. Lett. B* **710** (2012) 612–622, [arXiv:1111.5869 \[hep-ph\]](https://arxiv.org/abs/1111.5869).
- [191] P. Kant, O. M. Kind, T. Kintscher, T. Lohse, T. Martini, S. Mölbitz, P. Rieck, and P. Uwer, “HatHor for single top-quark production: Updated predictions and uncertainty estimates for single top-quark production in hadronic collisions,” *Comput. Phys. Commun.* **191** (2015) 74–89, [arXiv:1406.4403 \[hep-ph\]](https://arxiv.org/abs/1406.4403).
- [192] N. Kidonakis, “Two-loop soft anomalous dimensions for single top quark associated production with a W^- or H^- ,” *Phys. Rev. D* **82** (2010) 054018, [arXiv:1005.4451 \[hep-ph\]](https://arxiv.org/abs/1005.4451).
- [193] J. M. Campbell and R. K. Ellis, “ $t\bar{t}W^{+-}$ production and decay at NLO,” *JHEP* **07** (2012) 052, [arXiv:1204.5678 \[hep-ph\]](https://arxiv.org/abs/1204.5678).
- [194] A. Lazopoulos, T. McElmurry, K. Melnikov, and F. Petriello, “Next-to-leading order QCD corrections to $t\bar{t}Z$ production at the LHC,” *Phys. Lett. B* **666** (2008) 62–65, [arXiv:0804.2220 \[hep-ph\]](https://arxiv.org/abs/0804.2220).

- [195] R. Gavin, Y. Li, F. Petriello, and S. Quackenbush, “FEWZ 2.0: A code for hadronic Z production at next-to-next-to-leading order,” [arXiv:1011.3540 \[hep-ph\]](https://arxiv.org/abs/1011.3540).
- [196] **LHC Higgs Cross Section Working Group** Collaboration, D. de Florian *et al.*, “Handbook of LHC Higgs Cross Sections: 4. Deciphering the Nature of the Higgs Sector,” [arXiv:1610.07922 \[hep-ph\]](https://arxiv.org/abs/1610.07922).
- [197] ATLAS Collaboration, “Performance of the ATLAS track reconstruction algorithms in dense environments in LHC Run 2,” *Eur. Phys. J. C* **77** (2017) 673, [arXiv:1704.07983 \[hep-ex\]](https://arxiv.org/abs/1704.07983).
- [198] R. Frühwirth, “Application of Kalman filtering to track and vertex fitting,” *Nucl. Instrum. Methods Phys. Res., A* **262** no. HEPHY-PUB-503, (Jun, 1987) 444. 19 p. <https://cds.cern.ch/record/178627>.
- [199] T. Cornelissen, M. Elsing, I. Gavrilenco, W. Liebig, E. Moyse, and A. Salzburger, “The new ATLAS track reconstruction (NEWT),” *J. Phys.: Conf. Ser.* **119** (2008) 032014. <https://cds.cern.ch/record/1176900>.
- [200] ATLAS Collaboration, “Vertex Reconstruction Performance of the ATLAS Detector at $\sqrt{s} = 13$ TeV.” ATL-PHYS-PUB-2015-026, 2015. <https://cds.cern.ch/record/2037717>.
- [201] ATLAS Collaboration, “Reconstruction of primary vertices at the ATLAS experiment in Run 1 proton–proton collisions at the LHC,” *Eur. Phys. J. C* **77** (2017) 332, [arXiv:1611.10235 \[hep-ex\]](https://arxiv.org/abs/1611.10235).
- [202] ATLAS Collaboration, “Topological cell clustering in the ATLAS calorimeters and its performance in LHC Run 1,” *Eur. Phys. J. C* **77** (2017) 490, [arXiv:1603.02934 \[hep-ex\]](https://arxiv.org/abs/1603.02934).
- [203] ATLAS Collaboration, “Electron and photon performance measurements with the ATLAS detector using the 2015–2017 LHC proton–proton collision data,” *JINST* **14** (2019) P12006, [arXiv:1908.00005 \[hep-ex\]](https://arxiv.org/abs/1908.00005).
- [204] ATLAS Collaboration, “Measurement of the photon identification efficiencies with the ATLAS detector using LHC Run 2 data collected in 2015 and 2016,” *Eur. Phys. J. C* **79** (2019) 205, [arXiv:1810.05087 \[hep-ex\]](https://arxiv.org/abs/1810.05087).
- [205] ATLAS Collaboration, “Electron and photon energy calibration with the ATLAS detector using 2015–2016 LHC proton–proton collision data,” *JINST* **14** (2019) P03017, [arXiv:1812.03848 \[hep-ex\]](https://arxiv.org/abs/1812.03848).
- [206] ATLAS Collaboration, “Electron reconstruction and identification in the ATLAS experiment using the 2015 and 2016 LHC proton–proton collision data at $\sqrt{s} = 13$ TeV,” *Eur. Phys. J. C* **79** (2019) 639, [arXiv:1902.04655 \[hep-ex\]](https://arxiv.org/abs/1902.04655).
- [207] ATLAS Collaboration, “Muon reconstruction performance of the ATLAS detector in proton–proton collision data at $\sqrt{s} = 13$ TeV,” *Eur. Phys. J. C* **76** (2016) 292, [arXiv:1603.05598 \[hep-ex\]](https://arxiv.org/abs/1603.05598).
- [208] **ATLAS** Collaboration, “Muon reconstruction and identification efficiency in ATLAS using the full Run 2 pp collision data set at $\sqrt{s} = 13$ TeV,” [arXiv:2012.00578 \[hep-ex\]](https://arxiv.org/abs/2012.00578).
- [209] M. Cacciari, G. P. Salam, and G. Soyez, “The anti- k_t jet clustering algorithm,” *JHEP* **04** (2008) 063, [arXiv:0802.1189 \[hep-ph\]](https://arxiv.org/abs/0802.1189).

- [210] M. Cacciari, G. P. Salam, and G. Soyez, “FastJet user manual,” *Eur. Phys. J. C* **72** (2012) 1896, [arXiv:1111.6097 \[hep-ph\]](https://arxiv.org/abs/1111.6097).
- [211] M. Cacciari, “FastJet: A Code for fast k_t clustering, and more,” in *Deep inelastic scattering. Proceedings, 14th International Workshop, DIS 2006, Tsukuba, Japan, April 20-24, 2006*, pp. 487–490. 2006. [arXiv:hep-ph/0607071 \[hep-ph\]](https://arxiv.org/abs/hep-ph/0607071). [,125(2006)].
- [212] **ATLAS** Collaboration, G. Aad *et al.*, “Jet energy scale and resolution measured in proton-proton collisions at $\sqrt{s} = 13$ TeV with the ATLAS detector,” [arXiv:2007.02645 \[hep-ex\]](https://arxiv.org/abs/2007.02645).
- [213] M. Cacciari and G. P. Salam, “Pileup subtraction using jet areas,” *Phys. Lett. B* **659** (2008) 119–126, [arXiv:0707.1378 \[hep-ph\]](https://arxiv.org/abs/0707.1378).
- [214] ATLAS Collaboration, “Jet energy measurement with the ATLAS detector in proton–proton collisions at $\sqrt{s} = 7$ TeV,” *Eur. Phys. J. C* **73** (2013) 2304, [arXiv:1112.6426 \[hep-ex\]](https://arxiv.org/abs/1112.6426).
- [215] ATLAS Collaboration, “Determination of jet calibration and energy resolution in proton–proton collisions at $\sqrt{s} = 8$ TeV using the ATLAS detector,” [arXiv:1910.04482 \[hep-ex\]](https://arxiv.org/abs/1910.04482).
- [216] ATLAS Collaboration, “Performance of pile-up mitigation techniques for jets in pp collisions at $\sqrt{s} = 8$ TeV using the ATLAS detector,” *Eur. Phys. J. C* **76** (2016) 581, [arXiv:1510.03823 \[hep-ex\]](https://arxiv.org/abs/1510.03823).
- [217] ATLAS Collaboration, “Optimisation and performance studies of the ATLAS b -tagging algorithms for the 2017-18 LHC run.” ATL-PHYS-PUB-2017-013, 2017. <https://cds.cern.ch/record/2273281>.
- [218] ATLAS Collaboration, “ATLAS b -jet identification performance and efficiency measurement with $t\bar{t}$ events in pp collisions at $\sqrt{s} = 13$ TeV,” *Eur. Phys. J. C* **79** (2019) 970, [arXiv:1907.05120 \[hep-ex\]](https://arxiv.org/abs/1907.05120).
- [219] ATLAS Collaboration, “Measurements of b -jet tagging efficiency with the ATLAS detector using $t\bar{t}$ events at $\sqrt{s} = 13$ TeV,” *JHEP* **08** (2018) 089, [arXiv:1805.01845 \[hep-ex\]](https://arxiv.org/abs/1805.01845).
- [220] ATLAS Collaboration, “Performance of missing transverse momentum reconstruction with the ATLAS detector using proton–proton collisions at $\sqrt{s} = 13$ TeV,” *Eur. Phys. J. C* **78** (2018) 903, [arXiv:1802.08168 \[hep-ex\]](https://arxiv.org/abs/1802.08168).
- [221] **ATLAS Collaboration** Collaboration, “ E_T^{miss} performance in the ATLAS detector using 2015-2016 LHC p-p collisions,” Tech. Rep. ATLAS-CONF-2018-023, CERN, Geneva, Jun, 2018. [http://cds.cern.ch/record/2625233](https://cds.cern.ch/record/2625233).
- [222] D. Adams *et al.*, “Recommendations of the Physics Objects and Analysis Harmonisation Study Groups 2014,” Tech. Rep. ATL-PHYS-INT-2014-018, CERN, Geneva, Jul, 2014. <https://cds.cern.ch/record/1743654>.
- [223] M. Cacciari, G. P. Salam, and G. Soyez, “The Catchment Area of Jets,” *JHEP* **04** (2008) 005, [arXiv:0802.1188 \[hep-ph\]](https://arxiv.org/abs/0802.1188).
- [224] **UA1** Collaboration, G. Arnison *et al.*, “Experimental Observation of Isolated Large Transverse Energy Electrons with Associated Missing Energy at $\sqrt{s} = 540$ GeV,” *Phys. Lett. B* **122** (1983) 103–116.

- [225] **Aachen-Annecy-Birmingham-CERN-Helsinki-London(QMC)-Paris(CdF)-Riverside-Rome-Rutherford-Saclay(CEN)-Vienna** Collaboration, G. Arnison *et al.*, “Further evidence for charged intermediate vector bosons at the SPS collider,” *Phys. Lett. B* **129** no. CERN-EP-83-111, (Jun, 1985) 273–282. 17 p.
<https://cds.cern.ch/record/163856>.
- [226] D. R. Tovey, “On measuring the masses of pair-produced semi-invisibly decaying particles at hadron colliders,” *JHEP* **04** (2008) 034, [arXiv:0802.2879 \[hep-ph\]](https://arxiv.org/abs/0802.2879).
- [227] G. Polesello and D. R. Tovey, “Supersymmetric particle mass measurement with the boost-corrected contransverse mass,” *JHEP* **03** (2010) 030, [arXiv:0910.0174 \[hep-ph\]](https://arxiv.org/abs/0910.0174).
- [228] **ATLAS** Collaboration, G. Aad *et al.*, “Performance of the missing transverse momentum triggers for the ATLAS detector during Run-2 data taking,” *JHEP* **08** (2020) 080, [arXiv:2005.09554 \[hep-ex\]](https://arxiv.org/abs/2005.09554).
- [229] **ATLAS** Collaboration, G. Aad *et al.*, “Performance of algorithms that reconstruct missing transverse momentum in $\sqrt{s} = 8$ TeV proton-proton collisions in the ATLAS detector,” *Eur. Phys. J. C* **77** no. 4, (2017) 241, [arXiv:1609.09324 \[hep-ex\]](https://arxiv.org/abs/1609.09324).
- [230] ATLAS Collaboration, “ATLAS data quality operations and performance for 2015–2018 data-taking,” *JINST* **15** (2020) P04003, [arXiv:1911.04632 \[physics.ins-det\]](https://arxiv.org/abs/1911.04632).
- [231] ATLAS Collaboration, “Selection of jets produced in 13 TeV proton–proton collisions with the ATLAS detector.” ATLAS-CONF-2015-029, 2015.
<https://cds.cern.ch/record/2037702>.
- [232] N. Hartmann, “ahoi.” <https://gitlab.com/nikoladze/ahoi>, 2018.
- [233] **ATLAS** Collaboration, “Object-based missing transverse momentum significance in the ATLAS detector,” Tech. Rep. ATLAS-CONF-2018-038, CERN, Geneva, Jul, 2018.
<https://cds.cern.ch/record/2630948>.
- [234] A. Roodman, “Blind analysis in particle physics,” *eConf* **C030908** (2003) TUIT001, [arXiv:physics/0312102](https://arxiv.org/abs/physics/0312102).
- [235] ATLAS Collaboration, “A method for the construction of strongly reduced representations of ATLAS experimental uncertainties and the application thereof to the jet energy scale.” ATL-PHYS-PUB-2015-014, 2015. <https://cds.cern.ch/record/2037436>.
- [236] J. Bellm *et al.*, “Herwig 7.0/Herwig++ 3.0 release note,” *Eur. Phys. J. C* **76** no. 4, (2016) 196, [arXiv:1512.01178 \[hep-ph\]](https://arxiv.org/abs/1512.01178).
- [237] ATLAS Collaboration, “Simulation of top-quark production for the ATLAS experiment at $\sqrt{s} = 13$ TeV.” ATL-PHYS-PUB-2016-004, 2016. <https://cds.cern.ch/record/2120417>.
- [238] S. Frixione, E. Laenen, P. Motylinski, C. White, and B. R. Webber, “Single-top hadroproduction in association with a W boson,” *JHEP* **07** (2008) 029, [arXiv:0805.3067 \[hep-ph\]](https://arxiv.org/abs/0805.3067).

Acknowledgements

An dieser Stelle möchte ich mich herzlich bei allen bedanken, die mich bei der Anfertigung dieser Arbeit unterstützt haben. Insbesondere danke ich herzlich

- Prof. Dr. Dorothee Schaile für die Möglichkeit, diese Arbeit an ihrem Lehrstuhl durchzuführen sowie das Korrekturlesen der Arbeit.
- Dr. Jeanette Lorenz für die ausgezeichnete Betreuung, die vielen Anregungen, sowie die ehrliche und konstruktive Kritik beim Korrekturlesen dieser Arbeit. Sie hat es mir ermöglicht aktiv im 1-Lepton Analyseteam an der Suche nach Supersymmetrie mitwirken zu können.
- Dr. Nikolai Hartmann für die unzähligen Diskussionen über den Sinn und Unsinn der Datenanalyse mit und ohne ATLAS Software. Vielen Dank für die stets geduldige und ausführliche Beantwortung meiner Fragen, sowie das Bereitstellen unzähliger Zeilen Code, ohne die vieles schwieriger gewesen wäre.
- Allen Mitgliedern des Lehrstuhls Schaile für die angenehme und freundliche Arbeitsatmosphäre.
- Allen Freunden, die stets da waren, wenn ich sie gebraucht habe.

I also want to thank the entire 1-lepton analysis team, especially the coordinators Jeanette Lorenz, Da Xu and Alberto Cervelli. Thank you for the always supportive and enjoyable work environment. Many thanks also to Valentina Tudorache for patiently answering all my questions as well as all the entertaining conversations.

I would further like to thank Dr. Brian Petersen without whom the presented pMSSM studies would not have been possible.

En léiwen Merci och dem Yannick Erpelding fir d'Korrekturlesen—och wann en net alles verstanen huet—an dem Nick Beffort, fir all déi domm Reddit Posts, d'Korrekturlesen, an dei onzähleg Stonnen zesummen mat enger Spezi an der Hand.

Zu gudden Läschte, wëll ech op dëser Platz menger ganzer Famill merci soen, virun allem mengan léiwen Elteren an menger wonnerbarer Schwëster. Merci dass dir mëch bei allem waat ech maachen énnerstëtzzt an dass ech émmer op iech zielen kann, och wann ech weit fort sin. Ouni iech wier daat heiten net méiglech gewiescht. Besonneschen Merci och dem Nathalie Münster, dofir dass et mech seit Joren émmer énnerstëtzzt an émmer fir mech do as, och wann ech heiansdo depriméiert oder duercherneen sin.

Selbstständigkeitserklärung

Hiermit erkläre ich, die vorliegende Arbeit mit dem Titel

Search for electroweakinos using the ATLAS detector

Suche nach Elektroweakinos mit dem ATLAS Detektor

selbstständig verfasst zu haben und keine anderen als die in der Arbeit angegebenen Quellen und Hilfsmittel benutzt zu haben.

Eric Schanet

München, den 01. Mai 2021